UNIVERSITÀ DEGLI STUDI DI PALERMO
Dipartimento di Ingegneria

Enhancing Coastal Erosion studies: innovative methods and data integration

Pietro SCALA

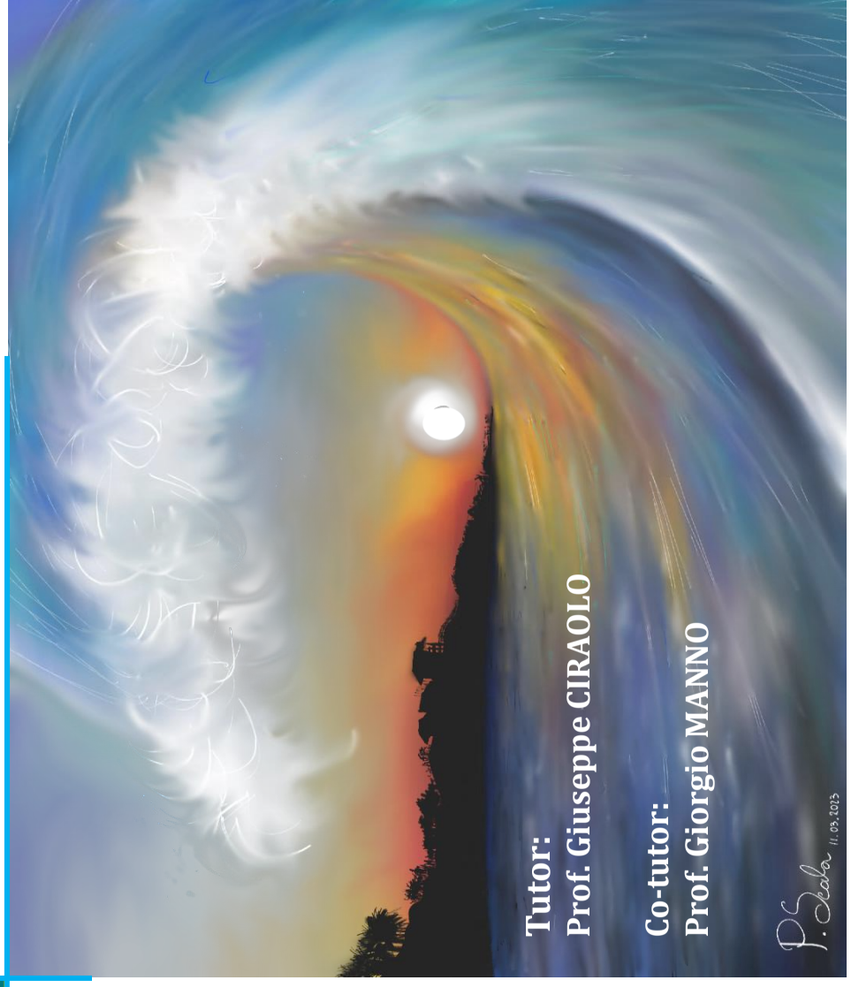

Palermo, 2025

CHEMICAL, ENVIRONMENTAL, BIOMEDICAL, HYDRAULIC AND MATERIALS ENGINEERING
XXXVII Cycle

Doctoral Thesis of ***Pietro Scala***

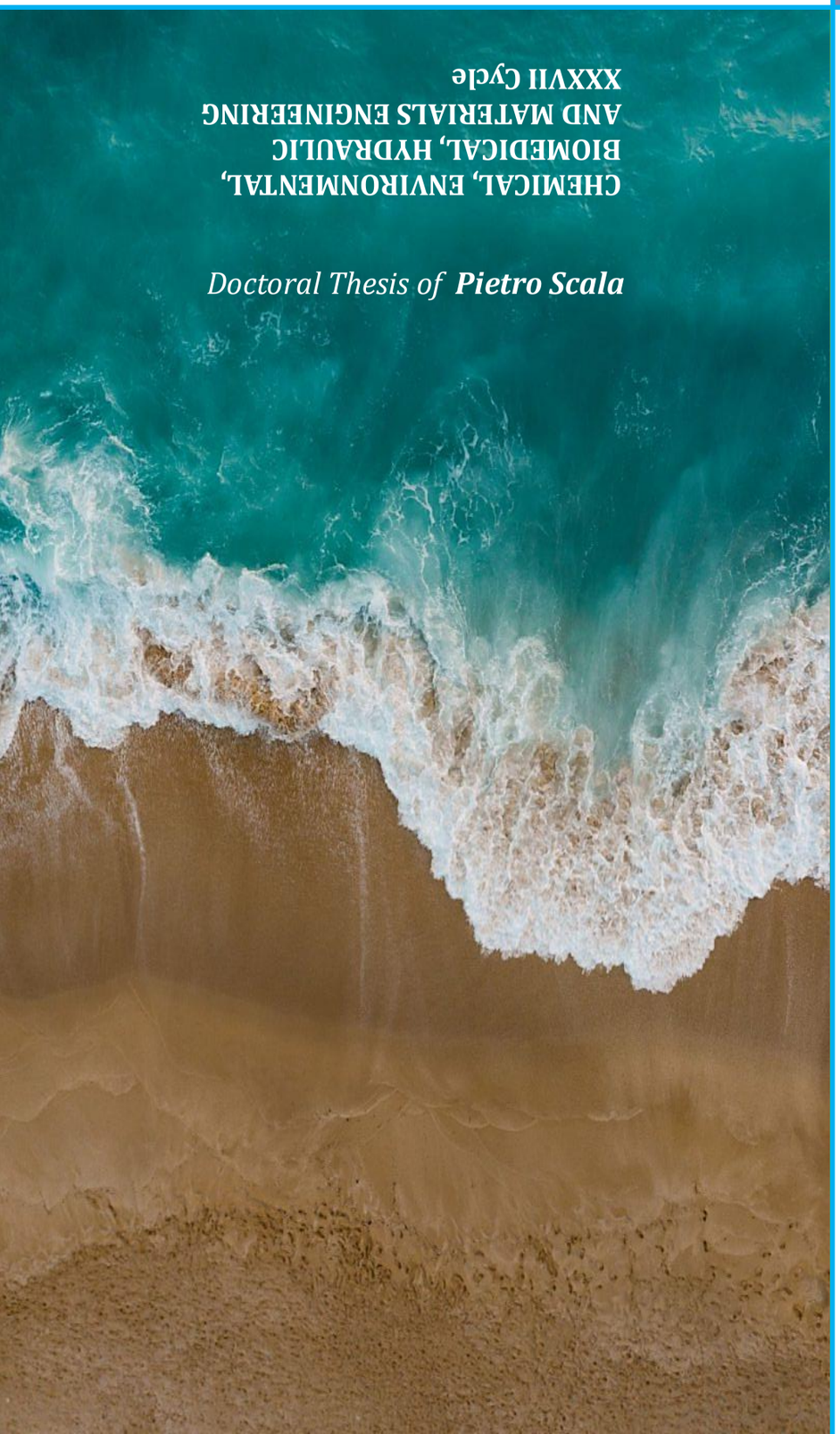

Enhancing Coastal Erosion studies: innovative methods and data integration

UNIVERSITÀ DEGLI STUDI DI PALERMO

PhD Course in Chemical, Environmental, Biomedical, Hydraulic and Materials Engineering

Dipartimento di Ingegneria

Settore Scientifico Disciplinare (CEAR-01/B)

Enhancing Coastal Erosion studies: innovative methods and data integration

PhD Candidate:

Pietro Scala

Phd Course Coordinator:

Prof. Giorgio Domenico Maria Micale

Supervisors:

Prof. Giuseppe Ciraolo

Co-Supervisors:

Dott. Geol. Giorgio Manno

XXXVII CYCLE

GRADUATION YEAR 2025

Ringraziamenti

Il completamento di questa Tesi di Dottorato è stato un percorso impegnativo ma ricco di soddisfazioni, che non sarebbe stato possibile senza il supporto e la guida di molte persone, a cui desidero esprimere la mia più sincera gratitudine.

Innanzitutto, desidero ringraziare il mio relatore, Prof. Giuseppe Ciraolo, per la sua preziosa guida, la pazienza, l'incoraggiamento, la fiducia e soprattutto l'immensa disponibilità che mi ha offerto durante tutta la mia ricerca. I suoi consigli e la sua competenza sono stati fondamentali per la realizzazione di questo lavoro, e sono davvero grato di aver avuto l'opportunità di imparare e lavorare da/con lui. Docente, ricercatore e persona come poche ce ne sono.

Un ringraziamento speciale va anche al mio co-relatore, Giorgio Manno, per i suoi suggerimenti sempre costruttivi e il suo supporto, che hanno contribuito in modo significativo a migliorare la qualità della mia ricerca. Lavorare con lui è stato ogni giorno sempre più piacevole e stimolante. Oltre che da un punto di vista professionale Giorgio si è distinto anche per le sue rare qualità umane.

Ringrazio anche al mio primo tutor di Dottorato, il Prof. Leonardo V. Noto, il primo a credere in me e nelle mie capacità e che ammiro per il suo modo di intendere l'insegnamento e la ricerca. Lavorare per un anno sotto la sua guida mi ha formato in questo mestiere nel periodo d'inizio e forse quello più delicato.

Un pensiero di riconoscenza va ai miei colleghi che hanno condiviso con me questo percorso durante tutte le giornate di lavoro… soprattutto durante i pranzi! Un ringraziamento speciale va a Dario Treppiedi e Francesco Alongi (i miei primi compagni di stanza e con cui ho iniziato) e Laura Corbari, per le chiacchierate e le pause noia condivise.

Ulteriori ringraziamenti a Giuseppe Cipolla, oltre che un collega un vero amico! Con lui è iniziato tutto (dalla Tesi Magistrale) e come in ogni cosa, ora che non lavora più con noi ne apprezzo maggiormente l'amicizia e ne sento di più la mancanza!

Grazie agli amici di "INCS", perché ci siete sempre stati e sempre ci sarete! Una menzione speciale va a Davide e Alessio, come diciamo sempre il "Triumvirato" non sarebbe lo stesso senza uno di noi tre! Un grazie di cuore va infine a Giulio, senza il suo preziosissimo supporto alcuni argomenti di questa Tesi non sarebbero stati gli stessi.

Uno dei più sentiti ringraziamenti va a zia e nonna, e soprattutto alla mia famiglia, i miei genitori e i miei fratelli, che mi hanno sostenuto in ogni momento con amore e comprensione. A voi, che avete creduto in me anche quando io stesso dubitavo, va la mia più profonda gratitudine. Grazie per avermi sempre incoraggiato a perseguire i miei obiettivi, anche nei momenti più difficili.

Desidero dedicare infine, ma non per importanza, un pensiero speciale a Verdiana, mia futura Moglie, il cui sostegno e amore sono stati fondamentali in ogni passo di questo percorso. Da quando ho iniziato il Dottorato, sei stata al mio fianco, condividendo gioie e fatiche, affrontando insieme le sfide che si sono presentate e celebrando i piccoli e grandi traguardi raggiunti. La tua pazienza, comprensione e la capacità di spronarmi anche nei momenti più complicati hanno reso tutto questo possibile. Sei stata la mia forza quando la motivazione vacillava, la mia ispirazione quando il lavoro sembrava troppo pesante e il mio sorriso quando serviva un po' di luce. Grazie per aver creduto in me e per aver reso questo "viaggio" speciale con la tua presenza. Questa Tesi è anche il risultato della tua vicinanza e del tuo affetto, e non sarei qui senza di te.

Questa Tesi è dedicata a tutti voi che, con il vostro supporto, avete reso possibile questo traguardo.

A mari inesplorati, spiagge insperate!

William Shakespeare

Index

List of Figures

List of Tables

List of equations

Abstract

Coastal erosion is a global environmental issue of growing significance, with considerable impacts on coastal ecosystems, infrastructure and human communities. Coastal environments are in fact dynamic ecosystems, continuously shaped by a complex interplay of climatic and anthropogenic factors that affect both shorelines and drainage basins. In recent decades, increasing human activities along coastal areas, coupled with the effects of climate change, such as rising sea levels and the heightened frequency and intensity of extreme weather events, have led to significant losses of land. As a result, awareness of the need for improved coastal zone management has grown considerably in recent years. This thesis addresses the coastal erosion main topic problem through a multidisciplinary approach, integrating predictive models, satellite analysis, socioeconomic assessments, and the development of innovative technical tools.

First, a Conv-LSTM model for forecasting meto-marine conditions is presented, with a focus on wave heights, period and direction, key forcing elements for erosion dynamics. Next, the use of a semantic segmentation model applied to satellite imagery allows monitoring of shoreline changes, an essential tool for long-term analysis. A socioeconomic analysis of coastal variations is then conducted through the creation of land cover maps covering a time frame from 1985 to 2022, with a focus on the entire Sicilian region.

Simultaneously, a plugin for QGIS is developed to facilitate Transect Based Analysis (TBA) of coastal variations using coastlines extracted from the segmentation model. The thesis finally includes the development approach and uses of a simulation model of shoreline trends following the construction of coastal defence works, validated through real case studies.

The results of this research Thesis provide a comprehensive and integrated view of coastal dynamics behaviours, offering useful tools for sustainable management and protection of coastal zones.

Chapter I

1.1 Introduction

Coastal zones are of strategic environmental, ecological and socio-economic importance (Mejjad et al., 2022; Zong et al., 2021). They provide critical habitats for many species, both marine and terrestrial, and play a key role in the conservation of global biodiversity (Mejjad et al., 2023; Setiyanto et al., 2022). Coasts also have a protective function, acting as natural barriers against extreme weather events such as storms and floods. Thanks to the presence of beaches, sand dunes, wetlands and coral reefs, wave energy is partially absorbed, reducing erosion and protecting inland areas from greater damage (Hernández-Delgado, 2024; Jordan & Fröhle, 2022).

From a socio-economic point of view, coastal regions are highly attractive and densely populated areas. Although they represent only a tiny fraction of the earth's surface, they are home to a large percentage of the world's population and to infrastructure that is crucial for sectors such as tourism, industry, fisheries and transport (Kim et al., 2021; Pomianowski & Doburzynski, 2021). It is estimated that around 10 % of the world's population lives in coastal areas, with urbanisation and population growth rates exceeding those of inland areas, especially in regions such as China and Bangladesh, where economic development has accelerated expansion into these areas (Liu & Balk, 2020; Zheng et al., 2020). The increase in human activities in coastal areas imposes the need for targeted and sustainable management, as these areas are subject to significant spatial and temporal variations due to both natural and anthropogenic factors. Planning and protection of these areas are, therefore, essential to balance their high ecological fragility with increasing socio-economic pressures.

In a country like Italy, with about 7500 km of coastline, of which about 30% is subjected to erosion (Celata & Gioia, 2024), proper management of coastal areas is essential. To implement good management practices, it is essential to understand the dynamic phenomena that affect the coastline and the factors that influence them.

In recent years, there has been a growing national and international awareness of the importance of the coastal strip not only for its environmental value, but also for its significant socio-economic impact, exacerbated by the challenges posed by climate change (A. k et al., 2023; McGranahan et al., 2007; Satta et al., 2017;

Toimil et al., 2020a). Consequently, the need has emerged to develop land planning and management strategies based on an accurate assessment of all the characteristics and dynamics (including those of the past) of the most distressed coastlines. This awareness has led to the dissemination of management principles that promote environmental sustainability, economic equity, social responsibility and cultural sensitivity, as indicated in the 2002 Recommendation of the European Parliament and Council on the implementation of Integrated Coastal Zone Management in Europe (2002/413/EC).

As already mentioned, the processes that regulate coastal dynamics are strongly influenced not only by natural phenomena, but also by human activities, as highlighted by Syvitski et al., (2009); Zhai et al., (2020); Zhao et al., (2021) studies. Human activities, ranging from the construction of artificial reservoirs, the extraction of river materials, reforestation, to the construction of port infrastructures and coastal defence works, have a direct impact on both catchment areas and coastal areas themselves (Cooper et al., 2020; Foti et al., 2020). The combination of reduced sediment supply and increasing shoreline rigidity due to the development of these activities has contributed to the occurrence of erosive phenomena along the coast (Franzen et al., 2021).

The effects of climate change, in particular the rise in sea levels and the increase in the frequency and intensity of extreme weather events, which amplify erosive phenomena (Franzen et al., 2021), are also contributing to the worsening situation.

In recent years, therefore, there has been a growing interest in coastal risk assessment methodologies, which are essential for the efficient management of areas at risk and for the proper allocation of economic resources dedicated to coastal protection, according to priority criteria (Morris et al., 2022).

To ensure effective planning and management of coastal areas, there is an increasing need to develop procedures capable of accurately assessing erosion risk, taking into account all factors involved and impacts related to climate change. For these assessments, however, the need for detailed and accurate data and methodologies is imperative.

To properly assess the overall process of coastal erosion, it is also necessary to consider the delicate dynamics of the coast, which is influenced by many natural and man-made factors such as:

- meteorological sea conditions, which, together with the characteristics of the seabed and the grain size composition of the sediments, determine the sediment transport processes in the foreshore zone;
- rising sea levels caused by melting glaciers due to global warming;
- the reduction of fluvial sedimentary inputs as a result of anthropogenic interventions such as the construction of dams or extraction of materials;
- the presence or absence of dune systems, which are the natural defence against erosion and which, today, are threatened by increasing urbanisation of the coastline;
- the influence of tides and sea currents, which in turn depend on variations in temperature and salinity;
- the presence of coastal works, which can alter the natural currents and, in some cases, help to exacerbate erosion;
- The presence or absence of trends of erosion or advancement of the coastline over time by means of specific studies and characterisations.

Therefore, the study of coastal erosion requires an integrated and multidisciplinary approach to fully understand the many parameters involved in the phenomenon.

For this reason, the following thesis aims to address the problem of coastal erosion through an integrated approach. The aim is to overcome the current difficulties in quantifying the parameters that influence this phenomenon, using innovative forecasting models, satellite data analysis and technical tools to monitor and predict coastal dynamics. The thesis is divided into sections, each of which contributes to outlining a more complete and accurate picture of coastal erosion, and to proposing solutions for its sustainable management. In particular, the structure of the thesis reflects the multidisciplinary nature of PhD research, and it is divided into a series of chapters, each one corresponding to a piece of research that has been published or is in the process of being published. Using advanced methodologies and innovative tools, the already published research makes significant contribution both in the development of tools for analysing and predicting coastal erosion, and in the creation and provision of the data needed to conduct such analyses. These studies cover both the prediction and monitoring

dimensions, providing essential information for effective understanding and management of erosion processes and their socio-economic impacts.

Due to the complexity of the topic addressed during the research period, the thesis was organized into several sections, each dedicated to a specific topic, described within a chapter.

The first objective of the research was to provide a brief review of the main parameters influencing coastal erosion phenomena, with a focus on shoreline detection techniques as an indicator of coastal erosion, their uses and a review of the main techniques for modelling littoral dynamics in coastal areas. (Chapter II)

Subsequently, attention was given to the development of a Conv-LSTM (Convolutional Long-Short Term Memory artificial neural network) model for predicting sea conditions that influence coastal erosion, such as wave heights, periods, and directions. This chapter lays the groundwork for understanding the sea forces that drive erosion and provides input for models used in later sections. (Chapter III)

Later, the focus shifted to the automatic extraction of coastlines using satellite imagery and Semantic Segmentation techniques. This innovative approach allows for monitoring the evolution of the coastline, offering crucial data for analysing long-term coastal changes. (Chapter IV)

Next, the analysis of socioeconomic impacts related to land cover changes was addressed, concentrating on the coastal regions of Sicily. By classifying satellite images from 1985 to 2022, this Chapter illustrates how changes in the coastal zones have affected human activities highlighting the economic and social impacts of reduced beach areas. (Chapter V)

A technical tool was then introduced, developed as a plugin for QGIS, which facilitates transect based analysis of coastlines. This tool automates the detection and classification of coastal variations and calculates indicators of coastal advancement or retreat, providing essential support for decision-making in management. (Chapter VI)

Finally, attention was also given to the simulation of shoreline dynamics following the construction of coastal defence structures, such as breakwaters and groynes. This chapter offers a quantitative assessment of the impact of artificial structures on erosion, valuable both for the design phase and for evaluating existing structures. (Chapter VII)

The thesis concludes with a summary of the findings from each chapter, discussing the significance of the methods and techniques applied to study and manage coastal erosion, and proposes perspectives for future developments in this field.

Chapter II

2.1 Overview of the coastal environment

The coastal environment or coastal zone can be defined as the area between the sea and the land, characterised by a constantly evolving ecosystem (REF). This evolution is influenced by a large number of factors, both natural and anthropogenic, which interact with each other and shape the morphological, physical and biological characteristics of the area. Therefore, the concept of "coastal dynamics" refers to the set of processes that govern coastal changes and evolution (*Earth Observations for Monitoring Marine Coastal Hazards and Their Drivers | Surveys in Geophysics*, 2020.). The coastal zone can be divided, from land to sea, into four areas shown in Figure 2.1.1: *i*) coast; *ii*) emerged beach; *iii*) submerged beach; and *iv*) continental shelf.

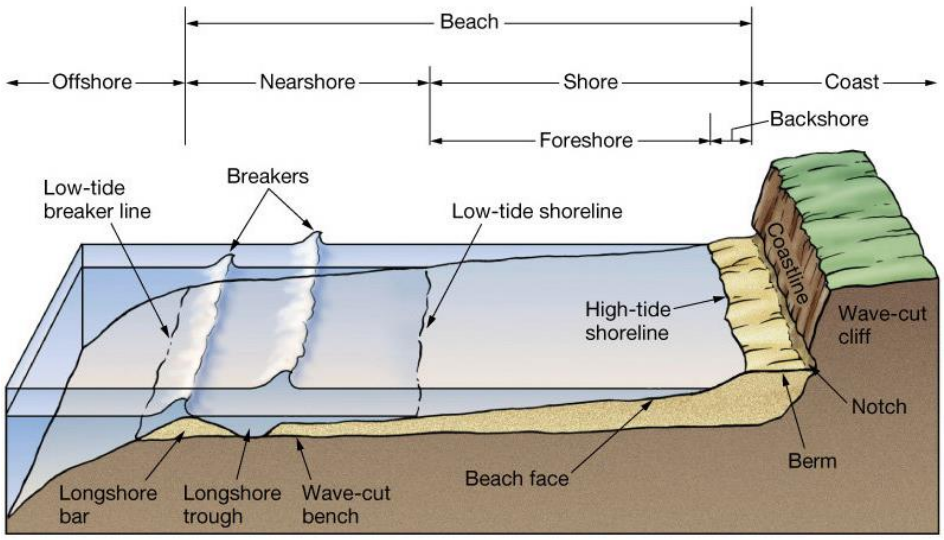

Figure 2.1.1 - Three-dimensional diagram of the coastal zone.

This subdivision is essential for a better understanding of coastal dynamics, which in turn influences how coasts can be classified. Coastal classification can be based on variety of criteria and, to date, there is no single universally accepted classification. Classification criteria may include:

- the geological origin;
- the age and durability of coastal materials;
- morphology;
- dominant processes;
- interaction with human activity.

The classification used in this thesis is a descriptive classification that divides them into depositional and erosion coasts, high or low. Deposition coasts are characterised by the accumulation of sediments, which may form beaches, sandy barriers, deltas (typically associated with river mouths) and lagoons. These types of shorelines are typical in areas where mainly sediment carried by rivers is deposited and this deposition is shaped by waves and sea currents.

In contrast, erosion coasts are dominated by processes that remove sedimentary materials from the shoreline, often due to wave action and currents in particularly energetic meteorological environments.

High coasts or cliffs rise above sea level and are found in areas of recent orogenesis, with magmatic or metamorphic origin. They can be hard (hardcliff) if they are made up of erosion-resistant rocks or soft (softcliff) if they are formed of loose, friable material that is easily changed by wave motion. Low coastlines, generally on the other hand, do not rise significantly and represent a continuation of the land without major changes in slope. In contrast, the opposite case occurs in the case of "marine terraces". Depending on their inclination, small changes in sea level can "cover or uncover" large areas of dry land. Low coastlines are found on cratons, very ancient lands shaped by past orogenies that led to their flattening. Low shorelines can be hard (shore platform) if they are evident in areas of strong tidal excursion, where the tide uncovers the continental shelf, or soft, i.e. sandy beaches. This thesis has looked more closely at the latter type of coastal environment.

2.1.1 The beach

The extent of beaches varies greatly: where they are close to rocky coastlines, they tend to form a narrow strip of loose sediment separating the rocky substrate from the sea, and then expand into small bays. Conversely, in lowland areas,

beaches may develop more widely, giving rise to vast dune systems. A particular type of beach is the so-called “pocket beach” - i.e. a beach confined between promontories or structures, characterised by the absence of longshore transport. These beaches are particularly vulnerable to processes that influence cross-shore dynamics, such as sea level rise (Castelle & Masselink, 2023).

Analysing the cross-sectional profile of the beach, we can divide it into three main zones:

- Backshore: This is the part exposed to the action of the sea only during storm events or when the tide reaches unusually high levels. It extends landward from the maximum high tide level and may be bounded seaward by ordinary berms formed by the deposition of sediment under normal wave conditions (Oliveira et al., 2024). Storm berms generated by extreme weather events may also be found within this area, together with sand dunes of wind origin, fed by dry sand from the backshore.

- Foreshore: This zone is subject to a continuous oscillation of the water surface due to wave and tidal motion and lies between the mean levels of high and low tides (Liu et al., 2024). It is further divided into two areas: the surf zone and the swash zone. In the surf zone, waves break, dissipating most of their energy and creating an area of turbulence bounded by the sea-side break-up point and the land-side run-down limit. The swash zone, on the other hand, is characterised by the alternation between surfacing and submergence of the beach, caused by the rising (run-up) and receding (run-down) phenomena.

- Submerged beach (Nearshore): This zone lies below the minimum low water level and extends to the depth limit, beyond which offshore conditions develop, where waves propagate without being influenced by the seabed. Longshore bars, separated by more inland areas, and channels perpendicular to the coast crossed by suction currents can also be observed in the nearshore zone.

Beaches can also be classified according to their slope:

- Dissipative beaches, which are characterised by low slope, fine sands and a large area of breakers.

- Reflective beaches, very steep and made up of pebbles, where waves tend to break near the shore.

- Intermediate beaches, which have a moderate slope precisely "intermediate" between the first two conditions.

The slope of the beach profile is mainly influenced by wave energy, increasing in direct proportion with the average wave height (Castelle & Masselink, 2023). Furthermore, sediment grain size has a significant impact on the degree of shoreline slope; in fact, sandy beaches tend to have low slope profiles (generally < 5°), while beaches with coarse sands or gravels, due to their high permeability and their geotechnical parameters such as internal friction angle and intercept cohesion, have steeply sloping profiles (> 5°).

During the backwash action of waves in the swash zone, which tends to transport sediments towards the sea, the high permeability of coarse sands and gravels mitigates this effect, leading to greater sediment deposition and hence higher slopes. Conversely, beaches with medium to fine sands, which are more sensitive to the action of the undertow, tend to have lower slope profiles and are often more stable than those with steep slopes.

From a sedimentological point of view, beach profiles generally show a decrease in grain size towards the open sea. Wave action acts selectively on solid materials according to grain size: larger and heavier particles tend to remain on the beach, while finer and lighter particles are set in motion by the waves and transported offshore. A more detailed discussion of the sedimentology of coastal areas and the movement of these in relation to waves is given in later chapters.

2.2 Sedimentary balance

To determine whether a coastline is subject to deposition or erosion, the sediment balance is used, which varies depending on the type and characteristics of the beach. The sediment budget (Figure 2.2.1) is an essential tool for analysing beach changes by estimating the main sources and losses of sediment.

Sediment sources include all inputs from both land and sea: sediment inputs from rivers, cliff erosion, wind transport, artificial spills and transport of sediment towards the beach, both parallel and perpendicular to the shoreline. Sediment losses, on the other hand, include landward transport by wind or storm surges past the dune line, offshore sediment run-off (both distributed and concentrated

through furrows), materials extracted from quarries on the shoreline, transport from the beach in both directions parallel and perpendicular to the shore, and wind erosion (Pranzini and Williams, 2021).

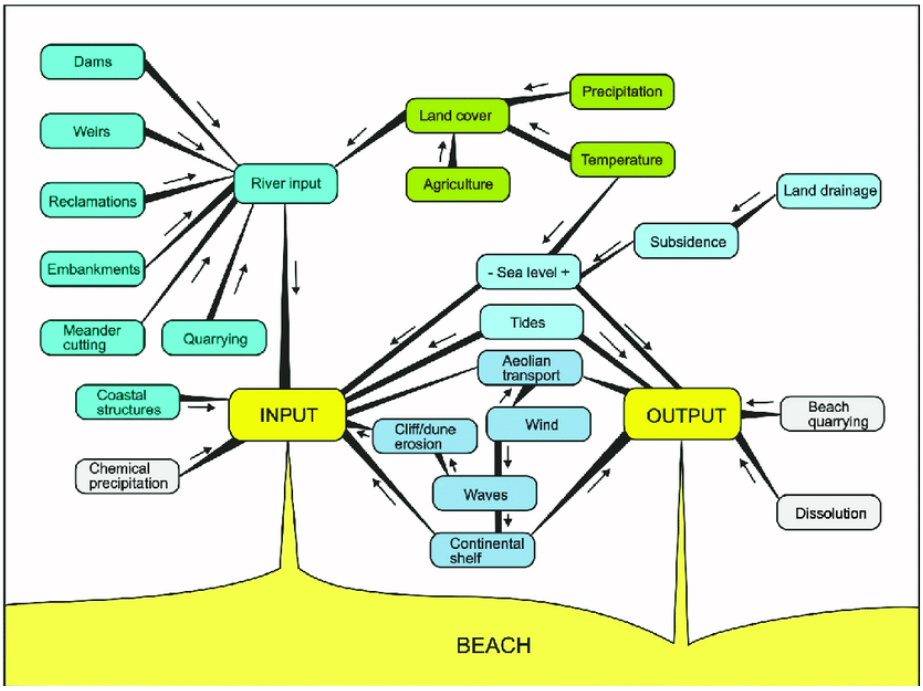

Figure 2.2.1 - Diagram of beach sediment balance Input and Output. The arrows show the direction of the process; the thickness of the lines increases and decreases depending on the effect (positive vs. negative) that each element has on the following (Pranzini, 2004a).

In sediment balance calculations, a beach is considered stationary when inputs equal outputs; if inputs exceed outputs, the beach grows by sediment deposition, while if outputs exceed inputs, the beach undergoes erosion. Again, human activities can significantly influence both sources and losses of sediment (Pranzini and Williams, 2021).

2.2.1 Coastal erosion process

Coastal erosion is the natural process by which material (such as sand, gravel, rock fragments) that makes up the coastline is removed and/or transported away,

leading to significant changes in the morphology of the coastline, causing beach reduction, dune retreat and loss of coastal habitats. The extent of this phenomenon is highly site-specific and can vary considerably from one area to another. It depends on several local factors, including the type of coastline in terms of exposure, tidal range, beach slope and the type of sediment in terms of composition, grain size, characteristics such as cohesiveness[1] , as well as the presence of coastal defence structures and human activity in the vicinity.

Although beach hydrodynamics and sedimentary processes are in fact three-dimensional phenomena, three-dimensional studies are still limited due to the technical difficulties and high costs associated with 3D modelling and data collecting. Three-dimensional simulations require a large amount of detailed data and significant computational capacity, which makes such studies less feasible (Alvarez-Cuesta et al., 2021; Toimil et al., 2020). However, for the purpose of engineering applications, the problem can be simplified by independently analysing longitudinal and transverse beach movements (Lim et al., 2022). Therefore, sediment movement can be studied by analysing the longitudinal (*longshore*) and transverse (*cross-shore)* components.

The former are mainly due to the presence of erosive and/or transport currents that can lead to deposition and hence accretion. These include tidal currents and wave-generated littoral currents. Tidal currents are periodic movements of the water levels due to the gravitational force exerted on the Earth by the Moon and to a lesser extent the Sun, generating significant sediment transport along the coastline. Littoral currents are currents generated by wind and waves that cause longitudinal movement of sediment along the coast. When waves break on the coast at an angle to the shoreline, they create littoral currents that transport sediment along the beach. This process is known as *littoral drift* or *littoral drift.* The strength and direction of the transport depend on the angle of incidence of the waves and their energy. Finally, the longitudinal components are influenced by anthropogenic factors: artificial structures such as jetties, breakwaters and dams can alter natural currents and influence sediment transport. These structures

[1] Particle cohesiveness refers to the force of attraction that holds sediment particles together. This property depends on the nature of the material, the presence of chemical binders and the interaction between the particles, influencing the sediment's resistance to erosion and compaction.

can create accumulation or erosion zones, altering the natural sedimentary balance (Silva et al., 2019).

Transverse sediment transport, i.e. the movement of sediment perpendicular to the coastline, on the other hand, is mainly due to several key factors. One of the most important of these is storm surges, which, favour the transport of sediment out to sea by hitting the coastline with greater force and often at an oblique angle. Another important role is played by *rip* currents, which are strong and narrow currents of water moving from the shoreline out to sea through wave breaking lines. *Rip currents* play an important role in coastal transverse erosion because they have the ability to transport large amounts of sediment from the beach out to sea, they can create deep erosion channels on the beach and in sandbars, and by interacting with other erosional processes such as waves and tides, they amplify transverse erosion (Thornton et al., 2007).

It is fair to say that the current coastlines are the result of coastal erosion and accretion phenomena that have occurred over time, contributing to a natural dynamic equilibrium. However, it is important to emphasise that this balance is often fragile and can easily be altered. Today, erosion is largely intensified due to human activities and climate change (McCarroll et al., 2024; Toimil et al., 2020).leading to an increase in the frequency and intensity of storm surges (McCarroll et al., 2024)resulting in more pronounced erosion. Recent studies show that the coastal area lost to erosion is significant - e.g. a global analysis found that from 1984 to 2015, the Earth lost approximately 28,000 km² of land area to coastal erosion, twice the land area gained over the same period (Luijendijk et al., 2018). This phenomenon is due to a combination of anthropogenic factors, including rapid urbanization and industrialization, and physical factors such as precipitation, wind erosion and wave action. Moreover, due to global warming and the ongoing rise in mean sea level, coastal erosion processes are expected to soon reach levels that will become extremely difficult to manage (A. de Gracia et al., 2018).

Coastal erosion can therefore have devastating impacts on infrastructure, human settlements and natural ecosystems. Sediment loss can lead to the destruction of coastal habitats, reducing biodiversity and compromising local economic activities. In addition, erosion increases the risk of flooding in inland areas, as eroded coastlines lose their ability to act as natural barriers to flooding from extreme events (Wahl & Plant, 2015).

To tackle the problem effectively, it is essential to understand the various processes that contribute to triggering this phenomenon and to study coastal erosion at the scale of the physiographic unit. Such a unit is defined as the area of coastline within which sediments are confined and where interchanges of material with neighbouring units can be considered zero. Physiographic units are delimited by natural structures such as headlands and canyons, or artificial structures such as groins and harbours. These structures reach depths comparable to the closing depth[2] of the beach, i.e. the depth at which the direction of sediment drift is reversed and the natural movement along the coast is interrupted.

2.2.1.1 Timescale of erosion processes

When dealing with erosion, it is crucial to distinguish between two-time scales of the phenomenon:

- short-term erosion;
- long-term, or structural, erosion.

Short-term erosion involves a temporary redistribution of sediment along the beach profile due to the rise in water level associated with storm surges. This type of erosion is a naturally occurring and usually cyclical phenomenon. A distinct summer and winter beach profile can be identified (Figure 2.2.2) (Hallermeier, 1980).

[2] The closure depth is a key concept in coastal morpho-dynamics, used to describe the depth beyond which sediment movement is negligible or absent due to wave and current action. In other words, it is the depth below which no significant change in the seabed profile occurs due to surface hydrodynamic processes.

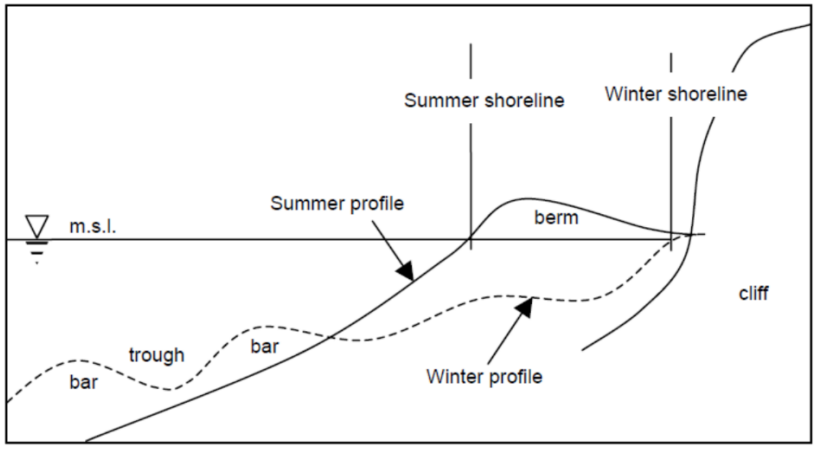

Figure 2.2.2 - Summer and winter beach profile (Seymour,R.J., 2005).

Summer and winter beach profiles show significant differences due to different wave conditions and seasonal currents in a climate such as the Mediterranean (Frihy et al., 2008). In summer, the waves are generally less energetic and shallower, allowing sediment to settle on the beach and leading to greater accumulation of the sand. This creates a wider, flatter beach, with a larger emerged area (berm) and a less pronounced beach slope. The generally calm summer conditions also favour the formation and stabilisation of coastal dunes, reinforced by vegetation.

In contrast, in winter, the waves are more energetic and higher due to storms and stronger winds, which erode sand from the beach and carry it offshore, forming underwater sandbars (bars). This leads to a narrower and steeper beach profile, with a more pronounced beach escarpment and a reduced surfaced area. Winter erosion can also reduce the size of the dunes, making them more vulnerable to wave and wind action. This means that the summer beach is characterised by more sand deposition, a wider and flatter profile, and stabilisation of the dunes, while the winter beach has more erosion, a narrower and steeper profile, and reduced or more vulnerable dunes.

Generally, during the erosion period, the eroded volume is significant, varying between 10 m^3 and 100 m^3 in a day, but in the summer period and in unaltered natural beach conditions the recovery to the original conditions should be complete (Casamayor et al., 2022).

Structural erosion, on the other hand, is more serious because it is progressive and permanent. The causes are to be found in human interventions. In Italy, in the 1960s, saw the greatest expansion of the building, industry, which required large quantities of sand and gravel, leading to an uncontrolled withdrawal of material from the beaches. Another anthropogenic factor that influenced the disruption of the natural dynamic equilibrium was the construction of hydraulic works (such as weirs or expansion tanks) along rivers that intercepted sediment transport, preventing sediment from reaching the beaches, as well as the construction of port jetties and inadequately engineered works. An even more worrying aspect is the location of many houses and civil structures, built not only near beaches, but in some cases directly on them, aggravating the impact of erosion. Illegal building has further accentuated this problem, with constructions that alter the natural balance of the coastline and contribute to the deterioration of the marine and coastal environment (Pranzini, 1992).

The volume of sand eroded can vary between 10 m^3 and 50 m^3 in a year, and although it is less than the amounts eroded in the short term, the irreversibility of the phenomenon in the long term is emphasized (Petti, 2021).

Both forms of erosion have important implications for coastal management. Seasonal variations in the beach profile require management strategies that consider the natural cycles of sediment deposition and erosion. At the same time, it is crucial to consider the long-term effects of human interventions and adopt sustainable solutions that mitigate structural erosion without further damaging the coastal ecosystem. Protection measures must be carefully planned to avoid interventions that could prove harmful, considering the natural dynamics and conservation needs of coastal environments.

2.3 Main factors of erosion processes

This section focuses on the detailed description and analysis of the main factors influencing coastal erosion processes (some of which have already been mentioned above) and is divided into sub-chapters for each element.

2.3.1 Sediment characteristics

Beach sediments, are fundamental elements in coastal dynamics and play a crucial role in erosion processes. Consisting mainly of sand particles, gravel, pebbles and other materials, sediments influence the stability and morphology of beaches, helping to protect coastal areas from erosive agents (Cunha et al., 2021).

Beach sediments vary mainly in terms of grain size, composition and spatial distribution. These characteristics influence the resistance to erosion and the ability of the beach to adapt to environmental changes (Rangel-Buitrago et al., 2018a).

It is therefore easy to see that the grain size of the sediments is one of the main factors determining the stability of beaches. Coarser sediments, such as gravel and pebbles, tend to resist erosion better than finer particles, such as sand. Beaches with fine grains are more susceptible to transport by waves and currents, increasing the risk of erosion. In fact, beaches with finer sediments tend to have low slope profiles, while those with coarser or pebbly sediments show steeper slopes. This relationship between grain size and slope is highlighted by Bujan et al., (2019) in which 2144 data points from 78 published studies were collected and analyzed. As shown in Figure 4, the data, which range from fine sand (0.07 mm) to medium-sized boulders (D_{50} =770 mm), indicate that with increasing grain size, there is a general trend of increasing beach slope. This trend is particularly evident for fine and medium sand, where the slope increases markedly, but becomes less clear for coarser sediments, especially in the boulder size range, where the paucity of data makes a definitive conclusion difficult.

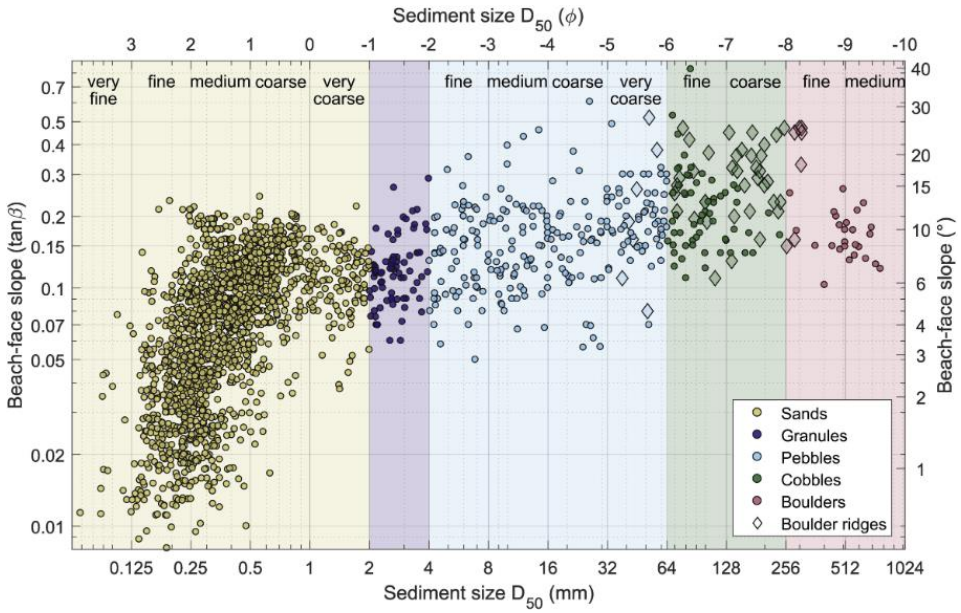

Figure 2.3.1 - Log-log plot of beach-face slope versus median grain size (Bujan et al., 2019).

Equally important is the chemical composition of sediments. Sediments composed of resistant minerals, such as quartz, tend to remain stable for longer than less durable materials (Abuzahrah et al., 2023). The presence of organic material or pollutants can alter the physical properties of sediments, affecting their ability to stabilize and protect the beach. In general, the predominant fraction of coastal sediments is quartz sand, which is chemically inert and very resistant to mechanical action; however, carbonates from the breakdown of organic structures, such as corals and shells, calcite, heavy metals, organic matter, silt and clay, may also be present, which obviously affect their specific gravity (*Trends and Composition—A Sedimentological-Chemical-Mineralogical Approach to Constrain the Origin of Quaternary Deposits and Landforms—From a Review to a Manual*, Geosciences, MDPI, 2020.). In the estimation of solid transport, reference is often made to the so-called relative density, given by the ratio between the density of the sediment and the density of the fluid in which it is immersed: for the most common sediments on our beaches, which consist mainly of quartz, the density of the sediment is approximately 2650 kg/m^3.

Finally, the distribution of sediments along the coast can vary considerably. Coastal areas with greater sediment deposition, such as river mouths, tend to have wider and more stable beaches, while areas with active erosion may have a shortage of sediment and greater vulnerability to erosion.

2.3.1.1 Sediment sources

Beach sediments can come from a variety of sources, each of which plays a key role in their availability and distribution.

The main source is rivers and streams which transport sediment from inland areas to the sea, contributing to the formation and maintenance of beaches (P. Wang & Beck, 2022). Variations in water flow, due to climatic factors or human activities (weirs, expansion reservoirs, dams), can affect the amount of sediment that is available and then actually reaches the sea mouth. Cliffs and coastal slopes are also a major source of sediment. Erosion of coastal rocks and soils generates material that is carried towards the beaches by waves and currents.

Dune systems, on the other hand, are the most important natural reservoir for the sedimentary replenishment of beaches.

Finally, human activities, such as the extraction of sand and gravel for construction purposes, can reduce the availability of sediment on beaches. This practice, combined with the construction of coastal structures, can compromise the natural supply of sediment and increase the risk of erosion. More details on these sediment sources and sinks are provided in the following paragraphs as factors of erosion processes.

2.3.2 Dunes

Coastal dunes represent geomorphological sand formations that develop along beaches and shorelines, playing a fundamental role in the processes of erosion and protection of surrounding areas (Gao et al., 2020). These natural features are formed by the combined action of wind, which lifts and transports sand particles, and waves, which deposit sediment along the coastline. Dunes are not only physical structures but are also habitats of great environmental and landscape value, being defined as “ecological niches” (Psuty, 2008).

Dunes (Figure 6) are dynamic systems, influenced by natural and anthropogenic factors, whose morphology can vary considerably in time and space (Sancho et al., 2011). They generally develop in littoral areas, under the aeolian accumulation of sediments, and can appear as linear structures parallel to the

shoreline, both vegetated and unvegetated. Their evolution and modelling are conditioned by interactions with the beach in front of them and by the presence of natural or artificial barriers that may influence sediment transport (Nordstrom et al., 1990).

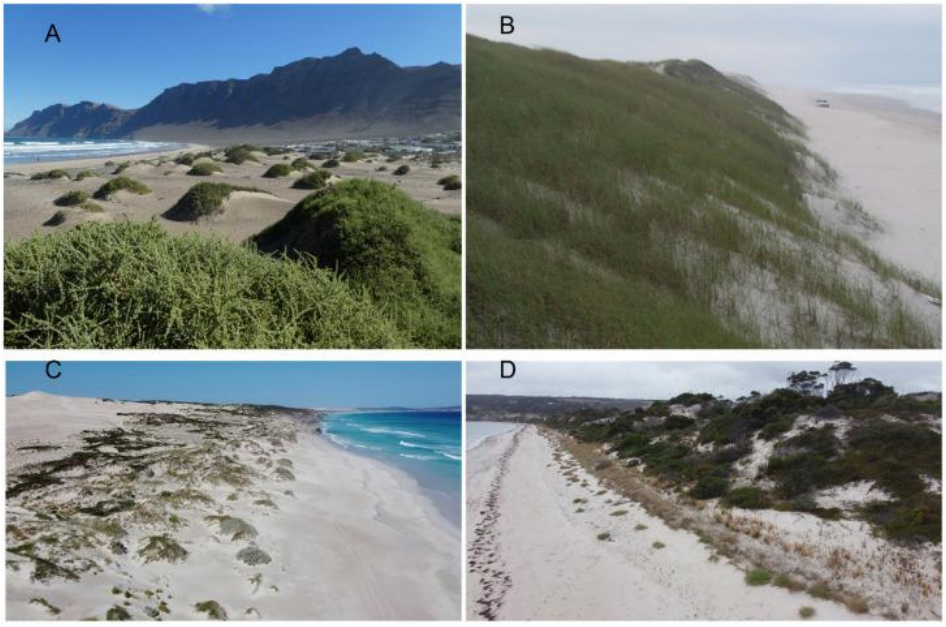

Figure 2.3.2 - Different dune configurations. In all subplots (especially in A, B, C and D), the presence of well-established and homogeneous dune vegetation can be seen.

In Figure 2.3.3, from Sampath et al., (2023) it is possible to see multiple aspects of protection constituted by the presence of dunes in the coastal environment, showing a conceptual schematisation of general dune evolution. In particular, coastal dunes increase the resilience of coastal systems (Du & Hesp, 2020; Gao et al., 2020) against erosion and flooding phenomena, acting as a sand reserve that can replenish beaches during intense storm surges. They represent a physical barrier that protects the territories behind them and an important hydro structure useful for containing salt intrusion (Konings, 1990).

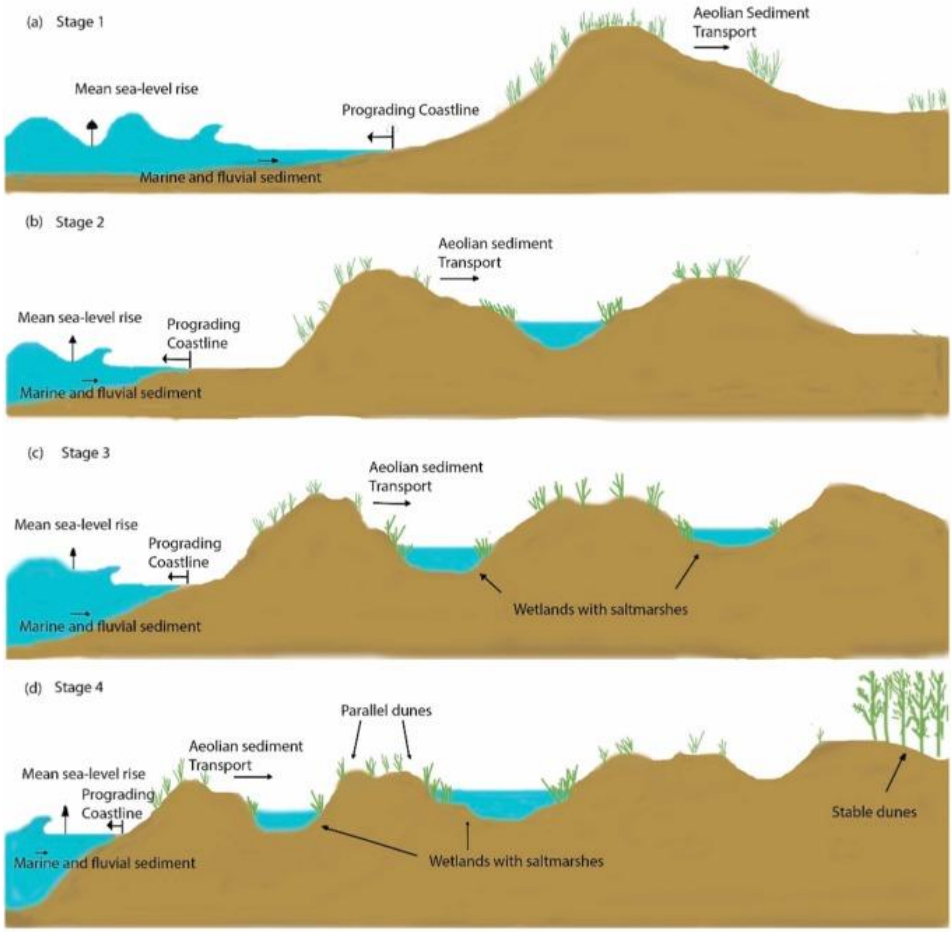

Figure 2.3.3 - Schematic diagram of dune evolution following the change in position and shape induced by the main environmental parameters (Sampath et al., 2023).

The dune ecosystem is characterised by strong environmental gradients; while rapid changes in abiotic factors, such as marine aerosol and salinity, are observed from the shoreline, the amount of organic matter and moisture in the soil increases with distance from the sea (Acosta & Ercole, 2015). These changes promote a zonation of coastal vegetation, with different floristic and structural compositions depending on the distance from the shoreline.

Vegetation adapted to live on sand plays a crucial role in the stabilisation and geomorphological evolution of dune systems. It prevents sand movement and favours the formation of embryonic dunes, making it the most stable vegetation zone (Figure 6). In fact, the presence of dune belts helps to attenuate the force of the wind, creating a microclimate favourable to the development of more stable plants, thus forming fixed dunes that can reach considerable size (Acosta et al., 2007).

However, coastal dunes are threatened by various factors, including climate change and anthropisation processes, which have led to the destruction of many dune systems, compromising the coastal balance and inducing beach and dune erosion (Cabrera-Vega et al., 2013; Cozzolino et al., 2017). Monitoring and management of these ecosystems, including through naturalistic engineering techniques, are essential for their conservation and to mitigate the effects of coastal erosion (Lo et al., 2017; D'Alessandro et al., 2020).

2.3.3 Tides and waves effects: currents and storms

Tides and waves are among the most crucial factors in coastal erosion processes, or more generally in the transport of solid material, as they directly influence the morphology of beaches and littoral structures. These two phenomena interact in a complex way, contributing to erosion, transport and sedimentation of coastal materials.

Tides are periodic variations in sea level caused mainly by the gravitational attraction of the Moon and, to a lesser extent, the Sun. These fluctuations in sea level generally occur twice a day and can vary considerably in amplitude depending on geographical location and local weather conditions. Tides affect shorelines in several ways.

The first mechanism of strike can occur by inundation and reabsorption. In practice, during high tide, coastal areas are temporarily inundated, allowing waves to reach portions of the beach that would otherwise remain dry (Tackley et al., 2023). This process favours the transport of sediment inland but can also contribute to the erosion of the lower part of dunes and reefs.

The second mechanism concerns beach erosion. In this case, the combined action of tides and waves generates a continuous alternation between erosion and sedimentation. During high tide, the force of the waves breaking on the beach can rapidly erode sediments, especially in areas where vegetation is absent or

damaged, as the wave breaking zone is enlarged (Luque et al., 2021). This behaviour is schematised in Figure 2.3.4.

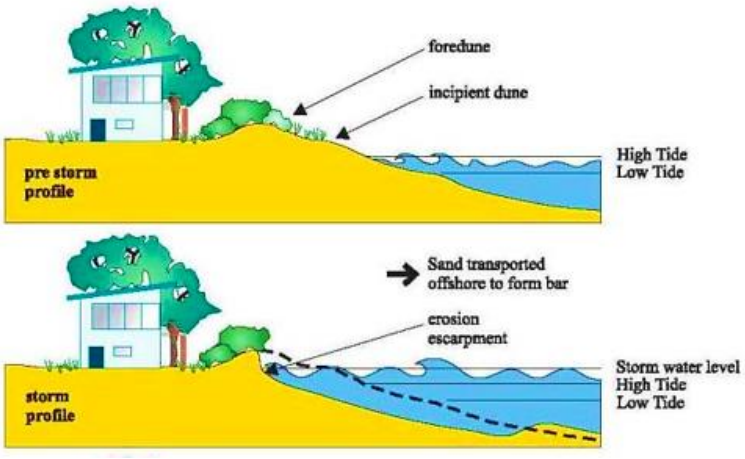

Figure 2.3.4 - Tide and storm erosion DLWC, NSW Gov, (2001).

Tides therefore create a dynamic environment in which the beach profile is constantly changing. Frequent sea level fluctuations can lead to a redistribution of sediment, affecting the shape and stability of beaches over time (Wells, 1995).

On the other hand, waves generated by winds blowing on the sea surface create movement in the water, which is converted into kinetic energy. They play a fundamental role in coastal erosion processes through the following mechanisms, breaking, cross and longshore transport and the interaction of the beach with storms.

The first phenomenon occurs when waves approach the coast and more specifically for beaches at the shoreline from the surf zone (Figure 2.3.5). The surf zone in fact represents the part of the beach where the waves break and dissipate. In this area, wave energy is higher and therefore the potential for erosion is high.

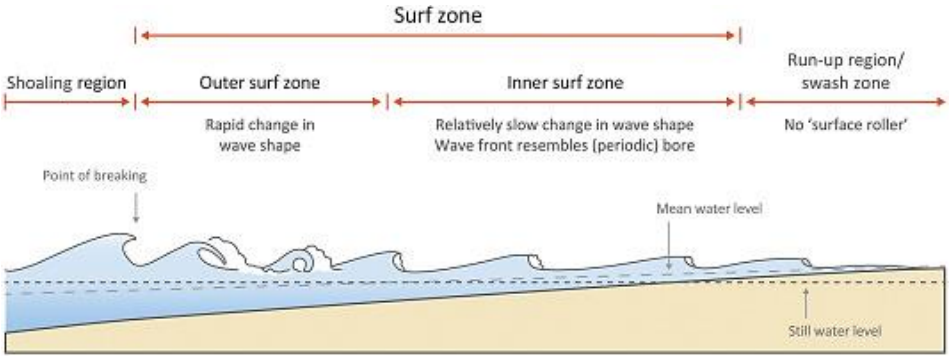

Figure 2.3.5 - Wave evolution in the surf zone (E. Power, 2020).

The morphological characteristics of the beach in this area can vary considerably depending on the intensity and direction of the waves. As waves reach shallower waters, their speed generally decreases, and their height increases until they break. This process, known as "breaking," releases a large amount of kinetic energy, which can erode beach and reef material, transporting sediment back out to sea via offshore currents. The types of wave breaking can be diverse and can be distinguished through the Iribarren number (Losada & Gimenez-Curto, 1979).

The equation for the Iribarren number is as follows (Equation 2.3.1):

Equation 2.3.1 – Iribarren number

$$\xi_0 = \frac{(\tan(\alpha))}{\sqrt{\left(\frac{H}{L_0}\right)}} \quad with \quad L_0 = \frac{g}{2\pi}T^2$$

where ξ is the Iribarren number, is the angle of the seaward slope of a structure, H is the wave height, L_0 is the deep-water wavelength, T is the period and g is the gravitational acceleration. All physical quantities can be seen in Figure 2.3.7. Depending on the application, different definitions of H and T are used, for example: for periodic waves the wave height H_0 at deep water or the breaking wave height H_b at the edge of the surf zone. Or, for random waves, the significant wave height H_s at a certain location.

As the number of Iribarren varies, the type of breakage varies, which can be surging or collapsing, plunging or spilling (Table 2.3-1 - Numerical values of the Iribarren number to identify the type of breaking wave. and Figure 2.3.6).

Table 2.3-1 - Numerical values of the Iribarren number to identify the type of breaking wave.

Breaker type	**ξ_0 -range**	**ξ_b -range**
surging or collapsing	$\xi_0 > 3.3$	$\xi_b > 2.0$
Plunging	$0.5 < \xi_0 < 3.3$	$0.4 < \xi_b < 2.0$
Spilling	$\xi_0 < 0.5$	$\xi_b < 0.4$

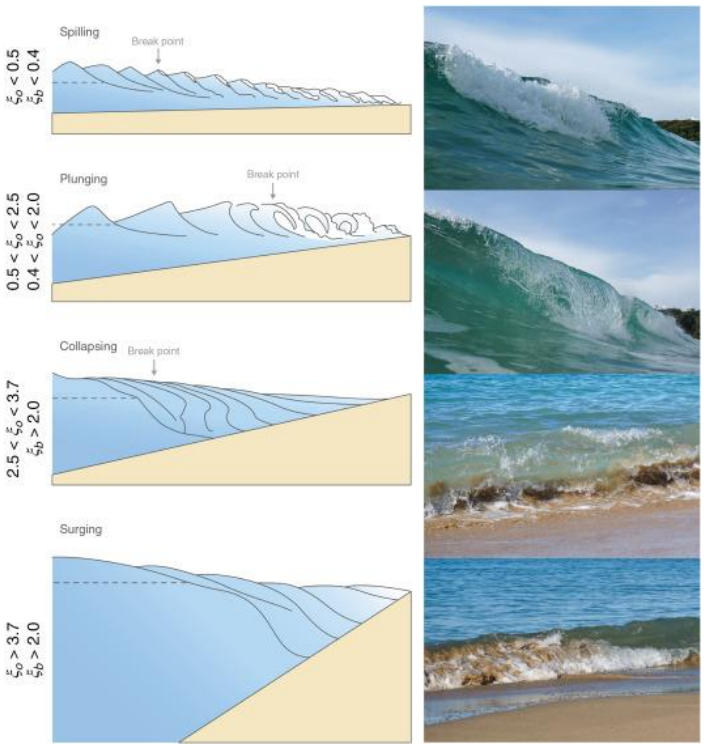

Figure 2.3.6 - The different types of breakage in relation to the Iribarren number. The column on the left shows a schematisation of the

fracture mechanisms while the column on the right shows actual images of the respective (E. Power, 2020).

In addition, the different amount of energy released by the waves in the surf zone can cause variations in sea level, generating two distinct phenomena: set-down and set-up (Figure 2.3.7). Outside the surf-zone, a slight depression of the mean sea level is observed, with the maximum lowering occurring at the breaking point, known as set-down, and which can generally reach a value of about 10 cm. Within the surf-zone, on the other hand, a rise in mean sea level, known as set-up, occurs due to both wave and wind action. The rise caused solely by waves is called wave set-up, while the rise caused by wind is called wind set-up. It has already been stated that when waves break, they dissipate a significant part of their energy. However, a part of this energy is converted into potential energy, resulting in the run-up phenomenon (Figure 2.3.7), i.e. the rising of the water mass along the beach or coastal defence works. The run-up represents the highest point reached by the water relative to the mean sea level and is composed of two elements: the set-up, which represents the change in the mean level, and the swash, which is the maximum fluctuation of the water.

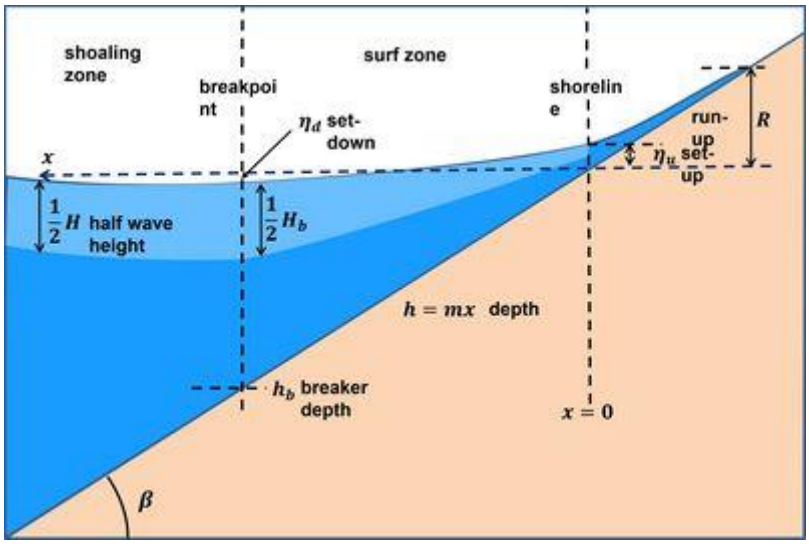

Figure 2.3.7 - Schematisation of set up, set down and run up.

The correct assessment of run-up and set-up is essential for understanding coastal erosion and flooding risks and for planning protection measures. Run-up, which contributes to beach and coastal dune erosion, can be estimated using analytical

formulae and statistical techniques. Again, to calculate the run-up, reference can be made to the formulation proposed by Maze (Equation 2.3.2) (2006) in which a key parameter is the Iribarren number.

Equation 2.3.2 – Run-up equation

$$R_{u(2\%)} = 1.86\,\xi_0^{0.71}\,H_0$$

This formula considers both the characteristics of the waves offshore and the slope of the beach and makes it possible to estimate the run-up value exceeded by 2% of the waves reaching the coast.

The dissipation of wave energy and the upwelling of waves on the beach have a direct effect on sediment transport.

In contrast, littoral transport, which concerns the movement of sediments near the shore, is a three-dimensional phenomenon that significantly influences coastal erosion and beach morphology. Although complex, it is often divided into two main components: longitudinal transport, parallel to the shoreline, and transverse transport, orthogonal to it. Longitudinal transport is related to long-term morphological changes of the shoreline and as already mentioned, is triggered when waves do not hit the shore uniformly and orthogonally, but at an angle to the shoreline. This causes a lateral movement of sediments along the beach. Transverse transport, on the other hand, mainly affects seasonal phenomena and short-term changes in the beach profile, often associated with storm surges. In this context, the determination of the closure depth (Figure 2.3.8) is essential for understanding coastal dynamics and is estimated using formulae such as Hallermeier's (1981) (Equation 2.3.3).

Equation 2.3.3 – Hallermeier depth of closure

$$h_c = 2.28\,H_{12h} - 68.5\left(\frac{H_{12}^2}{gT^2}\right)$$

Where H_{12h} is the effective wave height just seaward of the breaker zone that is exceeded for 12 hours per year - i.e. the significant wave height with a probability of yearly exceedance of 0.137%, T is the wave period associated with H_{12h}, and g is the acceleration of gravity.

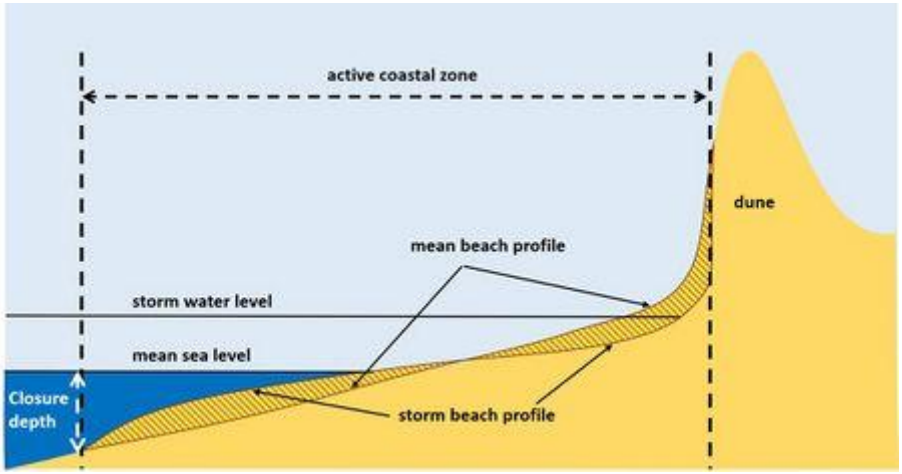

Figure 2.3.8 - Schematic representation of the active coastal zone for a dune coast and cross-shore sand redistribution for alternating storm and mild weather conditions.

Sediment may be transported by rolling, skipping, sliding or in suspension, depending on the speed of the current and the nature of the sediment. If part of the sediment is transported beyond the closure depth, however, this part generally does not return to the littoral sediment budget. Several theories and models have been developed to estimate longshore solid transport, such as the CERC formula (Shore Protection Manual, 1984), Kamphuis (J. Kamphuis, 1996), Van Rijn (van Rijn, 2011), CROSMOR 2000 (Grasmeijer & Kleinhans, 2004) (Table 2.3-2 - Summary of longshore sediment transport discharge formulas.).

Table 2.3-2 - Summary of longshore sediment transport discharge formulas.

Equation	Year	Formula	Variables
CERC formula	1984	$Q_{vol} = K\frac{\rho}{(s-1)\gamma_w}(H_{s,br})^{2.5}\sin(2\theta_{br})$	• $Q_{t,vol}$: Net volumetric transport of sediment along the coast (m^3/s). • K: Empirical calibration coefficient, usually 0.39 in marine environments. • ρ: Density of water (approx. 1025 kg/m^3 for seawater). • s: Ratio of sediment density to water density, usually about 2.65 for quartz sand. • γ_w: Unit weight of water (approx. 9810 N/m^3). • $H_{s,br}$: significant wave height at the breaker (m), i.e. the height of the waves when they break. • θ_{br}: Angle of incidence of waves at the breaker (in degrees).
Kamphuis formula	1991	$Q = 2.33(T_p)^{1.5}\, tan(\beta)^{0.75}\,(d_{50})^{-0.25}(H_{s,br})^2[\sin(2\theta_{br})]^{0.6}$	• $Q_{t,im}$: Longshore sediment transport (kg/s) • Tp: Peak wave period (s) • tanβ: Beach slope • d50: Median particle size (m)
CROSMOR2000 Model	2000	$Q = K1(H_{s,br})^{2.5}\, v_{wavel},\ with\ v_{wavel} = K2(gH_{s,br}^{0.5}\sin(2\theta_{br})$	• $Q_{t,mass}$: Longshore sediment transport (kg/s) • $V_{wave,l}$: Longshore current velocity (m/s) • g: Gravitational acceleration (m/s^2)
Van Rijn	2014	$Q_{mass} = 0.023(1-p)\rho_s g^{0.5}(\gamma_{br})^{-0.51}(H_{s,br})^{2.5}\sin(2\theta_{br})$	• p: porosity; • γ_{br}: breaking coefficient.

In parallel, coss-shore transport is more complex to quantify and depends on storm conditions, influencing the seasonal profiles of the beach, with berm profiles in summer and bar profiles in winter. There are specific models for this type of transport too, such as Dean's model (Dean & Dalrymple, 2004), which allows the intermediate profile between summer and winter, known as the equilibrium profile, to be estimated from the beach grain size, or Bailard's model (Bailard, 1981), which considers a combination of factors such as speed and bottom slope, and Larson & Kraus's model (*Analytical Solutions of One-Line Model for Shoreline Change near Coastal Structures | Journal of Waterway, Port, Coastal, and Ocean Engineering | Vol 123, No 4*, 1997), which takes into account the redistribution of sediments within the same sedimentological cell. These transport phenomena influence the shape of beaches and lead to significant changes in coastal configuration, creating areas of accumulation and erosion. If the shoreline is not disturbed from its natural equilibrium conditions, erosion and accretion phenomena generally remain stable and compensate. The presence and influence of protection or increases in the severity of marine weather forcing (e.g. climate change) can generally lead to a change in the equilibrium of the sediment budget, resulting in distinct areas of erosion and accretion that can no longer exchange sediment.

Finally, the influence of storms on the coast is briefly described. During extreme weather events, such as storms and hurricanes, waves can reach considerable heights and cause severe erosion. Storm surges can lead to significant beach abatement, destroying dunes and causing flooding in the areas behind them.

The interaction between tides and waves is therefore fundamental to understanding coastal dynamics, especially in areas of high tidal excursion. Changes in sea level affect the intensity with which waves hit the beach, and vice versa, waves can change the profile of the beach, influencing the areas that are inundated during tides. This complex interaction is essential for coastal management, as changes in tidal patterns or wave regimes can lead to increased coastal erosion, requiring protection or restoration.

2.3.4 River sediments

River sediments play a crucial role in the dynamics not only of rivers but also of coastlines, significantly influencing the morphological evolution of river basins and the coastal areas into which they flow. These sediments, consisting of particles of varying size and nature, are transported by watercourses through erosive processes involving the river bed, banks and drainage basins. They can

be divided primarily into cohesive and non-cohesive sediments, depending on their granulometric nature, with transport occurring by sliding, rolling, hopping (bedload) or suspension (suspended load). The mobility of river sediments is governed by hydrodynamic factors, such as current velocity, river slope and flow rate, as well as the geological structure and type of sediment present along the watercourse.

The process of river erosion occurs when the energy of the water overcomes the resistance of the material in the riverbed or banks, causing the mobilisation of sediments. These sediments are then transported downstream, contributing to changing the longitudinal profile of the watercourse and influencing, in the long term, the morphology of the riverbed and floodplains. A graphic description of this behaviour is shown in Figure 2.3.9.

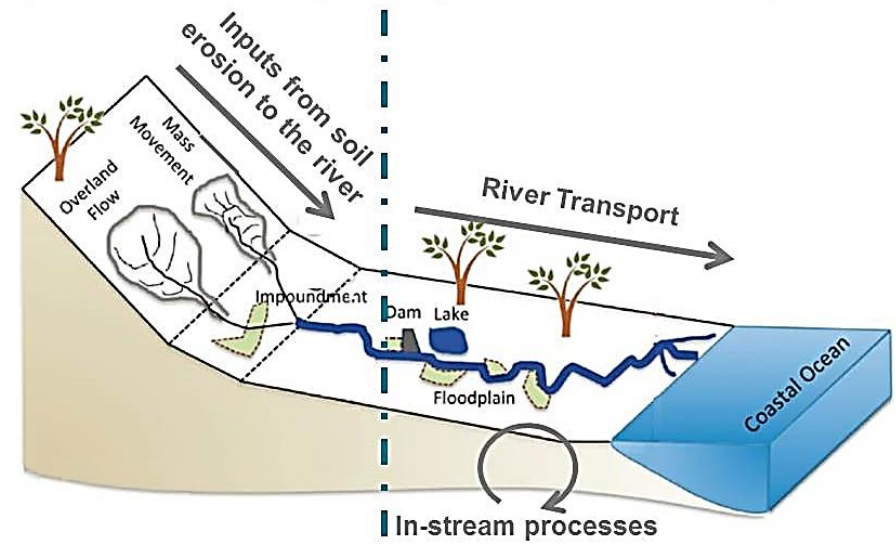

Figure 2.3.9 - Overview of the concept of soil loss erosion and transport to coastal areas.

In rivers with a torrential regime or those characterized by a high gradient, sediments tend to consist of coarse material such as gravel and pebbles, while in low gradient rivers with slower currents, sand, silt and clay prevail.

One of the fundamental aspects of river sediment transport is the seasonal variation of flow rates. During floods, the increased flow velocity increases the

transport capacity of the river, mobilizing large quantities of sediment and promoting erosion of the riverbed and banks. In lean periods, on the other hand, the erosive capacity decreases, with sediment accumulating along the watercourse. This alternation of erosion and deposition is the basis for the formation of various geomorphological features, such as river bars, temporary islands and deltas in the terminal sections of rivers.

River sediment transport is also influenced by the characteristics of drainage basins, such as land use, the presence of vegetation and the amount of rainfall. For example, in catchments characterized by large urbanized or agricultural areas, reduced vegetation cover and increased surface runoff can intensify erosion and, consequently, river sediment load. The introduction of dams, reservoirs, weirs or other hydraulic infrastructures along the watercourse can drastically alter sediment transport, favouring sediment deposition upstream of the works and reducing sediment load downstream, affecting coastal areas.

Another critical issue is the contribution of river sediments to coastal balance. In natural systems, rivers are one of the main sources of sediment for beaches, helping to counteract coastal erosion phenomena in a natural way. Reductions in the sediment load carried by rivers, due to human intervention or climate change, can have significant impacts on coastal erosion. For example, the decrease in river sediments in deltas, due to the construction of dams and the extraction of sand and gravel from rivers, has in many cases led to rapid coastal retreat and loss of coastal habitats.

2.3.5 Climate change effects on coastal areas

Climate change, mainly caused by global warming, has a direct and significant impact on coastal erosion. Rising global temperatures, as highlighted by the Intergovernmental Panel on Climate Change (IPCC), are accelerating the process of sea level rise, which has seen an average rise of about 20 cm between 1901 and 2018, with the rate continuing to increase in recent years. According to the Special Report on the Ocean and Cryosphere (SROCC), the rate of sea level rise has increased from 1.4 mm per year during the 20th century to an average of 3.6 mm per year between 2006 and 2015 (Stocker & Qin., 2013). This rise is the result of phenomena such as the melting of the Greenland and Antarctica ice caps, which alone contributed more than a third of the total rise, and the thermal expansion of the oceans due to warming waters.

The increase in the frequency and intensity of extreme weather events, such as storms and hurricanes, is exacerbating problems in coastal areas, increasing wave energy and promoting the erosion of beaches and reefs. It is estimated that annual coastal flooding, currently affecting about 100 million people, could affect up to 280 million people by 2,100 under the scenario of the highest sea level rise (RCP 8.5). The combination of these phenomena is leading to increased vulnerability of coastal areas, with an increasing risk of flooding and land loss (Toimil et al., 2020).

Future projections are worrying according to scenarios presented by the IPCC (2022), sea levels could rise by more than one metre by the end of the 21st century in the worst-case scenario, with devastating impacts on many coastal areas. The RCP 8.5 scenario (Figure 2.3.10) predicts that, by 2100, sea level rise could exceed 1.1 metres, further exacerbating erosion and endangering not only natural ecosystems, but also human settlements and infrastructure.

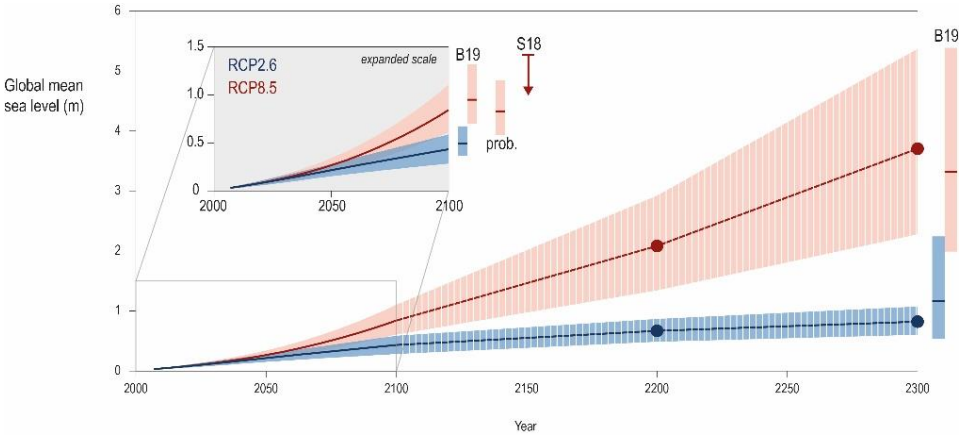

Figure 2.3.10 - Projected Sea level rise (SLR) until 2300. The inset shows an assessment of the likely range of the projections for RCP 2.6 and RCP 8.5 up to 2100 (medium confidence) IPCC report (2022).

Coastlines that already suffer from a reduced input of river sediments due to human activities are particularly exposed, as they cannot naturally compensate for accelerated erosion.

In this context, sustainable resource management and mitigation policies are crucial to address the effects of climate change and protect coastal areas.

Adaptation measures, such as the restoration of coastal ecosystems and the construction of resilient infrastructure, are key to reducing risks related to sea-level rise and extreme weather events.

2.3.6 Coastal defence works effects

As mentioned above, over the years coastal erosion has been a challenge for all coastal areas in the world. When the phenomenon of beach retreat reaches a critical level, threatening infrastructure, housing or areas of significant economic and environmental interest, it becomes necessary to take concrete measures to counter this process. However, it is crucial that such interventions are not dictated by urgency or the immediate pressure of catastrophic events that have already occurred. Improvised solutions risk further altering, and have altered, the natural balance of the coast, aggravating the problem rather than solving it (Gracia et al., 2018). Conscious and well-designed planning is therefore essential to effectively address coastal erosion. Strategic, adaptive and sustainable approaches are needed, taking into account both natural dynamics and anthropogenic activities. A proper assessment of site conditions and ongoing erosion dynamics allows the most appropriate intervention to be identified, avoiding irreversible damage to coastal ecosystems. This integrated approach must take into account the specific characteristics of the area concerned, while also considering the needs of the infrastructure and coastal communities living there.

Coastal defence measures can be classified into two main categories: hard and soft solutions. The former are artificial, permanent structures designed to directly counter erosion by building physical barriers; the latter, on the other hand, aim to work with natural processes, promoting ecological resilience and sustainability. The choice between these two categories depends on multiple factors, including the urgency of the intervention, the coastal sediment transport, coastal morphology and the importance of the tide.

Rigid works (Figure 2.3.11) include breakwaters, artificial reefs and groynes. These works aim to dissipate wave energy, thus reducing the erosive impact on the coast. Artificial reefs, for example, are made of boulders or prefabricated materials and play a fundamental role in defending the coastline by absorbing the force of the sea. Groynes, on the other hand, are transverse structures designed to trap sediments transported along the coast, helping to stabilise beaches. However, such works, if poorly designed, can cause undesirable effects such as erosion in the leeward area, so a correct assessment of their length and distance is fundamental (Foti, 2006).

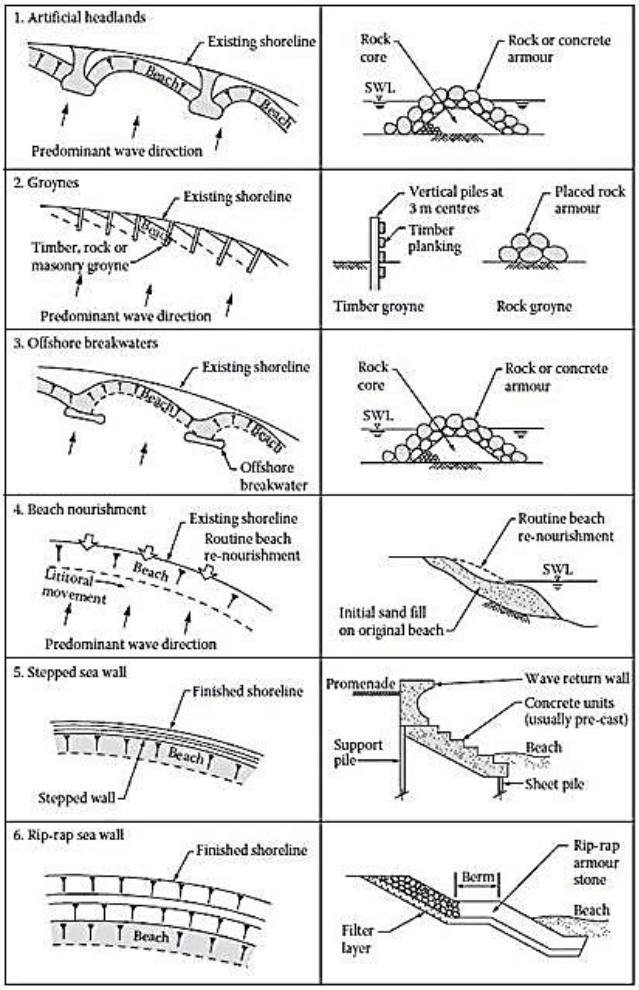

Figure 2.3.11 - Common types of coastal protection structures (Boateng & Bray, 2014).

On the other hand, soft works represent a more sustainable and environmentally friendly approach. Beach nourishment (Figure 2.3.12), for example, consists of adding sediment to the eroded area, seeking to restore the natural balance of the shoreline. Although less invasive than hard structures, this technique requires careful planning to ensure that the materials used have similar characteristics to those of the original sediments. For example, using materials that are too fine will

result in rapid sediment dispersal, while those that are too coarse can significantly alter the appearance and functionality of the beach.

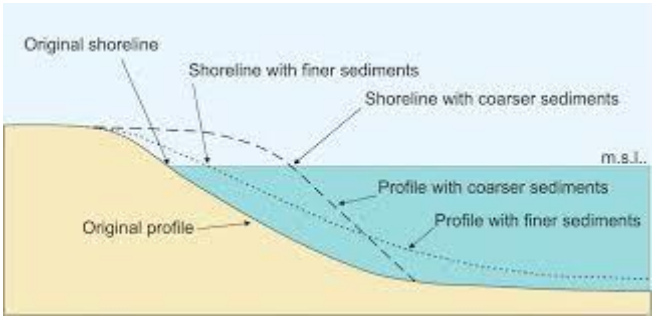

Figure 2.3.12 - Beach renourishment visual explanation. The figure shows the final equilibrium setting of the beach profile using different grain sizes diameters (from Interreg Italy-Croatia, Adriadapt - https://adriadapt.eu/adaptation-options/beach-nourishment/).

In addition to more traditional interventions, there are also unconventional solutions that are gaining more and more attention for their effectiveness and lower environmental impact (Figure 2.3.13). Dewatering, for example, is a technique based on removing interstitial water from coastal sediments, increasing beach stability and reducing erosion. The use of algal mats, which promotes sedimentation and stabilises sediments through the roots and fronds of algae, is another interesting innovation. This technique not only helps to mitigate erosion, but also enriches the marine environment in terms of biodiversity and water quality.

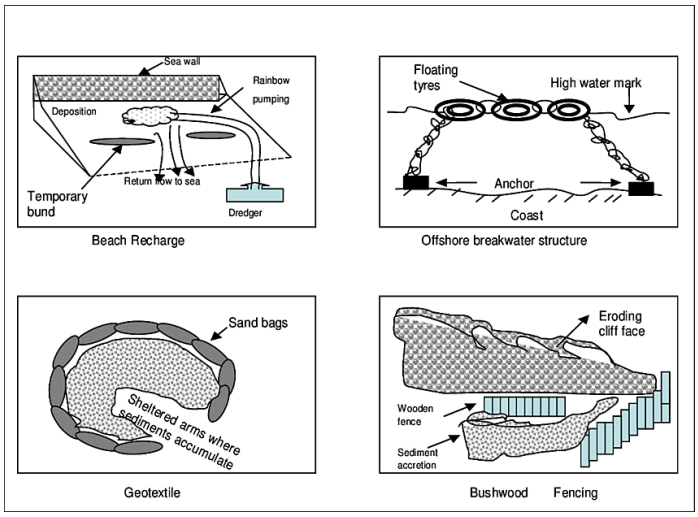

Figure 2.3.13 - Soft coastal protection structures (Boateng & Bray, 2014).

These “soft” approaches are often less environmentally impactful and can offer long-term benefits such as ecosystem protection and biodiversity enhancement. However, they require constant maintenance, with often high costs, and require careful monitoring to ensure their effectiveness over time (Petti, 2021).

Rigid structural works offer immediate protection against erosion but have a significant visual and environmental impact (Smith et al., 2010). The construction of breakwaters, seawalls or groynes can adversely affect natural sediment transport, causing increased erosion in adjacent unprotected areas. In addition, these structures are often difficult to remove or modify once built, making it necessary to carefully assess their possible long-term consequences. In fact, these types of works have an indirect interaction with sediment dynamics as they directly interfere with the wave regime (Black & Andrews, 2001). The interaction between waves and coastal structures can manifest itself mainly through two physical phenomena: reflection and diffraction (Sorensen et al., 2006). Reflection occurs when waves encounter an obstacle, such as a cliff, wall or artificial barrier. Some of the wave energy is reflected, creating a backward wave train that overlaps the incident wave train. In extreme cases, such as with vertical impermeable walls perpendicular to the wave motion, the reflection can be almost total, creating standing waves with twice the amplitude of the original wave (Mei et al., 2005; Goda, 2010). Partial reflection, on the other hand, occurs with less rigid or inclined structures, where only a fraction of the energy is reflected, while

the rest is dissipated or transmitted. Diffraction, on the other hand, occurs when waves encounter geometric discontinuities, such as harbour inlets or detached submerged or emerged barrier batteries (Holthuijsen, 2007). This phenomenon causes a dispersion of the wave energy, which redistributes along directions perpendicular to the original one, creating circular waves that propagate in the so-called “shadow zone” of the obstacle. As these circular waves move away from the obstacle, their height rapidly decreases, reducing the erosive effect on the area behind. Both phenomena, reflection and diffraction, play a crucial role in the design of coastal defence works, influencing both the stability of structures and the morphology of surrounding beaches (Dean & Dalrymple, 2004).

Among rigid structures, submerged barriers represent a solution that seeks to minimise visual impact by attenuating wave energy without significantly altering the coastal landscape. However, they are generally less effective than emerged barriers and may present hazards to navigation, thus requiring appropriate signalling.

The choice between hard and soft solutions depends mainly on the specifics of the coastal context and the long-term objectives of the intervention. While hard structures provide more immediate and lasting protection, soft solutions tend to be more ecologically and environmentally sustainable but require greater investment in terms of maintenance and monitoring.

Finally, in many cases, the combination of both solutions, such as beach nourishment coupled with groin construction, may be the most effective approach, especially in those areas where erosion is particularly intense. Such a combination makes it possible to obtain the immediate benefits offered by rigid structures, while reducing the long-term negative impact through integration with more natural and adaptable solutions.

2.3.7 Vegetation and Land Use

The loss of coastal vegetation and changes in land use are two of the most significant anthropogenic factors in accelerating coastal erosion (Chapman, 2016). Natural vegetation, such as dunes covered with pioneer plants, mangroves and salt marshes, but also submerged vegetation (Figure 2.3.14) plays a key role in coastal protection (Chapman, 2016).

Figure 2.3.14 - Submerged coastal vegetation.

When this vegetation is removed or degraded, the coastal territory becomes more vulnerable to erosive phenomena, especially in the presence of extreme weather and sea events (Figure 2.3.15). In parallel, changes in land use, often related to urban sprawl, intensive agricultural activities and tourism development, can further exacerbate erosion by altering the natural dynamics of sediment transport and reducing the resilience of the coastline to erosive forces. Coastal vegetation acts as a natural barrier against erosion. Plant roots consolidate soil and contribute to the stability of dunes and littoral soils, while vegetation cover reduces the direct impact of waves and wind. Species such as mangroves and herbaceous plants growing on dunes are particularly effective in intercepting sediment and dissipating wave energy. Mangroves, found mainly in tropical and subtropical areas, provide protection against coastal erosion through a combination of physical and biological effects. Their intertwined roots create a natural barrier that slows the flow of waves and tides, reducing water velocity and promoting the deposition of suspended sediment. In this way, mangroves help counter erosion and maintain coastal morphology. However, the deforestation of mangroves to make way for activities such as the construction of urban settlements or aquaculture facilities has led to the loss of a key natural defence, exposing the coastline to increased vulnerability.

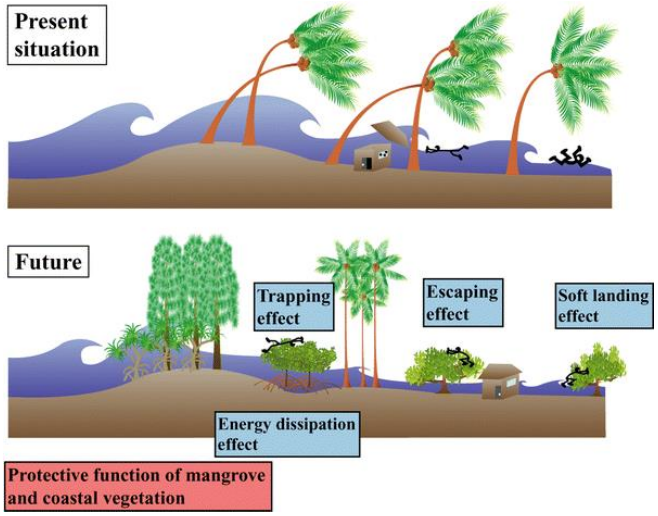

Figure 2.3.15 - Visual explanation of the protective effects of coastal vegetation during storm events (Tanaka et al., 2010).

Urbanization of coastal areas is another major factor in the intensification of coastal erosion (Luijendijk et al., 2018). The development of settlements, tourist infrastructure and roads along the coast often leads to the levelling of dunes, soil cementing and the destruction of protective vegetation. Impermeable surfaces, such as roads and car parks, hinder the natural infiltration of rainwater into the soil, increasing surface runoff that accelerates the transport of sediment to the sea and contributes to coastal instability (Goudie, 2013; Williams & Conway, 2009). In addition, the removal of vegetation barriers decreases water absorption capacity, exacerbating the risk of coastal flooding and erosion. Intensive agricultural activities in coastal areas are another important factor in soil alteration. Logging and large-scale cultivation practices remove native vegetation and introduce monocultures that do not possess the same soil-stabilizing capacity. The use of fertilizers and pesticides can also have a negative impact on soil quality and coastal biodiversity, further compromising ecosystem resilience (Mitsch & Gosselink, 2015; Stewart et al., 2011). Sediment-laden water from farmland, carried by rivers towards the coast, can alter littoral transport systems, promoting erosive phenomena in areas that previously enjoyed a sediment balance.

The combination of vegetation loss and changes in land use greatly amplifies the phenomenon of coastal erosion (Nicholls & Cazenave, 2010; Schmidt et al.,

2014). In the absence of vegetation barriers, waves and winds find land more exposed and easily eroded. At the same time, the alteration of natural sediment flows caused by urbanization works makes it more difficult for coastlines to regenerate naturally. In many areas, changes in land use are also reducing the capacity for sediment accumulation from inland, which is essential for maintaining the coastal balance. This leads to an erosion process that tends to be irreversible over time, unless targeted restoration and conservation measures are taken. An obvious example of these combined effects is found in coastal areas that have undergone rapid tourism development. Beaches once protected by dunes and vegetation have been transformed into open stretches of sand, with hotels and infrastructure built directly on the coast. In these cases, not only is erosion accelerated, but there is also increased vulnerability to storm surges and rising sea levels, putting both economic structures and the natural environment at risk.

To counteract the effects of vegetation loss and land-use changes, integrated and sustainable coastal management strategies are needed. The reforestation of mangroves, the planting of dune vegetation, and the creation of natural buffer zones between infrastructure and the sea can restore natural barriers and improve coastal resilience. In addition, the regulation of coastal urbanisation and the introduction of more sustainable agricultural practices are essential measures to reduce human impact on coastal erosion. In many regions of the world, the restoration of artificial dunes and the replenishment of coastal wetlands are also being experimented with as ecological protection methods that work with natural processes rather than against them (Sutton-Grier et al., 2015). These interventions, if accompanied by careful urban planning and education of local communities, can help mitigate coastal erosion and preserve coastlines for future generations.

2.4 The shoreline

The survey of the shoreline and its analysis are fundamental tools for understanding and monitoring coastal erosion. Throughout this thesis we refer to the term “coastline” to also identify the land-water boundary in the presence of rocky coasts (e.g. cliffs); with shoreline we refer to the predominantly sandy or gravelly beaches. The coastline can be defined in various ways, using various proxies like the top cliff line, seaward dune vegetation line, or wet/dry line, each with its pros and cons, depending on the study type (Boak & Turner, 2005a). Its movement over time provides valuable information on erosive or accretionary

processes taking place. Monitoring shoreline changes is essential for effective coastal management (Manno et al., 2022a; Molina et al., 2020a), but its considerable and continuous temporal variability makes precise determination difficult. Since the position of the shoreline is an instantaneous entity, monitoring should be carried out on several shorelines surveyed over time. Therefore, tools are needed to easily obtain these shorelines, as well as additional tools to effectively analyse them (Scardino et al., 2022a).

2.4.1 Importance of shoreline survey

The survey of the shoreline is crucial for several reasons. Firstly, it provides a direct measure of the health of the coastline. As has already been extensively discussed, the coastline is constantly changing due to waves, tides, currents and all the elements discussed in the previous subsections. Any advancement or retreat of the shoreline may indicate erosion or sedimentation phenomena, which in turn affect infrastructure, coastal communities and the natural environment. Through constant monitoring of this parameter, it is possible to assess the effect of natural phenomena, such as storm surges or cyclones, and anthropogenic phenomena, such as urbanisation of coastal areas and sediment alteration (such as sediment approvals).

The survey process can also provide historical data for modelling coastal erosion. By comparing the position of the shoreline at different time periods, the speed and extent of erosion can be analysed and the factors influencing these changes can be better understood. These data are particularly useful for predicting future coastal evolution, helping decision makers to plan coastal defence interventions.

2.4.2 Shoreline detection techniques

There are various techniques for shoreline detection, ranging from the use of traditional instruments to more modern and advanced technologies.

The techniques vary according to the scale of observation. The following are mainly regional-scale techniques.

- **Aerial and satellite photogrammetry**: One of the most common methods of monitoring the shoreline is the use of aerial or satellite imagery (McCarroll et al., 2024; Smith et al., 2021; Toure et al., 2019a). Photogrammetry allows data to be collected over large coastal areas and images to be compared over time to track the movement of the shoreline. With the increasing availability of high-resolution satellite images, this

method has become one of the most effective tools for monitoring shoreline changes on a large scale and with regular frequency.

- **GPS and LIDAR** surveys: Land and marine surveys using high-precision GPS technology and LIDAR (Light Detection and Ranging) provide detailed coastal mapping (Jamali & Mahdianpari, 2022; O'Connor & Mieras, 2022). GPS is used to record the exact position of the shoreline at different points, while LIDAR, through laser surveying, enables the creation of high-resolution three-dimensional models of coastal morphology. These data make it possible to study micro-variations of the coastline and monitor erosion processes in specific areas.

- **Drones and UAV sensors**: Drones (Unmanned Aerial Vehicles) equipped with optical and LIDAR sensors are becoming increasingly popular tools for coastal monitoring. With their ability to fly at low altitude and acquire high-resolution data, drones are used to detect local shoreline changes with great accuracy and speed. They also allow access to areas that are difficult to monitor by other means, such as remote or dangerous areas.

2.4.3 Shoreline data analysis and uses

Once the position of the shoreline has been determined, one can proceed with data analysis to better understand the erosion or accretion processes of a shoreline. Spatial analysis tools, such as Geographical Information Systems (GIS), make it possible to handle large amounts of spatial and temporal data and create maps illustrating shoreline evolution (Jacquez, 1998). These analyses can highlight areas most prone to erosion or sediment deposition, providing an overall view of coastal evolution.

Among the most commonly used analysis techniques are:

- The **Digital Shoreline Analysis System** (DSAS) is an extension tool for ArcGIS designed to analyze shoreline changes over time. DSAS makes it possible to calculate the advancement or retreat of the shoreline through a series of quantitative indicators such as the EPR (End Point Rate), see in the following, the NSM (Net Shoreline Movement), which represents the net movement of the shoreline, and the SCE (Shoreline Change Envelope), which calculates the maximum change in the

shoreline. These indicators provide an accurate assessment of coastal evolution, which is essential for studying the effects of climate change and for the sustainable management of coastal zones.

- **Shoreline Change Rate (or End Point Rate) EPR [m/year])**: This is a quantitative method that measures the rate at which the shoreline moves over time. This value can be expressed in metres per year and helps identify areas subject to rapid shoreline erosion or advancement (Terres de Lima et al., 2021). By comparing historical data with current data, the most vulnerable stretches of coastline can be identified and intervention strategies developed.
- **Sediment transport models**: Coastal erosion is often influenced by sediment transport along the coast. Shoreline analysis in combination with sediment transport data makes it possible to model the flows of littoral material and predict how the coast might evolve in the future. This type of analysis is particularly useful for understanding erosive processes induced by human activities, such as the construction of port infrastructure or artificial barriers, which alter natural sediment transport.
- **Predictive modeling**: Numerical modelling tools can use shoreline data to simulate future scenarios. These models take into account various factors, including sea level rise, storm intensity and human activities, and provide predictions on how the shoreline might shift in the following decades (Hinkel et al., 2014; Cowell et al., 2003). The results obtained can guide coastal planning processes and help develop erosion mitigation plans.

2.5 State of the art on coastal modeling

As extensively discussed in the opening chapters of this thesis, coastal zones are dynamic systems that undergo variations in time and space, sometimes of great intensity, influenced by natural and/or anthropogenic factors and their complex interactions. (Benassai, 2006; Petti, 2021; Toimil et al., 2020b).

One of the research goals of the PhD course was to understand and predict coastal evolution, a task made difficult by the challenges associated with multi-scalar interactions. Studies in the scientific community indicate that the joint resolution of all spatio-temporal scales is still unattainable (Toimil et al., 2020b). Adding to

the level of complexity are the effects of climate change, such as rising sea levels and increased frequency and intensity of storms, stochastic phenomena that are difficult to predict. These phenomena can accelerate erosive processes and significantly alter the sediment balance along the coast, causing significant land loss and changing coastal habitats (McCarroll et al., 2024; Toimil et al., 2020b).

Given the limited knowledge and complexity of coastal dynamics, it is often difficult to take appropriate action without the use of advanced numerical models. These models help simulate the different forces at play and predict coastal evolution under various scenarios, thus supporting sustainable coastal zone management. Numerical models provide an essential means to understand and predict the complex dynamics of beaches and coastlines. Their ability to simulate various scenarios of climate change, erosion and sediment deposition makes it possible to anticipate the consequences of human interventions and natural phenomena. Without the use of these models, predictions would be based on limited observations and simplified assumptions, leading to less effective and potentially damaging management strategies. For example, in the past, the installation of barriers and groins along some Italian coasts has often led to unforeseen negative effects. In particular, on the Adriatic coast, the construction of groins to combat erosion has accelerated sediment loss in the surrounding areas, worsening erosion instead of mitigating it (Pranzini, 1992). Numerical models, therefore, are fundamental tools for developing sustainable and resilient interventions that protect coastlines from natural and anthropogenic hazards.

However, the accuracy of such models strongly depends on the quality of the available data and the ability to faithfully represent the interactions between the different processes. Moreover, coastal management requires an integrated approach that considers not only physical dynamics, but also socioeconomic and environmental aspects. Collaboration between scientists, engineers, planners and local communities is crucial to develop effective and resilient adaptation strategies that can mitigate the negative effects of coastal erosion and climate change while protecting coastal ecosystems and resources.

Over the years, numerous numerical models have been developed, and today literature offers a wide range of models for comparison. They vary in terms of spatial and temporal resolution, i.e. the level of detail with which they represent coastal processes and the frequency of simulations, as well as in terms of shoreline prediction. These models fall into three main categories: empirical, numerical and conceptual. The choice of which model to use depends on the

specific needs of the study or project. Empirical and conceptual models are often used for preliminary analysis and understanding basic dynamics, while numerical models are used for detailed forecasting and advanced coastal management. The combination of different models can provide a more complete and accurate view of shoreline evolution.

2.5.1 Empirical models

Empirical models are based on observations and historical data to describe and predict shoreline changes. These models use statistical relationships derived from previous studies to make predictions.

2.5.1.1 Bruun's model (1962)

Bruun's model, proposed by Per Bruun in 1962, is one of the most widely used methods for estimating shoreline retreat due to sea level rise (diagram shown in Figure 2.5.1). This model is based on the principle that a beach maintains a constant equilibrium profile that migrates upwards and inwards in response to sea level rise. It therefore predicts that rising sea levels will cause the beach to retreat. The key concept of Brunn's model is therefore the equilibrium profile of the beach which, if not altered by human intervention or natural phenomena, tends to be maintained over time (Bruun, 1988, 1983, 1962; D'Anna et al., 2021).

The fundamental formula of Bruun's model is given in Equation 2.5.1:

Equation 2.5.1 – Bruun's model equation

$$R = \frac{S * L}{h + B}$$

In which:

- R is the horizontal shoreline setback (m);
- S is the sea level rise (m);
- L is the width of the continental shelf (m);
- h is the depth at the base of the active profile (m);
- B is the height of the beach above mean sea level (m).

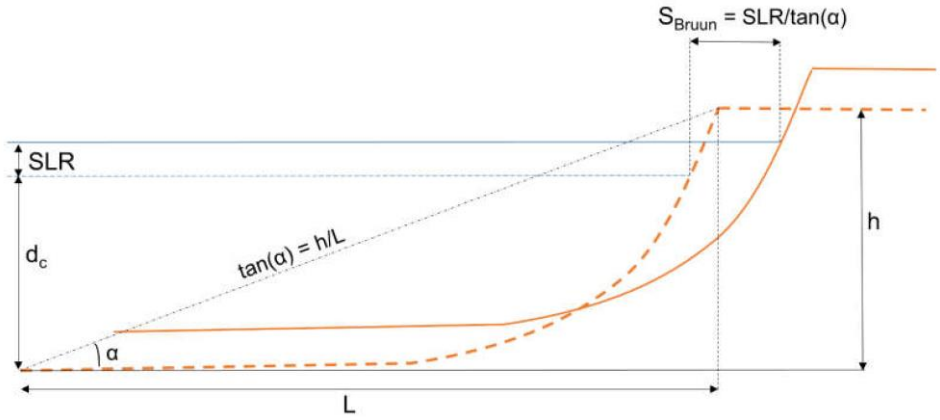

Figure 2.5.1 - Schematic diagram of the Bruun model. In which: SLR is the sea level rise, S_{Bruun} the respective recession of the coastline in the time period considered, d_c is the closure depth and tan(α) is the average slope of the active beach profile (D'Anna et al., 2021).

Although the model has been shown to be accurate under laboratory conditions or in specific natural contexts, applications have shown that results in the field are often variable. Among the main criticisms are assumptions underlying the model, such as the maintenance of a constant profile and the absence of sediment transport along the coast, as well as the fact that the model does not consider possible sediment inputs or losses to and from other areas: conditions that are not always realistic (Bruun, 1988, 1983, 1962; D'Anna et al., 2021).

2.5.1.2 Dean's model (1977)

The Dean Model, developed by Robert G. Dean in 1977, is one of the main models used to describe the equilibrium profile of beaches. This model represents how a beach reaches a stable profile in response to wave action by describing the distribution of sediment.

Its most common mathematical formulation relates water depth and distance from the shore according to the Equation 2.5.2 and Figure 2.5.2:

Equation 2.5.2 – Dean's model beach profile equation

$$h(y) = Ay^{\frac{2}{3}}$$

In which:

- *h(y)* is the depth of water at a distance *y* from the shoreline (m);
- *A* is a scale parameter that depends on sediment characteristics such as size (according to a link shown in Figure 2.5.2) and density ($m^{\frac{1}{3}}$):

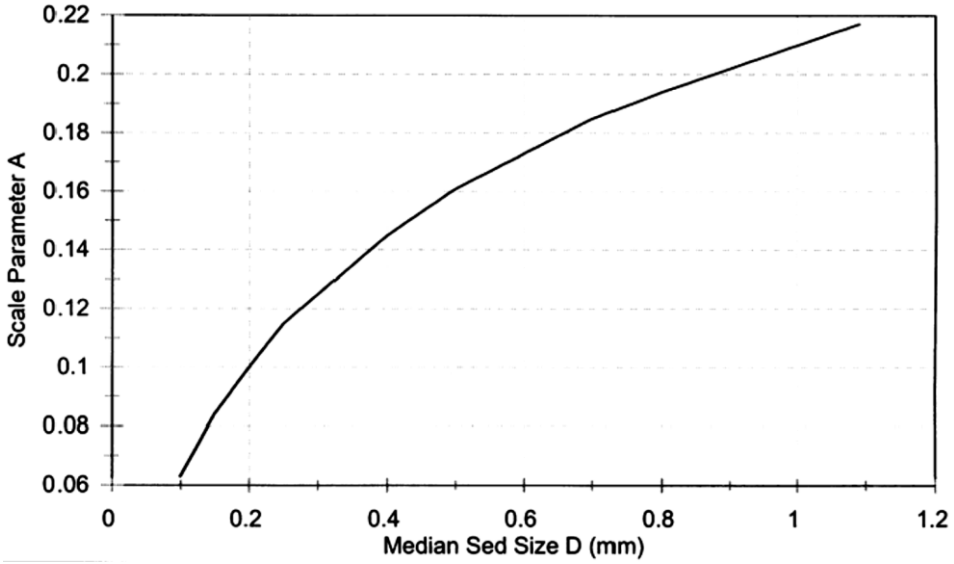

Figure 2.5.2 - Trend of parameter A of Dean's (1977) model as a function of average sediment size (Benassai, 2006).

Despite its wide use, the model has important limitations, some dependent on the *A* parameter, which can vary significantly depending on the specific characteristics of the beach. Furthermore, the assumption of a uniform beach is not always applicable. Finally, the model does not take into account complex processes such as the seasonal variation of waves and the interactions between waves and currents (Foti, 2006; Petruzzelli, 2012).

2.5.2 Conceptual Models

Conceptual models provide a simplified representation of coastal processes. These models are useful for understanding the general dynamics and identifying the main factors influencing shoreline evolution.

2.5.2.1 Pelnard-Considère model (1956)

The Pelnard-Considère model is one of the earliest and most influential mathematical models for describing shoreline evolution and provides a theoretical basis for understanding how the shoreline evolves over time due to the longshore transport of sediment. It assumes that shoreline change is controlled primarily by wave-induced longitudinal transport of sediment. It uses a simplified mathematical approach, if the shoreline profile remains unchanged during erosion and sedimentation processes.

Equation 2.5.3 of Pelnard-Considère is a parabolic differential equation that describes the temporal and spatial evolution of the shoreline:

Equation 2.5.3 – Parabolic differential equation of Pelnard-Considère model

$$\frac{\partial y}{\partial t} = \frac{K\,\partial^2 y}{h\,\partial x^2}$$

In which:

- y is the position of the shoreline (m);
- t is time (days);
- K is a coefficient proportional to the amount of sediment transported along the coast (m^2 /day);
- h is the average depth of the sediment transport zone (m);
- x is the distance along the coast (m).

To solve Equation 2.5.3 analytical or numerical methods are generally adopted, depending on the boundary conditions. In many cases, analytical resolution is possible for simple configurations such as a straight coastline with well-defined boundary conditions, using classical techniques of variable separation or Fourier transforms. However, for more complex conditions, such as irregular coastlines or variable sediment transport, numerical methods are used, such as the discretization of spatial and temporal derivatives, solving the equation using explicit or implicit differential schemes. This approach allows realistic conditions along the coastline to be taken into account, although it requires more computational capacity (Guimarães et al., 2016; Rodriguez-Delgado et al., 2019).

The equation implies that shoreline spread is proportional to shoreline curvature: concave stretches of the coast tend to erode, while convex stretches tend to accumulate sediment. Thus, the model is useful for predicting shoreline changes in regions where longshore transport is the dominant process.

However, the model does not account for transverse sediment transport and the simplicity of the equation may not capture all the actual physical processes influencing shoreline evolution (Guimarães et al., 2016; Rodriguez-Delgado et al., 2019).

2.5.3 Numerical Models

Numerical models use differential mathematical equations that describe wave motion, currents, and sediment transport to predict morphological changes over time. These models require large amounts of data and computational resources but offer detailed and accurate predictions.

2.5.3.1 Model XBeach

XBeach is an advanced numerical model used to simulate coastal dynamics, particularly for storm events affecting sandy coastal areas. It was developed by the Deltares Institute[3], in collaboration with the University of Delft in the Netherlands and the University of Miami in the US, to address the need to assess the vulnerability of sandy coastal areas to extreme events such as hurricanes and to design more effective coastal protection measures. The model is mainly used to study short-term processes as it is a storm response model.

XBeach is a model based on hydrodynamic equations including wave processes, coastal currents, mean sea level rise due to wave action and wave-current interactions. The fundamental equations on which the model is based are the Navier-Stokes equations, simplified in the form of equations for shallow water conditions (shallow water equations) to make the model computationally efficient (Yin et al., 2022)..

The main equations are the continuity equation and the momentum equation (Equation 2.5.4):

[3] Deltares is a leading independent water and subsurface research institute, known for its advanced studies in coastal and hydraulic engineering.

Equation 2.5.4 – Solving differential equations of the XBeach model

$$\frac{\partial \eta}{\partial t} + \frac{\partial (hu)}{\partial x} + \frac{\partial (hv)}{\partial y} = 0$$

$$\frac{\partial (hu)}{\partial t} + \frac{\partial (hu^2)}{\partial x} + \frac{\partial (huv)}{\partial y} = -gh\frac{\partial \eta}{\partial x} + F_x$$

$$\frac{\partial (hv)}{\partial t} + \frac{\partial (huv)}{\partial x} + \frac{\partial (hv^2)}{\partial y} = -gh\frac{\partial \eta}{\partial y} + F_y$$

In which:

- η is the elevation of the water level (m);
- h is the depth of the water (m);
- u and v are the velocity components in the x- and y-direction (m/s);
- g is the gravitational acceleration (m/s^2);
- F_x e F_y are force terms representing wave, current and turbulence effects (N/m^3).

Despite its effectiveness and wide application, the accuracy of the model is highly dependent on the quality and resolution of the data input. Furthermore, although XBeach is designed for storm events, its ability to simulate extreme conditions such as very intense hurricanes or climate change scenarios may require further improvements and adaptations (Alvarez-Cuesta et al., 2021; Mucerino et al., 2014; Pan et al., 2018; Roelvink et al., 2009; Yin et al., 2022a).

2.5.3.2 GENESIS Model (GENEralized Model for SImulating Shoreline Change)

The GENESIS model is a numerical model developed to simulate long-term shoreline changes produced by spatial and temporal variations of sand transport along the coast due to wave breaking. It is designed to simulate shoreline changes in time and space, with a particular focus on changes due to coastal structures such as jetties, detached breakwaters, dykes and artificial beach nourishments (Pan et al., 2018; Pombo et al., 2022).

The governing relationship is given by Equation 2.5.5:

Equation 2.5.5 – GENESIS differential equation for mass balance (one line model)

$$\left(\frac{dy}{dt}\right) + \left(\frac{1}{D_B + D_C}\right)\frac{dQ}{dx} = 0$$

In which:

- x indicates the distance along the coast (m);
- y indicates the distance out to sea (m);
- D_B is the height of the berm (m);
- D_C is the closing depth (m);
- Q is the longshore sand transport discharge which is given by (m^3/s) Equation 2.5.6:

Equation 2.5.6 – Long shore sediment transport equation in GENESIS model

$$Q = \left(H_s^2\, C_g\right)_b \left[a_1 \sin 2\theta_{bs} - a_2 \cos\theta_{bs} \left(\frac{\delta H_s}{\delta x}\right)\right]_b$$

In which:

- H_s is the significant wave height (m);
- C_g is the speed of the wave group given by linear wave theory (m/s);
- b is the subscript denoting the wave breaking condition;
- θ_{bs} is the angle of the breaking waves, i.e. breaking, relative to the local coastline;
- a_1 e a_2 are dimensional parameters that can be calculated through two calibration parameters respectively K_1 e K_2 (Hanson et al., 1989).

The model has some limitations, including not taking into account transverse sand transport to the coast, the absence of simulation of short-term storm-induced shoreline change, and the lack of reflection of waves from structures. In addition, it does not take tidal level changes into account.

2.5.3.3 Model Delft3D

Delft3D is one of the most advanced and versatile models available for the study of coastal and river dynamics. Developed by Deltares, this model is widely used worldwide to analyse and predict three-dimensional hydrodynamic circulation, sediment transport and coastal morphodynamics. The model simulates three-dimensional hydrodynamic circulation, considering tides, currents, waves and the interaction between fresh and salt water. It takes into account refraction and diffraction phenomena in wave propagation and sediment transport, both along and across the coast.

Delft3D is based on a system of partial differential equations that describe fluid motion. The Navier-Stokes equations, modified for the hydrostatic approximation and for an incompressible fluid, form the basis of the model and are given in Equation 2.5.7:

Equation 2.5.7 – DELFT 3D solving differential equation

$$\frac{\partial u}{\partial t} + u\frac{\partial u}{\partial x} + v\frac{\partial u}{\partial y} + w\frac{\partial u}{\partial z} = -\frac{1}{\rho}\frac{\partial p}{\partial x} + \mu\left(\frac{\partial^2 u}{\partial x^2} + \partial\frac{\partial^2 u}{\partial y^2} + \frac{\partial^2 u}{\partial z^2}\right) + F_u$$

In which:

- u, v, w are the velocity components in the *x, y, z* directions (m/s)*;*
- p is the density of the fluid (kg/m);[3]
- p is the pressure (N/m);[2]
- μ is the kinematic viscosity (kg/(m*s));
- F_u represents the external forces (N/m).[3]

Although it is widely used, its application, however, requires in-depth knowledge of physical processes and numerical modelling techniques, and three-dimensional simulations can be very expensive in terms of computational resources (Alvarez-Cuesta et al., 2021; Lesser et al., 2004; Pan et al., 2018).

2.5.3.4 MIKE Models

The MIKE model, developed by DHI (Danish Hydraulic Institute), is a suite of advanced numerical modelling tools used to simulate coastal and river dynamics as well as water quality and urban hydrology. MIKE is recognised worldwide for

its accuracy and versatility, and is widely used in coastal engineering, water resource management and environmental planning projects.

MIKE offers a wide range of specialised modules to address different aspects of hydraulic dynamics and water quality:

- MIKE 21: simulates two-dimensional hydrodynamic flows, sediment transport, morphodynamics and waves. It is mainly used for coastal, estuarine and lake applications;
- MIKE 3: which provides three-dimensional hydrodynamic simulations, taking into account processes such as thermal and salt stratification, pollutant dispersion and sediment transport;
- MIKE 11: which is used for water resource management, flood control and flood analysis;
- MIKE SHE: is an integrated model for the simulation of the hydrological cycle, combining surface and subsurface processes.

Like the similar models previously analysed, the MIKE model is based on the Navier-Stokes equations, modified for an incompressible fluid, given in Equation 2.5.7.

The MIKE 21 package is available in four versions that differ according to the geometric schematisation adopted:

- single grid: equations are solved using an implicit finite difference technique on a rectangular, uniform grid;
- multiple grid: offers the possibility of inserting individual grids in the domain with increasing resolution in areas where greater detail is required;
- finite volumes: the finite volume approach provides maximum flexibility, and it is possible to use triangular or quadrangular elements;
- curvilinear mesh: used for river morphology applications.

In recent years, the MIKE model has undergone numerous improvements, including the integration of machine learning techniques to improve the

prediction of hydrodynamic phenomena and the use of satellite data for model calibration and validation. Despite its power and versatility, using the MIKE model requires a thorough understanding of the physical processes involved and numerical modelling techniques. Complex simulations can require significant computational resources, and the quality of the results is highly dependent on the accuracy of the input data (Mandal & Chaudhuri, 2023; Sanhory et al., 2022; Warren & Bach, 1992).

2.5.3.5 SWASH model (Simulating WAves till SHore)

SWASH (Simulating WAves till SHore) is an advanced numerical model for simulating wave behaviour and sediment transport in coastal areas. The model is based on a simplified approach of the Navier-Stokes equations for shallow water conditions, making it possible to accurately describe wave motion and wave-seabed interaction phenomena such as refraction, reflection and breaking.

The SWASH model is mainly used for the simulation of waves and swells in shallow areas, but, although not specifically designed for this purpose, it is also suitable for predicting phenomena such as erosion and sediment accumulation along the coastline. On the other hand, it is not optimal for the simulation of extreme and prolonged events, such as tsunamis and storms of long duration. It uses a finite spatial grid to simulate changes in the coastal profile and seabed. Thus, it is able to resolve small-scale local phenomena, making it particularly suitable for simulations in areas with complex geometries, such as harbours, jetties or irregular beaches. However, it requires high resolution for accurate simulations, which significantly increases its computational load. It is an optimised model for shallow waters, so it is often less accurate for deeper areas. Finally, as with the other models reported, the accuracy of the results is highly dependent on the quality of the initial data and boundary conditions (Vasarmidis et al., 2024; Zijlema et al., 2011).

2.5.3.6 Models Comparison

As mentioned above, numerical models for coastal simulation offer different solutions depending on specific study needs. XBeach is particularly suitable for simulating extreme events such as storms and tsunamis, with a specific focus on short-term erosional processes and sediment transport, making it ideal for handling intense temporary phenomena. In contrast, GENESIS focuses more on long-term shoreline modelling, with an emphasis on sediment transport along the coast, making it very useful for managing coastal protection and infrastructure projects on an extended time scale. Delft3D is one of the most versatile models,

capable of simulating both complex hydrodynamic processes and coastal and river morphodynamics, providing a comprehensive and detailed overview of phenomena ranging from current circulation to sediment transport, although it requires considerable computing power. Similar to Delft3D, DHI's MIKE model is distinguished by its intuitive interface and the possibility of integrating several modules to manage floods, waves and water quality, although the licence fee may be a limitation. Finally, SWASH is characterized by its accuracy in simulating waves in shallow water and describing wave-structure interaction, making it ideal for small-scale modelling in coastal environments, although it is less suitable for simulations over long periods or very large areas. In summary, the choice of model depends strongly on the characteristics of the phenomenon to be studied and the temporal and spatial scale of the analysis.

2.5.4 Hybrid downscaling

As has been reported in the previous paragraphs, numerical wave modelling is a crucial element in understanding marine dynamics in coastal areas. However, the availability of high spatial and temporal resolution data to describe the wave climate along the coastal strip is often limited by the scarcity of instrumental data and the high computational cost of numerical models. To address this challenge, a methodology is needed to transfer data from large-scale global models to local models with finer resolution. For this purpose, a *hybrid downscaling* approach integrating *dynamical downscaling* and *statistical downscaling* techniques was developed by Camus et al., (2011).

The hybrid downscaling method developed by Camus et al. (2011) combines the use of a numerical wave propagation model (SWAN) with mathematical tools to reduce computational complexity. Specifically, this approach involves the use of a Maximum Dissimilarity Algorithm (MDA) to identify a representative subset of sea states in deepwater areas. The MDA allows for the selection of a small number of sea states covering the entire climate variability, including extreme events, significantly reducing the number of simulations required to describe the wave climate. Once representative cases are identified, they are propagated to coastal areas using a state-of-the-art wave propagation model. This model considers wave motion evolution, considering the effects of refraction, breaking and interactions with coastal morphology. The result is a detailed description of the wave motion transformation that occurs as waves approach the coast.

One of the main challenges of hybrid downscaling is the reconstruction of complete time series of wave parameters in shallow water areas from the few

selected representative cases. For this purpose, a non-linear interpolation technique based on Radial Basis Functions (RBFs) is used. RBFs allow time series to be reconstructed with high accuracy, even in high-dimensional spaces and with irregularly distributed data. This methodology guarantees an accurate representation of the sea conditions, reliably reproducing even extreme events that can significantly influence coastal dynamics.

The hybrid downscaling method has several advantages over traditional downscaling approaches. First, it allows for a detailed description of the wave climate in coastal areas with a significant reduction in computational effort. In addition, the selection of representative cases using MDA ensures that all sea conditions are considered, including less frequent but high-impact conditions such as intense storm surges.

The validation of the method was performed by comparing the reconstructed time series with instrumental data available at [insert location] and showed an excellent ability of the model to reproduce the statistical characteristics of shallow-water waves. In particular, the comparison between the reconstructed parameters (significant height, peak period, wave direction) and the observed data showed a high correlation, with RMSE and BIAS values confirming the robustness of the proposed approach.

Throughout this Thesis, the approach presented by Camus et al. was used in Chapter VII. For more information see the work of Camus et al., (2011).

Chapter III

In the previous chapter, we explored the importance of wave data for estimating sediment losses, highlighting how waves are one of the key elements in coastal erosion. Continuing this line of investigation, this chapter presents a research, part of a paper currently under review, in which an artificial intelligence-based model has been developed using a Conv-LSTM network. This model, starting from wind data, allows for the accurate generation and prediction of key wave parameters, such as significant height (H_s), peak period (T_p) and direction, over the entire Mediterranean Sea. This new methodology provides an essential tool for improving coastal dynamics analysis and forecasting by exploiting model output data as input for coastal erosion models.

The topics and contents of this chapter are taken from a research article under review at Elsevier, "Ocean Engineering" scientific journal, entitled "Combining Conv-LSTM and Wind-Wave Data for Enhanced Sea Wave Forecasting in the Mediterranean Sea".

3.1 Why a Wave Modeling and Forecasting Model?

The Mediterranean Sea (about 2.5 million km²) is a semi-enclosed basin of great socioeconomic and environmental importance, characterised by unique and complex oceanographic conditions (Azzopardi et al., 2020; Danovaro et al., 2020; Lionello et al., 2006; Lloret et al., 2022; Salhi et al., 2021). Accurate modelling of wave conditions in this region is crucial for a wide range of applications, from maritime safety and coastal resource management to the energy industry and climate change risk mitigation (Bolaños-Sanchez et al., 2007; Cavaleri et al., 2010, 2018; Sartini et al., 2017).

Traditionally, wave forecasting has been carried out using physical-mathematical models such as spectral wave models, including well-known models such as WAM (Group, 1988; Komen, 1986), SWAN (Booij et al., 1999), and WaveWatch III (Tolman, 1991). These models are based on the solution of the wave action balance equation and are widely used for operational wave forecasting due to their ability to simulate wave growth, propagation, and dissipation over large domains. For example, WAM, was one of the first models to successfully integrate the effects of wind input, wave-wave interactions, and dissipation, while SWAN, developed later, allows for detailed wave modelling in coastal areas with complex bathymetry. WaveWatch III, an evolution of the earlier models, has become one of the standard tools for global and regional wave

predictions, widely applied in both research and operational environments. These models have been further refined and validated through numerous studies, helping to improve the accuracy of wave forecasting in various marine environments. Although these models are robust and well-established, they have limitations, especially in terms of their spatial resolution and their ability to represent the complexity of non-linear interactions between waves and meteorological conditions at regional scales (Casaioli et al., 2014; Cavaleri et al., 2012, 2018; Hewitt et al., 2017; Sherwood et al., 2022; Toimil et al., 2020c). Recently, the application of artificial intelligence-based approaches, in detail neural networks and deep learning models, has shown promising results in the field of marine and coastal engineering (Scala et al., 2024c; N. Wang et al., 2022; Zhou et al., 2020) and especially in wave forecasting which can improve the representation of temporal and spatial variability of waves (Bento et al., 2021; Habib & Zarillo, 2024; Zhang & Li, 2020; Zheng et al., 2020).

In this context, Convolutional Long Short-Term Memory (Conv-LSTM) models provide a particularly suitable framework for predicting time series with strong spatial dependencies, such as wave motion (Hu et al., 2023; Upreti et al., 2023; Wang et al., 2021). Conv-LSTM models are designed to capture not only temporal, but also spatial dynamics, combining the capabilities of convolutional networks to extract spatial features with the ability of LSTMs to model long-term temporal dependencies (Shi et al., 2015). Several studies have demonstrated the effectiveness of such approaches in predicting of complex atmospheric and marine phenomena, such as weather conditions (O"Donncha et al., 2022; Shi et al., 2015) and waves (Ding et al., 2023; Hu et al., 2023; Liu et al., 2023; Ouyang et al., 2023; Upreti et al., 2023), suggesting that they can be a powerful tool to improve the prediction of weather and sea conditions in areas of high interest such as the Mediterranean Sea.

In this chapter, is presented the application of a Conv-LSTM model for wave prediction at the scale of the whole Mediterranean basin, using bathymetric data and wind fields (easterly and northerly components) as inputs as proposed by Song et al., (2022), Feng et al., (2022) Li et al., (2024). The model was trained to predict three fundamental variables for describing the sea state: significant wave height (H_s), peak period (T_p) and wave direction (θ). These quantities, essential for characterising wave dynamics, are widley used in sea modelling and forecasting (Cañellas et al., 2024; Zheng et al., 2023).

The results show how the proposed approach can provide accurate predictions, in some cases exceeding the performance of CMEMS (Copernicus Marine Environment Monitoring Service) model, particularly in situations where the complexity of local interactions between wind and bathymetric features plays a crucial role. Our work is part of a line of research that aims to harness the increasing availability of high-resolution data and the power of machine learning tools to improve the prediction of marine conditions at regional level (Ding et al., 2023; Donnelly et al., 2024; Jörges et al., 2023).

3.2 Approach and datasets

3.2.1 Wave and wind

The Conv-LSTM model has been used to predict time series of waves characteristics based on forcing data as eastward and northward wind data (m/s) and bathymetry for the whole Mediterranean Sea. This study has been conducted using E.U. Copernicus Marine Service Information datasets. The model was trained with a robust and valuable dataset of waves, in particular *Hs*, *Tp*, θ (https://doi.org/10.25423/cmcc/medsea_multiyear_wav_006_012 - last access 24 oct 2024), wind (https://doi.org/10.48670/moi-00185 - last access 24 oct 2024) and bathymetric data belonging to the Copernicus service. The Copernicus Marine Environment Monitoring Service (CMEMS) or Copernicus Marine Service (CMS) provides free and open access data and information related to the physical state of the global atmosphere and ocean. Hourly wave, bathymetric and wind data were downloaded using the web interface provided by CMEMS (last accessed on 20th June 2024) in netCDF format with, imposing a regional domain as shown in **Figure 1 (subplot A)**. The wave product is obtained using a WAM 4.6.2 model, provided by the Hellenic Centre for Marine Research (HCMR), in Greece, using a regular grid with a spatial resolution of 1/24° (approximately 4.6 km). The wind product is provided by the Royal Netherlands Meteorological Institute (KNMI) based on near real time and multi-year wind observations from scatterometers and on numerical weather prediction model fields, with a spatial resolution of 1/8°. The scatterometer products from the EUMETSAT Ocean and Sea Ice Satellite Application Facility have been extensively validated (Kokkos et al., 2021). Since the models grid resolution are different as shown in Figure 3.2.1 (subplot B), the data preprocessing was needed to resampling the wind data with a wave grid spatial resolution using a triangular linear interpolation.

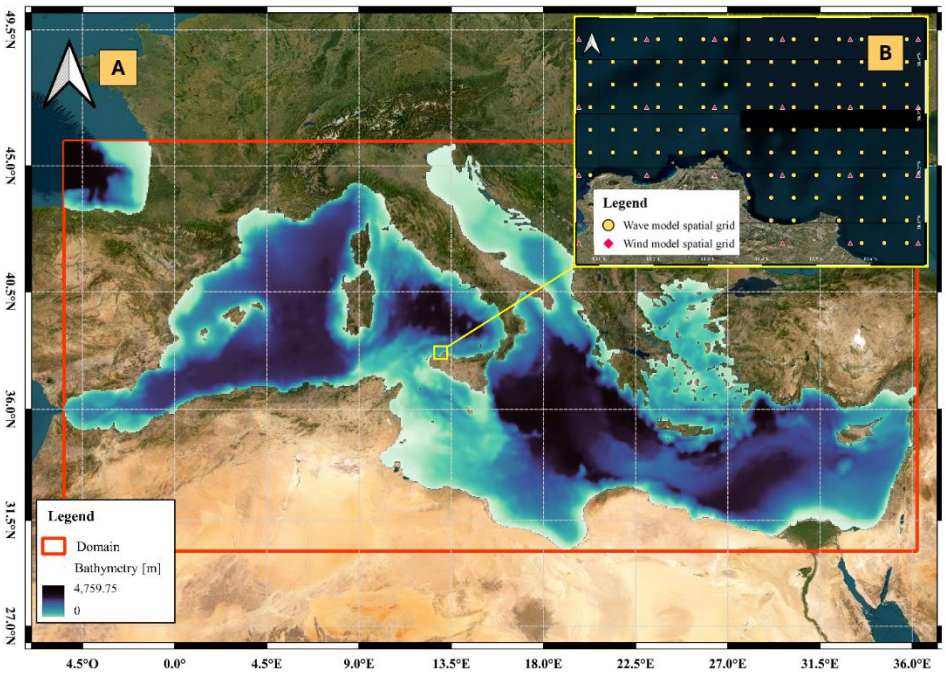

Figure 3.2.1 - Study Area and Dataset Grid Resolution. The regional domain used for the study is highlighted in red, covering the entire Mediterranean Sea (subpolot A). Subplot B is a Zoomed-in view showing the different grid resolutions of the CMEMS datasets. System Reference: WGS 84 Pseudo-Mercator EPSG 3857.

In addition, during the model training and validation processes Italian buoy service data were used.

The Italian Institute for Environmental Protection and Research, ISPRA (*Istituto Superiore per la Protezione e la Ricerca Ambientale*) is the national institute that is on charge, among other activities, to manage, collect the data and maintain the national wave buoy network (*Rete Ondametrica Nazionale*, RON). The network, after a maximum expansion period, is now composed by 9 wave buoys, equipped with different instrument as accelerometers, meteorological station and GPS (Figure 3.2.2). All wave data area free available from the main ISPRA sea data dedicated web page (https://www.mareografico.it/en/homepage.html - last access 24 oct 2024).

To evaluate the effectiveness in model training between measured (RON) and simulated (CMEMS) data, we substituted all available *Hs*, *Tp*, and θ data measured by RON for the corresponding CMEMS domain calculation cells. In detail, Mazara del Vallo, Alghero, La Spezia, Ponza, Monopoli and Crotone since 1993 and finally Ancona since march1999.

For the dates/periods when the buoys did not work or were under maintenance (so there were no acquisitions) we kept CMEMS data.

The Conv-LSTM was first compared with the CMEMS data model, and then with the buoy data from the RON to obtain an estimate of local accuracy. Four different 24-hours events, shown in Table 3.2-1, were selected to validate the model.

Table 3.2-1 - Dates of the events used for further validation model.

Event	**Date**
1	09-20-2020
2	11-26-2021
3	07-11-2022
4	01-27-2022

We chose the events shown in Table 3.2-1 - Dates of the events used for further validation model. to test the model under heterogeneous conditions, considering both stormier (both wind and sea) and calmer scenarios. On 20 September 2020, the Mediterranean was still under the influence of Medicane Ianos, a powerful tropical cyclone that had swept through the region earlier in the month. The storm hit Greece in particular, with sustained winds reaching up to 40 metres per second (144 km/h) and causing severe storm surges along the eastern Mediterranean coasts. Coastal areas in Greece experienced significant flooding due to the combination of high winds and high sea levels.

By 26 November 2021, the Mediterranean Sea was recovering from the impact of Cyclone Apollo, which had brought strong winds and heavy rains to the central Mediterranean in late October and early November. Apollo had mainly affected areas such as Sicily and Malta, leaving rough seas conditions and localised flooding in its wake. Although the cyclone had dissipated by the end of November, the region is likely to have experienced residual unsettled weather with moderate winds and waves.

In contrast, the weather on 11 July 2022, was typical of the Mediterranean summer, characterised by generally calm seas and stable conditions. While no significant cyclones or storms were recorded during this period, localised winds such as the Mistral or Sirocco which are common in the Mediterranean during the summer, may have caused occasional periods of increased wind and waves. However, the overall sea conditions were likely relatively tranquil compared to other dates.

Finally, by 27 January 2022, the Mediterranean was experiencing strong winter storms linked to extratropical cyclones. These winter systems are often accompanied by intense winds and rough seas, especially in the western part of the basin. As a result, maritime conditions would have been rough, with elevated wave heights and dangerous seas, typical of winter storms in the region.

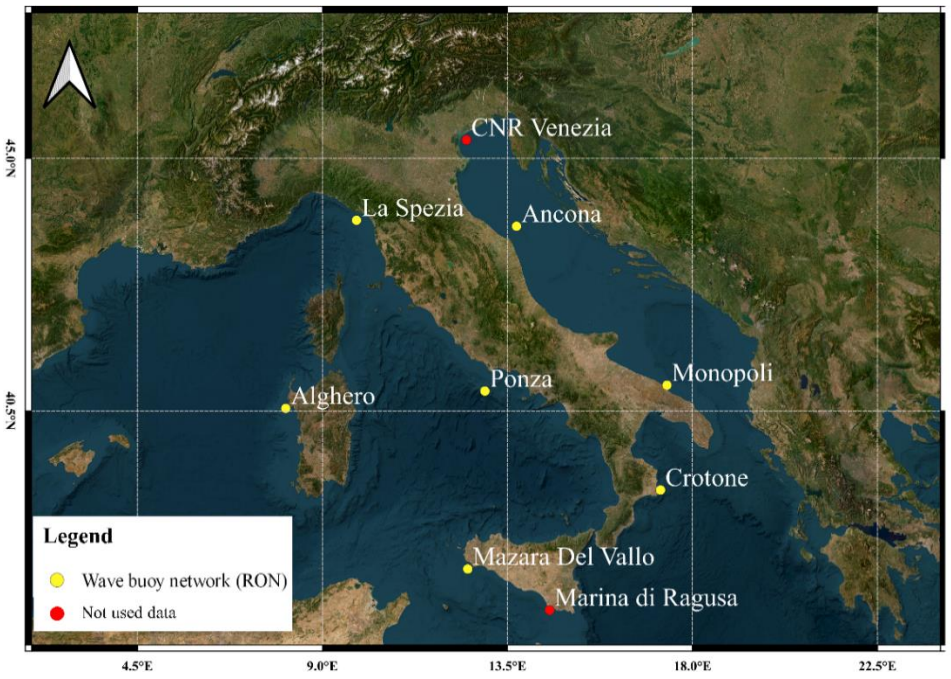

Figure 3.2.2 - ISPRA RON buoy network. Buoy data used are shown in yellow, while those not used are shown in red (System Reference: WGS 84 Pseudo-Mercator EPSG 3857).

3.2.2 Model description

A model based on Convolutional Long Short-Term Memory (Conv-LSTM) neural networks (Fu et al., 2022) has been developed to predict wave height, period and direction in the Mediterranean Sea. This model integrates spatial and temporal information from wind and bathymetry datasets to predict wave characteristics 24 hours in advance. The architecture and simulation processes of the model are described in the following sections. A graphic visualisation of the workflow is shown in Figure 3.2.3.

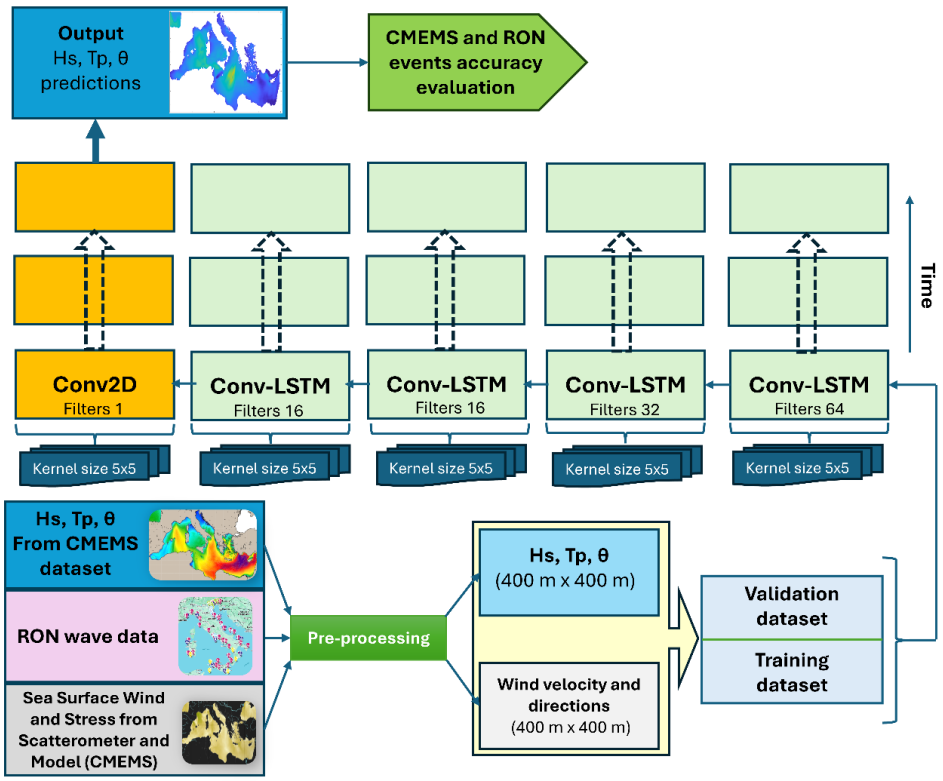

Figure 3.2.3 - Schematic representation of the Conv-LSTM model architecture for wave characteristics prediction in the Mediterranean Sea. The model is fed with wind velocity and directions, and wave data (significant wave height *Hs*, peak period *Tp*, and wave direction θ) obtained from the CMEMS dataset, as well as RON buoy data for validation. Input data undergoes pre-processing to match spatial resolution (400m x

400m). The network consists of Conv2D and sequential Conv-LSTM layers, with progressively increasing filters and kernel sizes of 5x5. The final output is the predicted *Hs*, *Tp*, and θ, with an accuracy evaluation performed using CMEMS and RON events.

3.2.2.1 Model Input

Model inputs include wind data, which are provided on a fine resolution spatial grid, representing wind speed and direction over the entire surface of the Mediterranean Sea, and bathymetry data, which represent seabed depth, a key variable influencing wave formation and behavior.

The wind data are pre-processed to produce spatial maps on which convolutions are applied. The bathymetry data, which is stationary in time, are combined with the wind maps to provide the model with geophysical context.

3.2.2.2 Model Architecture

The architecture of the Conv-LSTM model (Hashmi et al., 2020) consists of several layers, each of which has a specific role:

The first is Convolutional Layers (Conv) which are used to extract spatial features from wind and bathymetry maps. The Conv(X, W) convolution is defined as Equation 3.2.1:

Equation 3.2.1 – First convolutional layer equation

$$Y_{i,j,k} = \sum_{p=0}^{P-1} \sum_{q=0}^{Q-1} X_{i+p,j+q,a} \, W_{p,q,a,k}$$

where X is the input (wind maps and bathymetry), W is the convolutional kernel, and Y is the convolutional output. More specifically, $Y_{i,j,k}$ is the element of the output tensor located at position (i,j) of channel k. $Y_{i,j,k}$ thus represents the value obtained after applying convolution to the portion of the input image and the filter associated with channel k.

$X_{i+p,j+q,a}$ is the input tensor element located at position $(i+p, j+q)$ of channel a. The input tensor X is the two-channel wind map (wind in x direction and wind in y direction).

$W_{p,q,a,k}$ is the element of the convolution kernel (filter) located at position (p,q) between channels a (input channel) and k (output channel). The filter W has size P per Q and is applied to all channels a of the input to produce channel k of the output.

The summations $\sum_{p=0}^{P-1}\sum_{q=0}^{Q-1}$ are double sums that iterate over the indices p and q respectively, which run over the values of the kernel window W that is applied to the input tensor X.

To capture the temporal dynamics of the wave features, the model uses LSTM layers applied to the spatial feature maps produced by the convolutional layers. The temporal dynamics is modelled by a combination of memory cells and LSTM gates, with the following equations (from 3.2.2 to 3.2.6):

Equation 3.2.2 – Forgetting gate equation

$$f_t = \sigma\left(W_f\,[h_{t-1}, x_t] + b_f\right)$$

Equation 3.2.3 – Input gate equation

$$i_t = \sigma(W_i\,[h_{t-1}, x_t] + b_i)$$

Equation 3.2.4 – Cell state equation

$$C_t = f_t\,C_{t-1} + i_t \tanh\,(W_C\,[h_{t-1}, X_t] + b_C)$$

Equation 3.2.5 – Output gate equation

$$\partial_t = \sigma(W_\partial\,[h_{t-1}, x_t] + b_\partial)$$

Equation 3.2.6 – Hidden output equation

$$h_t = \partial_t \tanh\,(C_t)$$

where ft, it, C_t, δt, and h_t represent the forgetting gate, input gate, cell state, output gate and hidden output at time t respectively.

More specifically, the forgetting gate determines how much of the past information should be retained or forgotten.

The Input Gate decides which new information updates the cell state, the Cell State stores the important information that needs to be remembered over time, the

Output Gate regulates how much of the stored information is to be used to generate the output at the current time, and the Hidden Output identifies the final representation of the LSTM cell that will be used for predictions or to pass information to the next time step.

More information on all terms in the equations can be found in the supplementary materials.

The model was configured with *stateful=True* (Ghasemirahni et al., 2024; Khan et al., 2019), which means that the hidden state and cell state of the LSTM are maintained between batches during training or inference, rather than being reset. This is useful when dealing with long training sequences or with data that is split into batches but represents a single continuous sequence as in the present work. An example of what a stateful LSTM architecture looks like is shown in Figure 3.2.4.

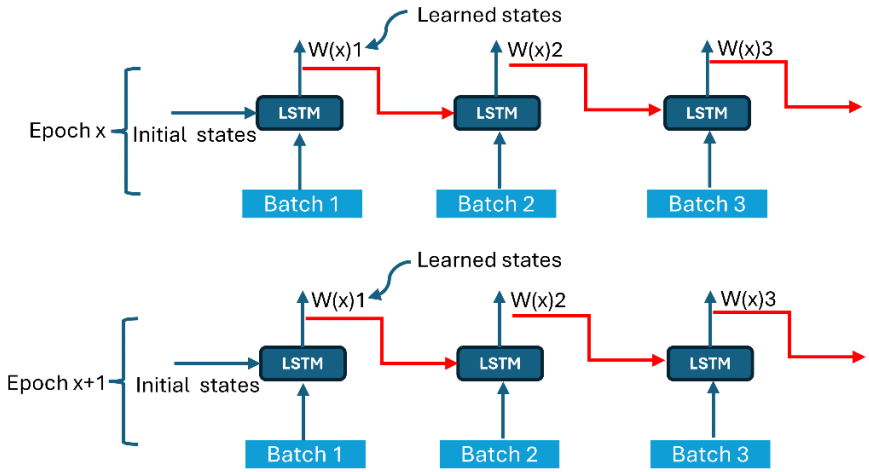

Figure 3.2.4 - Schematic representation of a stateful LSTM architecture.

Specifically, in a traditional (non-stateful) LSTM network, the hidden state (ht) and cell state (C_t) are initially reset after each batch. In a stateful LSTM, these states are instead carried over to the next batch, allowing the model to "remember" previous information and maintain the continuity of the sequence.

Furthermore, in the stateful network, the batches are organised in such a way that the temporal sequence is preserved. This means that the next batch contains the

next sequence from the previous batch. A more fine-grained visualisation showing this propagation across the batches is shown below (Figure 3.2.5).

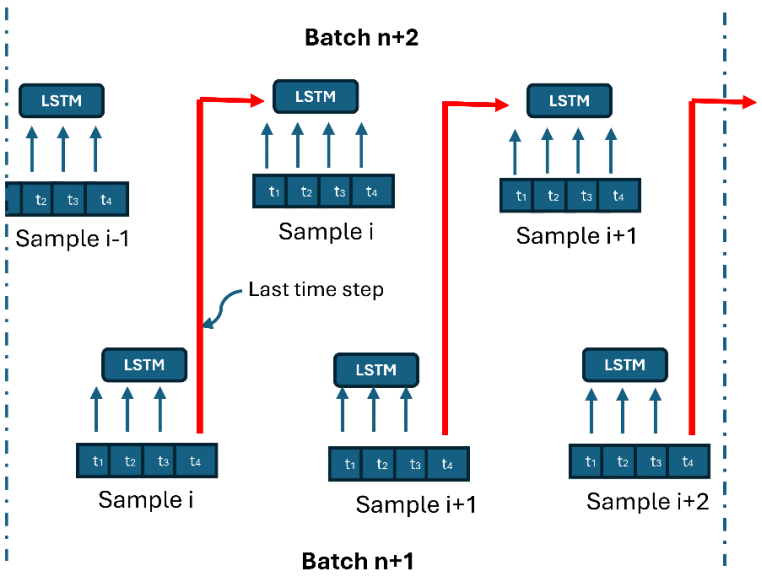

Figure 3.2.5 - Visual propagation between batches in a stateful LSTM architecture.

Finally, for State Initialisation and State Reset, at the start of a new sequence or epoch, the LSTM states were reset, so as not to carry information between different sequences or between different training epochs.

3.2.2.3 Model Output

The output of the model is a temporal sequence of maps of H_s, T_p and θ predicted for the next 24 hours. Each forecast takes into account the initial meteorological and oceanographic and bathymetry conditions.

3.2.2.4 Layers and hyperparameters

The model uses a sequential network, in which the first layer is an LSTM with 64 memory units. This layer is designed to process long and complex time sequences, exploiting the ability of LSTMs to retain relevant information through extended time steps. The layer receives input with a specific time dimension, corresponding to the number of time steps and the number of features for each time step. To ensure that the entire time sequence is propagated to subsequent

layers, the *return_sequences=True* argument is used, which ensures that the output of each time step is passed to the next layer (Graves, 2013).

Following this first layer, a second LSTM layer with 32 memory units was inserted, which reduces complexity while still maintaining a strong representation capability of temporal dependencies. Again, the *return_sequences = True* option was retained, allowing the model to transmit detailed information on temporal patterns to subsequent layers.

To prevent overfitting, a dropout layer was inserted at a rate of 20%. Dropout is a regular technique used to improve the model generalization, reducing the risk of the model overfitting the training data (Srivastava et al., 2014).

The third LSTM layer of the model consists of 16 memory units and is designed to distill the information already processed in the previous layers into an even more compact representation. In this layer, the *return_sequences* option has not been activated, as the goal is to obtain a single output representing the final synthesis of the processed temporal information.

The final output is processed by a dense layer with eight neurons, selected to produce the predicted wave features. This number of neurons was chosen to adequately represent the outputs required by the model, providing a detailed prediction for each of the desired features.

The model was optimised using the Adam algorithm, which is known for its effectiveness in handling complex gradients in deep neural networks (Kingma, 2014). The learning rate was set at 0.001 to ensure gradual and stable learning, minimizing the risk of fluctuations during training. The model was trained for 40 epochs, with a batch size of 200, allowing the model's weights to be updated frequently, while still maintaining the stability required for training on complex data (Bengio, 2012).

3.2.2.5 Loss and Optimization Function

For training the model, a loss function based on the Mean Square Error (MSE) between predictions and observed values was used, which is one of the most common loss functions in regression problems (Chen et al., 2022; Martin-Donas et al., 2018), such as the prediction of marine parameters (wave height, period, direction). The MSE (Equation 3.2.7) calculates the mean squares of the errors between the values predicted by the model and the actual values. More specifically, for each predicted value and the corresponding actual value, the error

is squared and then the average of all these values is calculated. The MSE penalises larger errors, making it suitable for applications where it is important to minimise large deviations between prediction and reality (Port & Korte, 2008).

Equation 3.2.7 – Mean Square Error equation

$$MSE = \frac{(\sum_{i=1}^{n}(x_i - \hat{x_i})^2)}{n}$$

Where *xi* is the *i-th* forecast and *xi^* is the estimator.

Another metric estimated during the learning and validation processes is the Mean Absolute Error MAE, which is described in detail in the following section.

3.3 CMEMS - Conv-LSTM error metrics

The first error metric used to assess the performance of the model on case studies is the Mean Absolute Error (MAE). The MAE measures the mean absolute error between predicted and observed values. It is the average of the absolute differences between predicted and observed values. A MAE value of 0 indicates that there is no difference between the predicted and observed values. Lower values are better as smaller differences indicate minimal error. The MAE equation is shown below (Equation 3.3.1).

Equation 3.3.1 – Mean Absolute Error equation

$$MAE = \frac{1}{n}\sum_{i=1}^{n}|y_i - \hat{y_i}|$$

With *yi* representing the actual value, *y^i* the expected value and n the total number of observations.

The second metric is MAPE (Mean Absolute Percentage Error), which measures the mean absolute percentage error. It is the average of the absolute percentage differences between predicted and actual values. The MAPE equation is shown below (Equation 3.3.2).

Equation 3.3.2 - Mean Absolute Percentage Error equation

$$MAPE = \frac{100\%}{n}\sum_{i=1}^{n}\left|\frac{(y_i - \hat{y_i})}{y_i}\right|$$

The optimal MAPE value is 0%, which indicates a perfect match between predictions and observed values. Lower values indicate higher model accuracy. A MAPE value of less than 10% is generally considered very good in many contexts (Vivas et al., 2020).

The third metric, MASE (Mean Absolute Scaled Error), compares the mean absolute error of the model to the mean absolute error of a reference model, typically a naïve model. It is useful for comparing different models on different scales. The equation is shown below (Equation 3.3.3).

Equation 3.3.3 - Mean Absolute Scaled Error equation

$$MASE = \frac{\left(\frac{1}{n}\sum_{i=1}^{n}|y_i - \hat{y}_i|\right)}{\frac{1}{n-1}\sum_{i=2}^{n}|y_i - y_{i-1}|}$$

The optimal value of MASE is less than one, which indicates that the prediction model is better than the reference model. A MASE value of one means that the model is not better than the naïve model.

Finally, MDA (Mean Directional Accuracy), Equation 3.3.4, measures the percentage of times the model correctly predicts the direction of change (increase or decrease). It is a measure of directional accuracy.

Equation 3.3.4 - Mean Directional Accuracy equation

$$MDA = \frac{1}{n}\sum_{i=1}^{n} 1\left(\left(\frac{(y_i - y_{i-1})(\hat{y}_i - \hat{y}_{i-1})}{|y_i - y_{i-1}||\hat{y}_i - \hat{y}_{i-1}|}\right) > 0\right)$$

With 1 indicating the indicator function which is worth 1 if the condition is true, 0 otherwise.

An MDA of 100% indicates that the model always correctly predicts the direction of change. Higher values are better and anything above 50% is considered better than a random prediction.

3.3.1 Accuracy metrics

To quantitatively assess the difference between the predictions of Conv-LSTM model and the reference data provided by CMEMS, two main statistical indicators are used: the BIAS and the Correlation Coefficient (CC). These two

indices allow to characterise the accuracy and the correlation between simulated and observed values, respectively.

BIAS represents the average difference between simulated values H_s^{sim} and observed values H_s^{obs}, and is defined as follows (Equation 3.3.5).

Equation 3.3.5 – Bias equation

$$BIAS = \frac{1}{n}\sum_{i=1}^{n} H_s^{sim}(i) - H_s^{obs}(i)$$

Where $H_s^{sim}(i)$ are the significant wave height values simulated by the Conv-LSTM or CMEMS model, $H_s^{obs}(i)$ are the values observed by buoys or other measuring instruments, and n is the number of observations.

A BIAS of zero indicates a perfect agreement between simulated and observed values, while a positive or negative BIAS indicates an over- or underestimation of wave heights by the model, respectively.

The Pearson correlation coefficient r or CC, on the other hand, measures the strength of the linear relationship between simulated and observed values, and is defined as follows (Equation 3.3.6).

Equation 3.3.6 – Correlation coefficient equation

$$r = CC = \frac{\left(\sum_{i=1}^{n}\left(H_s^{sim}(i) - \bar{H}_s^{sim}\right)\left(H_s^{obs}(i) - \bar{H}_s^{obs}\right)\right)}{\sqrt{\left(\sum_{i=1}^{n}\left(H_s^{sim}(i) - \bar{H}_s^{sim}\right)^2\left(H_s^{obs}(i) - \bar{H}_s^{obs}\right)^2\right)}}$$

Where H_s^{sim} and H_s^{obs} are the averages of the simulated and observed values respectively, the other terms are as defined above.

The correlation coefficient varies between -1 and 1, where 1 indicates a perfect positive correlation, 0 indicates no correlation, and -1 indicates a perfect negative correlation. A value of r close to 1 suggests that the model reproduces the observed pattern of wave heights well, while lower values indicate a poor ability to capture real patterns.

3.4 Does the model work?

3.4.1 Training and validation accuracy

Figure 3.4.1 shows the trend of the training and validation results for the Conv-LSTM model. In particular, the loss and Mean Squared Error (MSE) values are plotted during both the training and validation phases.

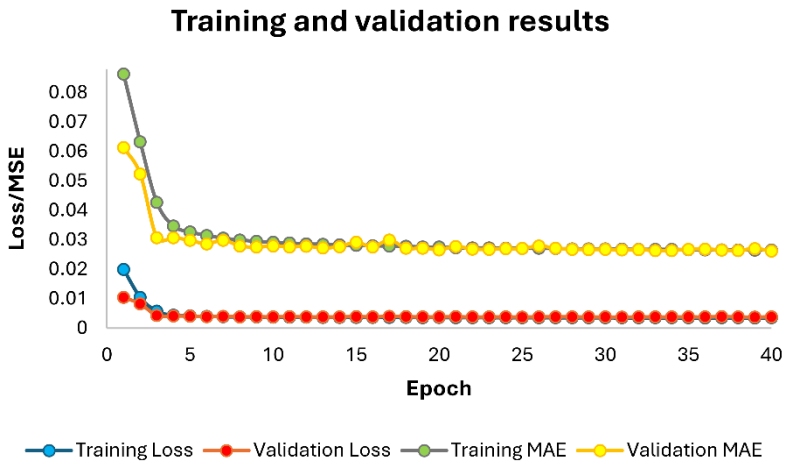

Figure 3.4.1 - Results of the training and validation processes of the Conv-LSTM model. The plot shows both Loss and MAE results through Epochs.

Figure 6 shows the trend of Training Loss, Validation Loss, Training MAE, and Validation MAE as a function of epochs (up to 40) during the training of a model.

The y-axis in Figure 6 represents the loss and MAE values, while the x-axis represents the number of epochs (up to 45). Training Loss is indicated by the blue line, Validation Loss by the red line, Training MAE by the grey line with green dots and Validation MAE by the yellow line.

At the beginning of the graph, the Loss values start with the Training Loss at around 0.078. Within a few epochs, the Training Loss decreases, stabilizing around the value of 0.008 already after the fifth epoch. The Validation Loss, which starts with a value very close to that of the Training Loss, undergoes similar behaviour and stabilizes around 0.008, suggesting that the model is not

significantly overfitting, as the loss curves for training and validation are close and stable.

The Training MAE, represented by the grey line with green dots, starts at a value of around 0.088 and falls rapidly until it stabilizes around 0.028 after the tenth epoch. The Validation MAE also follows a similar behaviour, stabilizing just above 0.028 after a rapid initial drop.

The behaviour of the graph suggests that the model achieves good convergence, with similar values of training and validation for both loss and MAE. The absence of significant divergence between Training Loss and Validation Loss, as well as between Training MAE and Validation MAE, indicates that there is no obvious sign of overfitting, as the values remain close and stable after a few epochs.

3.4.2 Mediterranean CMEMS-ConvLSTM application

This section focuses on the comparison between Hs and Tp predictions generated by the Conv-LSTM model and data provided by the Copernicus Marine Environment Monitoring Service (CMEMS) operational system for the Mediterranean Sea. The main objective is to assess the ability of the neural network-based model to produce satisfactory maps of H_s evolution over time and to compare them with CMEMS data, thus identifying strengths and weaknesses of the Conv-LSTM approach. A detailed analysis of the simulations identified significant similarities in the spatial and temporal distribution of the waves were identified, as well as discrepancies that may affect operational predictions in real-world scenarios.

Figure 3.4.2 (first and second rows, subplots A to F and G to L, respectively) shows a comparison of the H_s predictions provided by two models, CMEMS (Copernicus Marine Environment Monitoring Service) and Convolutional Long Short-Term Memory (Conv-LSTM), for 20 September 2020. Figure 3.4.2 is organised in a grid of eight panels for each model, with snapshots at four-hour intervals covering the entire day (00:00, 04:00, 08:00, 12:00, 16:00, 20:00).

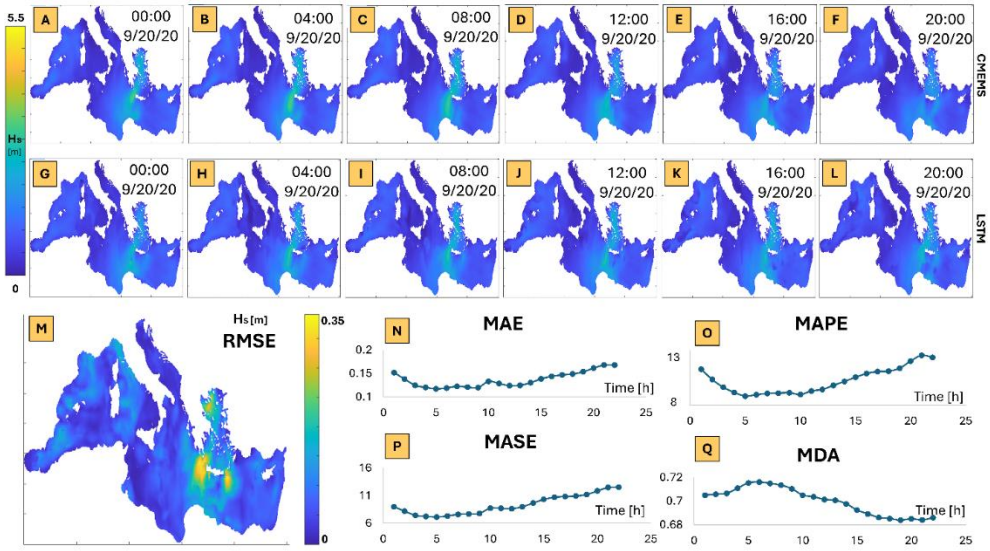

Figure 3.4.2 - Comparative results between CMEMS wave data (first row from top) and Conv-LSTM model predictions (second row from top) for H_s over the Mediterranean Sea on September 20, 2020, at different time intervals (00:00 Subplot A-G, 04:00 Subplot B-H, 08:00 Subplot C-I, 12:00 Subplot D-J, 16:00 Subplot E-K, 20:00 Subplot F-L). The bottom-left plot (Subploit M) shows the spatial distribution of the Root Mean Square Error (RMSE) between the two datasets. The time-series plots on the bottom right display the model's performance metrics: Mean Absolute Error (MAE) (Subplot N), Mean Absolute Percentage Error (MAPE) (Subplot O), Mean Absolute Scaled Error (MASE) (Subplot P) and Mean Directional Accuracy (MDA) (Subplot Q), evaluated over a 24-hour period. The reference system used is EPSG:9834 - Mollweide to allow a distorted view of the entire Area considering the longitudinal and latitudinal axes equal.

The colour scale on the left varies from blue (indicated for H_s values close to 0 metres) to yellow (for maximum H_s values up to 5.5 metres). This range allows areas with different wave heights to be visually identified. In both models, the areas with the highest wave heights are mainly concentrated in the central part of the Mediterranean region, especially near the Greek archipelago and the island of

Crete. These areas, shown in green/yellow, highlight wave heights ranging from about 2.5 to 5.5 metres.

At 00:00 (subplots A, G), both models show high waves, with CMEMS predicting up to 5 meters and Conv-LSTM around 4.5 meters. At 04:00 and 08:00 (subplots B-C, H-I), both models show decreasing wave heights, though CMEMS remains slightly higher. At 12:00 (subplots D, J), both predict peaks around 4 meters, with CMEMS showing a wider distribution. By 16:00 (subplots E, K), wave heights increase again, with CMEMS nearing 5 meters and Conv-LSTM slightly lower at 4.5 meters. At 20:00 (subplots F, L), both models show wave heights decreasing to around 4 meters.

Both models predict a similar wave development during the day, with the highest heights concentrated in the central-eastern Mediterranean region (Greece) and a general decrease in wave heights towards the end of the day. The main differences are observed in the peak wave values. CMEMS tends to predict slightly higher wave heights than Conv-LSTM at almost all times of the day, especially during the night and afternoon hours (00:00 and 16:00). However, the general trends and spatial distribution of the waves are comparable between the two models, indicating that both models correctly capture the main dynamics of the marine phenomenon in question.

Subplot M (third row bottom left) in Figure 3.4.2 shows the RMSE map for H_s between Conv-LSTM and CMEMS predictions. The map, covering the Mediterranean, uses a blue-to-yellow scale (0 to 0.35 meters). Most of the region shows low RMSE (< 0.1 meters), indicating strong agreement between models. Higher RMSE values (up to 0.35 meters), shown in green and yellow, appear near the Greek coasts and Crete, where the models diverge the most. Overall, the models align closely across the Mediterranean.

The final subplots in Figure 3.4.2 (subplot N to Q) present the temporal evolution of four metrics used to evaluate the predictions of H_s between Conv-LSTM and CMEMS over the 24 hours: Mean Absolute Error (MAE, subplot N), Mean Absolute Percentage Error (MAPE, subplot O), Mean Absolute Scaled Error (MASE, subplot P), and Mean Directional Accuracy (MDA, subplot Q).

MDA starts at approximately 0.1 m, remains stable until 12.00, and then increases to about 0.2 m by the end of the period, indicating growing discrepancies between the models. MAPE begins at around 13%, decreases to 8% in the morning, and returns to 13% by evening, reflecting a decline in the accuracy of Conv-LSTM

relative to CMEMS. MASE follows a similar pattern, starting at approximately 6 and rising to about 16 later in the day, signifying increased error. Finally, MDA starts at 0.72, indicating high predictive accuracy, but decreases to about 0.68, suggesting again reduced ability to predict wave height changes in the evening hours.

Figure 3.4.3, on the other hand, shows the results obtained for the simulation of the day 11/26/2021, again comparing the H_s CMEMS data with those obtained from the Conv-LSTM model.

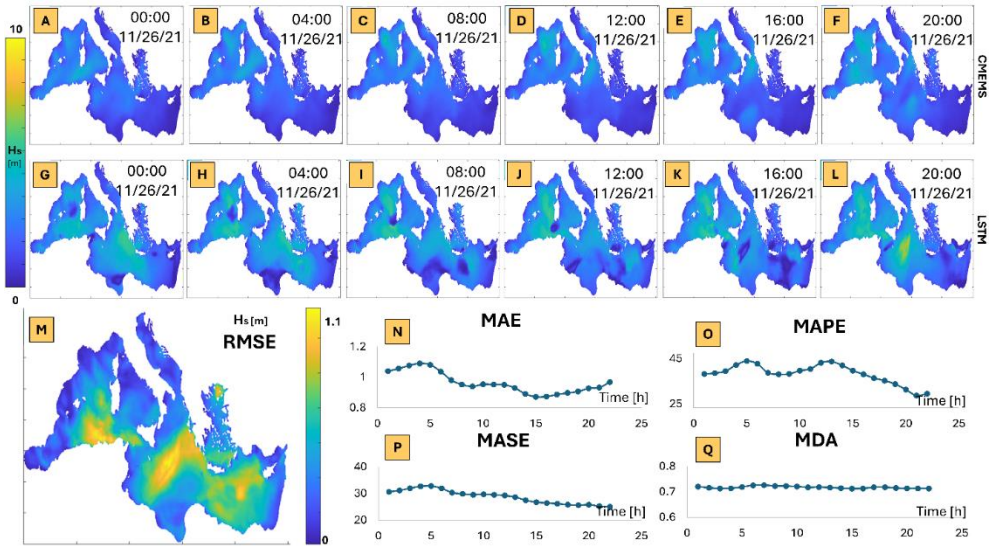

Figure 3.4.3 - Comparative results between CMEMS wave data (first row from top) and Conv-LSTM model predictions (second row from top) for H_s over the Mediterranean Sea on November 26, 2021, at different time intervals. The arrangement of the subplots in this figure follows the same structure as in Figure 7. The reference system used is EPSG:9834 - Mollweide to allow a distorted view of the entire Area considering the logitudinal and latitudinal axes equal.

Figure 3.4.3 (first and second rows, subplots A to F and G to L respectively) shows a comparison of the H_s predictions provided by two models. The organization of the panels is the same as in Figure 7.

At 00:00 (subplots A and G), both models indicate calm conditions with wave heights (H_s) below 2 m across most of the basin, except for the eastern Mediterranean and Aegean Sea, where heights reach 2-3 m. By 04:00 (subplots B and H), waves increase to 4-5 m in the eastern Mediterranean and North African coasts, with Conv-LSTM showing a broader area of high waves than CMEMS, suggesting some overestimation. At 08:00 (subplots C and I), wave heights rise to 6 m, with Conv-LSTM again predicting a larger area of high waves, though both models are generally in agreement. At 12:00 (subplots D and J), high waves exceed 5-6 m in the eastern Mediterranean, with Conv-LSTM predicting a slightly larger area with such heights. By 16:00 (subplots E and K), a decrease in wave heights is observed, particularly in the central and eastern regions; Conv-LSTM continues to show isolated areas of higher waves. Finally, at 20:00 (subplots F and L), both models indicate further reduction in wave heights, returning to calmer conditions (2-3 m), although Conv-LSTM still predicts some localized higher waves in the eastern Mediterranean, while CMEMS shows a more uniform decline.

The yellow areas in the third row of Figure 3.4.3 indicate a higher RMSE, mainly in the Algerian coastal area, in the central Mediterranean belt between the Greek archipelago and the Libyan desert, and west of the island of Cyprus, suggesting a larger discrepancy between the models in these areas. The remaining blue areas indicate a lower error, with better agreement between the forecasts, in the Adriatic Sea belt and in the extreme eastern and western parts of the Mediterranean.

The temporal error plots shown in the bottom right-hand corner of Figure 3.4.3 again provide a detailed view of the different error metrics used to evaluate model performance. Subplot N shows that the average absolute error remains relatively stable throughout the day, with slight fluctuations around the value of 1.0. This indicates that, overall, the models maintain a constant mean error, with no major fluctuations at different times of day. MAPE (subplot O), on the other hand, shows a percentage of absolute error ranging between 30% and 45%. As for MASE (subplot P), the graph shows a stable trend with values below 0.8. This value signals a good ability of the model to predict values with a proportionally small error. Finally, in the MDA (subplot Q), shows a slight oscillation around the value of 0.7 is noted, indicating that most of the errors remain close to the median of the absolute errors, suggesting that the deviations do not deviate are significantly different from the central value, thus contributing to a fairly uniform distribution of the errors.

Figure 3.4.4 shows the time series of simulations from 07/11/2022 for both models, again accompanied by the Root Mean Square Error (RMSE) map and four graphs of error metrics to assess the discrepancy between the simulations of the two models.

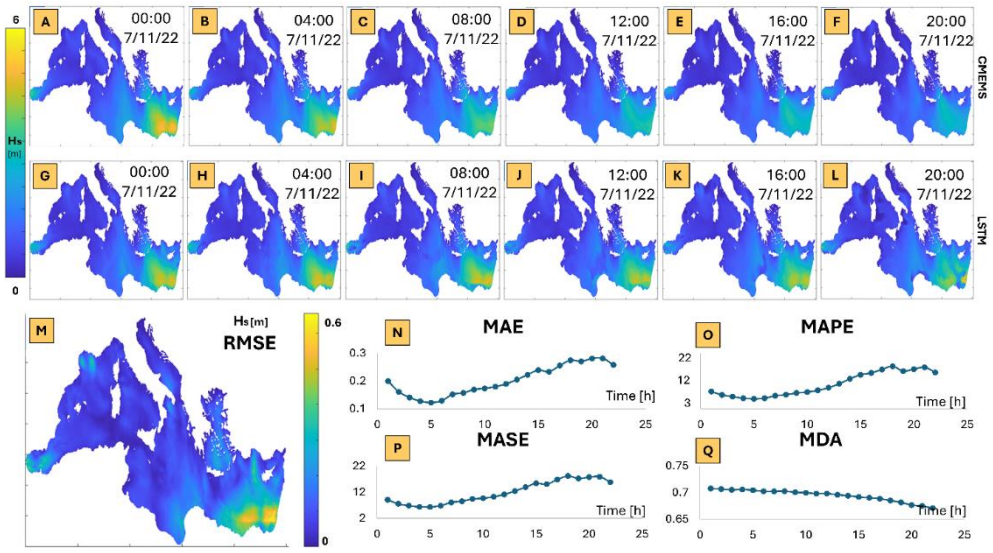

Figure 3.4.4 - Comparative results between CMEMS wave data (first row from top) and Conv-LSTM model predictions (second row from top) for H_s over the Mediterranean Sea on July 11, 2022, at different time intervals. The arrangement of the subplots in this figure follows the same structure as in Figure 7. The reference system used is EPSG:9834 - Mollweide to allow a distorted view of the entire Area considering the logitudinal and latitudinal axes equal.

In the A-F and G-L subplots of Figure 3.4.4 (for CMEMS and Conv-LSTM respectively), the colour scale on the left varies from 0 to 6 metres, with blue indicating lower wave heights and yellow/green representing the highest waves. As far as CMEMS forecasts are concerned, at 00:00, the highest waves are observed in the southern part of the Mediterranean, near the Egyptian and Israeli coasts, with H_s around 5-6 meters. These values remain high in the same areas until 20:00, with a reduction of about 2 m in their intensity at the end of the day.

The rest of the Mediterranean shows H_s values between 2 and 4 meters, with green transition zones showing moderate waves between 2 and 3 meters, especially in the eastern part of the Mediterranean (near the islands and coasts of Turkey). The simulations produced by the Conv-LSTM model (subplot G-L in Figure 3.4.4) follow the same time interval as the CMEMS. Again, high Hs values are observed at 00:00 in the southern areas near the coasts of Libya, Egypt and Israel, with waves of up to 6 metres. The rest of the Mediterranean follows the same wave pattern obtained from the CMEMS data. Although the spatial distribution of the high waves is similar between the two models, the Conv-LSTM model tends to slightly overestimate the wave heights in some coastal regions, especially after 12:00, when the differences become more pronounced (1.5 m).

In the RMSE map, positioned at the bottom left (subplot M in Figure 3.4.4), the regions with the highest RMSE (0.4-0.6 meters) are concentrated along the southern coasts and in the eastern part of the Mediterranean. In contrast, much of the western Mediterranean has relatively low errors, with values below 0.2 meters.

The plot of the MAE (subplot N in Figure 3.4.4), shows that the metric starts from an initial value of about 0.12 meters in the early hours of the day and gradually increases, reaching a maximum of 0.25 metres around 20:00. MAPE (subplot O), starts at around 7 % in the early hours of the day and remains relatively stable until 10:00 am. Then, it starts to increase and reaches a peak of about 13% around 20:00. As for the MASE (subplot P), it starts at about 6 in the early hours of the day and gradually increases until it reaches a value of 22 in the evening hours. Finally, the MDA (subplot Q), shows an initial value of about 0.75, signaling a high accuracy in forecasting direction in the early hours of the day. This value gradually decreases over the course of the day, dropping to around 0.65 in the final hours.

In summary, all metrics show good agreement between the Conv-LSTM and CMEMS model forecasts in the early part of the day, with discrepancies becoming slightly larger in the evening hours, as evidenced by the progressive increase in error metrics (MAE, MAPE, MASE) and the decrease in directional accuracy (MDA). The southern coastal regions of the Mediterranean present the highest discrepancies, with RMSE values up to a maximum of 0.6 metres.

The last forecast simulation of the Conv-LSTM model on CMEMS data is presented in Figure 3.4.5 for 01/27/2022. Again, the configuration of the Figure is the same as the previous ones (Figure 3.4.2, Figure 3.4.3 and Figure 3.4.4).

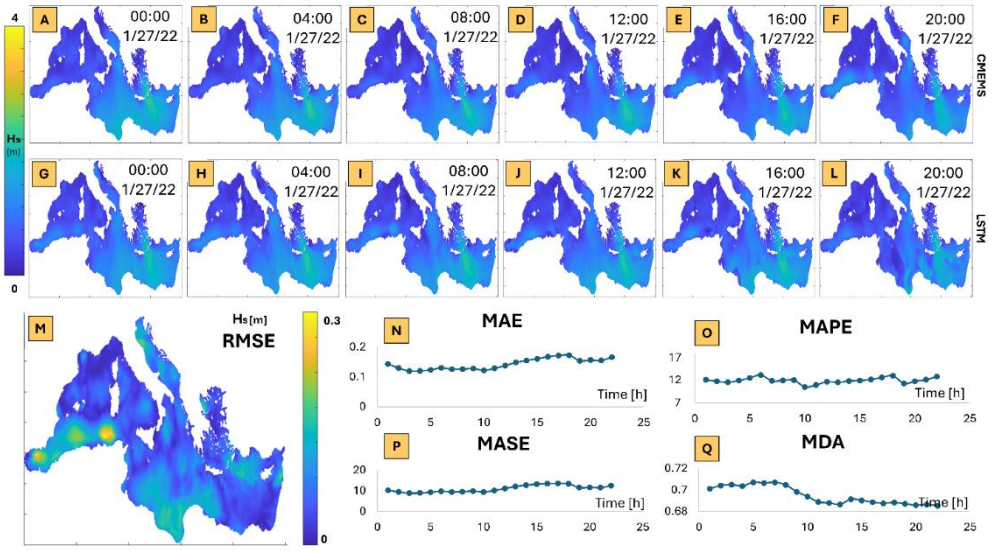

Figure 3.4.5 - Comparative results between CMEMS wave data (first row from top) and Conv-LSTM model predictions (second row from top) for H_s over the Mediterranean Sea on January 27, 2020, at different time intervals. The arrangement of the subplots in this figure follows the same structure as in Figure 7. The reference system used is EPSG:9834 - Mollweide to allow a distorted view of the entire Area considering the logitudinal and latitudinal axes equal.

In subplots A-F and G-L, the color scale ranges from 0 to 4 meters, with blue indicating low waves and green/yellow representing higher waves. At 00:00, high waves (~2-3 meters) are present in the eastern Mediterranean near Greece, Turkey, and Egypt, with this pattern remaining stable until 20:00, albeit with a slight shift southeast. From 04:00 to 08:00 (subplots B-C, H-I), Hs decrease slightly in the central Mediterranean, though peaks near Libya persist around 3 meters. CMEMS generally predicts higher wave propagation than Conv-LSTM in this region. At 12:00 and 16:00, the pattern remains similar, with higher waves in the southeastern part; however, Conv-LSTM tends to show slightly lower values compared to CMEMS. The areas around Crete and the Aegean Sea exhibit

higher waves than other regions. By 20:00, maximum Hs are around 2.5-3 meters off the Egyptian and Greek coasts, with differences in wave distribution between the models, particularly in the central Mediterranean where CMEMS shows a broader, more uniform propagation. Both models indicate an increase in Hs south of Spain, but Conv-LSTM attenuates the pattern seen in CMEMS near Algeria.

The RMSE map (subplot M in Figure 3.4.5) clarifies and highlights the discrepancies between the two models' predictions in terms of wave heights, with a colour scale ranging from 0 to 0.3 m. The result confirms the smallest variations by showing the regions with the highest RMSE, with a maximum of 0.3 m, in the western part of the Mediterranean, especially along the southwest coast of Spain and in the Alborán Sea (between Spain and Morocco). These areas coincide with the highest wave areas in the last hours of the day, suggesting that the differences between the two models are greatest where the waves were most intense but at the end of the day. The RMSE is generally lower in the eastern and central areas, with values below 0.1 meters.

In subplot N of Figure 3.4.5, the MAE remains constant around 0.12 meters for most of the day, with a slight increase around 20:00, when it reaches about 0.15 meters. The discrepancies between the two models are relatively stable over time for most of the day. MAPE (Subplot O) varies between 8% and 10% in the early hours, with a slight increase towards 20:00, where it peaks at around 12%. Again, the Conv-LSTM model maintains reasonable accuracy in comparison with CMEMS. The MASE (subplot P) remains relatively stable during the day, varying between 7 and 10. The scale of the discrepancies between the two models, therefore, does not change drastically over the course of the day, but the differences only become more evident in the last few hours. Finally, the MDA (subplot Q of Figure 3.4.5) starts from a value around 0.72 in the early hours of the day and gradually decreases to around 0.68 at 20:00. The accuracy in predicting the direction of changes in the waves throughout the day also follows the patterns of the other metrics.

Another parameter for comparison on the ability of Conv-LSTM to accurately predict the Mediterranean meteorological climate was the *Tp*. RMSE maps of *Tp* (between CMEMS and Conv-LSTM) were reported for the events discussed above and are shown in Figure 3.4.6.

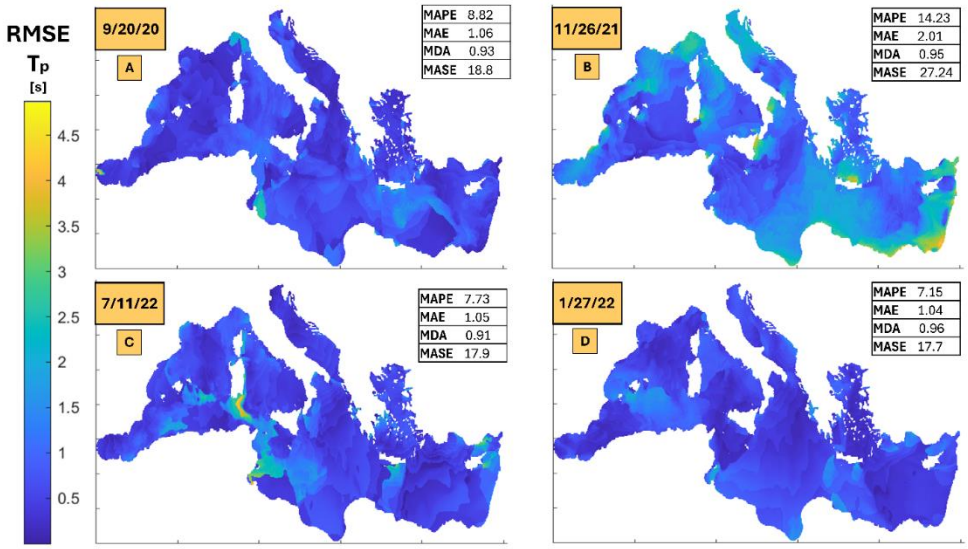

Figure 3.4.6 - Spatial distribution of RMSE for the peak period T_p [s] across the Mediterranean Sea, shown for all simulated events. The color scale represents the error magnitude in seconds. The statistical metrics MAPE, MAE, MDA, and MASE for each date are displayed in each date subplot (from A to D respectively for event 1 to 4 of Table 3.2-1 - Dates of the events used for further validation model.). The reference system used is EPSG:9834 - Mollweide to allow a distorted view of the entire Area considering the longitudinal and latitudinal axes equal.

The color scale on the left ranges from blue (low RMSE values) to yellow (high RMSE values), spanning 0.5 to 4.5 seconds. The maps illustrate the spatial evolution of peak period estimation error, highlighting geographical variations. On 20 September 2020 (subplot A), RMSE values are generally low, with most of the Mediterranean in blue (error < 2.5 seconds), while higher errors are concentrated along the northern and eastern coasts. Statistical indicators show a MAPE of 8.82, MAE of 1.06, MDA of 0.93, and MASE of 18.8, indicating good overall accuracy, particularly in coastal areas.

On 26 November 2021 (subplot B), RMSE values increase significantly, particularly in the eastern and southeastern regions, reflected in a MAPE of 14.23, MAE of 2.01, MDA of 0.95, and MASE of 27.24, suggesting difficulties in

predicting peak wave periods due to complex atmospheric conditions. By 11 July 2022 (subplot C), errors decrease compared to the previous date, with central and western Mediterranean regions showing low errors, though some coastal areas still exhibit higher values. The indicators confirm this reduction: MAPE of 7.73, MAE of 1.05, MDA of 0.91, and MASE of 17.9, indicating a more uniform error distribution. Finally, on 27 January 2022, a similar pattern emerges with low RMSE values (below 1.5 seconds), but with further improvements, particularly in the southeastern Mediterranean. The statistical values are the lowest of all analyzed dates: MAPE of 7.15, MAE of 1.04, MDA of 0.96, and MASE of 17.7, indicating enhanced prediction quality over time, culminating in the best performance on this date.

Overall, the maps show significant spatial variability in the forecast error of the peak wave period, with marked differences between the dates considered. The highest errors are often associated with coastal areas and the eastern part of the Mediterranean Sea, where meteorological and oceanographic conditions may be more complex and difficult to model with the wind and bathymetric information layer alone. The time evolution suggests an improvement in the forecasts, with a reduction of the number of errors at later times.

Results on the comparison of simulated θ against CMEMS data are shown in the supplementary materials.

3.4.3 Validation RON Buoy-CMEMS-ConvLSTM

In order to test the accuracy of the Conv-LSTM predictions and assess the magnitude of deviations from the CMEMS data, we compared for three different scenarios (2, 3 and 4 events of Table 3.2-1), the predictions obtained from the model with data from the Italian RON at 7 different locations in Italy (Alghero, Ancona, Crotone, La Spezia, Mazara, Monopoli and Ponza) as shown in section 3.2.1. Event 1 of the comparison in Table 3.2-1 is not shown as data from RON are not available in 2020.

Figure 3.4.7 shows three subplots for each location: (first column) the comparison between the data measured from the respective wave buoy (Buoy in red) and the predictions of the models (in yellow and blue for CMEMS and Conv-LSTM respectively); In the second column, the scatter plots between the values predicted by the models and those observed from the buoy (Ground Truth, GT). Finally, the third column shows the tables with the CC and the bias against the respective GT for the two models.

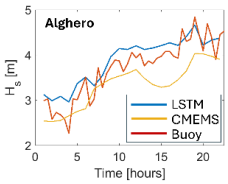

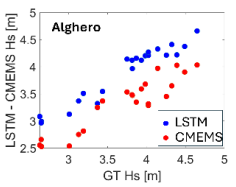

Alghero

MODEL	CC	BIAS
CMEMS	0.93	0.38
Conv-LSTM	**0.97**	**0.20**

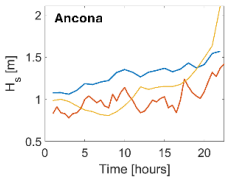

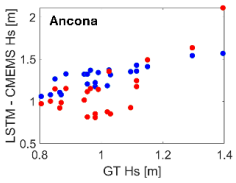

Ancona

MODEL	CC	BIAS
CMEMS	0.75	**0.20**
Conv-LSTM	**0.85**	0.29

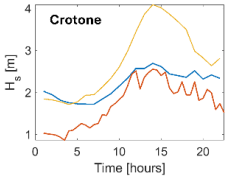

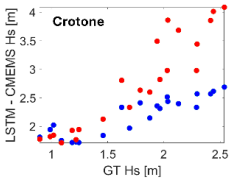

Crotone

MODEL	CC	BIAS
CMEMS	**0.93**	1.01
Conv-LSTM	0.90	**0.46**

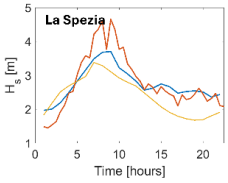

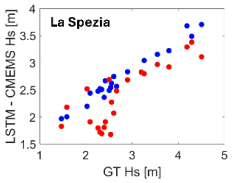

La Spezia

MODEL	CC	BIAS
CMEMS	0.83	0.55
Conv-LSTM	**0.98**	**0.29**

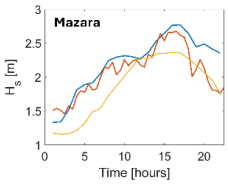

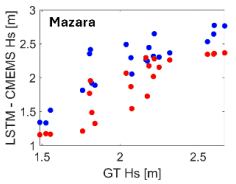

Mazara

MODEL	CC	BIAS
CMEMS	**0.87**	0.25
Conv-LSTM	**0.87**	**0.17**

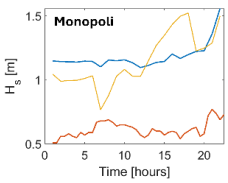

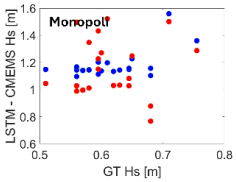

Monopoli

MODEL	CC	BIAS
CMEMS	0.05	**0.54**
Conv-LSTM	**0.59**	0.57

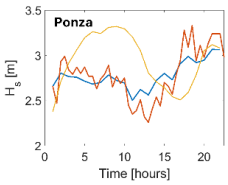

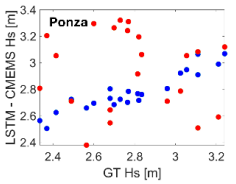

Ponza

MODEL	CC	BIAS
CMEMS	-0.09	0.36
Conv-LSTM	**0.93**	**0.11**

Figure 3.4.7 - The figure shows comparisons between H_s predictions using the Conv-LSTM model and the CMEMS dataset against RON

buoy observations at various locations (Alghero, Ancona, Crotone, La Spezia, Mazara, Monopoli, and Ponza) for the 2 event (Table 3.2-1). The first columns display time series plots of Conv-LSTM (blue), CMEMS (yellow), and buoy data (red). The second columns show scatter plots comparing the predicted values from Conv-LSTM and CMEMS against buoy data. On the right, CC and bias values for each model are provided for each location.

At several locations off the Italian coast, the comparative analysis between the Conv-LSTM and CMEMS models shows that the Conv-LSTM model offers more accurate predictions of H_s. At Alghero, the time course shows that Conv-LSTM closely follows the actual measurements, while CMEMS tends to slightly overestimate heights in the first hours and has larger oscillations than Conv-LSTM. Also in the scatter plot, Conv-LSTM shows a closer correlation with the real data than CMEMS. In terms of correlation (CC) and bias, Conv-LSTM has a CC of 0.93 and a bias of 0.20, while CMEMS has a CC of 0.63 and a bias of -0.36. At Ancona, a similar trend is found, with Conv-LSTM following the observed measurements more accurately, while CMEMS overestimates the wave height at various times of the day. Again, the scatter plot shows less dispersion for Conv-LSTM than CMEMS. In numerical terms, Conv-LSTM has a CC of 0.85 and a bias of 0.29, while CMEMS has a CC of 0.75 and a bias of 0.20. At the Crotone buoy, both models show similar oscillations, but Conv-LSTM captures the peaks better, especially in the central hours of the day. The dispersion plot also suggests a higher accuracy of the Conv-LSTM model, with less dispersion than CMEMS. The CC of Conv-LSTM is 0.93 with a bias of 0.46, while CMEMS has a CC of 0.83 and a bias of 0.68. At La Spezia, the Conv-LSTM model again proves to be more accurate in following the wave peaks, while CMEMS has small oscillations that are not present in the observed data. The scatter plot confirms this trend, showing a narrower distribution for Conv-LSTM around the perfect match line. At this location, Conv-LSTM has a CC of 0.89 and a bias of 0.29, while CMEMS has a CC of 0.63 and a bias of 0.56, again highlighting the higher accuracy of the Conv-LSTM model. At Mazara, both models manage to follow the general trend of wave heights well, but Conv-LSTM is slightly more accurate in the peaks. In terms of correlation and bias, Conv-LSTM has a CC of 0.87 and a bias of 0.17, while CMEMS has a CC of 0.77 and a bias of 0.15. As far as Monopoli is concerned, Conv-LSTM shows greater accuracy in following the trend of the observed measurements, while CMEMS tends to overestimate the wave height at certain times. The dispersion of the data

is narrower for Conv-LSTM, confirming a lower tendency to overestimate than CMEMS. At this location, Conv-LSTM has a CC of 0.59 and a bias of 0.57, while CMEMS has a CC of 0.65 and a bias of 0.42. Finally, at Ponza, Conv-LSTM proves more accurate in following the observed data than CMEMS, which tends to slightly overestimate wave heights. The scatter plot shows that Conv-LSTM is closer to the ideal line, signaling a more accurate prediction. Conv-LSTM has a CC of 0.93 and a bias of 0.11, while CMEMS has a CC of -0.06 and a bias of 0.39.

Overall, the results indicate that, at all locations analyzed, the Conv-LSTM model provides more accurate predictions than CMEMS, as confirmed by the higher correlation coefficients and lower bias. Conv-LSTM is particularly effective in capturing peak wave heights and has a lower dispersion than the observed data.

Figure 3.4.8 also shows eight subplots arranged in three columns, illustrating the weather forecasts for the same locations as RON.

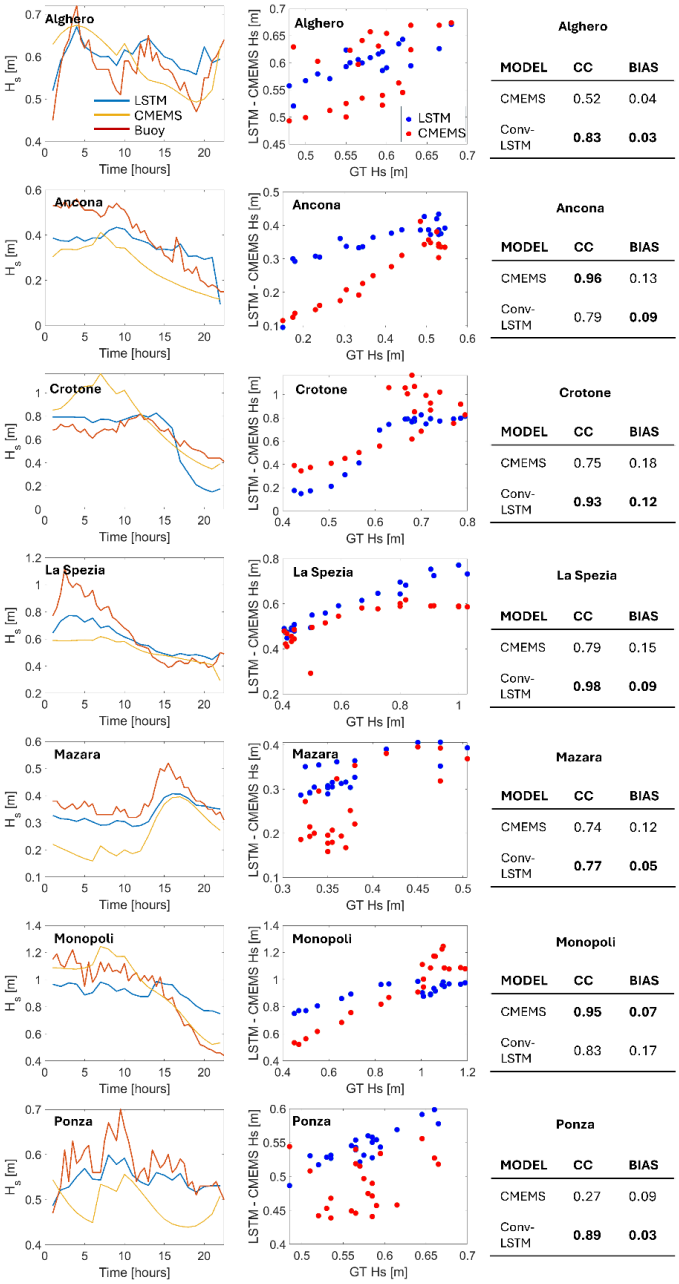

Alghero

MODEL	CC	BIAS
CMEMS	0.52	0.04
Conv-LSTM	**0.83**	**0.03**

Ancona

MODEL	CC	BIAS
CMEMS	**0.96**	0.13
Conv-LSTM	0.79	**0.09**

Crotone

MODEL	CC	BIAS
CMEMS	0.75	0.18
Conv-LSTM	**0.93**	**0.12**

La Spezia

MODEL	CC	BIAS
CMEMS	0.79	0.15
Conv-LSTM	**0.98**	**0.09**

Mazara

MODEL	CC	BIAS
CMEMS	0.74	0.12
Conv-LSTM	**0.77**	**0.05**

Monopoli

MODEL	CC	BIAS
CMEMS	**0.95**	**0.07**
Conv-LSTM	0.83	0.17

Ponza

MODEL	CC	BIAS
CMEMS	0.27	0.09
Conv-LSTM	**0.89**	**0.03**

Figure 3.4.8 - The figure shows comparisons between H_s predictions using the Conv-LSTM model and the CMEMS dataset against RON

buoy observations at various locations (Alghero, Ancona, Crotone, La Spezia, Mazara, Monopoli, and Ponza) for the 3 event (Table 3.2-1). The arrangement of the subplots in this figure follows the same structure as in Figure 12.

At Alghero (Subplot 1), the Conv-LSTM model slightly underestimates wave heights compared to CMEMS, with both models following a similar trend. However, the CMEMS has slightly higher peaks. The scatter plot shows a moderate linear correlation, with Conv-LSTM being more densely distributed around the 1:1 line. The correlation of Conv-LSTM is higher (0.83) than CMEMS (0.52), with very similar biases (0.03 and 0.04, respectively). In Ancona (subplot 2), both models predict a rapid decrease of waves in the first hours, but CMEMS is closer to the actual data. Conv-LSTM tends to underestimate slightly, although it shows a higher correlation (0.69) than CMEMS (0.56). Here too, the bias of Conv-LSTM is slightly lower (0.13 vs. 0.15). For Crotone (subplot 3), the two models predict a gradual decrease in wave heights, with Conv-LSTM being more accurate, especially in the second part of the day, while CMEMS tends to underestimate the values. The scatter plot confirms the greater closeness of Conv-LSTM to the 1:1 line. The Conv-LSTM has a higher correlation (0.83 compared to 0.65 for CMEMS) and a lower bias (0.12). At La Spezia (Subplot 4), both models show a similar trend, but Conv-LSTM overestimates the waves in the later hours of the day. Although CMEMS presents a slightly lower correlation (0.79 vs. 0.88 for Conv-LSTM), the latter has a higher bias (0.09), suggesting a slight overestimation. At Mazara (subplot 5), the forecasts of both models are very close to the measured data, with Conv-LSTM slightly overestimating in the early hours of the day. The scatter plot shows a good fit of both models, with Conv-LSTM maintaining a higher correlation (0.87) than CMEMS (0.74), albeit with a slightly higher bias (0.17 vs. 0.12). At Monopoli (subplot 6), both models underestimate the heights in the first hours, but follow a similar trend. Conv-LSTM overestimates in the last hours and shows a higher dispersion, with a lower correlation (0.65 vs. 0.27 for CMEMS). The bias of Conv-LSTM is also significantly higher (0.57 vs. -0.17 for CMEMS), suggesting a tendency to overestimate. For Ponza (subplot 7), the Conv-LSTM model follows the general pattern but tends to overestimate compared to CMEMS, especially during peaks. The scatter plot confirms a higher dispersion of Conv-LSTM. However, Conv-LSTM shows a better correlation (0.83 vs. 0.46 for CMEMS), although the bias is similar (0.11 for Conv-LSTM).

In summary, the Conv-LSTM model shows a higher correlation with real data than CMEMS in almost all locations, proving to be more effective in capturing the general trend of wave heights. However, in this case, Conv-LSTM tends to overestimate in some regions, especially during peaks periods, while CMEMS appears more conservative, with a slight tendency to underestimate (behaviour already confirmed by Dodet et al., 2021; Ravdas et al., 2018; Sanchez-Arcilla et al., 2021).

Figure 3.4.9 also shows the same setup as the previous two (Figure 3.4.7 and Figure 3.4.8).

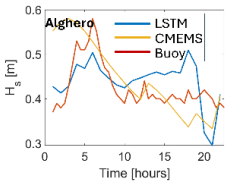

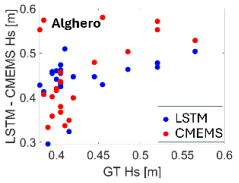

Alghero

MODEL	CC	BIAS
CMEMS	**0.54**	**0.05**
Conv-LSTM	0.42	**0.05**

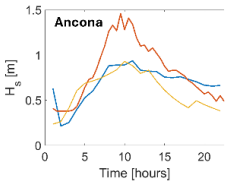

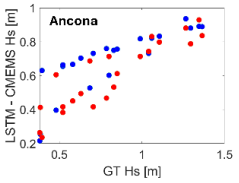

Ancona

MODEL	CC	BIAS
CMEMS	**0.89**	0.23
Conv-LSTM	0.82	**0.19**

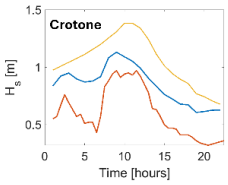

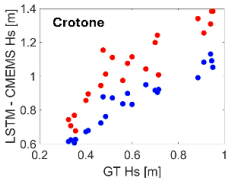

Crotone

MODEL	CC	BIAS
CMEMS	0.91	0.45
Conv-LSTM	**0.96**	**0.24**

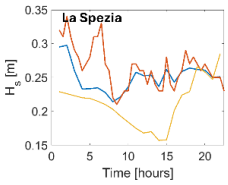

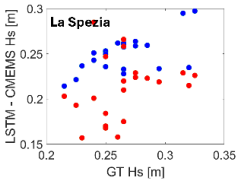

La Spezia

MODEL	CC	BIAS
CMEMS	0.26	0.06
Conv-LSTM	**0.61**	**0.02**

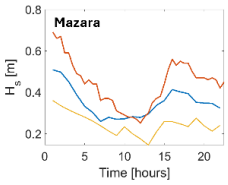

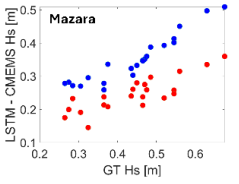

Mazara

MODEL	CC	BIAS
CMEMS	0.84	0.19
Conv-LSTM	**0.94**	**0.09**

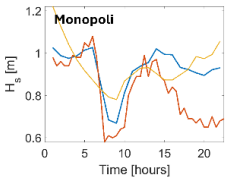

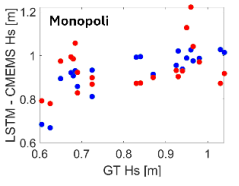

Monopoli

MODEL	CC	BIAS
CMEMS	0.34	0.15
Conv-LSTM	**0.76**	**0.11**

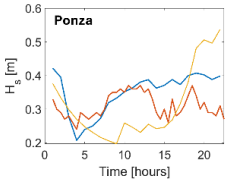

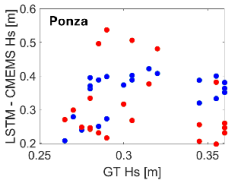

Ponza

MODEL	CC	BIAS
CMEMS	-0.18	0.09
Conv-LSTM	**0.40**	**0.06**

Figure 3.4.9 - The figure shows comparisons between H_s predictions using the Conv-LSTM model and the CMEMS dataset against RON

buoy observations at various locations (Alghero, Ancona, Crotone, La Spezia, Mazara, Monopoli, and Ponza) for the 4 event (Table 3.2-1). The arrangement of the subplots in this figure follows the same structure as in Figure 12.

At Alghero, both models adequately capture the wave pattern, but the Conv-LSTM model shows a higher accuracy in the peaks, especially around 5 and 18 o'clock. The scatter plot shows a closer correlation between Conv-LSTM and the observed data, with points closer to the diagonal than CMEMS. The metrics confirm the superiority of Conv-LSTM, with a correlation coefficient (CC) of 0.83 and a bias of 0.03, while CMEMS has a lower CC of 0.42 and a bias of 0.05. In Ancona, the two models follow the general trend of the waves, but Conv-LSTM better represents the peaks, especially around hour 10. Also in the scatter plot, Conv-LSTM shows a better correlation with the actual data than CMEMS. The metrics show a CC of 0.82 for Conv-LSTM and a bias of 0.19, while CMEMS has a CC of 0.69 and a higher bias of 0.23. For Croton, both models capture the general trend, but Conv-LSTM is more accurate in representing the peaks than the CMEMS data. The scatter plot confirms a closer correlation between Conv-LSTM and the observed data. Conv-LSTM has a significantly higher CC (0.98) and a bias of 0.24, while CMEMS stops at a CC of 0.60 with a bias of 0.12. In La Spezia, Conv-LSTM is more accurate, especially in the peak around hour 12, while CMEMS overestimates the waves. The scatter plot shows a significantly better correlation for Conv-LSTM, with points closer to the diagonal. The metrics show a CC of 0.81 for Conv-LSTM and a bias of 0.02, while CMEMS has a much lower CC (0.26) and a bias of 0.05. At Mazara, both models correctly capture the general pattern, but Conv-LSTM shows greater accuracy in detail. The scatter plot confirms that Conv-LSTM is closer to the ideal line than CMEMS. The metrics indicate a CC of 0.84 for Conv-LSTM with a bias of 0.09, while CMEMS has a CC of 0.64 and a bias of 0.19. At Monopoli, Conv-LSTM provides a more accurate estimate, particularly in the higher peaks, where CMEMS tends to underestimate. Even in the scatter plot, Conv-LSTM shows a much better correlation, with more concentrated points near the diagonal. The metrics show a CC of 0.78 for Conv-LSTM and a bias of -0.11, while CMEMS has a CC of 0.43 and a bias of 0.15. Finally, at Ponza, both models follow the general trend, but Conv-LSTM captures wave peaks better than CMEMS. The scatter plot shows a significantly better correlation for Conv-LSTM, with the points much closer to the regression line than CMEMS. Conv-

LSTM has a CC of 0.40 and a bias of 0.08, while CMEMS shows a negative CC of -0.18 and a slightly negative bias of -0.11.

The metrics clearly show the superiority of the Conv-LSTM model over CMEMS at all sites, with higher DC values and lower bias. At Ponza, CMEMS showed very poor performance, with a negative correlation coefficient, suggesting significant limitations of the model in calm conditions.

3.5 Reflections on findings

The simulations conducted in Chapter III illustrate the effectiveness of the Conv-LSTM model in forecasting sea conditions that influence coastal erosion, particularly wave heights, periods, and directions in the Mediterranean region. Despite the strong agreement with CMEMS data, the study reveals some limitations in the Conv-LSTM model, especially in coastal areas and the eastern parts of the basin, where the model's accuracy is impacted by geographical complexity and atmospheric dynamics. The Conv-LSTM model tends to overestimate wave heights during peak periods, likely due to its sequential neural network structure, while the CMEMS model is more conservative but stable over time. This disparity highlights the Conv-LSTM's strengths in short-term dynamics but also its limitations under extreme conditions, where errors become more noticeable (e.g., RMSE and MAPE). These issues are more prominent in regions like the eastern and southern Mediterranean, where oceanographic complexities are higher (Pinardi & Masetti, 2000; Robinson et al., 1991).

Simulations from key dates, such as 20 September and 26 November 2021, show increased error during intense weather events, highlighting the challenges faced by the Conv-LSTM model in predicting waves amidst significant atmospheric disturbances. However, the model's performance has shown improvement over time, as evidenced by results from 3 July 2022, particularly under stable meteorological conditions. The Conv-LSTM's comparative analysis with RON wave data in various locations such as Alghero, La Spezia, and Crotone further underscores its capability to accurately capture wave peaks, outperforming CMEMS in these contexts, although some overestimation remains in areas such as Monopoli and Ponza.

Despite its strengths, the model's absence of crucial variables such as air temperature and atmospheric pressure, along with limited bathymetric detail near the coast, constrains its ability to achieve precise predictions. Future improvements could involve the integration of these additional variables and

enhanced resolution of bathymetric data, offering potential for more accurate forecasting, particularly in coastal zones and during extreme weather.

Finally, in a context such as the Mediterranean, where there is a lack of adequate statistical distributions for the peak period (T_p) of waves (Cañellas et al., 2024; Cherneva et al., 2005; Isaacson & MacKenzie, 1981; Muraleedharan et al., 2015), such a model offers a more accurate and reliable prediction, contributing to a better statistical inference of meteo-marine data and reducing uncertainty in long and short term analyses.

The insights from this chapter provide a foundation for the subsequent research discussed in this thesis. The ability to accurately predict sea conditions can be critical to the analysis and management of coastal dynamics discussed in subsequent chapters. For example, accurate wave forecasting is particularly useful for understanding the socioeconomic impacts of shoreline changes (Chapter V). In addition, the forecasting capabilities developed in Chapter III support the technical tools and methodologies presented in Chapters VI through VIII, which focus on monitoring and managing changes in coastal morphology and the impacts of protective structures. Finally, the ability of the Conv-LSTM model to make detailed weather forecasts enhances the broader scope of coastal erosion analysis, providing a significant component for both short-term forecasting and the generation of reliable data for long-term studies.

Chapter IV

Having explored the role of waves as a major factor in coastal erosion, we now focus on the need for accurate coastline monitoring, a crucial element in understanding coastal dynamics over the long term. However, such data are sometimes lacking, incomplete or time-sensitive. On the other hand, the availability of satellite data is constantly increasing, and therefore there is a need to be able to use such data to generate coastal datasets or coastlines for subsequent analysis. This chapter presents, a model based again on the application of AI to coastal engineering problems, in particular a semantic segmentation model will be presented and exploits the potential of convolutional neural networks (CNNs) for automatic and accurate coastline extraction from satellite images. This methodology, based on the U-Net architecture, allows for more accurate identification of the separation between land and sea, enhancing traditional "water/land" segmentation through the innovative use of a Sobel-edge loss function and the classification of multiple land categories by exploiting a training dataset purely made for coastal environments. The model has been applied and validated on the Sicilian coast, demonstrating not only accuracy but also great potential for the analysis and sustainable management of coastal areas.

The topics and contents covered in the following chapter are taken from a research article published by Elsevier, "Computer and Geosciences" scientific journal (Scala et al., 2024c).

4.1 Coastline, why and how to identify

As already mentioned in section 2.4, the proxy used to analyze the dynamics of the coast and to identify if the coast is in accretion or retreatment, due to storm surge events or sea level rise, is the coastline (Pollard et al., 2020; Sapkota & White, 2019).

Coastlines, the boundary between land and water, play a crucial role in studying coastal dynamics and are influenced by both natural events and human activities (Anfuso et al., 2012, 2013; Anfuso & Martínez Del Pozo, 2009; Borzì et al., 2021).

The coastline can be identified using different proxies like the top cliff line, seaward dune vegetation line, or wet/dry line, each of which has advantages and disadvantages depending on the type of study. Wu et al. (2019) found that coastlines are easily identified where boundaries have sharp slope, such as

seawalls, or in areas with rough terrain such as rocky or vegetated coasts. In addition, the wet-dry line, which takes into account the effects of waves and tides, can be helpful in detecting coastlines. (Boak & Turner, 2005b).

Monitoring coastline changes is therefore essential for effective coastal management (Manno et al., 2022a; Molina et al., 2020b) but its perennial and considerable temporal variability makes it difficult to determine. In fact, the coastline position change at any instant, and this characteristic should be considered when satellite/aerial images are used (Manno et al., 2017).

Satellite remote sensing provides continuous observations of coastal morphology, and the conventional method for detecting coastlines involves visual interpretation by experts. However, automated and semi-automated approaches are becoming more prevalent, and several methods have been developed using different instruments (Toure et al., 2019; Zhu et al., 2021)

Recent innovations have seen the rise of automated local-scale approaches. These can be broadly categorized into boundary detection techniques (Liu & Jezek, 2004; Paravolidakis et al., 2018) and segmentation methods (Cao et al., 2020). The latter often employs Machine Learning (ML) and Deep Learning (DL) strategies, such as Convolutional Neural Networks (CNNs) (Aghdami-Nia et al., 2022; Chang et al., 2022; Kattenborn et al., 2021; Sultan et al., 2020). For instance, studies by Dang et al. (2022) and Chang et al. (2022) successfully used deep learning models to detect coastlines using high-resolution satellite imagery. Seale et al. (2022) also employed segmentation methods to distinguish between sea and land.

However, coastlines detection from satellite imagery is challenging due to various environmental characteristics and the problems of “poor spatio-temporal generalization” and “scaling” (Liu et al., 2017; Toure et al., 2019b). To address these issues, the current research uses a CNN model based on semantic segmentation for coastline identification, using the segmentation technique differently from existing methods. This approach discerns the land-sea boundary and also detects human-made structures, vegetation, and other land cover. The research uses the Sobel-edge loss function from Seale et al. (2022) and employs the Coast Train dataset for model training (Buscombe et al., 2023a; Wernette et al., 2022). In fact, we trained the model with a dataset specific to coastal areas thus building a specialized classifier for these types of areas.

4.2 Experimental approach and application area

This section provides an overview of the data utilized and the methodology employed for detecting and delineating the coastline. To identify the coastline from satellite/aerial images, an automatic recognizing approach was used. In detail, a neural network was used, and its training and validation was made by means of the Coast Train dataset. The post-processing of the model output for the extraction of the coastline is also described. Finally, a description of the study area and the images used to test the model on the Sicilian case study is provided.

The flowchart in Figure 4.2.1 describes the working principle of the proposed model.

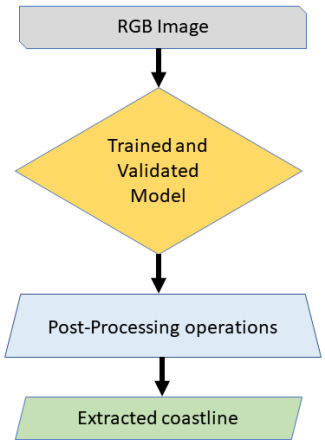

Figure 4.2.1 - Model operation flowchart.

The Coast Train dataset (Wernette et al., 2022) includes 10 coastal images with 1.2 billion labeled pixels covering 3.6 million hectares. These free-to-use images vary in resolution, with aerial orthophotos ranging from 0.05 m to 1 m and satellite images from 10 m to 15 m. The dataset, which covers regions from 26 to 48 degrees North latitude and 69 to 123 degrees West longitude, includes diverse coastlines from the Pacific, Atlantic, and Gulf coasts. Features include rocky cliffs, wetlands, and sandy beaches in both rural and urban settings across different energy levels (Buscombe et al., 2023a).

Sources for the dataset include NAIP aerial imagery (2010-2018), Sentinel-2 (2017-2020), Landsat-8 (2014-2020), USGS aerial imagery (2008-2012), and

UAS orthomosaic imagery (2008-2012). Coastal experts classified the images into broad categories, with all datasets labeled at least for "water" and "sand". For accuracy, only high-confidence data was annotated. The labelled data, organized into four to twelve categories, reflects the image features (Buscombe et al., 2023a). The Coast Train dataset provides an invaluable resource to study coastal environments, such as deltas, estuaries, barrier islands, salt marshes, etc. This data can be downloaded from https://www.usgs.gov/data/coast-train-labeled-imagery-training-and-evaluation-data-driven-models-image-segmentation (last access - 24 oct 2024) in which all data specifications are also described. To apply, we carefully selected a dataset of 134 images (*.jpeg) and their corresponding label masks. To ensure the highest possible quality, we began by removing any images that did not clearly depict a land-water interface. To ensure that the training dataset adequately represented the variability of the Sicilian coastline, we selected images that reflected similar color characteristics, beach sizes, and urbanized settings as Sicily. This selection was made by hand to provide the model with a variety of examples sufficiently diverse to ensure a good level of generalization during the classification phase. Although not all possible variants of the Sicilian coast were included, we focused on the most representative ones to effectively train the model. We also limited our selection to a maximum of 10 images per environment, each with different sea states. By employing this rigorous selection process, we were able to construct a final dataset that is both relevant and diverse, providing an excellent basis for our research.

4.2.1 The “Coast Train” dataset augmentation

To avoid the issue of overfitting the model and obtaining a larger dataset, the authors utilized data augmentation on the Coast Train images and their masks. The CNN model reads the images as a three-dimensional array of numbers, representing the color values of each pixel. Using the data augmentation technique, these pixels can be modified to generate new, augmented images that resemble the original dataset, but with additional information to improve the generalisation of the ML algorithm.

Overfitting arises when a model excels on the training data but underperforms on previously unencountered data, and this can happen when the dataset is small. To prevent this from happening, the authors used the Python library *Albumentations* (Buslaev et al., 2020) for data augmentation, that employs an array of image transformation techniques fine-tuned for optimal performance.

The original dataset consisted of 134 images, with 100 used for training and 34 for validation. However, given the limited size of the dataset, data augmentation techniques were employed to synthetically expand the amount of training data by a factor of four. The final training dataset consisted of 502 images and the validation dataset remained at 34 images. The data augmentation processes used were random cropping, horizontal and/or vertical flipping, rotation, adjustments to brightness and contrast, and grid distortion.

4.2.2 Model architecture and used loss function

U-Net is a renowned convolutional neural network (CNN) initially designed for biomedical image segmentation tasks (Ronneberger et al., 2015). In the study, it was used for sand/sediment, built-up, vegetation, land and water/sea segmentation at the pixel level. Each pixel without segmentation is labelled as "No Label".

The U-Net framework is structured around two main components: the encoder and the decoder.

Similar to a conventional CNN, the encoder can be likened to a contracting path. Each segment within the encoder consists of a pair of 3 x 3 convolutional layers, which are subsequently followed by a Rectified Linear Unit (ReLU) activation function. To wrap up each block, a max-pooling layer with a 2 × 2 kernel and a stride of 2 is incorporated. The inherent nature of the encoder is to methodically reduce tensor dimensions while amplifying feature channels, aiming to capture intricate low-level image details. As a result of this are that the number of feature channels doubles after each encoder block, preserving the rich content of the image within a compact feature vector.

The decoder works as an expansive pathway. Each segment of the decoder comprises up-sampling procedures, concatenation layers, and two 3 × 3 convolutional layers. Its task is to methodically expand the tensor dimensions back to their original metrics, while superimposing the valuable features extracted by the encoder onto their corresponding spatial regions. Throughout each decoder block, the tensor dimensions double courtesy of the up-sampling mechanism.

The concluding phase of the architecture uses a 1 × 1 convolution applied to the decoder's output. This serves to map the feature vectors of individual pixels to the requisite number of classifications, culminating in a pixel-by-pixel

segmentation mask. Notably, the values within this map quantify the likelihood of a given pixel's belonging to a particular class.

Figure 4.2.2 illustrates the U-Net model's architecture.

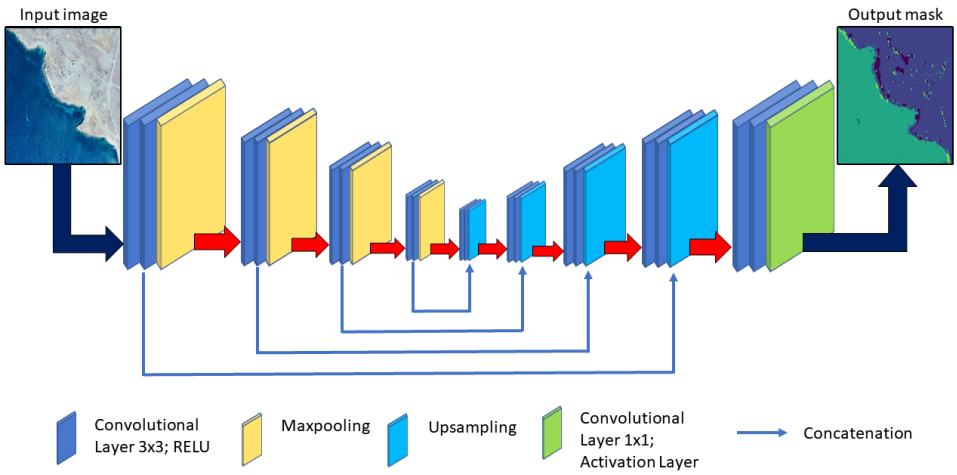

Figure 4.2.2 - Diagram framework illustration of the U-Net architecture.

Choosing an appropriate loss function for coastline segmentation is crucial. It directs the training process to determine the best parameters and plays a role in how these parameters are adjusted (Galeone, 2019).

For this reason, Sobel-edge-loss was used as the loss function (Seale et al., 2022). In particular, As described by Seale et al. (2022), the filters used in the analysis calculate the gradients on the x and y axes of an image labeled A, as shown in Equation 4.2.1 and Equation 4.2.2 below (Seale et al., 2022):

Equation 4.2.1 – X gradient equation estimation in filters

$$G_x = \begin{vmatrix} 1 & 0 & -1 \\ 2 & 0 & -2 \\ 1 & 0 & -1 \end{vmatrix} * A$$

Equation 4.2.2 - Y gradient equation estimation in filters

$$G_y = \begin{vmatrix} 1 & 2 & 1 \\ 0 & 0 & 0 \\ -1 & -2 & -1 \end{vmatrix} * A$$

In the Sobel edge detection method (Vincent & Folorunso, 2009), the gradient magnitude G is typically computed using the following equation (Equation 4.2.3):

Equation 4.2.3 – Gradient image magnitude equation

$$G = \sqrt{G_x^2 + G_y^2}$$

The Sobel loss, comparing the target (p) with the prediction (p'), is defined as a loss function, with "i" representing a sample from the training image. The authors (Seale et al., 2022) provide the formula for this loss function, which is as follows (Equation 4.2.4):

Equation 4.2.4 – Sobel loss function

$$Sobel(p, p') = \frac{1}{n}\sum_{i=1}^{n}\left(G_{p_i} - G_{p_i'}\right)^2$$

4.2.3 Architecture settings

Within the framework of our proposed architecture, we have incorporated various hyperparameters that influence both the training process and the overall performance of the model. These parameters, which are external to the model itself, are described below.

The batch size is the number of data samples used to compute a single iteration during the training process. A larger batch size may lead to faster training but could require more memory. In our model, the batch size was set to 16 according to Kandel and Castelli, (2020). The number of epochs represents the number of complete passes through the entire dataset during the training process. While a higher number of epochs may promote better learning of the training data, there is a risk of overfitting if not controlled. In our case, the maximum number of epochs was set to 60. Regarding the optimizer, the Adam algorithm was employed, which relies on adaptive estimates of first and second-order moments to iteratively update the model weights to minimize the loss function. During the training process, three different callbacks were utilized:

1. EarlyStopping: this callback stops training if the loss on the evaluation set does not improve for a specific number of consecutive epochs (patience), which in our case was set to 10 epochs.

2. ReduceLROnPlateau: this callback reduces the learning rate if no improvement is observed in the monitored evaluation metric. The chosen metric is evaluation accuracy. In addition, a learning rate reduction factor of 50% was defined each time the metric does not improve.

3. ModelCheckpoint: this callback saves the model with the lowest loss during training, ensuring the preservation of the best-performing model.

A lower bound on the learning rate was set at 10^{-5} to prevent further reductions when the learning rate reaches or falls below this value (Kandel & Castelli, 2020). This maintains a sufficiently small learning rate to facilitate convergence or prevent oscillations around the global minimum of the loss function.

We also utilized an Input Size of 512 × 512 pixels. According to recent studies (Lin et al., 2019; Nekrasov et al., 2018; Tanveer et al., 2022), this resolution enhances model training and accuracy, enabling better differentiation between land, sea, and other classes. A 512 × 512 resolution, compared to 256 × 256, provides more detail and context. It captures fine details and allows the model to consider spatial relationships between objects, improving accuracy (Lin et al., 2017). This resolution also reduces aliasing, where high-frequency information is misrepresented (Zou et al., 2023), and the border effect, critical for distinguishing between water and land, is enhanced at this resolution (Dhingra et al., 2021). Moreover, despite the higher computational demand, models trained at this resolution show greater robustness and generalize better to new data (Nekrasov et al., 2018; Shi et al., 2021).

To confirm all these aspects, we conducted a sensitivity analysis on the performance of the model by training it with a smaller input size, 256 × 256. Lower sizes were not taken into account considering the nature of coastal images that would be poorly represented by resolutions smaller than 256 × 256. We trained the proposed architecture using 256 × 256 as the input size and actually obtained lower metrics confirming what has been reported by (Lin et al., 312 2019; Nekrasov et al., 2018; Tanveer et al., 2022). All other hyperparameters were left unchanged.

The two best training accuracy scores are 0.85 and 0.79 and training IoU 0.75 and 0.72 obtained from the 512 × 512 input (Kernel Size 3 × 3) and 256 × 256 input (Kernel Size 3 × 3) configuration, respectively. On the other hand, the two best validation accuracy scores are 0.85 and 0.80 while validation IoU of 0.72 and

0.68 obtained from the 512 × 512 (Kernel Size 3 × 3) input and 256 × 256 (Kernel Size 3 × 3) input configuration, respectively.

Note that the 256 × 256 metrics are worse than the results obtained by DeepLabV3 but if we consider that the computational training times of the latter are longer (about 24 hours) and still comparable to those of UNet with input size of 512 × 512 then the U-Net architecture this input size appears to be the most suitable for coastal image segmentation.

Regarding class weights, during model training, different weights are usually assigned to classes based on their frequency in the dataset. This procedure ensures that the model gives more importance to the less represented classes during the optimization of the loss function (Fernando & Tsokos, 2021; Tyagi & Mittal, 2020). However, we did not adopt this practice but considered that each class contributes equally to the overall loss of the model during the training process. This was because the initial training dataset was already balanced, and the data augmentation was performed during preprocessing to avoid computational overhead in training the classification model. Since the main goal was to achieve accurate segmentation of water boundaries with respect to other classes, we accepted this compromise.

The model was developed using TensorFlow 2.11 and Python 3.9. All training tasks were executed on a Desktop Computer powered by Windows 11 Pro, an Intel® Core™ i7-12700 12th Gen processor, 16 GB DDR4 3200 MHz RAM, Intel 770 UHD onboard graphics, and a 1TB nvme SSD storage. In our work, the semantic segmentation model was executed on a dedicated GPU to ensure optimal performance and computational efficiency.

4.2.4 Training and validation approaches

To assess how well the model classifies, we employed the Accuracy (Albon, 2018.; Brownlee et al., 2021) and Intersection over Union (IoU) or Jaccard index (Girshick et al., 2014; He et al., 2018; Ronneberger et al., 2015), as metrics.

In computer vision and image processing fields, two key metrics used to gauge the effectiveness of object detection and image segmentation algorithms are Accuracy and Intersection over Union (IoU), commonly referred Jaccard index.

Accuracy is a straightforward metric, primarily gauging the ratio of accurate predictions to the overall number of predictions. This value lies between 0 and 1, with 1 indicating impeccable accuracy and 0 denoting absolute inaccuracy.

Conversely, IoU is a nuanced metric aimed at assessing the degree of overlap between the forecasted regions and the actual bounding boxes or segmentations. This metric also varies between 0 and 1, where 1 signifies an exact match and 0 indicates no intersection. IoU is especially pertinent for tasks that emphasize pinpointing the precise region of an object within an image. The mathematical expressions for these metrics are described in the following.

To encapsulate, while accuracy predominantly counts correct predictions, IoU delves deeper, analyzing the degree of overlap with true regions. The mathematical expressions for these metrics are provided below (Equation 4.2.5 and Equation 4.2.6):

Equation 4.2.5 – Accuracy equation

$$Accuracy = \frac{TP + TN}{TP + TN + FP + FN}$$

Equation 4.2.6 - Intersection over Union (Jaccard Index) equation

$$IoU = \frac{TP}{TP + FP + FN}$$

Let TP denote the number of pixels correctly identified as being part of a particular category, while TN denotes the number of pixels correctly identified as not being part of that category. FP represents pixels incorrectly categorised as part of the group, and FN represents pixels incorrectly excluded from the group. Figure 3 shows a diagram illustrating the whole process of generating data and training the neural network model. Given as input an image representing a coastal environment, the pre-trained model provides as output a mask image (prediction image) of the same environment.

We have also trained a widely used architecture in the field of semantic segmentation, DeepLabV3 (Chen et al., 2017) with the same training and validation dataset used in UNet to compare the classification ability of the architecture proposed in this work against DeepLabV3.

DeepLabv3 (https://github.com/AvivSham/DeepLabv3?tab=readme-ov-file – last access 24 oct 2024) unlike UNet is a deep neural network (DNN) architecture widely used in semantic segmentation. It uses Atrous (Dilated) Convolutions to control the resolutions of the receptive field and feature map without increasing the total number of parameters. In addition, through the use of Atrous Spatial

Pyramid Poolingl, the architecture is able to effectively extract multiscale features that contain useful information for segmentation. In general, the network can capture dense feature maps with rich long-range information that can be used to accurately segment images. Because of these features, the DeepLab V3 architecture is an excellent performance comparison tool for the model presented in this research.

Figure 4.2.3 shows a diagram illustrating the entire procedure of creating data and instructing the neural network model. By giving as input an image depicting a coastal environment, the pre-trained model provides as output a mask image (prediction image) of the same environment.

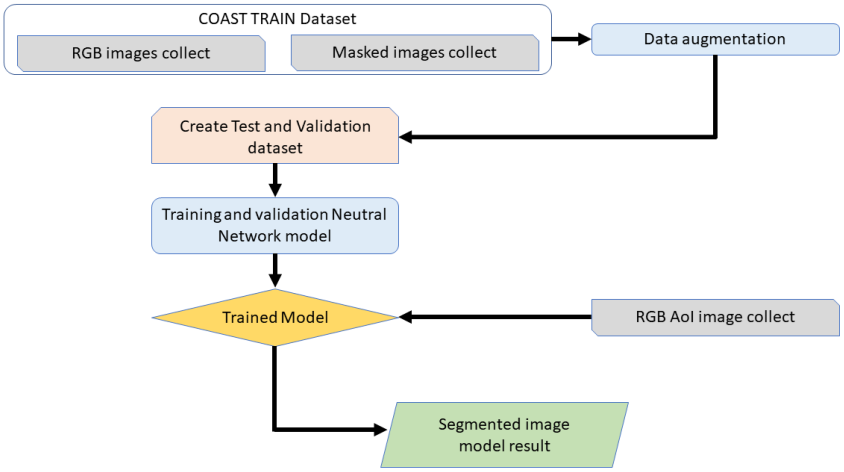

Figure 4.2.3 - Flowchart of the procedure to create data for train and validate the convolutional neural network model to identify segmented images.

Once the coastal prediction image is obtained from the model, it is subjected to an image thresholding process. In this work we used the global thresholding: in fact a unique threshold value is used for the entire image, which can result in loss of information because the image has multiple regions with different intensity values. The image is thus filtered with respect to all pixels that have RGB band values lower than those corresponding to the mask of the 'sediment' category representing the beach or cliff, thus leaving out the plume regions of the sediment.

The intermediate pixels are a kind of disturbance in the image. A conversion to unsigned bytes is then applied to the thresholding result, followed by a mean blurring operation to eliminate the disturbance of the intermediate pixels and maintain the edges.

Mean blurring is a technique that smoothens images by reducing noise or intricate details. This method calculates the average value of nearby pixels and uses it to replace the original pixel value. This is achieved by using a kernel, a small square-shaped matrix, where the numbers dictate the significance of adjacent pixels. The extent of the blur is determined by the kernel's size. A larger kernel means a broader average, leading to more pronounced blurring. In our study, we utilized a kernel with a size of 5. After this, binary thresholding is employed to divide the image into two clear categories. The result of this binary thresholding is a binary image, or a black and white image, which is used for coastline detection. This image is then cropped to reduce its size, and thus computation time, by applying a 50-metre buffer of a probable coastline indicative in shape-file vector format (*.shp) of the area under consideration.

The coastline is not determined by the edge between black and white pixels but by an isoline within the pixels that passes through the threshold value. Buffer clipping and shoreline extraction operations are performed by exploiting QGis software. This method, proposed by Doan (2021), creates a coastline that resembles a natural coastline with a curved shape instead of a rough boundary between pixels.

The above-mentioned post-processing method is performed following the flowchart in Figure 4.2.4.

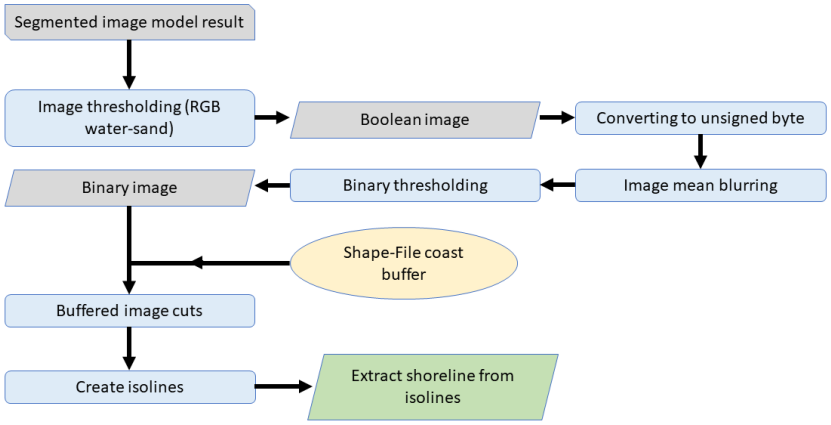

Figure 4.2.4 - Flowchart of the post-processing process for identifying coastlines using convolutional neural network model image result.

There are several morphotypes along the coasts of Sicily. The north-eastern Tyrrhenian sector and northern Ionian coasts are made up of headlands and pocket pebble beaches. On the southern Ionian coast, the landscape changes into sandy beaches, low rocky coast interrupted by cliffs. Finally, long sandy beaches and cliffs coastal sectors characterize the Mediterranean coast. The influence of human activity on the coastline is evident along the entire coastline. As stated in Manno et al. (2022a), the Sicilian coastline was divided into 22 coastal cells referred to as "Littoral Cells (LC)" (Figure 4.2.5). A littoral cell is defined as a portion of the coastal territory that has no exchange of sediments with neighboring cells. In this study, we used the term "Littoral Cells" specifically for the second-degree LCs. These LCs have both natural and anthropic divisions, such as large ports or marine structures. Each LC is designated by a pair of numbers: the initial number indicates the first-order LC, and the subsequent one represents the second-order LC (Manno et al., 2022a).

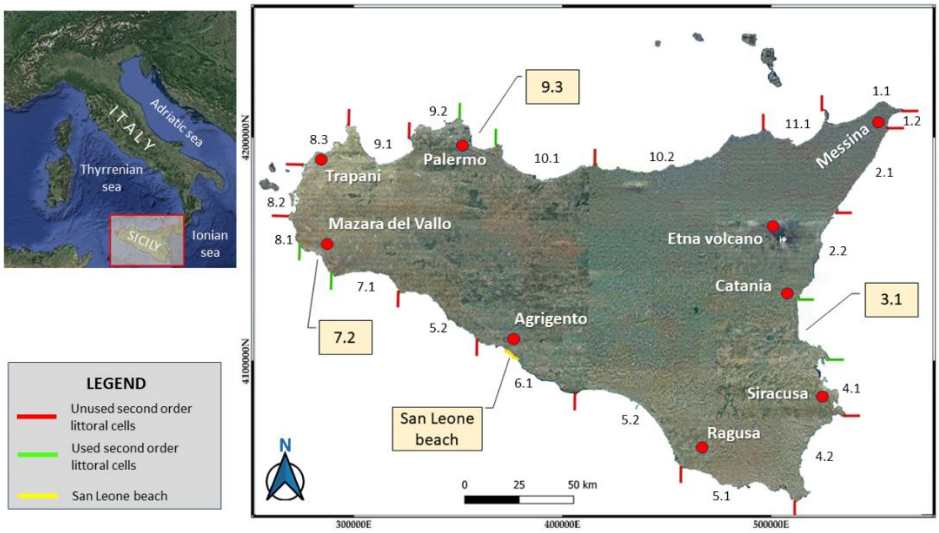

Figure 4.2.5 - Breakdown of Sicilian macro-coastal regions into second-level LCs. The 2013 ATA flight images of coastlines between the green segments are extracted in this work. (Reference System: WGS84-UTM33N-EPSG: 32633).

For the coastline extraction accuracy analysis, we applied the model on the coastline of San Leone in Sicily (Italy).

The beach of San Leone (near to Agrigento) is a part of the Sicilian LC no. 6.1 (Capo Bianco-Lido Rossello) and stretches for about 9 km including the mouths of the river Naro. The beach at San Leone is composed of golden sand and has sections with dunes of varying heights (3-4 m). Over the last decades, the coast of San Leone has undergone uncontrolled development, turning the fishing village into a chaotic seaside resort. The beach is divided into three sub-areas, each with specific characteristics. Along the coast is located also the tourist-fishing harbour of San Leone, which has become the most important coastal structure in the area. The presence of structures such as breakwaters and gabions along this stretch of coastline has had an impact on the morphology of the beach and the coastline, causing significant changes (Manno & Ciraolo, 2015). This beach was chosen because it contains several elements with which to efficiently test the detection model, after the training and validation phase. These elements are represented by the presence of a harbour, coastal protection structures, the presence of an estuary as well as the possibility of testing the behaviour of the

model on a sufficiently extended beach. For this reason, the coastline of the study area, besides encompassing the previously mentioned San Leone coastline, extends for a further 1.8 km south of the mouth of the River Naro with a beach with similar characteristics to those of San Leone and without the presence of anthropic structures. This coastline was obtained by digitizing the 1: 10,000 map sheets of the ATA 2000 flight and can be consulted at http://www.pcn.minambiente.it/mattm/progetto-coste/ (last access – 24 oct 2024).

For this further goodness-of-fit analysis of the model, transects were created orthogonal to the ground truth line with an average inter-distance of 6 m and 30 m in length (Figure 4.2.6). The transects have a smaller spacing in stretches where the ground truth line appears to have little variation in shape while the presence of transects appears to be denser where the ground truth coastline has particular variations in shape. The total number of transects analyzed is 1887.

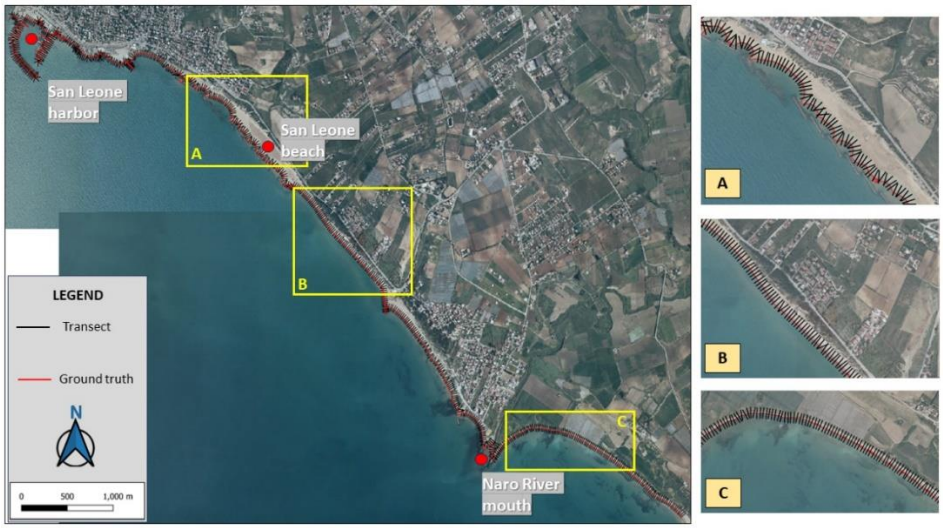

Figure 4.2.6 - Transects (segments in black) perpendicular to the ground truth line (red line) in the first column of the plot. The transects have an average inter-distance of 6 m and a length of 30 m (SR – EPSG 32633). Sub-plot A, B and C show enlargement of the San Leone area (second column).

Once we further tested the model with images representing a heterogeneous stretch of the Sicilian coastline, we extracted coastlines from a complete and

diverse range of coastal environments (such as the presence of harbors, cliffs and beaches, anthropic defense structures, etc.). In detail the LCs 3.1 (Ionian coast), 9.3 (Tyrrhenian coast), and 7.2 (Mediterranean coast) were chosen. In Figure 5, the Sicilian macro-coastal sectors divided into second-level LCs and the chosen cells can be seen. For the detection of these coastlines orthophotos from the Italian *Geoportale Nazionale*, taken during the 2013 ATA flights, in the three chosen coastal regions of Sicily were utilized. Each LC is divided in 17, 8 and 11 1:10,000 scale images for 3.1, 9.3 and 7.2 LC respectively, with the 512 × 512 number of pixel image resolution.

4.3 Coastline detection results: impacts and meanings

This section delves into the analysis and discussion of outcomes achieved during the model's training and validation phases, based on the U-Net architecture. The focus is on the accuracy, IoU, and loss metrics as detailed in section 4.2.4. In this section, the aforementioned metrics are analyzed and discussed using a Sicilian case study and the detected case study coastline is compared with a validated coastline representing the ground truth.

The efficiency of the proposed coastline detection approach in three different Sicilian coastal areas (LCs of section 4.2) is also examined, and the detection performing for the different littoral zones is analyzed.

4.3.1 Trained model efficiency metrics

The model performance was automatically evaluated by the metrics described in section 4.2.4. Our model based on the U-Net structure achieved an accuracy of more than 80 percent and reached the maximum value of around 87 %.

Analysis of the training and validation accuracy plot (Figure 4.3.1) highlights some interesting features of the semantic segmentation model during the training process.

Figure 4.3.1 - Training and validation model Accuracy plot.

First of all, it can be noted that the accuracy curves during training and validation processes show steady and gradual growth in the early epochs, indicating that the model is effectively learning the patterns of the different classes in the image.

However, from the fifth epoch onward, the curves stabilize around 80-87 % accuracy with less steep growth for both training and validation. This suggests that the model has reached a saturation point and may have difficulty improving performance further. It is possible that the complexity of the problem or the image dataset used limit the potential for improvement beyond this point.

Another important observation is that the validation accuracy curve remains slightly below the training accuracy curve throughout the training process. This discrepancy could indicate the presence of slight overfitting, i.e. the model has learned to classify training data correctly but may not to generalise as well to new data not seen in training.

In general, the trend of the curves in the graph indicates that the model achieved a good accuracy around 80 % already in the early epochs and maintained a steady but modest growth in the later epochs. However, it is also important to evaluate

other metrics such as Loss and IoU to get a complete view of the performance of the semantic segmentation model and avert overfitting issues.

Figure 4.3.2 shows the trend of IoU, which appears to be similar to that of accuracy. This indicates that the two measures are correlated, and that the semantic segmentation model is achieving good results in segmentation accuracy.

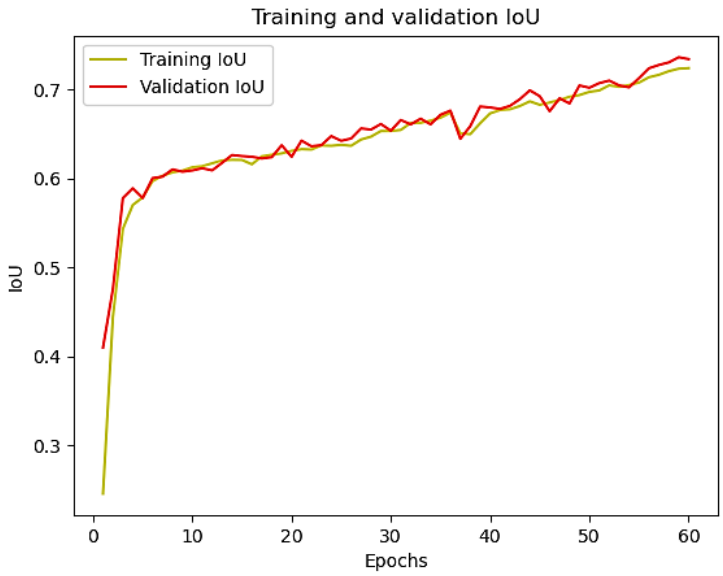

Figure 4.3.2 - Training and validation Jaccard coefficient plot (IoU).

A high IoU indicates that the segmentation predicted by the model overlaps significantly and accurately with the reference segmentation. If the graph of IoU follows a similar trend to that of accuracy, it therefore means that the increase in accuracy is accompanied by an improvement in IoU.

In general, the IoU graph shows high growth in the first 5 epochs, reaching a maximum value of 80%. However, the growth becomes slower in the later epochs. Unlike the accuracy graph, here the validation curve is not always below that of training curve. This indicates that the model generalises well to new data during the validation phase, maintaining a similar performance to the training phase. The maximum IoU achieved of 74 % suggests that the model is able to generate accurate segmentations that overlap significantly with the reference segmentations.

This is therefore a positive fact, since IoU is a more specific measure for assessing the quality of semantic segmentation than accuracy, which may be affected by unbalanced classes or dominant background regions.

However, it is important to note that although IoU and accuracy show a similar trend, IoU provides more detailed information about the quality of segmentation, as it also considers the overlap of specific classes.

Finally, Figure 4.3.3 shows the graph of the loss which shows a strong decrease in the first 5 epochs, from 1.015 to 0.93, and then continues to decrease slowly until the 60th epoch reaching a minimum value of 0.904. As the training and validation curves almost overlap, the figure indicates that the model is well generalized and maintains good predictive ability even on new data. The decrease in Loss indicates that the model is gradually learning to generate more accurate and consistent predictions during the training process on new examples.

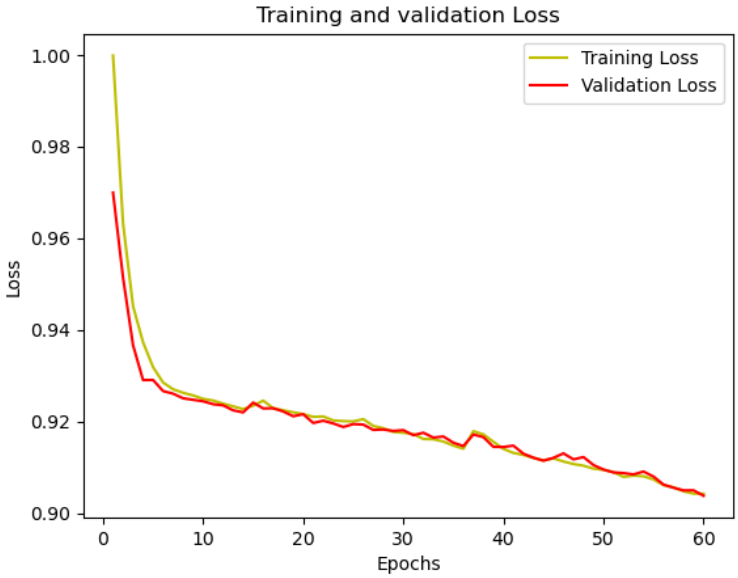

Figure 4.3.3 - Training and validation model Loss plot.

Overall, graph analysis suggests that the model achieves good accuracy and IoU in semantic segmentation relatively early in the training process. However, the subsequent growth is slower, suggesting that the model's performance has reached a saturation point. The validation curve is generally slightly lower than

the training curve, but the difference being small, thus indicating good generalization ability.

We also compared the training and validation metrics with those obtained from the DeepLabV3 network trained with the same preprocessed Coast Train dataset (see section 4.2.1). The results are shown in Table 4.3-1.

Table 4.3-1 - Comparison of metrics (Accuracy and IoU) for the proposed architecture and DeepLabV3, both trained on the same dataset. In bold the best values of the metrics.

Architecture	Training Accuracy	Validation Accuracy	Training IoU	Validation IoU
Proposed CNN architecture	**0.87**	**0.87**	0.74	**0.75**
DeepLabV3	0.85	0.83	**0.76**	0.73

Table 4.3-1, shows that although the DeepLAbV3 metrics are found to be acceptable for classifiers of this type, however, the U-Net architecture provides slightly better performance especially in the validation phase. The results obtained suggest that the UNet architecture can generate (albeit slightly) more accurate predictions and has a greater ability to correctly segment coastal images than DeepLabv3. In fact, The U-Net model is known to be efficient in capturing spatial details due to its U-shaped structure, which allows it to preserve detailed information during the encoding and decoding process. On the other hand, DeepLabv3 which uses Atrous convolution to expand the field of view and capture contextual information at different scales, might be less suitable in purely coastal image segmentation with few segmentation classes, falling into overfitting. Results on validation suggest this behavior. Similar results were obtained and reported in Gonzalz-Perez et al., (2022).

4.3.2 Model's performances on the Sicilian case study: San Leone beach

As the performance evaluation of the model was carried out exclusively on the dataset imported for training and validation (Coast Train), it is not possible to

measure the effectiveness of the model on one dataset by using the metrics of another dataset. Moreover, since the coastline is derived from isolines, evaluating accuracy purely based on pixels in the pre-processing phase would be both imprecise and potentially misleading. To further evaluate the quality of the model after training, the model was used to define the coastline on orthophotos different from those in the training and validation dataset.

The images A1, B1, C1 in Figure 4.3.4. were used as input to the model (flowchart in Figure 4.2.1), which provided graded images (A2, B2, C2 in Figure 4.3.4) as output. Note how the pixels in the image belonging to the port facilities are classified as sand. The color of these pixels is in fact very similar to that of the beach. However, since the interest is to make the detection of the coastline, the classification is deemed acceptable. After post-processing operations, the coastline was extracted (panel D in Figure 10). The entire coastline extraction process averages less than one minute of processing time.

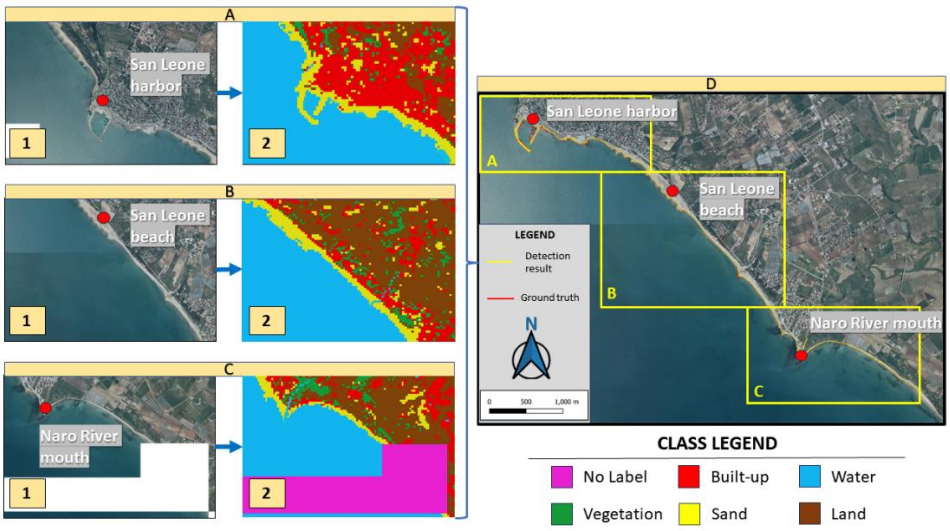

Figure 4.3.4 - San Leone coastline detection. Panels A1, B1, C1 represent the merge of input images provided to the model. Panels A2, B2 and C2 represent the merged output of the model (classified images). Panel D shows the overlay between the ground truth coastline (red line) and the coastline extracted from post processing operations (yellow line). The yellow boxes of panel D represent orthophotos A1, B1 and C1.

The coastline extracted from the model and the one for comparison, representing the ground truth are shown in yellow and red lines respectively in Figure 4.3.4 (panel D). This coastline represents the ground truth of comparison and denotes the transition line between water and land/sand. Figure 10, panel D, shows for the entire coastline section analyzed, about 11 km, that the two lines tend to blur suggesting good detection by the model.

Each transect built on the ground truth shoreline in Figure 4.2.6 (see section 4.2.4) was cut at the two coastlines in Figure 10, and its length was calculated for each resulting section. Cut transects longer than 1 m are shown in red and transects shorter than 1 m are shown in green in Figure 4.3.5.

Figure 4.3.5 - Cut transects between the ground truth line and the detected line. Transects with lengths less than 1 meter (in green) transects with lengths greater than 1 meter (in red).

Figure 4.3.6, panel A, shows a histogram representing the number of cut transects having a length less than 1 m and the number of cut transects having a length

greater than 1 m. The lengths are divided into classes with a variation of 0.50 m. The number of cut transects in the first two length classes of Figure 12 represent all cut transects with lengths less than the image resolution (can be understood as a surrogate for the IoU).

Specifically, the number of cut transects with length less than the pixel resolution of the image used was 1498 while transects with length greater than 1 m were found to be 389.

The percentage of cut transects that therefore identified a detected coastline deviation of less than pixel resolution from ground truth is 80 percent. Consequently, the error percentage for all transects with length greater than one meter is 20 %.

Considering that the geometric resolution of an image pixel is 1 m, it was assumed that the accuracy can be set equal to 2 times the geometric size of the pixel. Thus, cut transects with a length of less than 2 m represent those points where the coastline derived from the model has an uncertainty of at most 1 m with respect to the pixel where the real coastline is present.

In this case, the percentage of model error is 15% resulting in an increase in model goodness-of-fit of 85%. Figure 4.3.6, panel B shows the trend in model goodness-of-fit as a function of the chosen geometric accuracy size (1 m to 2 m).

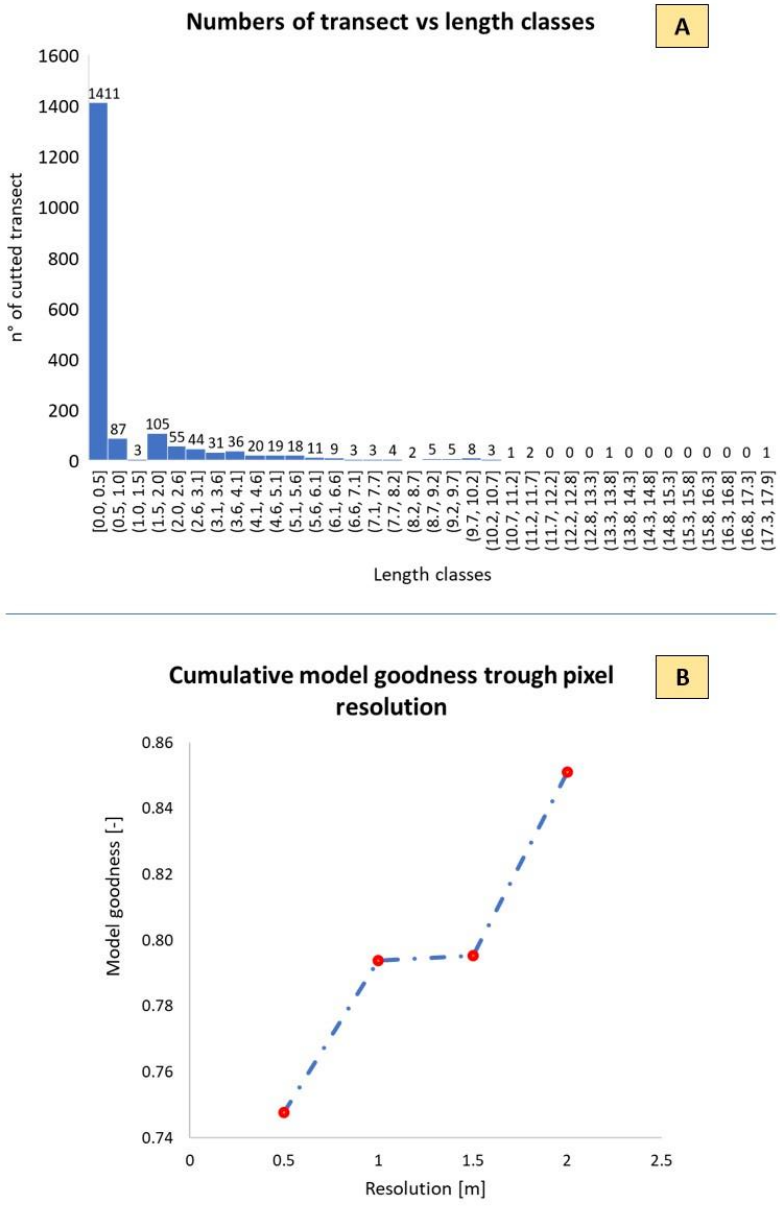

Figure 4.3.6 - In panel A is shown a histogram plot of transect lengths divided by length classes. Panel B shows the trend in model

goodness-of-fit as a function of the chosen geometric accuracy size.

These analyses confirm what was reported in section 4.3.1, suggesting how the model metrics of accuracy and IoU (for both testing and validation) well represented the real behavior of the model, even with images different from the starting dataset used for the testing and validation phase. In fact, considering transects with lengths less than 1 m, the goodness-of-fit value achieved is comparable to the IoU value while the accuracy is almost like the goodness-of-fit values considering even transects with lengths less than 2 m.

Details of the surveyed coastline and the ground truth datum are shown in Figure 4.3.7, where six zoom particular images are shown to represent the significant differences (first row of Figure 4.3.7) and similarities (second row) parts of the comparison.

In particular, the size of the transects turns out to be larger in some parts of the port area (A and B in Figure 4.3.7). It should be noted that the model manages to faithfully reproduce the course of the boulders of the harbor breakwater reef unlike the ground truth line which is represented as a single straight line.

Figure 4.3.7 - Details of comparison between the coastline measured by the model (yellow line) and ground truth (red line). The first line (A to C) represents the details where the two lines deviate the most. The second line (D to F) represents the details where the two lines almost overlap.

In this case the transect length is greater than 1 meter, suggesting therefore an error statistic of the model that might be lower when detection is done on images without harbors. In any case, since the coastline in the presence of ports is practically invariable and static over time, detection errors in these areas can be neglected. A zone of the study area in the presence of the foam produced by breaking waves is shown in panel C of Figure 4.3.7. In these areas the model was probably unable to recognize these pixels as white-water because the breaking was captured practically attached to the coastline.

The second row of Figure 4.3.7 (D to F), on the other hand, shows some details in which the ground truth line and the line obtained from the model are almost identical. The transects in these areas therefore have the lowest length values. In these zones (particularly around the river mouth) the yellow line (detection model) seems to more naturally represent and follows the coastline, identified as the transition line between water and land.

4.3.3 Coastline detection on second order Sicilian littoral cells

Figures 14, 15 and 16 show the extracted coastlines with the red line for the Ionian, Tyrrhenian and Mediterranean coast, respectively. The proposed NN-based model effectively and successfully identified the coastline in images showing sandy beaches. The system also extracted the coastline in almost all features depicting cliffs, however, it had some shortcomings in extracting the coastline in areas where relatively darker pixels were sporadically present on the terrain. More in detail, the LC, with a worse detection was 3.1, with 2.2 km of unidentified coastline compared with a total of 110 km. Figure 4.3.8 shows the coastline extracted from the model for LC 3.1.

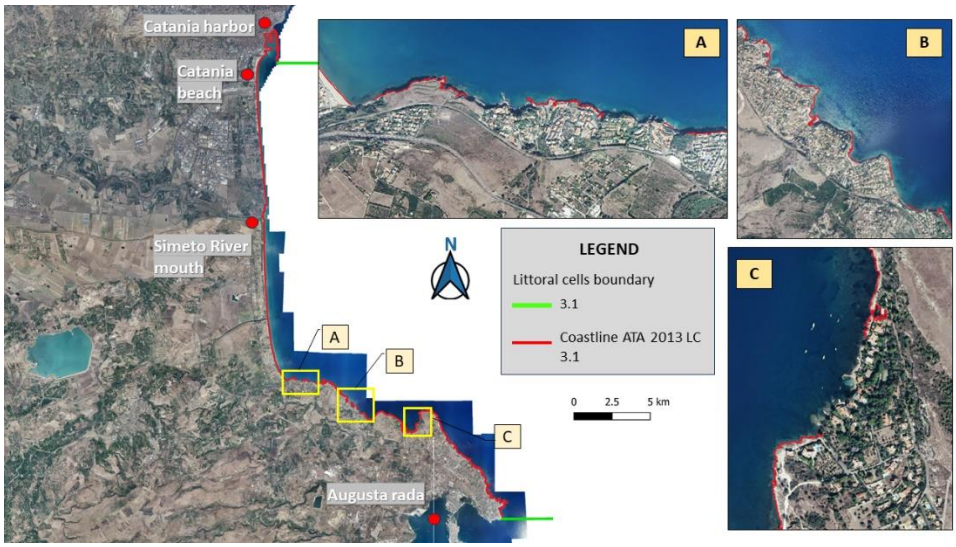

Figure 4.3.8 - 3.1 Littoral cell coastline (showed in red). Panels A, B, C represent three areas where the model did not extract the coastline.

In Panels A, B and C of the same Figure, zooms on some of the areas where the coastline was not identified are plotted. In LC 9.3, the unidentified coastlines represent a total length of 0.6 km out of a total of 97 km. Again, Figure 4.3.9 shows the coastline extracted from the model for LC 9.3. In panels A and B of the same Figure, zooms are plotted on some of the areas where the coastline was not identified. The coastline related to LC 7.2 was fully extracted for a total of 64 km (Figure 4.3.10). A histogram summarizing what has just been reported is shown in Figure 4.3.11.

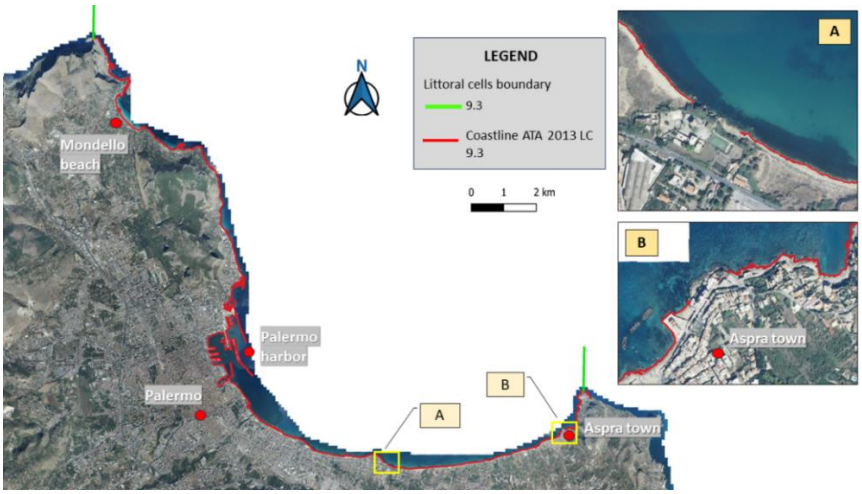

Figure 4.3.9 - 9.3 Littoral cell coastline (showed in red). Panels A, B, C represent three areas where the model did not extract the coastline.

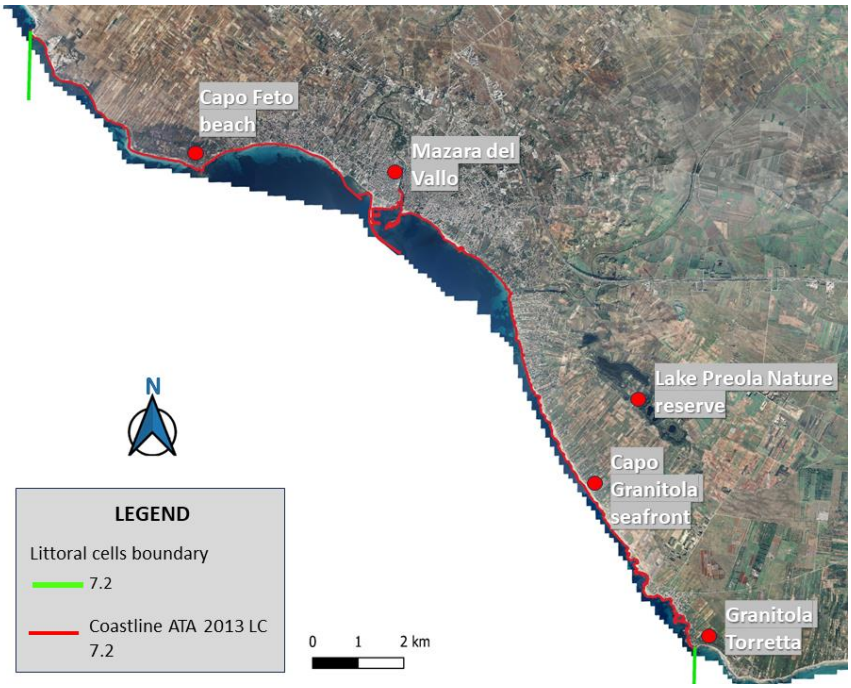

Figure 4.3.10 - 7.2 Littoral cell coastline (in red). In this case there are no areas where the model did not extract the coastline.

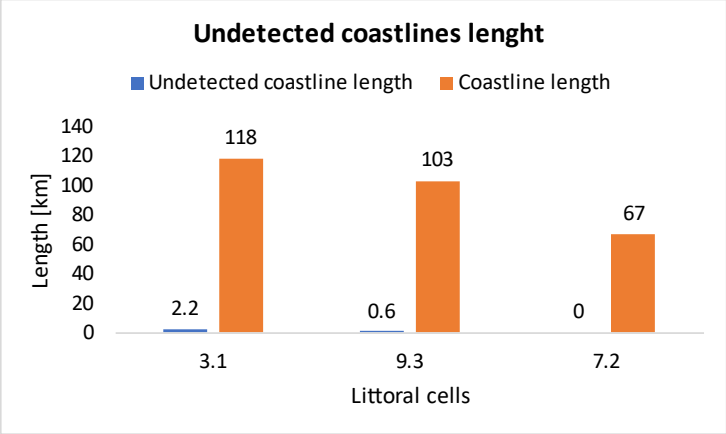

Figure 4.3.11 - Comparison of coastline's total length (orange bars) and total length of non-extracted coastline (blue bars) for each second order LC.

4.4 Chapter summary and future developments

This research demonstrates the use of satellite remote sensing as a fundamental tool for monitoring coastal changes while simultaneously addressing its inherent challenges. Using the U-net architecture with an input resolution of 512 x 512 pixels proved advantageous for training the model and generating accurate semantic segmentations for regional-scale image analysis. The model was improved using the recently published Coast Train dataset to ensure that it is based on the most up-to-date and especially specific coastal data. The multiclass segmentation capability of our model, which differs from traditional models, allows it to distinguish not only “water” and "land," but also the classes "built-up," "vegetation," bare land” and “beach”. This granularity provides a more comprehensive perspective of the landscape.

Applying the model in post-processing to define coastlines as the boundary between "water" pixels and all other types shows its advanced coastline extraction capabilities. These sophisticated features ensure precise separation between different elements, resulting in more accurate coastline extraction. Performance metrics reveal an accuracy saturation point of 87 percent and an IoU close to 76 %, reinforcing the quality of the segmentation achieved.

However, it is important to note some limitations. The model may not excel in high-resolution coastal studies (local scale - i.e.1: 5,000; 1: 1,000; etc.), and in some cases, it encountered difficulties in detecting coastlines in regions with darker pixels (i.e. shadows areas or seaweed).

In the case of the image dataset used (satellite/airborne with respective ground truth classifications), although balanced, some pixel categories with similar bands (e.g., Dark Vegetation and Sea) may be subject to confusion by the classifier, especially if the input images intended for segmentation have already unbalanced RGB band classes of pixels. Such an occurrence can lead to model confusion, which may erroneously assign the two categories to the same group, generating higher error rates. Moreover, the coastal environment is known for its complexity, with variations in color, shape, and texture that can pose challenges even for an expert human eye. This complexity makes it challenging for the model to accurately identify and segment the various features of the environment. In addition, overlapping of different land or cover classes in some areas of the image further complicates the model's task of delineating precise boundaries between them, resulting in partially correct or inaccurate segmentations.

On the other hand, when the classes are well balanced, the classifier works effectively (Lee et al., 2022), with a final accuracy of 87 %. Future studies will focus on further validating the model's classification capabilities on all specified classes. To further improve the classification process and achieve even greater accuracy, we might consider differentiated assignments of class weights during training. Specifically, implementing an additional *Keras* callback, "*class weight*", during the training phase of the model. This callback will allow differentiated assignment of class weights during model loss calculation, considering the imbalance of classes in the dataset. Specifically, through the "*balanced*" function, the least represented classes will receive higher weights, while the most represented classes will receive lower weights. This will ensure that the model gives adequate attention to all classes during training, even if some classes are less frequent than others in the dataset.

Despite these difficulties, the performance of the proposed model in the Sicilian case study underlines its adaptability even in highly anthropised areas. Tests carried out in different Sicilian coastal regions further confirmed its robustness, even in environments as diverse as sandy coasts and cliffs.

The efficiency of our model is not only theoretical; its high speed in generating coastlines has practical implications, enabling fast and efficient mapping and analysis of coastal areas. This speed makes it valuable for applications that require rapid assessment of coastal conditions, such as emergency response scenarios. The model potential extends beyond simply surveying the current coastline; it opens the way for analysis of historical shoreline shifts, rather than analysis of land cover changes, offering valuable insights for coastal planning and management.

Our forward-looking approach is to further enhance the model's capabilities, especially in terms of land use classification, ensuring that it remains at the forefront of coastline detection and geographic analysis.

Chapter V

This chapter describes the application of the model presented in the fourth chapter for analyzing land cover (LC) dynamics in coastal areas, with reference to the Sicilian coast. It was highlighted in the second chapter that coastal zones are complex and dynamic environments where land cover and land use undergo continuous changes, both due to natural processes and human activities. Monitoring and understanding these changes is essential for preserving critical ecosystem services, such as coastal protection, biodiversity conservation, and recreational areas, as well as for improving the sustainable management of these regions. For this reason, part of the research has focused on developing the present analysis

By using classified satellite images from the Landsat and Sentinel missions, along with the semantic segmentation model, it was possible to map land cover transformations across the entire Sicilian coastal area from 1988 to 2022. This approach provided a detailed view of the spatial and temporal dynamics of land cover, highlighting key drivers of change, such as urban expansion and the reduction of vegetated areas, and revealing correlations with economic and demographic growth, which were used as socioeconomic indicators of the coastal area.

The topics and contents covered in the following chapter are taken from a research article developed with IH Cantabria (Spain) Coastal Erosion research group and published by Nature, “Scientific Reports” journal (Scala et al., 2024).

5.1 Dynamics of coastal land cover, an aspect to be explored further

In this section we delve deeper into the topics briefly covered in section 2.3.7. In particular key aspects of land use and cover change as a global phenomenon in coastal areas and its implications were highlighted, then move down to the regional scale, particularly in Sicily.

Knowledge of Land Use (LU) and Land Cover (LC) changes is in fact a key information for effective management of agricultural production, natural resource use, and understanding of various environmental drivers such as local and global temperature regimes, precipitation, and shifts in biodiversity and ecosystem health (Gibbard et al., 2005; Perugini et al., 2017). These changes in LU are driven by many factors, including climatic variations on land(Borrelli et al., 2020;

Froese & Schilling, 2019) due to changes in rainfall patterns and vegetation, and rising temperatures. Additionally, human activities(Bai et al., 2020; Briassoulis, 2009) can significantly affect LU through urbanization, deforestation, intensive agriculture, and infrastructure construction. Such practices can lead to a rapid transformation of the environment, thereby influencing LU trends. In coastal zones, these changes occur more rapidly due to the dynamic nature of these areas, which undergo changes at different temporal scales(Harley et al., 2006; Toimil et al., 2020; Toimil et al., 2020c). Coastal landscapes and shorelines are modified by erosion and sedimentation caused by waves and water levels and by anthropogenic interventions that have been deployed to protect communities from erosion and flood risks(Crain et al., 2009; Spalding et al., 2014) and provide them with recreational services.

Historically, humans have settled along the coast where they have developed ports and commercial centers. Industrialization catalyzed the expansion and transformation of coastal cities, fostering infrastructure growth. Over the past six decades, there has been a significant shift of the population and economic activities towards the coast(Desmet et al., 2018; Kummu et al., 2016), which in turn has increased environmental degradation through deforestation, pollution, and habitat destruction. Degradation of dune vegetation can increase beach erosion, amplify coastal flooding and pose risks to both the tourism sector and the safety of coastal population (Feng et al., 2022; Shilland et al., 2021). Likewise, human-induced loss of coastal habitats can negatively affect both marine and terrestrial biodiversity (García-Nieto et al., 2018; Salvati et al., 2014). The historical evolution of LU and LC reflects many of these dynamics and analyzing them can help understand the origin of changes, the pace at which they have occurred, and even what might happen in a few years (Findell et al., 2017; Kim et al., 2015; Winkler et al., 2021). This information can help improve resource and land planning (Nath et al., 2023; Ngondo et al., 2021), especially in coastal areas, with all indications pointing towards their continued growth in the future.

LC mapping has evolved considerably over the last 30 years. Initially this was done through visual analysis of aerial imagery(Foody, 2002; Phiri & Morgenroth, 2017), and then moved to automatic categorization of multispectral satellite imagery(Grimes et al., 2024) using non-supervised(Thanh Noi & Kappas, 2018; H. Zhou & Liu, 2008) or fully supervised (Hussein et al., 2020; Liu et al., 2020) approaches. In recent years, it has become increasingly common to use neural networks techniques (Wang et al., 2024) (especially CNN, convolutional neural

networks) for of LULC maps detection (Carranza-García et al., 2019; Chachondhia et al., 2021; Mansour et al., 2023; Shetty, 2018.; Tassi & Vizzari, 2020). Most of the LULC products available to date, which are not obtained from photo-interpreted datasets, have low spatial resolutions (1 km and 300 m for GLCC and ESA Land Cover - CCI respectively). In contrast, products obtained by state-of-the-art methods, such as Artificial neural networks, and with higher spatial resolution (10 m) are still tested and validated through the use of visual photo-interpretation images (ESRI Land Cover (Abdullah et al., 2019; Feng et al., 2019) without including datasets specific to coastal areas. Since the quality of the dataset is crucial to the classification process, complex environments such as the coast require a tailor-made solution. This is something that has not yet been fully developed to date. Although several LULC products have already been developed and used for the analysis of changes at different spatial scales, the real gap lies in coastal-specific LULC maps. The Coastal Zone (Clemente et al., 2022) is the only LULC product specific to coastal environments but it is also obtained by visual interpretation and therefore only available for two reporting years. While the ESRI 2020 Global Land Use Land Cover is obtained by employing artificial intelligence but being a global product and trained mainly with images of the hinterland, it is not specific and has gaps especially in coastal environments. Classifying coastal LC is a challenging task in remote sensing because of the complex and fragmented nature of coastal landscapes. Starting from the work of Liu et al.,(2020) in which global-scale urbanization maps are provided for each year from 1985 to 2015, it can be seen that while from an urban perspective one map per year of coastal LULC is acceptable for coastal LULC, an annual map is not sufficient to capture both short- and long-term changes in, for example, beaches (the case of Coastal Zone product). On the opposite side (Truong et al., 2024) introduced a methodology for obtaining a high resolution (10 m) LULC map for Vietnam, using a CNN approach based on temporal rather than spatial features. Due to the aforementioned coastal dynamism and the complex nature-human interactions in coastal environments, it is of particular interest to obtain LC classifications specific to coastal environments. Especially at appropriate spatial and temporal scales and sampling intervals to capture their dynamism. A summary of the discussed LULC products and their acquisition method, spatial and temporal scales (time sampling) is given in Table 5.1-1. All the LULC products reported in Table 5.1-1 are characterized by one map per reported years (e.g. ESA Land Cover – CCI, 1 image per year from 1992 to 2015).

Table 5.1-1 - Collection and comparative analysis of LC data products across varied spatial scales.

Published products	Training dataset	Classification method	Time window	Map spatial scale	Spatial resolution	Overall accuracy
GLCC (Global Land Cover Characterization)	-	Unsupervised classification	1992 to 1993	Global	1 km	60 %
ESA Land Cover - CCI	-	Combination product of global surface reflectance from different satellite missions	1992 to 2015	Global	300 m	71 %
Witjes et al., 2022	LUCAS and Corine Land Cover datasets	Spatiotemporal ensemble machine learning framework (Random Forest – Gradient-boosted trees – Artificial Neural Network)	2000 to 2019	Europe	30 m	83 %
Coastal Zones LC/LU	-	Visual interpretation	2012 - 2018	Europe (730,000 km2 of coastal landscape up to 10 km inland)	10 m	85 %
ESRI Global Land Use Land Cover	Dataset of more than 5 billion Sentinel-2 pixels, manually labelled	Deep Learning model based on U-Net	2017 to 2022	Global	10 m	75 %
Abdullah et al., 2019	Dataset of pixels7areas identified through photointerpretation	eXtreme Gradient Boosting and Random Forest classifier	1990 to 2017	Coastal Region of Bangladesh	30 m	82 %
Feng et al., 2019	Training and testing sample dataset derived from visual inspection	Multibranch convolutional neural network	2018	Yellow River Delta (China)	10 m	90 %
Liu et al., 2020	ESA – CCI Land Cover product	Analysis of surface reflectance data from Landsat satellites in Google Earth Engine shell	1985 to 2015	Global	30 m	80 %

A key novelty of our work is the use of a semantic segmentation model trained with an extensive dataset specific for coastal environments, the Coast Train (Buscombe et al., 2023b). State-of-the-art artificial intelligence techniques are employed to recognize the characteristics of coastal environments and to classify large coastal regions efficiently, achieving both high accuracy and reduced computational times. This methodology and its potential were demonstrated along the coast of Sicily (Italy). An extensive hindcast of classified images was developed for each month from 1988 to 2022, offering valuable insights into LC dynamics in the region over three decades. Landsat and Sentinel-2b images were acquired and processed through semantic segmentation techniques based on CNN. The LULC spatial model was correlated with scalar indicators, such as socio-economic development. A historical analysis of the evolution of socioeconomic indicators for Sicilian coastal cities (population and income) was conducted in relation to coastal urbanization trends. Additionally, the annual and seasonal evolution of Sicilian beaches was examined, focusing on patterns of erosion and accretion observed over the three decades under study.

The main objective of this study is therefore to obtain coastal maps over time classified using a specifically trained model and to analyze the resulting coastal dynamics by exploring trends in variations of land cover classes and the main sources of conversion, providing information relevant for coastal management policies in the Sicilian coastal environment.

5.2 Methodology framework and study area presentation

To analyze LC changes in Sicily from 1988 to 2022 we developed the methodology presented in Figure 5.2.1. As already underlined, the semantic segmentation model of Chapter 4 was employed to process satellite images from Landsat and Sentinel datasets. This allowed us to create classified images of the entire Sicily for each month within the specified time frame. These images helped us identify different LC classes, including Water, Vegetation, Beaches, Bare Land, and Built-up areas. To ensure the accuracy of our results, we validated our model by comparing its classified images with ground truth images. Once we achieved a satisfactory level of accuracy, we conducted a comprehensive data analysis to understand the nature of the changes.

The research focused on the transition from LC to urban areas, quantifying growth rates, loss and stability of vegetation, bare land and built-up areas. The analyses carried out were devoted to the impacts of increasing urbanisation, considering the complex relationship with urban expansion, population growth and income patterns, which are fundamental for interpreting the social, economic, and environmental consequences. In addition, the analysis of LICELs in Sicily assessed trends in beach areas, highlighting the regions that are most susceptible to change and revealing whether they were accreting or receding.

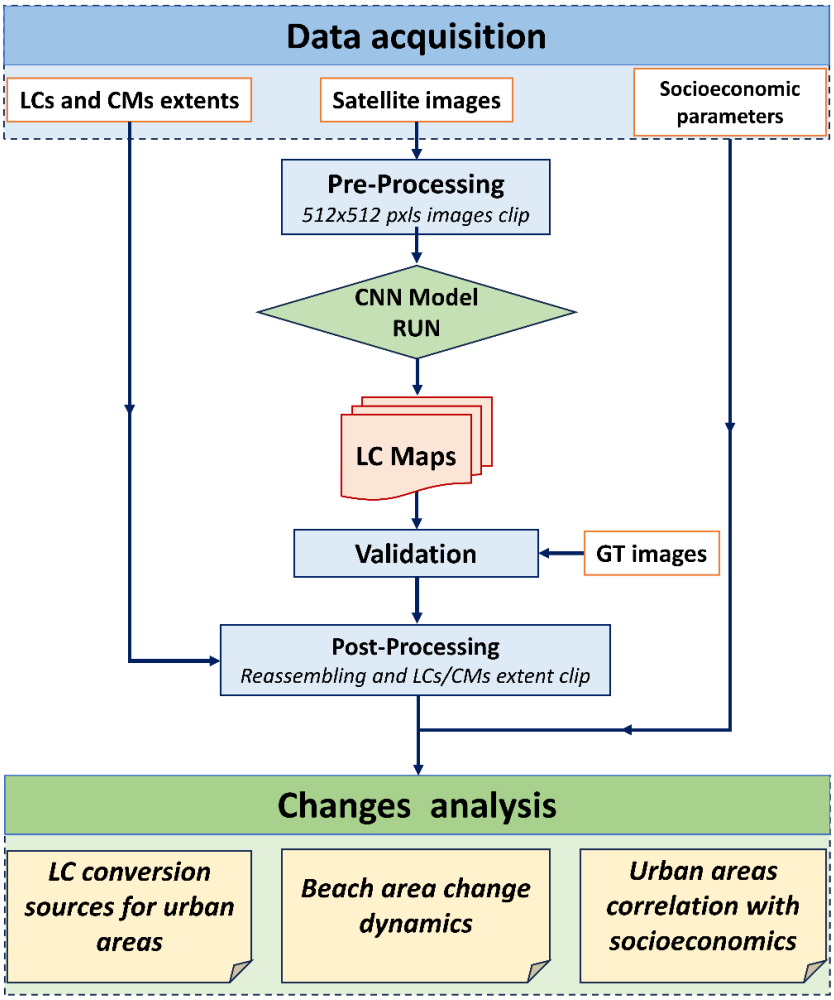

Figure 5.2.1 - Constructed methodology for analyzing changes in Land Cover.

5.2.1 Framing of the application area

Sicily, the largest island in Italy and the Mediterranean, boasts a topography dominated by hills and mountains, with a coastline that serves as a major attraction. From a coastal point of view, Sicily has a coastline of about 1600 km, characterised by a variety of coastal environments that differ in terms of geology,

shape, marine climate, human influence and much more. Approximately 30% of this coast is rocky, transitioning between shallow carbonate platforms and elevated rocky cliffs. The remaining 70% primarily consists of sandy or pebbly shores, which are often long and subject to erosion, prompting demands for local government intervention. As already suggested in (Manno et al., 2022b) in this research we will refer to the Sicilian coast into three significant segments: firstly, the Tyrrhenian segment from Boeo Cape to Peloro Cape (Thyrrenihan sea); secondly, the Ionian segment from Peloro Cape to Passero Cape (Ionian sea) and thirdly, the Central Mediterranean stretch from Passero Cape back to Boeo Cape (Mediterranean sea). We will refer hereinafter to these three macro-regions. A concise representation of Sicily and its geographical location is shown in Figure 5.2.2. Considering this territorial complexity and transformation through years, is surprising that there is still a lack of a complete picture regarding LC changes in coastal Sicilian areas, which are certainly characterized by areas with complex and heterogeneous coastal landscapes. The 2020 Regional Plan Against Coastal Erosion (PRCEC) is currently the only cognitive tool for coastal land in Sicily.

The communities of Sicily's coastal centers show considerable variation in size and demographic composition. Large coastal cities such as Palermo, Trapani and Catania have hosted dense populations due to their strategic location and sea-related economic opportunities. However, in recent years, there has been a considerable exodus from these cities to neighboring towns, probably due to the declining quality of life in the main cities. In addition, Sicily has suffered protracted depopulation, mainly due to the migration of young people seeking work or educational opportunities elsewhere. Socio-economically, Sicily's coastal centers present a diverse range of situations. Some benefit from prosperous economies related to tourism and maritime activities, particularly those with private marinas (e.g., Marina di Ragusa), while others face more significant economic challenges due to a dearth of job opportunities, especially in smaller communities. These conditions have contributed to a steady decline in Sicily's overall population in recent years, influenced mainly by residents of inland cities and towns.

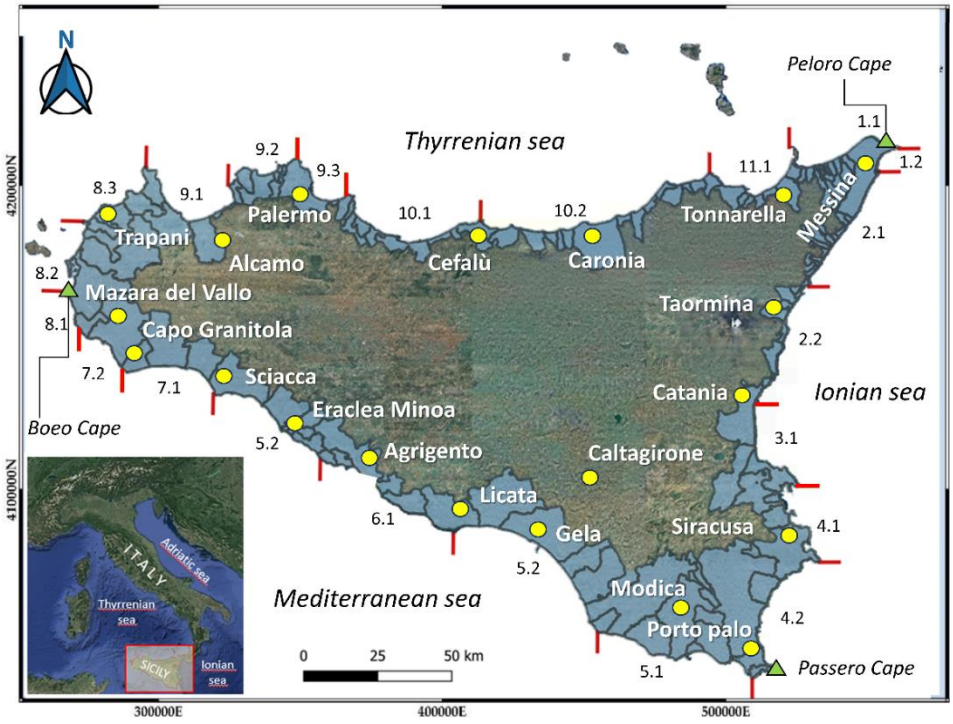

Figure 5.2.2 - Representation of Sicily, depicting Coastal Municipalities (CMs) in shaded blue areas, LICELs (LCs) segments in red, and highlighted locations (yellow points) referenced in the study (Reference System: WGS84-UTM33N-EPSG: 32633).

5.2.2 Satellite images used

The core of our methodology is based on the acquisition and processing of satellite imagery, covering the period from 1988 to 2022, to obtain a monthly, detailed view of Sicily's changing landscape. The imagery was sourced from various satellite platforms, including Landsat 5, 7, 8, and the more recent Landsat 9, as well as Sentinel 2. The satellite images were acquired with a spatial resolution of 30 meters (Sentinel products with 10 m resolution but upscaled to 30 m resolution in order to work with a single resolution) using the Google Earth Engine (GEE) shell. We used a bilinear interpolation method for down sampling. This method was chosen to maintain a smooth transition between pixels and minimize information loss (Hirahara et al., 2021; Zhang et al., 2011), visually examining the images to identify any artifacts or loss of significant detail.

We primarily focused on the RGB bands of satellite images to capture a vivid representation of the Earth's surface.

Central to our satellite image acquisition methodology was the stringent requirement of cloud cover, which we set at or below 20%. This criterion was essential to ensure that the images we used for our analysis were as clear and free from atmospheric distortions caused by cloud cover as possible. Our objective was to provide the subsequent semantic segmentation model (as detailed in the following section) with high-quality, clear input images. To achieve this, we meticulously selected images that met this specific criterion. Subsequently, each image underwent a cropping process, via QGIS raster tools, to obtain an identical extent of 512 by 512 pixels for each resulting image. In total, therefore, we obtained for each monthly image 280 images of 512x512 pixels resolution (so as to cover the entire extent of Sicily). Considering 12 images per year (one per month), over 35 years, the total number of images acquired was 117,600.

5.2.3 Littoral Cells, Coastal Municipalities, and socio-economic indicators

For the study of coastal dynamics and erosion/accretion movements, we divided the Sicilian coastline into 22 secondary-level shoreline segments (LICELs). Each segment, or sediment cell, has distinct sources of sediment, transportation routes, and deposition areas, making it an individual unit for management purposes (Manno et al., 2022b).

In this Chapter, we defined “Coastal Area” as that portion of land that extends from one LICEL boundary to the other with landward extension delimited by areas with elevation less than or equal to 15 m. Coastal zones are usually considered to be the areas between 0 and 10 m (McGranahan et al., 2007). In this case, we have extended the 10 m limit to 15 m. This choice is justified considering that Sicilian beaches are predominantly sandy and characterized by a low slope (1-3%), with an average width of about 60 meters. The mask thus defined proved to effectively include all beaches, ensuring an accurate representation of the areas of interest. The 15-meter threshold made it possible to exclude headlands, focusing attention on beaches, which by their nature have greater dynamism. In addition, this extension also made it possible to include the urbanizations closest to the beaches, which are essential for a comprehensive analysis of the interaction between the coastal environment and human settlements that press directly on the beaches. We obtained the mask for the definition of these areas using the Digital

Elevation Model of the terrain (DEM) with 2 x 2 m resolution of the Sicilian Region.

We conducted the analysis of the correlation between changes in built-up area and changes in socio-economic indicators by defining the extent of each CM, 109 in total, through the shape file provided by the *Istituto Nazionale di Statistica* (ISTAT) regarding all the Italian municipal administrative boundaries. We chose as socio-economic indicators the population and income data provided by the ISTAT and the Ministry of Economy and Finance, respectively. These data allowed us to examine demographic and economic trends over three decades and better understand the development dynamics at the scale of Sicilian CMs.

5.2.4 Recompositing of classified images

Once all the satellite images were processed by the semantic segmentation model, we reassembled them to obtain a unique image of Sicily, month by month, segmented by the classes mentioned previously. In this way we obtained 420 classified images representing a huge dataset of satellite images with their respective LC masks, for a previously non-existent observation period for the entire area of Sicily.

Regarding resampling and cropping effects, it should be noted that in the context of satellite image processing, each image can be represented as a three-dimensional matrix, where the three dimensions correspond to the red (R), green (G) and blue (B) colour channels. Given a large initial image size, we can proceed to its cropping into sub-images of more manageable size while keeping the original resolution intact (e.g., 512 x 512 pixels for each sub-image). This subdivision process does not alter the original matrix: each pixel in the sub-images retains the same RGB color values it had in the global image. Therefore, if the classified sub-images are reassembled in their original positions, the source image is reconstructed without loss of information or distortion due to cropping, in order to obtain a coherent and continuous map of the entire island. This process ensures spatial continuity and consistency of the segmented classes, reconstructing an overall image that preserves the resolution and accuracy of pixel-level analysis. The semantic segmentation applied uniformly on each sub-image ensures that the classification is consistent across the entire study area. This pixel-wise approach ensures that the results are equivalent, regardless of whether the model is applied to sub-images or the whole image. Therefore, the methodology used in our study preserves the integrity of the analysis even during the process of image cropping and reassembly.

5.2.5 LC classification validation

We used several indicators to determine the accuracy of the semantic segmentation model. Class accuracy, overall accuracy and Kappa coefficient were the main indicators used for this evaluation.

- Class accuracy (Brownlee et al., 2021b; Q.-H. Zheng et al., 2021), denoted as AC_i, measures the accuracy of the predictions of individual LC classes. The equation for class Accuracy is defined as (Equation 5.2.1):

Equation 5.2.1 – Single class accuracy

$$AC_i = \frac{TP_i}{TP_i + FN_i}$$

Where TP_i represents True Positives (correctly classified pixels) for class *I* and FN_i denotes False Negatives (pixels misclassified as not belonging to class *i*).

- Overall accuracy, often referred to as *OA*, provides a comprehensive assessment of model performance over all LC classes. It is calculated using the following equation (Equation 5.2.2):

Equation 5.2.2 – Overall accuracy

$$OA = \sum \frac{AC_i}{n}$$

Where $\sum AC_i$ represents the sum of class accuracies for all LC classes and n indicates the total number of classes.

- The Kappa coefficient (κ) (J. Cohen, 1960; van Vliet et al., 2011) evaluates the performance of the model considering the agreement between the predicted and reference classifications (Ground Truth, GT). It is calculated as (Equation 5.2.3):

Equation 5.2.3 – kappa coefficient equation

$$k = \frac{(P_o - P_e)}{1 - P_e}$$

Where P_o is the observed agreement while P_e is the expected agreement by chance.

P_o represents the fraction of cases in which the two image classifications (between GT and detection) agree. P_o is calculated using the following equation (Equation 5.2.4):

Equation 5.2.4 – Fraction of agreement classification in kappa equation

$$P_o = \frac{Number\ of\ obesrvation\ in\ agreement}{Total\ number\ of\ observation}$$

P_e represents the agreement that would be expected by chance. P_e is calculated using the following equation (Equation 5.2.5):

Equation 5.2.5 – Fraction of agreement in classification expected by chance in kappa coefficient equation

$$P_e = \sum_{i=1}^{n} \frac{\sum row_i \ \sum column_i}{(\text{Total number of samples})^2} \quad (5)$$

Where n is the number of classes, $\sum row_i$ and $\sum column_i$ represents the sum of the values of the i-th row and i-th column respectively.

The k coefficient measures the agreement between predictions and Ground Truth (GT), considering random matches; it is used to assess how much better the agreement is than would be expected by chance. Note that the subscript i is not present in this case since the metric refers to the overall classification.

We performed an accuracy analysis by comparing model predictions with reference images (GT) generated by manual classification. To provide an additional qualitative perspective, further visual comparison was made with other existing LULC classification maps in the area of interest, including the based LUCAS dataset (Witjes et al., 2022a), Copernicus Coastal Zones maps and ESRI's Sentinel-2 10-meter LU and LC time series maps. Segmented images postprocessing

For the temporal analysis of each LC class area, the classified images of the whole of Sicily were cropped (for each month and year), using the CM and LC masks. Area values for each LC class were extracted. These area values represented the areas covered by each class in terms of the number of pixels (at a resolution of 30 x 30 meters). In this way, the monthly area values (for each year) for each segmentation class were computed. Through this methodology, we conducted a

temporal analysis of urban expansion in coastal municipalities and for other LU classes at both CMs and LICELs scales.

For the analysis of the Builtup class at the level of CMs, we considered an annual time scale, aggregating the monthly Builtup area data on an annual basis by averaging, since the monthly variations for this class were insignificant. On the other hand, for LICELs, the analysis was conducted at the monthly level, as we were interested in the month-to-month changes in beach areas, (as well as for the remaining coverage classes). To examine the correlations between socioeconomic indicators and built-up areas in each CM, we employed the correlation analysis approach. This method made it possible to evaluate the relationships between different time series, such as the trend in urban expansion and the population of each CM. This evaluation was based on Pearson's correlation coefficient (I. Cohen et al., 2009), an index that measures the degree of linear relationship between two variables. Using this approach, it was possible to quantify the link between urban sprawl and population growth over the years for each CM. In addition, we conducted a correlation analysis between income and built-up area and between income and population.

Further, the Mann Kendall Test (McLeod, 2005) was used to analyze trends related to changes in beach areas in each LICEL. This test made it possible to examine the temporal trends of coastal areas, providing important information on the trend of accretion or erosion of beaches in each LICEL area.

5.3 Analysis results

5.3.1 Validation of the model classification process.

In the previous Chapter (III), the process used to validate the model's ability to detect the shoreline was discussed, with discussion of the results of this process. In this case, the validation of the ability to correctly classify the various classes is discussed. To assess the CNN model’s ability in segmenting various LC types and validate its performance, we implemented the methodology outlined in the 5.2.5 section across four distinct sites in Sicily. Each manually generated Ground Truth image covered an area of 10 km², totaling 40 km².

Figure 5.3.1 shows a graphical comparison between the reference satellite images (Capo Granitola,2006, beach in panel A, the Catania airport area, 2013, in panel B, the Porto Palo coastal area, 2009, in panel C and the urban coastal center of Palermo, 2019, in panel D) and the ground truth by hand classified images

(second line, respectively from E to H panel) with the images classified by the semantic segmentation model (third line, from I to L panel). As can be seen, the semantic segmentation provides the classification value predicted by the model at pixel scale. This comparison visually demonstrates the similarities and differences between the GT and model-generated LC classifications. The significant dissimilarities primarily arise from the nature of semantic segmentation, which delivers, as already reported, a pixel-level classification outcome, with each pixel classified based on the model's prediction. In this scenario, classes may exhibit greater fragmentation compared to GT images. However, semantic segmentation can yield more precise results in areas with elevated LC variability.

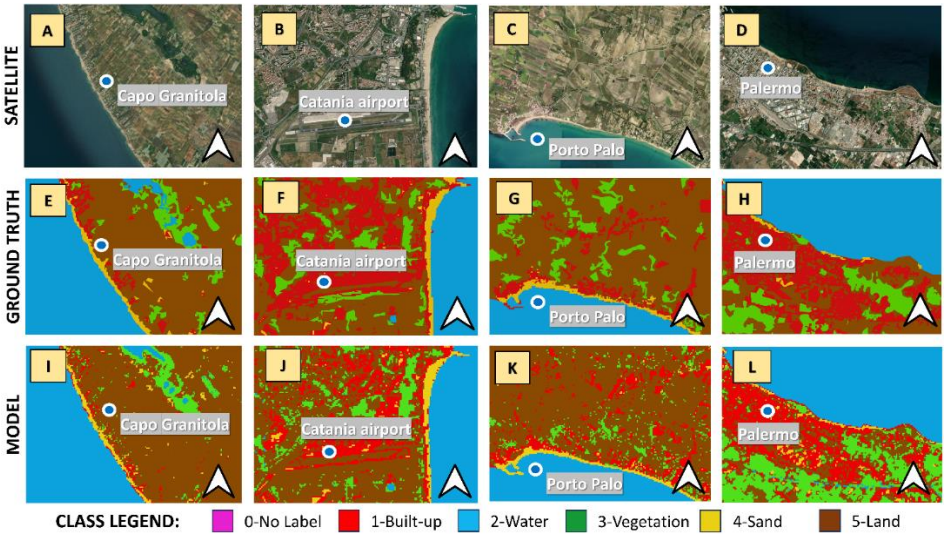

Figure 5.3.1 - Visual validation of the image segmentation algorithm at four coastal sites. Panels A-D (first row), E-H (second row) and I-L (third row) show the reference satellite images, the ground-truth detection, and the model classification, respectively.

To validate the model results quantitatively as well as qualitatively, we estimated the degree of accuracy and coefficient. The results are shown in Table 5.3-1.

The image validation results of four locations (Capo Granitola, Catania, Porto Palo, Palermo) are shown in Table 5.3-1. Each sub-table links the ground image to the model output, showing the number of correctly classified pixels for each LC class. The diagonals in bold indicate the correct detections, i.e. the pixels

classified in the same way in the reference map and in the survey result (TPi). As can be observed, the detection of water pixels, for all images, is always above 98%. This is because the model used was extensively trained with coastal images. The results also show that no category (for any of the four images) has a Class Accuracy that is less than 50 percent. The lowest Class Accuracy values are for the Vegetation and Beach classes in the Capo Granitola map, for the Vegetation class in the Porto Palo map, and for the Vegetation and Bare Land classes for the Palermo map. The classes that show lower Class Accuracy than the others each time are the least frequent in each image. Conversely, the classes with a higher occurrence of pixels (e.g. bare land for Capo Granitola, Builtup for Catania and Palermo, and bare land for Porto Palo) are always recognized by the model with an accuracy degree higher than 80%. For three out of four comparisons the class related to Beach always has a degree of accuracy greater than 60%. Only Capo Granitola shows a rate of 56 percent, but again the total number of pixels is significantly lower than those of the other classes. Overall, the comparison on Capo Granitola shows an OA of 87.9%, Catania 88.2%, Porto Palo 82.3%, and Palermo 76.6%.

Table 5.3-1 also shows the values of the k coefficient for each comparison, again obtaining Substantial Agreement (SA) or Almost Perfect Agreement (APA) (van Vliet et al., 2011) for each image analyzed. Specifically 0.79 (SA), 0.83 (APA), 0.7 (SA) and 0.67 (SA) for Capo Granitola, Catania, Porto Palo and Palermo, respectively.

CAPO GRANITOLA

Ground truth: Class ID	Model 1	2	3	4	5
1	**326**	67	12	88	13
2	0	**8057**	54	0	8
3	26	279	**688**	9	217
4	103	68	6	**394**	128
5	595	18	795	183	**11965**
Class accuracy	64 %	99 %	56 %	56 %	88 %

Overall classification accuracy: 87.9 %

Kappa value: 0.79

CATANIA

Ground truth: Class ID	Model 1	2	3	4	5
1	**4820**	18	118	29	481
2	4	**3316**	0	1	2
3	76	0	**1018**	0	333
4	35	54	0	**405**	1
5	303	1	546	16	**5515**
Class accuracy	88 %	100 %	71 %	82 %	86 %

Overall classification accuracy: 88.2 %

Kappa value: 0.83

PORTO PALO

Ground truth: Class ID	Model 1	2	3	4	5
1	**1448**	10	84	113	643
2	3	**3709**	1	18	12
3	54	0	**587**	15	418
4	70	66	1	**336**	70
5	672	0	1266	28	**10413**
Class accuracy	63 %	99 %	55 %	62 %	84 %

Overall classification accuracy: 82.3 %

Kappa value: 0.70

PALERMO

Ground truth: Class ID	Model 1	2	3	4	5
1	**3076**	51	43	55	1084
2	76	**8339**	11	2	54
3	668	3	**1936**	1	1063
4	32	7	10	**320**	80
5	1284	0	176	6	**1759**
Class accuracy	71 %	98 %	53%	71 %	55 %

Overall classification accuracy: 76.6 %

Kappa value: 0.67

Class ID : 1) Builtup – 2) Water – 3) Vegetation – 4) Beach/Sand – 5) Bare land

Table 5.3-1 - Quantitative validation at four coastal sites using confusion matrices where the pixels classified by the segmentation algorithm are confronted with ground truth detection. Each diagonal (in bold) represents the correct detections. The classification accuracy, the overall accuracy and the kappa coefficients are displayed for each class.

Further validation, of a qualitative nature, of the classified images obtained is shown in Figure 5.3.2.

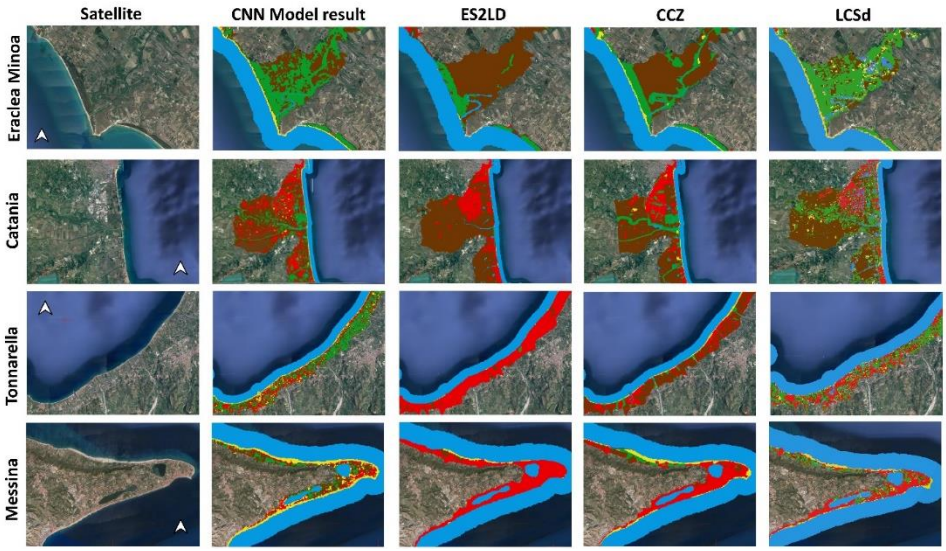

Figure 5.3.2 - Comparison of CNN model-classified images with Copernicus Coastal Zones (CCZ), LUCAS dataset (LCSd), and ESRI Sentinel-2 Land Cover (ES2LD) products. Figure displays distinct Sicilian locations in each row, with the first column presenting the reference satellite image. The second column shows images from the semantic segmentation model, while columns three, four and five present land covers from CCZ, LCSd, and ES2LD, respectively.

We compared CNN model classified image results visually with Copernicus Coastal Zones (CCZ), LUCAS dataset (LCSd) and ESRI Sentinel-2 Land Cover (ES2LD) products. **Figure S1** shows for each row a different Sicilian location. First column represents the reference satellite image, second column shows the images obtained from the semantic segmentation model while columns three, four and five show the LC provided by the CCZ, LCSd and ES2LD products, respectively. We compared the locations of Eraclea Minoa, Catania, Tonnarella and Messina from the first to the fourth rows of Figure 5.3.2, respectively.

A remarkable aspect that emerged from this comparison is that CCZ and ES2LD products, for all images displayed, tend to provide LC represented as large patches. In other words, if within a LC class, for instance, there are small areas of other LC classes, these products fail to consider them individually, grouping them under the same main LC category. In contrast, the semantic segmentation

model, due to its ability to segment at the pixel scale, is able to distinguish finer details, such as individual LC types within the main (more extensive) ones. As a result, the outputs obtained from the semantic segmentation model differ, in these finer details, significantly from those provided by the CCZ and ES2LD products. Anyway, CCZ dataset still provides better LC classifications than ES2LD. It should be noted that the LUCAS dataset proved to be the most accurate dataset. It is able to capture more refined and specific details of LC than the other products considered, confirming its reliability and accuracy in the context of satellite image classification. In summary, the comparison highlights the limitations of the CCZ, LCSd, and ES2LD products in capturing the finer details of satellite imagery, while emphasizing the accuracy of the semantic segmentation model and the LUCAS dataset. This qualitative analysis underscores the importance of careful selection of datasets based on specific classification objectives and is a significant contribution to improving the understanding of LC in satellite imagery of the Sicilian region.

5.3.2 Built-up area evolution

Figure 5.3.3 shows the time series of built-up areas for the localities of Salemi, Mazara del Vallo, Modica, Tre Fontane/Triscina, Marsala-Lido Signorino and Caltagirone, with a classified image (second column) showing the trend of the built environment in the years from 1988 (light blue) to 2022 (red) for the areas within the grey boxes in the satellite images of the first column.

In general, for all selected locations, the pixels (green to red) of new urbanisation (after 1988) represent the majority of built-up pixels. The urbanisation rates in relative terms were 380, 88, 435, 63, 142 and 485 % of increase respect to 1988 built-up areas from Salemi to Caltagirone, respectively. For all the locations analyzed, therefore, urban expansion occurred mainly in suburban areas, particularly for Salemi, Modica and Caltagirone. For Salemi it is possible to note one of the largest and “necessary” urban expansion that occurred in the years after 1968 (and thus included in the scale of visualization of this work) following the "Belice Earthquake" of magnitude 6.4 that affected the area in 1968. Similarly, for Caltagirone where we note the 485 % building expansion (compared to 1988) that led to the construction of the new town and the growth of services and commercial activities and Modica with 435 % due to the expansion of the city into the suburbs (also as a result of increased tourism).

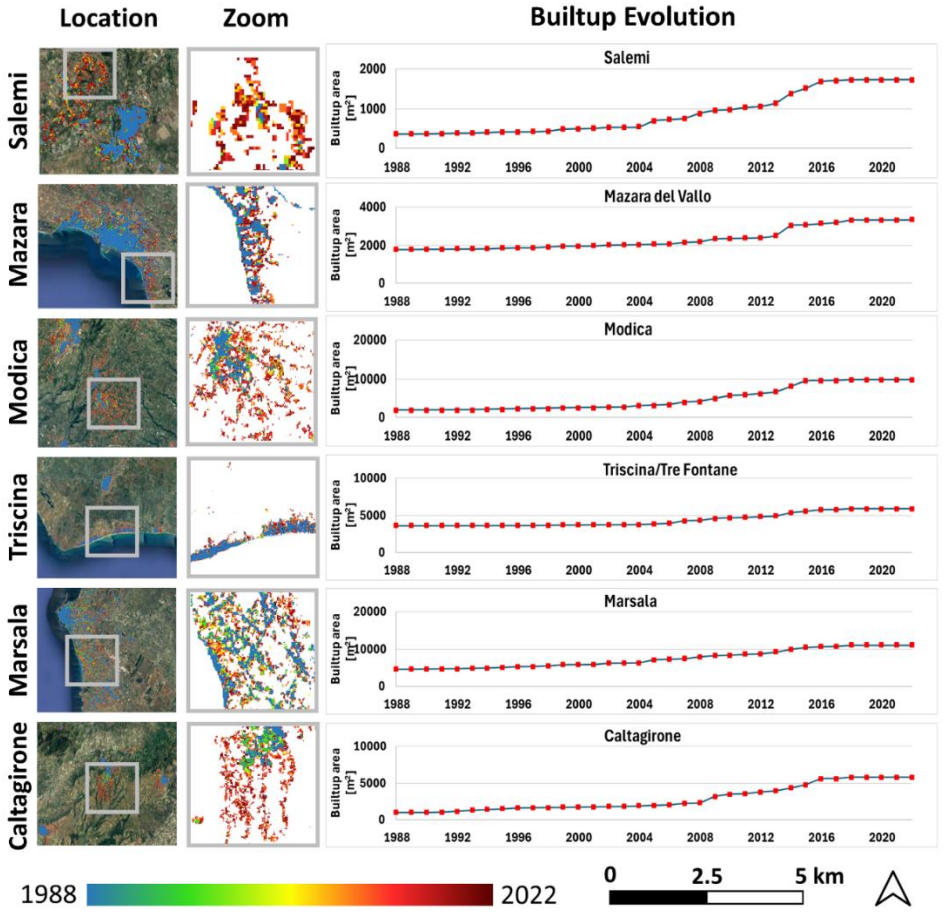

Figure 5.3.3 - Built up land expansion over the 1988-2022 period at six different cities: Salemi, Mazara del Vallo, Modica, Tre Fontane/Triscina, Marsala and Caltagirone. The second column shows the zooms (grey boxes in first column) temporal evolution of the built-up area overlaid with satellite images while the time series of built-up areas for all the localities is reported on the third column.

5.3.3 Spatial distribution of Land Cover Changes

Figure 5.3.4 shows the spatio-temporal variation of the Vegetation class (subplot A), Bare Land (subplot B) and Built-up land (subplot C and D) from 1988 to

2022. For each class type, we provide the LC gains, losses and stable areas and the evolution of the builtup area, which has increased by 47.3% from 1988 to 2022. This graphic provides a comprehensive view of the evolution of Sicily's terrains over a period of 35 years. The northeast part of the Sicilian coastal area is characterized by a very dense presence of vegetation (top right area of panel A), which has remained largely stable over the years (except for losses near urban areas). In contrast, the southern area shows an almost complete absence of vegetation. This can be attributed to the fact that the latter part of Sicily is densely populated with greenhouses. The western region, on the other hand, has experienced the most significant loss of vegetation, 77% of the total vegetation loss on the entire island. An almost opposite behaviour to that of vegetation is shown by the bare land map (panel B). In this case, where vegetation increases, there is a corresponding loss of bare land (50% of the total bare land loss). Conversely, where vegetation is decreasing and not due to human causes, a form of desertification may occur, leaving bare land.

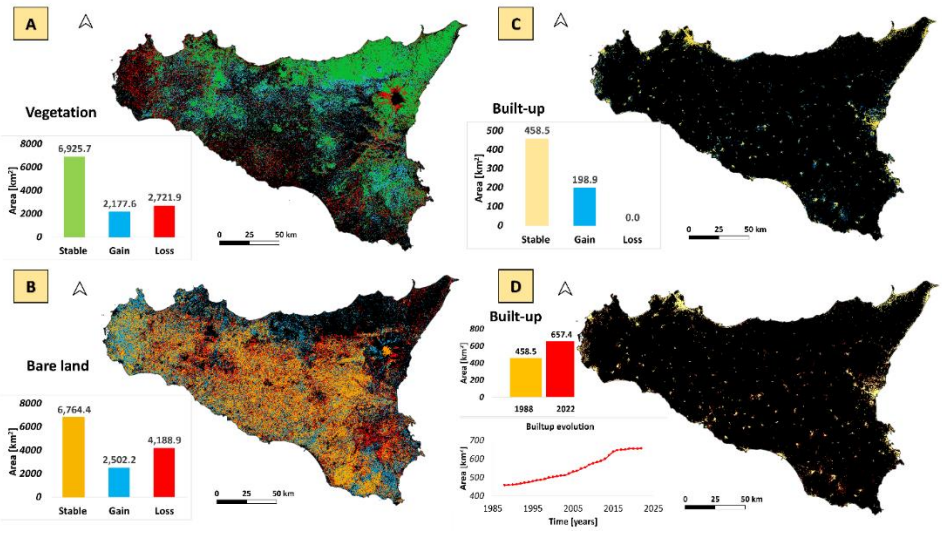

Figure 5.3.4 - Spatial distribution of stability, gains and losses in vegetation (subplot A), bare-land (subplot B) and built-up area (subplots C and D) in Sicily between 1988 and 2022. Each subplot illustrates the variations in LC types, accompanied by a summary bar plot indicating gain, loss, and stable area values

(subplot A, B and C). The time trend and relative bar plot of the built up on regional scale is shown in subplot D.

More details on trends over the years for LC classes are presented in Figure 5.3.5**.**

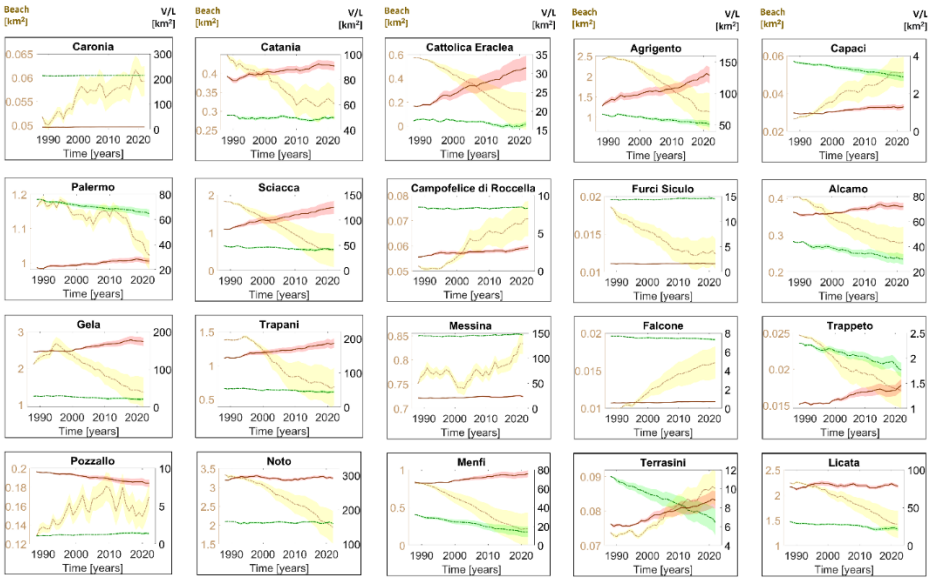

Figure 5.3.5 - Temporal trends in LC. The subplots depict trends over the years, showcasing sand (yellow), vegetation (green), and land (brown) areas for 20 sample locations around Sicilian Coastal Municipalities (CMs). The left y-axis in yellow represents the areal values of beach, while the right y-axis in black represents the areal values of vegetation and bare land. Variance bands are also displayed.

The subplots show trends from various years illustrate the areas of sand (yellow), vegetation (green), and land (brown) for 20 samples location around Sicilian CMs. The y-axis on the left in yellow refers to the areal values of beach and the y-axis on the right (in black) to the areal values of vegetation and bare land. For each plot, the respective variance bands are associated with each time series.

In all the subplots of Figure 5.3.5, regarding LC trends with p value always less than 0.05, we noticed that at the beach level all trends, except for Caronia, Capaci and Terrasini, are prevalently negative. Caronia, Capaci and Terrasini subplots show positive trends in beach area values over time, albeit still with slow growth

(e.g Caronia from 0.05 to 0.06 km^2 in 35 years). Pozzallo and Messina subplots show instead, a trend that is certainly prevalently upward but with the presence of many fluctuations over the years. Particularly negative was the trend in the beach area in Sciacca (from 2 to 0.5 km^2 in 35 years). Gela, on the other hand, showed a positive trend in the early 1990s, reaching a peak in 1995. Subsequently, a decrease in beach area values is also recorded for this CM. Each time series of the subplot beaches also shows a variance band that is narrow at the beginning of the series but widens going forward in time. This behavior may indicate greater stability and consistency of the beach area data at the beginning of the time series, with little variation from the mean. As one moves forward in time, the fluctuations or variations in the data have become more significant, creating wider bands. This behavior suggests increased uncertainty and greater variability in beach area data over time. Only Palermo, in contrast, shows a variance band of beach area values with an almost constant thickness over time. This behavior indicates that beach areas in Palermo have remained relatively stable and consistent throughout the period considered. In other words, there have been no significant changes or variations in the beaches over time. Similar to the behavior of beaches is that of the Vegetation class for all subplots of CMs, thus confirming opposite trends to that of builtup. In a complementary manner, on the other hand, are the Bare Land trends, which are obviously increasing.

5.3.4 Changes in conversion sources for urban areas

Figure 5.3.6 shows the impacts of urban growth on major LCs (Vegetation and Bare Land) for each coastal municipality in absolute and relative terms over the period 1988-2022. The spatial representation of Sicily in the same figure shows the primary source of conversion of built-up area expansion in each CM. As can be observed, all the coastal municipalities in the north/northeastern part of Sicily have experienced expansion at the expense of the vegetation class. The opposite holds true for bare land. As described in Figure 5.3.5, the spatial subdivision of the two classes is apparent. During the period considered, the trend is always increasing for both vegetation and bare land. In particular, an increase of about 20 times the 1988 urbanised area conversion value for the bare land class and about 7 times for the vegetation class was detected. In recent years (2017-2022), a growth trend has been observed in the built-up class, which is mirrored by a similar trend in the vegetation class. This suggests that the limited urbanization that occurred during this period had a more pronounced impact on the bare land class. In the early years, vegetation and soil values are similar or close in percentage terms, suggesting that there is a balance between the two. However,

over time, a significant change is noted. The fact that the percentage of vegetation decreases relative to bare land indicates that building expansion has had a greater impact on vegetation than on bare land. In fact, while the vegetation class has a decrease from 54 % to 34 %, the bare land class shows the mirror-like trend. This means that as urbanization has progressed, green areas, such as forests or cultivated areas, have been converted into built-up areas. This has resulted in a significant reduction in vegetation. The rapid decrease in vegetation until 1992 (from 54 % to 39 %) suggests that there were very intense land transformations during that period, which led to a rapid loss of vegetation. After 1992, the decrease in the percentage of vegetation continued, but at a slower, almost constant rate. This could indicate that soil transformations have stabilized, with fewer vegetation conversions to unvegetated land, or that the remaining vegetation areas have been more effectively conserved.

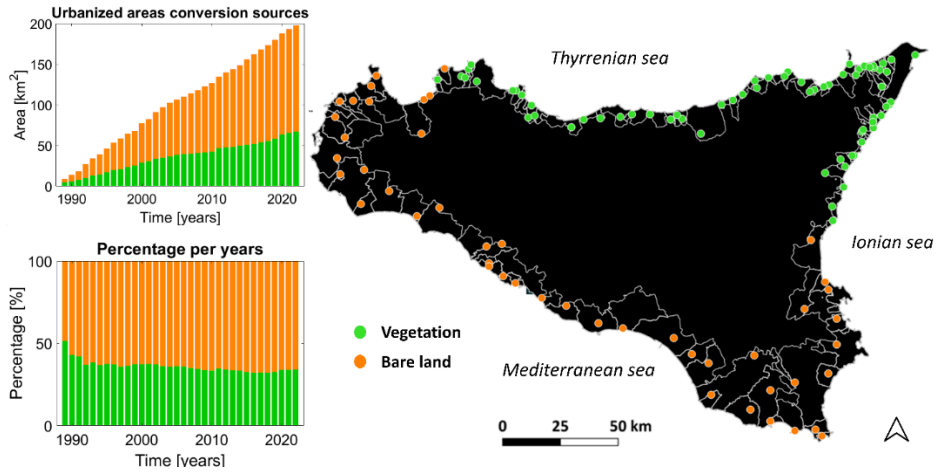

Figure 5.3.6 - Impacts of urban growth on the main LUs (vegetation and bare land) for each coastal municipality in absolute a) and relative terms b) over the 1988-2022 period. In panel c) the primary conversion source of built-up area expansion is highlighted in each coastal municipality.

5.3.5 Changes in urban areas and correlation with socioeconomics

Figure 5.3.7 shows the correlation between these LU shifts and their relationships with various socio-economic indicators. The trend tests, all statistically consistent according to the Mann-Kendall test (p-value always less than 0.05), reveal distinct patterns. Coastal areas between the Mediterranean and Ionian stretches show a predominant population increase (first subplot to the left of the first row), while Tyrrhenian CMs generally experience depopulation, with some reversal west of Palermo (Gulf of Castellammare). In terms of income trends (second subplot from the left of the first row), negative patterns are observed in most Mediterranean municipalities, while the Tyrrhenian and Ionian CMs are more heterogeneous. The Mediterranean coastal area shows the highest urbanization trends, followed by the Ionian area, whereas the Tyrrhenian CMs, especially in the eastern part, exhibit fewer positive trends. In the second row of Figure 5.3.7, contrasting trends are evident between built-up evolution and population. Sciacca experiences population growth of 3.9%, while other CMs show population decreases of 12.3 % for Palermo, 25.5 % for Caronia, 16.7 % for Catania, 18.6 % (a smaller decrease of 7.1 % until 2017 and then a steep decrease) for Trapani and 5.3 % for Gela. Caronia and Sciacca record the largest relative percentage increases in built-up areas (78% and 79.6%, respectively), which can be attributed to civil infrastructure development. Conversely, Palermo, Catania, Trapani, and Gela exhibit more moderate increases in built-up areas (8.4%, 22.1%, 43.5%, and 33.8%, respectively). Trapani, despite a decreasing population since 1988, shows a recent slowdown in population loss.

Also, in Figure 5.3.7, it can be seen how, over time, the urbanization of the large Scillian cities (e.g. Catania or Palermo) has grown at a high rate and a decline in the city's population. In fact, incomes have also fallen in these areas, probably due to unrestrained buildings in the periphery that may not have contributed significantly to the growth of the local economy. It is necessary, however, to point out how the trend scales, which while also showing positive values, are predominantly unbalanced for both population and income. In fact, the color graded scales in the first row of Figure 5.3.7, show a significant imbalance between negative and positive trends. We obtained negative maximum of -2124 res/year and -834 €/res year, while positive ones stop at +676 res/year and +143 €/res year for population and income, respectively. Finally, we found no clear correlations between population and urbanization. In fact, observation of decreasing population, increasing urbanization and variable, but often decreasing

trends within LC areas reveals a complex picture of socioeconomic and environmental dynamics in Sicilian coastal communities.

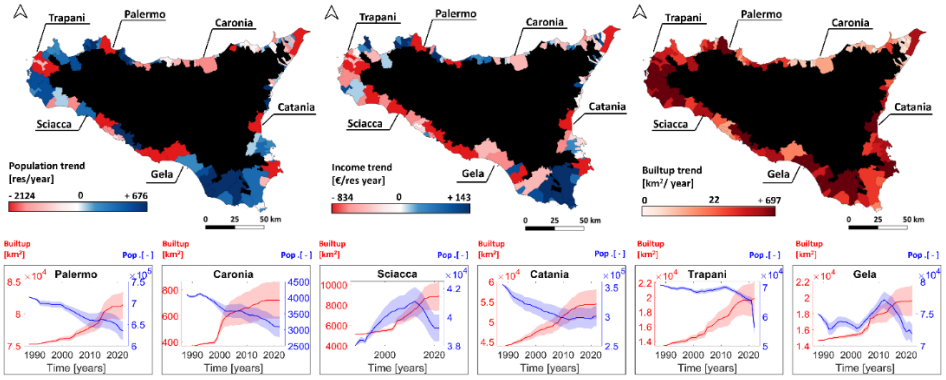

Figure 5.3.7 - Urbanization and LC dynamics in Sicilian coastal cities: correlating built-up area, population, and income trends from 1988-2022. In the figures of the first column, for each CM, population, income, and built-up area trends are shown. The second row presents trends in built-up areas (red) and population (blue) for six CM, with respective variance bands for each timeseries. Axis annotations indicate specific category values.

For a greater understanding of the correlations between the built environment and the socioeconomic indicators analyzed, we created a map of the correlations between built-up, income and population (Figure 5.3.8).

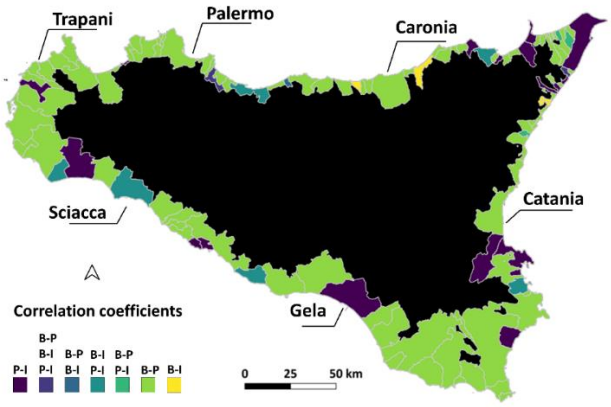

Figure 5.3.8 - Socioeconomic Correlations in Sicilian Coastal Municipalities. Figure presents a map of Sicily highlighting strong correlations (positive or negative coefficients greater than 0.5 and -0.5, respectively) between urbanization, population, and income.

The representation of Sicily in Figure 5.3.8 shows for each coastal city the type of strong correlation with the three previous categories. Strong correlation refers to those positive or negative correlation coefficients greater and less than 0.5 and -0.5 respectively. For example, CMs shaded in yellow represent those municipalities where there is a strong correlation only between built-up and income (B-I). Conversely, coastal cities in light violet represent those municipalities where there is a strong correlation between built-up and population (B-P), built-up and income (B-I) and population and income (P-I). To understand whether each strong correlation coefficient is positive or negative, it is possible to look at the reference trend values in Figure 5.3.7 for the same coastal municipality. We noticed that often, for most Sicilian CMs, there are strong negative correlations (thus less than -0.5) between built-up and population and between income and Builtup. Obviously, then, there are strong positive correlations between income and population. The map of correlations between population, income and urbanization thus reveals interesting socioeconomic dynamics. The strong negative correlations between built-up and population and between Income and built-up suggest that urban sprawl is often associated with a decrease in population and income. This could indicate that urbanization has not led to an increase in quality of life or economic attractiveness in these coastal communities. The strongly positive correlations between Income and Population

indicate that both incomes and population often decrease simultaneously. This suggests a connection between these two factors and could be due to the overall decrease in economic opportunity and the resulting decrease in population.

In sum, these dynamics reveal the complexity of the interactions between population, urbanization and economy in Sicilian coastal communities. While urbanization is growing, population and incomes often decline, indicating that urban expansion may not necessarily improve the quality of life or economic prospects of these localities.

5.3.6 Changes in beach area dynamics

Figure 5.3.9 provides a visualization of beach erosion and accretion trends at the LICEL scale and the loss/gain conversion sources for beach areas. The figure also highlights year-on-year erosion, stability, or accretion trends (second row). Distinct behaviors of LICELs, such as LICEL 4.2; 5.2,; 7.1 and LICEL 9.3, are showcased, underscoring the diverse coastal processes influencing each cell. As can be seen, the region showing strongly negative trends (ranging from 4 to 8.5 % of beach eroded in 2022 compared to the initial beach values) is primarily in southern Sicily's coast (Strait of Sicily. In contrast, the beaches of the Tyrrhenian area of Sicily (North) have shown much lower decreasing trend values and even positive in some areas (LICEL 11.1 and LICEL 1.1 with percentage of increasing around 1-2 % respect 1988 beach area values). Lastly, the Ionian area of Sicily (East) shows predominantly negative trends, especially in the south closer to the Strait of Sicily. Moving from Catania (in the middle) to the north of the Ionian stretch we reached mostly positive (accretion) trends (from 2 to 3.5 % of beach increased in 2022 compared to the initial beach values). The observed erosion/accretion patterns align with wave energy variations in Sicily, consistent with findings reported by (Iuppa et al., 2015; Lo Re et al., 2019a; Menna et al., 2019; Monteforte et al., 2015) and (Lo Re et al., 2019b). The comparison between these results and the values reported in PRCEC (2020) are in Table 6.4-1 reported below.

Table 5.1-1 - Comparison between erosion/accretion beach areas from PRCEC and work results.

	Area [km^2]	Length [km]
PRCEC – Erosion beach	21.9	438.2
PRCEC – Accretion beach	16.23	324.6
Model – Erosion beach	27.271	545.42
Model – Accretion beach	22.262	445.24

Comparison results	% of eroded/increased area
Total eroded area / PRCEC Erosion beach	7.3
Total increased area / PRCEC Accretion beach	0.5
Total eroded area / Model Erosion beach	5.9
Totale increased area / Model Accretion beach	0.4

Analyzing erosion/accretion rates for all Sicilian LICELs, we estimated 27.3 km^2 related to 545.42 km of eroded coastline and 22.3 km^2 related to 445.2 km of accreted coastline (Table 6.4-1). PRCEC (as of 2020) gives 21.9 km^2 (438.2 km length) and 16.23 km^2 (324.6 km length) for erosion and accretion, respectively. Therefore, the values obtained are in line with those provided in the official instrument of the Sicily Region. Furthermore, of the actual areas computed, we estimated that 1.6 km^2 of coastline was competitively lost from 1988 to 2022 while 0.085 km^2 was gained. With reference to the above values, it means that 7.3 % of the areas that are in erosion (computed by PRCEC) have already been lost while only 0.5 % of the areas in accretion (computed by PRCEC) have had actual beach gain. On the other hand, the percentages calculated on the areas in erosion and accretion computed in this work turn out to be lower at 5.9 % and 0.4 %, respectively.

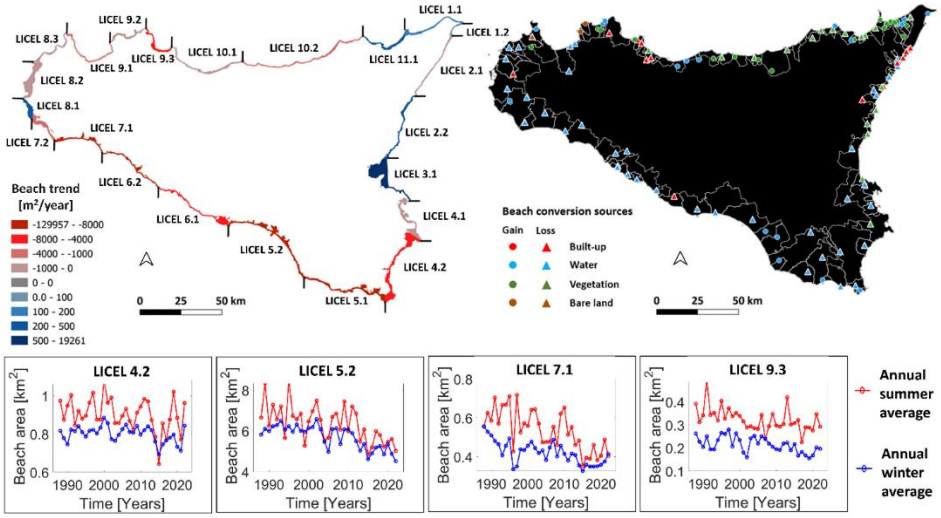

Figure 5.3.9 - Illustration of the LICELs temporal dynamics. The top left plot showcases the accretion and erosion trends expressed in km^2/year. Dark blue indicates maximum positive trends, while dark red signifies maximum negative trends. In the top right plot, beach conversion sources for both loss and gain are represented for each CM, using triangles for loss conversion and dots for gain conversion. Colors represent conversion sources: red for built-up, light blue for water, green for vegetation, and brown for bare land. The second row displays average annual trends in red for summer months (May to September) and in blue for winter months (November to March), explaining erosion, stability, or accretion trends for specific LICELs (in particular LICEL 4.2; 5.2; 7.2, and LICEL 9.3).

In the Mediterranean section (upper right panel), almost all of the beach conversion sources are of loss in favor of water. From the 109 CMs studied, 36 belong to the Gain class while the remaining 76 to the Loss class. Thus, only 33 % of Sicilian CMs show a predominance of gain beach conversion sources while 67 % of loss conversion sources. In the western Tyrrhenian zone, there is greater heterogeneity in beach conversion sources with a few beaches showing gains on the vegetation (probably due to loss of dune vegetation) and bare land (beach advance due to sediment deposition) classes. The central-western zone of the Tyrrhenian section is the one most affected by beach loss conversion sources in

favor of the built-up, while the eastern part shows losses and gains mainly on the vegetation class. The northern Ionian zone continues with the neighboring behavior of the the Tyrrhenian zone while also showing losses due to built-up. In these areas the beach loss is very small (percentage) so the major conversions are caused by the fact that parts of these beaches are affected by the construction of bathing lidos. The southern zone of the Ionian section in turn fits to the neighboring Mediterranean zone showing a prevalence of loss conversion sources of water. Finally, in the second row of Figure 5.3.9, LICEL 5.2, along with LICEL 9.3, displays the steepest erosion trend values, while 4.2, and especially 7.2, showcase less pronounced declining patterns. In relative terms of erosion or accretion, all the LICELs in the second row of Figure 5.3.9 experienced (negative) erosion percentages. In particular 8.3 %, 5.1 %, 4.1 % and 2.8 % of beach erosion in 2022 relative to the initial beach values for LICEL 7.1, LICEL 4.2, LICEL 5.2 and LICEL 9.3 respectively. Furthermore, although the absolute values of loss for LICEL 8.2 and 2.1 were among the lowest of the sand losses in relative terms the beach loss was 15.8 % and 5.6 % respectively.

We computed that only 0.14 km^2 (0.2 %) of the beaches in Sicily was converted to urbanized land between 1988 and 2022. This decrease can be attributable to the presence of many illegal properties along the coast, which represent 40-60% of the coastline (Romano et al., 2021; Zanfi, 2013). Built in the 1970s without an approved plan, many of these summer residences have remained illegal despite amnesties and demolition orders. This persistent situation has caused lasting environmental impacts, including erosion, loss of biodiversity, and pollution of coastal and groundwater (Angeli, 2019; Cirelli et al., 2003). For further information, refer to Figure 5.3.10.

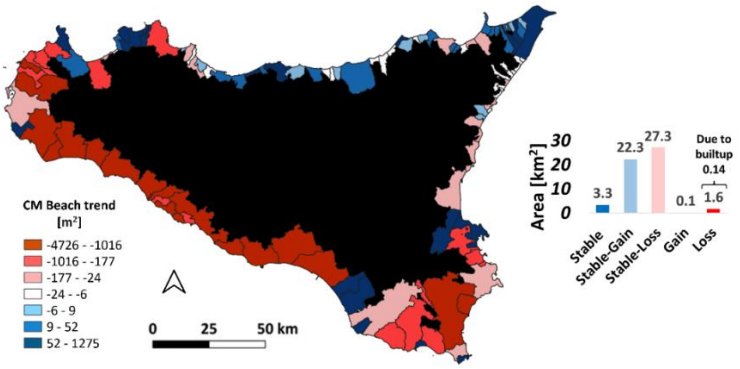

Figure 5.3.10 - Coastal Dynamics in Sicilian CMs. Figure portrays beach erosion/accretion trends at the Coastal Municipality (CM) level. The left subplot highlights areas with the highest negative (red) and positive (blue) trends. The right subplot presents km^2 values of Sicilian municipal beaches categorized as Stable, Stable-Gain, Stable-Loss, Gain, and Loss.

The subplot on the left of Figure 5.3.10 shows beach erosion/accretion trends at the CM level. Again, red shows the beaches that experienced the highest negative trends while blue shows the highest positive trends. Again, the classes are skewed toward negative trends. In contrast, the subplot on the right of Figure 5.3.10 shows the values in km^2 of Sicilian municipal beaches under the categories Stable, Stable-Gain, Stable-Loss, Gain and Loss. We denote by Stable all pixels that have never had a transition to other classes over the years. By Stable-Gain the stable pixels with pixels from other classes that have experienced a transition to the Beach class in at least one year. With Stable-Loss the Beach pixels that instead have shown continuous transitions to other classes over the years. Loss represents pixels belonging to the Beach category that by 2022 never belonged to the Beach class again, and with Gain the opposite.

Notably, there is a consistent alignment with the findings presented in Figure 5.3.9 with the ones in Figure 5.3.7. The choice to do this type of analysis was pursued in order to understand how much urbanization trends have actually impacted the municipal beaches of each LICELs. We obtained that only 0.14 km2 of beach was converted to built-up land throughout Sicily between 1988-2022 (right subplot of Figure 5.3.10). These findings confirmed an already anticipated behavior. In fact, it was already expected that the decrease in beach areas was not due to increasing urbanization in the years considered. Instead, “the story” in the

years prior to the time scale to which this work refers is different. The percentage of squatter properties, in fact, in the island is very high, with between 40-60 % of the coastline being squatted (Romano et al., 2021; Zanfi, 2013). In the 1970s, many summer residences were built without an approved plan, by families from urban centers located a few kilometers inland (e.g., the case of Alcamo, Caltagirone, Acate etc.). Many of these buildings have been regularized through building amnesties, although a significant portion has not yet been regularized, as they are located less than 150 meters from the sea and survive despite several pending demolition orders. The services and infrastructure to be built for these homes have never been implemented, and due to the absence of adequate (and almost in all cases non-existent) drainage systems, sewage from private homes pollutes the sea and groundwater. In addition, uncontrolled development along the dunes (Alcamo Marina is a case in point) has had the negative effect of triggering a lack of sediment in these areas. The situation of many of Sicily's coastlines is characterized by environmental and urban planning challenges that require urgent remediation and redevelopment. Thus, past construction squatting still has a significant and lasting impact on the current coastal situation. These unregulated constructions continue to cause environmental alterations, including loss of natural vegetation, LC, and alteration of coastal habitats. This certainly leads to several issues, including erosion, loss of biodiversity, and coastal water and groundwater pollution problems. In addition, unplanned urbanization and past squatting have made coastal communities more vulnerable to natural disasters such as floods and storms, as they often lack adequate defense infrastructure. These areas crowded with squatter buildings also often present problems with public access to beaches and coastlines, generating tensions between the local community and visitors.

5.3.7 Observations and implications

In this study, we conducted an extensive retrospective analysis of classified imagery of the entire Sicilian coastal region for each month from 1988 to 2022. This analysis used images from Landsat-5, Landsat-7, Landsat-8, Landsat-9 and Sentinel-2b. These images were processed with semantic segmentation techniques based on CNN. Our primary goal was to fill the gap in high-resolution LICEL data by employing an advanced artificial intelligence model trained with a large database specifically designed for coastal areas (Buscombe et al., 2023b). Furthermore, this research contributed to generating an extensive dataset that was previously nonexistent, enhancing the scope and specificity of coastal LC analysis.

The presented classification method resulted in coastal classifications with a high degree of accuracies (as described in the validation process) compared to the products available to date (seventh column of Table 5.1-1), which present overall accuracy in the range of 60 (Bai et al., 2020; Scepan, 1999), 71 (Wang et al., 2023) and 75 (Venter et al., 2022) percent for GLCC, ESA Land Cover - CCI and ESRI Global Land Use Land Cover, respectively. We also point out that products obtained purely for coastal areas (Coastal Zones LC/LU (Q. Feng et al., 2019)) show higher accuracy percentages, 85 (Eea, s.d.) and 90 % respectively confirming the need for specific maps for these types of environments. The use of specific, appropriate and accurate datasets processed through machine learning algorithms, as in Witjes et al., (2022b), also achieves good overall accuracy values in the classifications (83 %) confirming again how crucial the quality of the training data is. In our work we combined these concepts using a purely coastal dataset and obtained 35 years of monthly classified maps of maximum overall accuracies of 88 %.

We have been able to study the socio-economic evolution of Sicilian coastal municipalities in relation to the dynamics of coastal urbanisation, thanks to the availability of this precise and classified data. The analysis represents a first step towards the understanding of land-use dynamics in this region over three decades, focusing on urban expansion, land-use changes, and changes in Sicilian beaches over the period under consideration. Our approach sheds light on the intricate relationship between socio-economic development and coastal land use changes and underscores the utility of cutting-edge AI techniques in enhancing our understanding of environmental dynamics in coastal areas.

The results section, as well as validating the methodology adopted, delves into the LC dynamics in Sicily. The temporal evolution of built-up areas reveals urban sprawl in coastal municipalities, emphasizing variations in growth rates. Spatial distribution analysis highlights distinct patterns in Vegetation, Bare Land, and Builtup Areas, offering insights into environmental dynamics along the Sicilian coast. The sources of change in LC indicate direct influences of urban growth on vegetation conversion. An in-depth overview of erosion and accretion dynamics along Sicilian beaches, emphasizing LICELs is provided. Urbanization contributes modestly to beach loss, with illegal ownership being a significant factor, causing lasting environmental impacts. With the available data, we did not find a direct correlation between urban sprawl and socio-economic indicators. This fact highlights the complexity of linking LC changes with socio-economic

dynamics such as income and population. The analysis of potential correlations of LC with met-oceanic data can also benefit future research.

Integrated management strategies are crucial to preserve the coast of Sicily and any other coast worldwide amid the complex interactions between natural and anthropogenic factors. Understanding LC dynamics can contribute to improving current and future land planning by informing decision-making processes aimed at promoting sustainable coastal development and resilience. This research sets a foundation for further studies in coastal LC dynamics and highlights the need for continued monitoring and analysis of coastal environments in the face of ongoing and future challenges, including climate change and need for adaptation, using specific coastal datasets and with appropriate sampling intervals for short-term and long-term analysis.

Our study has some limitations that may be potential areas for improvement. The first limitation is related to the training dataset. Despite Coast Train is specific to coastal regions its representativeness may not be exhaustive in fully covering the variability of the Sicilian coast, since the selection of images may not include all possible variations in the island's coastal features. With that in mind, we manually selected images reflecting similar color characteristics, beach sizes, and urbanized contexts to those in Sicily. This careful selection provided the model with a diverse range of examples, ensuring a good level of generalization during the classification phase. In addition, we reviewed the results and made the required corrections. For example, greenhouses were misclassified by the model as built-up areas. The absence of these features in the training dataset meant the model struggled to classify them correctly. To address this issue, we created a mask to eliminate the false information caused by the greenhouses.

The second limitation is the statistical methods used, such as the Mann-Kendall test and correlation analysis, which may not account for the complex interactions between socioeconomic factors and changes in land cover, suggesting the need to consider more sophisticated nonlinear multivariate approaches in future studies.

The last limitation could be represented by the limited number of classes used in the semantic segmentation model, which includes 5 categories. Although this approach is suitable for regional scale analyses, it may not be sufficiently detailed for local studies that require higher precision on high-resolution images and thus a larger number of classes to represent. Improving the ability of the semantic segmentation model to distinguish a wider range of classes may therefore be

useful to enable a more accurate interpretation of coastal landscape features in high spatial resolution contexts.

Chapter VI

In Chapter 4, we saw how coastlines can be quickly and accurately derived from orthophotos or satellite imagery. Given the wide availability is of this type of data, it is therefore possible to draw a considerable number of coastlines or shorelines. Section 2.4.1 has also shown how such lines can be used to analyse and study both the short- and long-term effects of shoreline erosion or accretion. But how can we effectively analyse these shorelines? We need a tool that allows us to do this quickly and accurately. Accuracy is ensured by using a Geographical Information System (GIS), which allows us to use processing tools on vector-type geometries, automating the analysis of shoreline changes.

In this chapter, we will introduce the Coastal Dynamics Analyzer (CDA), a plugin developed for QGIS that provides transect-based analysis for studyng shoreline change, improving both the accuracy and efficiency in the coastal erosion studies. CDA integrates seamlessly into QGIS, providing an open-source, easy-to-use tool that automates the calculation of key metrics for shoreline change analysis, such as End Point Rate (EPR), Net Shoreline Movement (NSM), Shoreline Change Envelope (SCE), and Linear Regression Rate (LRR). We will discuss the rationale behind the development of CDA, its relevance in overcoming the limitations of existing tools such as the Digital Shoreline Analysis System (DSAS) and Analyzing Moving Boundaries Using R (AMBUR) and illustrate its functionality with a case study in the Mediterranean Sea. The aim is to demonstrate how CDA can produce accurate and reliable data, and become a reference for researchers, coastal engineers, and decision makers involved in coastal erosion management.

The topics and content covered in the following chapter are taken from a research article published by Elsevier, “SoftwareX” journal (Scala et al., 2024a).

6.1 A new free tool for coastal dynamics analysis

Analysis of shoreline change is crucial for understanding coastal dynamics and planning land management interventions. Shoreline changes can significantly affect the ecosystem and coastal infrastructure. Saengsupavanich, (Saengsupavanich, 2021) highlights how these sandy deposits (sand spits), shaped by natural and anthropogenic processes, can undergo shifts and transformations that alter the coastal habitat and its biodiversity, and shows how knowledge of their evolution can lead to planning for appropriate management of these spits (e.g., dredging, community livelihood adaptation, economic

development, and even tourism promotion). Similarly, Saengsupavanich et al., (2022) studied shoreline change at coastal structures such as jetties, showing how such infrastructure can both protect and alter coastal morphology and understanding how waves and water currents interact with the jetties. These, and other examples (Boumboulis et al., 2021; Di Paola et al., 2022; Apostolopoulos & Nikolakopoulos, 2020) demonstrate the importance of monitoring and understanding shoreline evolution to ensure sustainable coastal zone management.

Studies on shoreline evolution are also crucial to assess the rate of beach accretion or retreat (Armenio et al., 2017, 2019; Del Río et al., 2013). In recent years, researchers have developed many methods with different techniques belonging to various disciplinary fields. Today, Shoreline Change Analysis (SCA) is the most widely used method to assess shoreline evolution (Burningham & Fernandez-Nunez, 2020; James et al., 2024). In fact, SCA is necessary to implement management strategies that respond to current or potential erosion problems. In the context of coastal erosion management and the development of coastal hazard adaptation plans, it is essential to study the relationship between coastal and marine morphological changes (Gracia et al., 2018b; Rangel-Buitrago et al., 2018b).

Traditionally, these analyses were conducted through field surveys (Yun et al., 2023), aerial photographs, and historical maps. SCA was scientifically introduced in the late 1970s (Dolan et al., 1978; LeBlond, 1979). These methods required a lot of time and resources, and the data collected were often difficult to compare because of different scales and survey techniques. However, with the advent of GIS technologies and Earth Observation (EO) imagery, it has become possible to carry out these analyses more quickly and with greater spatial accuracy (Abd-Elhamid et al., 2023; Dong et al., 2023; Pepe et al., 2023; Scala et al., 2024c).

The integration of these data into GIS systems is crucial for the analysis of coastal dynamics. The main methods for shoreline analysis are Transect Based Analysis (TBA) and Area Based Analysis (ABA), with TBA being the most popular method (Anfuso et al., 2016; Manno et al., 2022c; Manno et al., 2022b). The most widely used tools in the field of SCA using TBA are the Digital Shoreline Analysis System (DSAS) (Himmelstoss et al., 2021; Oyedotun, 2014) and Analyzing Moving Boundaries Using R (AMBUR) (Jackson Jr et al., 2012).

DSAS (Digital Shoreline Analysis System) developed by the U.S. Geological Survey is a free tool for ESRI's ArcGIS that calculates rates of change in shoreline

position using historical vector data. This tool uses the baseline method to calculate shoreline velocity or change at user-specified intervals and is able to assess and resolve the nature of coastal dynamics and trends. However, DSAS is not supported by newer versions of ESRI ArcGIS (10.8) and ArcGIS Pro, and many countries and small management agencies have limited budgets for commercial software such as ArcGIS. Other options, such as SCARPS and BeachTools, also require ArcGIS to work. Due to ESRI ending support for ArcMap, the DSAS software has been updated in April 2024 to version 6.0 to function independently of any specific GIS (https://www.usgs.gov/centers/whcmsc/science/digital-shoreline-analysis-system-dsas - last access 28 oct 2024). However, due to tight deadlines, this new version has limited functionality. This means that the user must first set up all the necessary input files on a GIS platform, extract them in GEOJSON format and then run the tool, making the process longer and more fragmented.

To solve this issue, a free and open-source alternative to DSAS called AMBUR, based on R, was created. AMBUR allows analysis of shoreline change at different time scales but has the disadvantage of being complex to install and configure, requiring modifications to GIS systems such as QGIS or ArcGIS. The lack of user support makes AMBUR less attractive as an open-source option.

One of the most popular open-source geospatial tools is Quantum GIS (QGIS) (http://www.qgis.org/ - last access 28 oct 2024). QGIS offers many tools for data visualization, processing and analysis, making this software useful for researchers in many fields. Thanks to its API, its functionality can be extended by developing plugins in Python language. However, QGIS has not yet provided users with plugins or software that automatically performs SCA based on TBA methods. Considering the large number of users it has (de Oliveira Dias et al., 2024; Rosas-Chavoya et al., 2022), especially in the fields of coastal geomorphology, maritime hydraulic engineering, and other related disciplines (Hoptsii et al., 2023), there is a need to develop a rapid tool to perform all TBA-based shoreline change analyses.

With this in mind, Terres de Lima et al. (2021) presented the End Point Rate (EPR) tool for QGIS (EPR4Q), a tool integrated into the QGIS graphical modeler to calculate shoreline change using the end point rate method. However, this plugin allows only one of the metrics offered by the DSAS package to be calculated.

For these reasons, this research presents CDA (Coastal Dynamics Analyser), a QGIS plugin based on an automatic method for SCA with improvements in accuracy and speed. The new tool, written in PyQGIS, adopts the TBA described and presented by Manno et al., (2022b). CDA offers a range of features to process and analyse data from baselines and coastal transects, allowing the calculation of End Point Rate (EPR), Net Shoreline Movement (NSM), Shoreline Change Envelope (SCE) and Linear Regression Rate (LRR) metrics.

The CDA plugin represents an advance over the limitations highlighted for example in Albuquerque et al., (2013). The authors pointed out that the methodology adopted in DSAS, while showing good correlation between the data, had the drawback of using equidistant transects, which skipped some morphological features, such as ridges or depressions in the study area.

The newly developed CDA plugin distinguishes itself by incorporating the morphological characteristics of the beach, such as roughness and irregularity indices (M. J. Smith & Cromley, 2012), into the baseline creation process. Irregularity is defined as the ratio of the total number of minima and maxima in the shoreline position and the smoothed shoreline length. Consequently, roughness is defined as irregularity multiplied by the mean height of irregularities. For further information, see (Manno et al., 2022b). Using these parameters the plugin automatically calculates the threshold space between transects as the inverse of irregularity. This threshold value represents the upper limit of transects spacing.

This advanced feature provides a more comprehensive analysis compared to traditional tools like DSAS, which do not account for these morphological and shape crucial factors.

6.2 Description of the CDA plugin

The CDA plugin is easily installed using the QGIS plugin manager, either by downloading it online or installing it from a zipped file. The plugin can also be run as a Python script using the Processing Script Editor within the Processing Tools. The plugin builds on a set of QGIS algorithms and scientific libraries to provide a comprehensive and intuitive environment for coastal transect analysis.

The CDA plugin uniquely requires as input a linestring shapefile, which connects Ground Control Points (GCPs) to ensure the baseline passes through specific and critical points. In addition, it requires all desired shorelines for analysis as

separate shapefiles (one per shoreline), leveraging these inputs to account for beach morphological characteristics. Specifically, it allows the initial definition of a piecewise polynomial baseline to improve the accuracy in evaluating changes in shoreline position. The tool can also calculate new roughness and irregularity indices to define transect spacing relative to the polynomial baseline as reported in Manno et al., (2022b).

Then, using the baseline generated by the plugin or entered by the user, it will be possible to generate transects for shoreline advance/retreat analysis. The intersection analysis of transects with shorelines allows the generation of reports in .csv format and shapefiles of the most used metrics in DSAS, such as End Point Rate (EPR), Net Shoreline Movement (NSM), Shoreline Change Envelope (SCE), and Linear Regression Rate (LRR). The description of the indices just given is provided below in Equations 6.2.1, 6.2.2, 6.2.3 and 6.2.4.

Equation 6.2.1 – Shoreline Change Envelope equation

$$SCE = D_{max} - D_{min} \ [m]$$

Equation 6.2.2 – Net Shoreline Movement equation

$$NSM = D_y - D_o \ [m]$$

Equation 6.2.3 – End Point Rate equation

$$EPR = \frac{D}{T} \ \left[\frac{m}{time}\right]$$

Equation 6.2.4 – Linear Regression rate equation

$$y = mx + b \rightarrow LRR = m \ \left[\frac{m}{time}\right]$$

The *SCE* represents the maximum distance between the first and last shoreline positions over time. It is not a rate but a measure of total change. In Equation 6.2.1, D_{max} represents the maximum distance between all shorelines while D_{min} the minimum distance of all coastlines from the baseline.

NSM measures the net change of the shoreline over time, calculated as the difference between the final and initial positions. In Equation 6.2.2 D_y is the distance from the baseline of the most recent shoreline while D_o is the from the baseline of the older shoreline.

Instead, *EPR* calculates the rate of change between the two points of intersection of the generic transect and two shorelines by dividing the result by the elapsed time between the two locations. In fact, in Equation 6.2.3, *D* is the shoreline displacement distance between the "start" point and the "end" point whereas *T* is the time period between the two survey dates. In general, *EPR* is calculated as *NSM*/time.

Finally, the *LRR* calculates the rate of change using a linear regression on all available data points along the generic transect (all intersections between shorelines and the transect over time). It is defined by the slope of the regression line. In Equation 6.2.4, *y* represents the shoreline position on the generic transect, *x* is time, *m* represents the slope of the regression line (representing the *LRR* rate of change) and *b* is the intercept.

A visual explanation of all the presented parameters is shown in Figure 6.2.1.

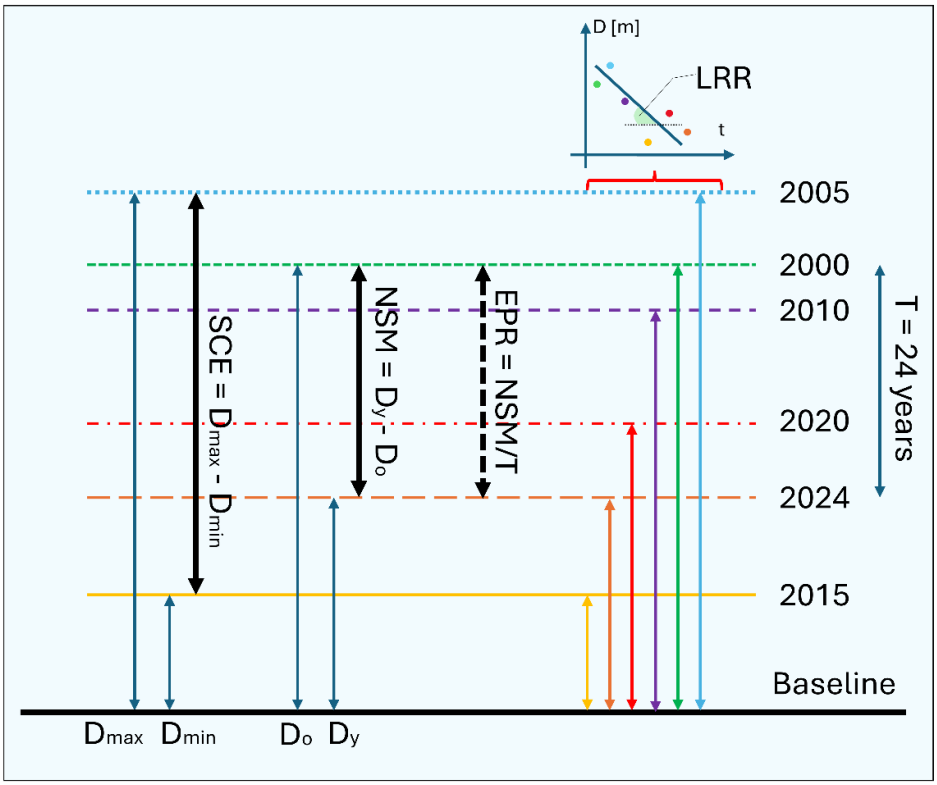

Figure 6.2.1 - Graphical explanation of SCE, NSM, EPR and LRR

The TBA approach, on which the plugin is based, has been validated both by synthetic benchmarks and in a case study (Manno et al., 2022b), providing interesting results in terms of accuracy and ease of use.

The CDA plugin delivers high-quality results at a remarkable speed, making it suitable for regional studies and directly providing the parameters needed for erosion management strategies.

6.3 Framework of CDA operation

The QGIS CDA plugin is structured to guide the user through various steps of analysing coastal dynamics. Each step in the process is detailed to automate specific tasks and use QGIS features effectively. Below is a summary of the main steps and implemented features:

Step 1: Main dialog box

- The code begins by importing the necessary libraries for QGIS and defining a dialog box (*NumberInputDialog*) that guides the user through the possible calculation steps of the plugin.

Step 2: Implementation of the NumberInputDialog class.

- **Window configuration**: T The dialogue box is configured with titles, layouts and elements such as information labels, text boxes for user input and buttons for interaction. This window represents the main GUI (*Graphical User Interface*) of the CDA plugin (Figure 6.3.1).
- **Event handling**: The on_ok_clicked function is defined to handles the "Run CDA" button click event, validate the user input and close the window if the input is valid.
- **User interface**: The interface includes formatted instructions for each step of the coastal dynamics analysis, helping the user to easily navigate through the process.

Step 3: Automating Analysis Processes (AA Steps)

- **AA = 0**: Creation of the baseline.
    - Selection of folders for input and output files.

    - Interpolation parameterization and creation of new points on the baseline.
    - Saving the results as shapefiles and adding them to the QGIS Table of Content (TOC).
- **AA = 1**: Calculation of transects.
    - Using QGIS tools to generate points along the baseline, transform them into paths, and create perpendicular transects.
    - Calculation of intersections between transects and shoreline for subsequent analysis.
- **AA = 2**: Selection and correction of transects.
    - Implementation of a custom dialog box for selecting transect layers to be corrected.
    - Using algorithms to automatically identify and correct transects with invalid or inconsistent lengths.
- **AA = 3**: Saving selected transects.
    - Export selected transects to a Comma-Separated Values (CSV) file for external analysis.
- **AA = 4**: Analysis of saved transect data for SCE and LRR calculation.
    - Statistical analysis of transect data to calculate rate of change and other parameters of interest (SCE and LRR).
    - Aggregation of results into a CSV file for further analysis.
- **AA = 5**: Clipping of transects for calculation of NSM and EPR.
    - Algorithm for calculating the distance expressed in meters between the oldest and youngest shoreline and then (NSM) and then the 'EPR which is obtained from the ratio of the NSM divided by the time that has elapsed in detection between the two shorelines.

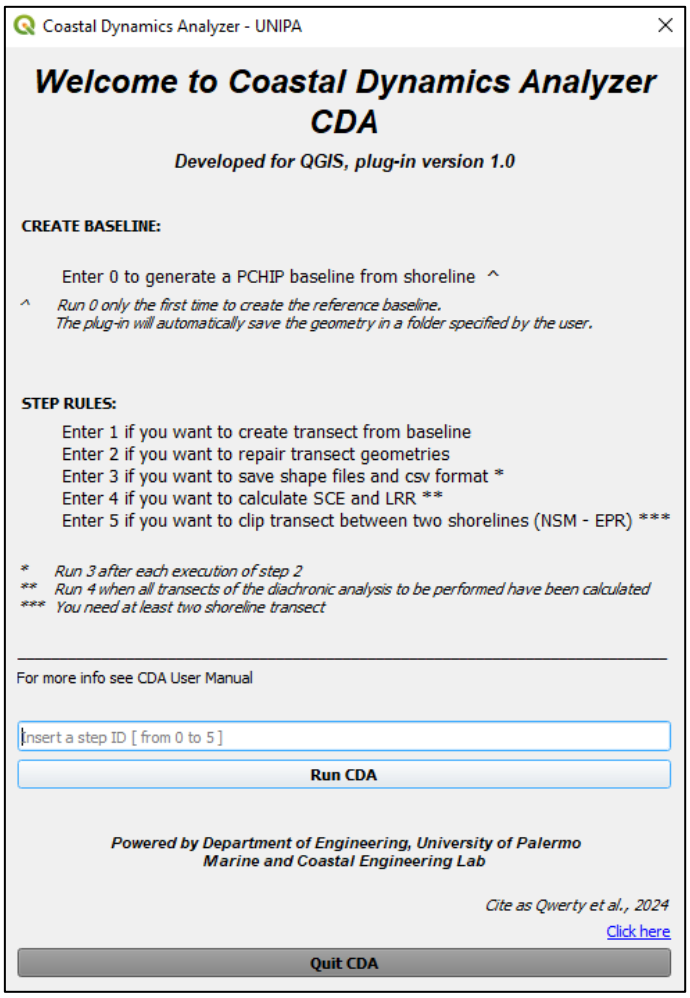

Figure 6.3.1 - Main GUI of CDA. From this window shown, all AA steps can be accessed by entering their respective identifier. The window notes explain to the user how and when to use the generic step. The Run CDA button allows steps to be executed only if a valid step (between 0 and 5) is entered. The link in the lower right hand corner redirects to the plugin web page where the documentation and related manuscript can be downloaded.

In addition, each step of the CDA plugin is meticulously designed to integrate seamlessly with QGIS, utilizing its API (*Application Programming Interface*)

and processing tools. The user interface is thoughtfully crafted to provide clear instructions and relevant information, guiding the user through the various steps of the analysis. Additionally, the code incorporates robust validation mechanisms to ensure that user inputs are accurate, providing appropriate feedback in case of errors. This approach not only simplifies the coastal dynamics analysis process but also illustrates how QGIS can be extended via plugins to automate complex geoprocessing and data analysis tasks. More information on the operations performed specifically by each step can be found in Supplementary Materials in which user guide manual is presented.

6.4 Application to a case study and results

The application area of the plugin is the beach of Eraclea Minoa (Figure 6.4.1) located along the southern coast of Sicily (south Italy). This area has already been analyzed by Manno et al. (2022b), who provided a detailed description in their study on diachronic analysis methodology, from which the plugin takes its cue.

According to Manno et al. (2022b), Eraclea Minoa beach has experienced significant shoreline retreat since 1989. The beach, 5605 meters long, is bordered to the north by the promontory of Capo Bianco and to the south by the promontory of Torre Salsa, both in protected natural areas. Capo Bianco, with a cliff about 30 meters high, is home to the archaeological site of Eraclea Minoa, while Torre Salsa, about 20 meters high, is characterised by the presence of the 16th-century tower of the same name.

The coastal area belongs to the Sicilian Physiographic Unit No. 11 and has no coastal defense structures or ports. North of Capo Bianco, the mouth of the Platani River, with a basin of 1,784 km², has a reduced sediment flow due to various river structures (for more information on the spatial setting see Manno et al., 2022b). The prevailing littoral current has a NW-SE direction. At the base of the marly cliff, a narrow beach about 3 meters wide and 600 meters long is interrupted by boulders. The cliff is connected to the beach by clastic deposits. Towards the south-east the beach of Heraclea has a slope of about 5°, behind which there is a retreating pine forest. The beach ends with the promontory of Torre Salsa, at the base of which is a small beach about 20 meters wide, exposed to SE and W-NW swells.

Figure 6.4.1 - Map showing the input baseline and PCHIP baseline generated by CDA for the shoreline change analysis in Eraclea Beach and Bovo Marina. The yellow line represents the input baseline, while the red line indicates the Piecewise Cubic Hermite Interpolating Polynomial (PCHIP) baseline. Ground Control Points (GCPs) are marked with black and white dots. The images on the right provide detailed views of two stretches of beach where the differences between the PCHIP baseline and the input baseline with GCPs can be appreciated. Bottom left subplot shows the beach setting in Sicily region (south Italy).

For the case study under consideration, the roughness coefficient was found to be 1.98 while the irregularity was 0.11.

The tool described in this work was used to develop the SCA analysis of the sandy beach in the study area. Initially, a GIS project is created in which to insert all the coastlines to be analysed and a linear type layer that joins the control points for baseline construction. This last layer can be a break joining the aforementioned points.

The shorelines used cover the period from 1989 to 2020 and are the same as those used by Manno et al., (2022b). Moreover, the shorelines proxy used was the wet/dry boundary as defined by Boak and Turner, (Boak & Turner, 2005c).

Next, starting the plugin and running Step 0 from the main GUI automatically generates the PCHIP baseline related to the input required layer (the GCP baseline union line type layer of Ground Control Points).

The baseline thus generated is automatically loaded into the Table of Content (TOC) of QGIS and saved in a folder chosen by the user during execution. It should be specified that, to obtain an optimal baseline result, the plugin will ask the user to also select the folder where all the shorelines to be analysed are located. This condition was included to generate a PCHIP spline that is as concordant as possible with the roughness variations of all shorelines and to allow transect generation as perpendicular as possible for all shorelines. More details are reported in Manno et al., (2022b).

The second step is to start step 1 from the CDA GUI that allows transect generation via the *CDA - Calc_Transect* algorithm by entering as input the baseline layer (obtained from step 0), the date of shoreline acquisition, the shoreline layer (one shapefile per shoreline), the transect length, the resolution (transect-transect interdistance) and the side of the baseline on which to generate transects.

The process can be run serially to generate transects associated with each shoreline by filling in the input dialogue box only once in Figure 6.4.2.

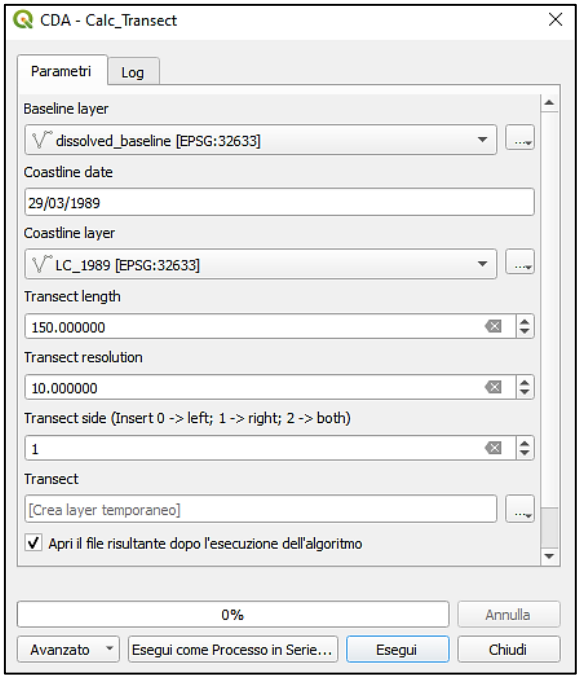

Figure 6.4.2 - Screenshot of the CDA algorithm - Calc_Transect of the CDA plugin (Step 1). Calculation of transects from the baseline for each shoreline in QGIS. Parameters set include baseline, shoreline date, shoreline layer, transect length, transect resolution, transect side, and option to open the resulting file after running the algorithm.

In the present case, 515 transects with an average resolution of 10 m (according to an irregularity of 0.11) were generated for each shoreline. Each transect has as its start point a point belonging to the baseline and as its end point the intersection of the transect with the generic shoreline.

The next step is to start Step 2. At this point, a window is opened that allows the user to select (flag) in the TOC the shapefiles of the transects to be repaired. The term “repair” indicates that the plugin will select the correct transects, i.e., those whose extremes are the green stars in Figure 6.4.3. These errors occur in transects when sand spit or folding of shorelines back on themselves are present in the shorelines.

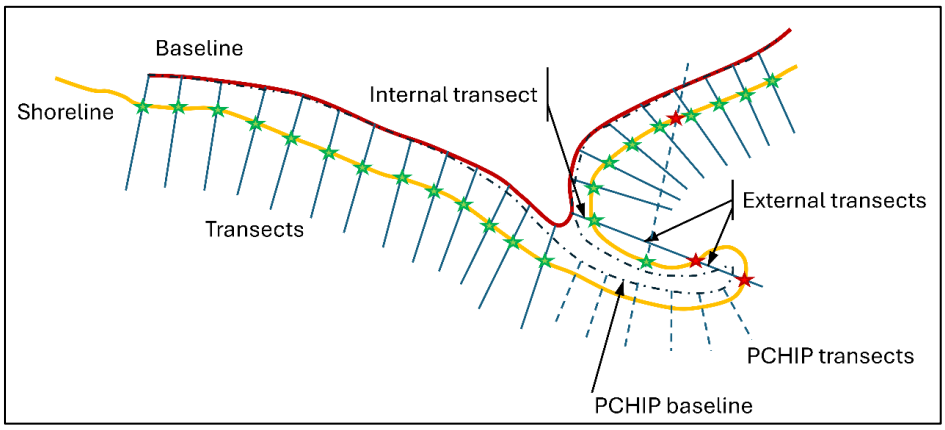

Figure 6.4.3 - The image depicts a diagram illustrating the process of selecting transects for repair in the context of shoreline analysis. The diagram shows a baseline and a shoreline with several transects extending from the baseline (land side) to the shoreline. The green stars represent the correct transect-shoreline intersection while the red stars represent the incorrect transect-shoreline intersection.

The user then can start step 2, and the plugin will automatically select all the correct transects - i.e., those that cross the green stars. If the red and green star conditions shown in Figure 6.4.3 do not occur during the analysis, this means that all the transects are already “correct”, and the plugin will simply select all starting transects, since they are found to be already correct and valid. Next, the user can start step 3, and the plugin will ask at this point to select the folders where to save the corrected transects in CSV and shapefile formats. It is important to note that the transects that cross the green stars are those that start from the baseline and first meet the shoreline. Subsequent intersections of the same transect are not considered. The same reasoning is applied by the plugin if the baseline is drawn on the land side. In either case, the user can choose to perform TBA on all transects (internal and external) and thus bypass step 2 or to repair them. In this case study, there were no transects to repair.

At this point, once the plugin has saved the csv and shapefiles of the transects in appropriate folders, the user can continue by starting step 4 from the CDA GUI. In this case, the user only needs to select the folder where the csv files were saved in the previous step. The algorithm will automatically calculate the SCE and LRR

for each transect in relation to all shorelines on the same csv and shapefiles. It is important to note that the user can only proceed to step 4 once all transects have been calculated relative to each shoreline.

Figure 6.4.4 reports the results of SCE and LRR for the Eraclea Minoa case study. Transect are labelled from 1 to 515 respectively starting from Capo Bianco to Torre Salsa (Figure 6.4.1).

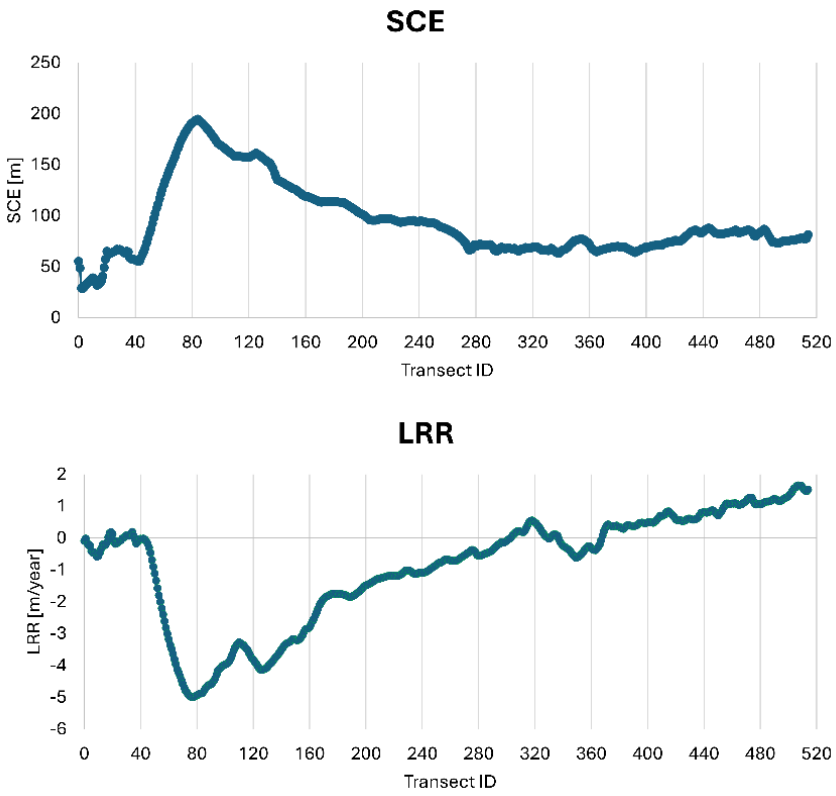

Figure 6.4.4 - SCE and LRR results for Eraclea Minoa Beach. In x axis are reported the transect number ID, in y-axis the SCE and LRR respectively for the top and bottom subplots.

The first row (top) of Figure 6.4.4 shows the trend of SCE along ID transects. The values of the SCE vary from around 0 m to over 190 m. A significant peak is observed between transects 60 and 100, where the SCE reaches maximum values around 190 m, indicating a higher variability in shoreline position in that

area. Thereafter, the SCE tends to decrease gradually, stabilizing around 50-100 m for transects beyond 200.

The bottom row of Figure 6.4.4 shows the trend of LRR. The LRR values vary from about -5 m/year to +1.9 m/year. An initial negative trend (up to -5 m/year) is observed between transects 0 and 80, a sign of significant erosion in this area. Thereafter, a reversal of the trend is observed with LRR values increasing, reaching up to +1.9 m/year towards transects over 400, indicating an advancement of the shoreline or otherwise a reduction in erosion.

The final step to complete the diachronic analysis is to start Step 5 from the CDA GUI. In this case, the user will see the data input window of the CDA algorithm - TRANSECT_Clip, shown in Figure 6.4.5.

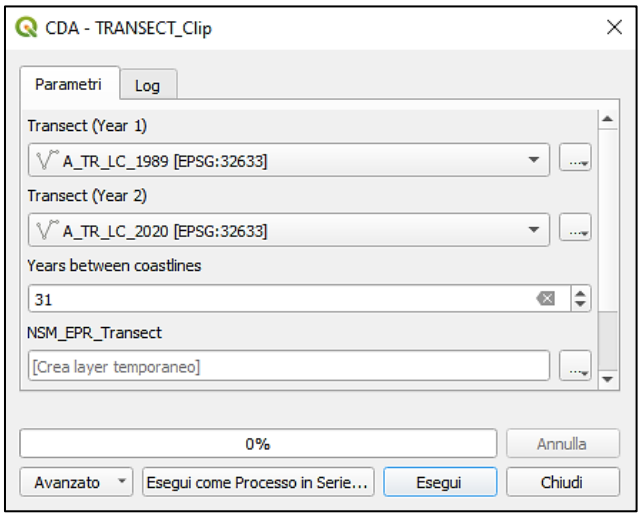

Figure 6.4.5 - CDA algorithm screenshot - TRANSECT_Clip (Step 5). The window allows the user to select the two transect layers for which the SCE and EPR metrics are to be calculated and to enter the elapsed time between the two transect reference shorelines.

The inputs to be entered are the transect referenced at time T1, and the transects at time T2 with T1<T2. Another input parameter is the time elapsed between the two transect layers and thus between the two connected shoreline acquisitions. Again, the algorithm can be run serially (in batch) for all pairs of transects to be

analysed in order to speed up the process and facilitate handling a large number of transects to be processed.

The plugin outputs shapefiles contain the attribute table where the calculations of the NSM and EPR indices are stored. The results are shown in Figure 6.4.6 (NSM) and Figure 8 (EPR).

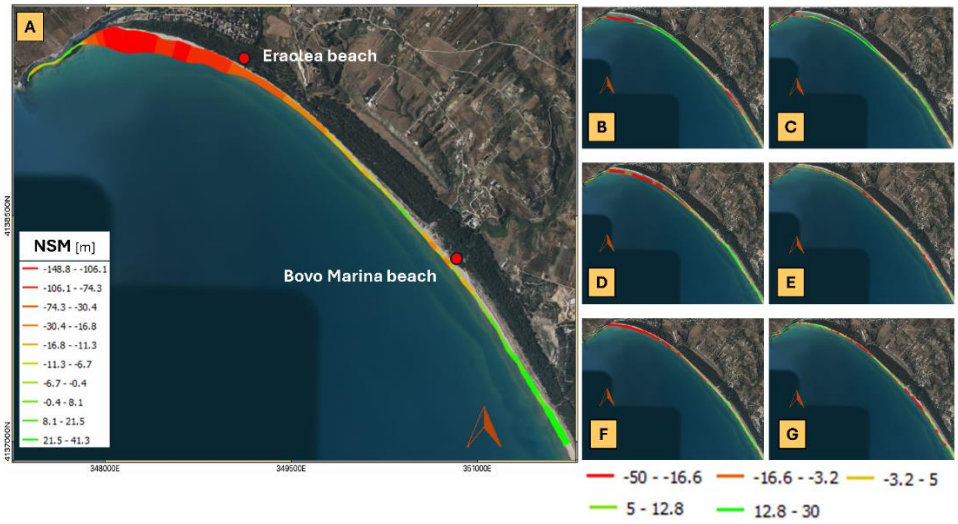

Figure 6.4.6 - Maps showing the results of the NSM metrics for the study area. Subplot A shows the calculated NSM for the 1989 and 2020 shorelines. Subplots B through G show the results of the same metric for 1989-1997, 1997-1998, 1998-2005, 2005-2010, 2010-2019 and 2019-2020, respectively.

The transects in Figure 6.4.6 have been colored according to the degree of erosion or accretion. In particular, the areas in red and orange show severe erosion, with NSM values ranging from -148.8 m to -16.8 m. The northern area of Heraclea Beach appears to be particularly prone to severe erosion. Areas in yellow and green indicate less erosion or even accretion, with NSM values ranging from -16.8 m to +41.3 m. The Bovo Marina Beach area shows signs of accretion, especially in the terminal part.

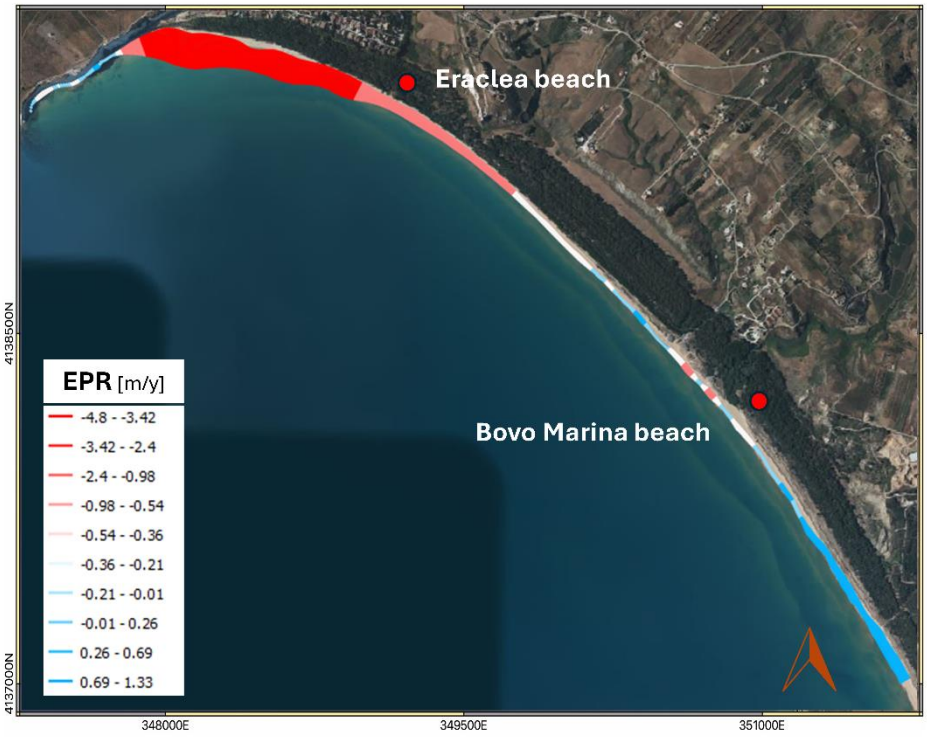

Figure 6.4.7 - Map showing EPR results for shorelines 1989-2020 thus considering T = 31 years.

In Figure 6.4.7, the areas in dark red show significant erosion rates, with EPR values ranging from -4.8 m/yr to -3.42 m/yr, particularly evident in the northern area of Heraclea Beach. Areas in blue and light blue represent shoreline stability or advancement, with EPR values ranging from -0.01 m/yr to +1.33 m/yr, most prevalent near Bovo Marina Beach.

The results obtained from the CDA framework are consistent with those described in (Manno et al., 2022b). Indeed, there is strong agreement between the numerical data obtained in Manno et al., (Manno et al., 2022b) and the results produced by the CDA, confirming the validity of the results obtained from the plugin. The quantitative comparison of the two results is shown in Table 6.4-1. Minor discrepancies can be attributed to differences in rounding or interpolation. Thus, both research confirm that the studied beach is subject to significant

erosion, with high values of shoreline retreat, and that the area has undergone large surface changes over time.

Table 6.4-1 - Comparison between results obtained by Manno et al., (2022) procedure and CDA plugin

Parameter	***Manno et al., 2022***	**CDA**
Minimum NSM	-149 m	-148.8 m
Maximum NSM	+41 m	+41.3 m
Minimum LRR	- 4.9 m/year	- 5 m/year
Maximum LRR	+1.8 m/year	+1.9 m/year
Maximum EPR	+1.4 m/year	+1.3 m/year
Minimum EPR	-4.8 m/year	-4.8 m/year
Maximum SCE	170 m	190 m

In addition, the plugin returned the output(s) of each Step on average in 5 seconds. The times mentioned refer to the shoreline section examined with the resolution already discussed (10 m). The plugin was run on a version of QGIS 3.34.32 Prizren on an Intel(R) N95 1.70 GHz, 16.0 GB RAM V23H2 computer with a 64-bit operating system.

6.5 Impact and application

The CDA plugin has the potential to become a valuable tool for the scientific community, industry professionals, and coastal managers.

Its versatility covers a range of critical tasks, making it essential for monitoring coastal change over time, identifying areas at risk of erosion, and evaluating the effectiveness of mitigation measures.

One of the most important applications of the CDA plugin is its ability to comprehensively assess shoreline change. This includes the analysis of long-term shoreline evolution, which is critical for understanding the dynamics of coastal environments. By utilizing CDA, users can evaluate how coastlines have moved

over time, helping to predict future changes and identify regions that are particularly vulnerable to erosion or accretion (Uda, 2022).

Moreover, CDA proves to be instrumental in assessing the effects of coastal structures on shoreline morphology. Coastal infrastructure, including revetments, seawalls, groynes, and breakwaters, can significantly alter natural sediment transport processes, leading to patterns of erosion and accretion (Sanitwong-Na-Ayutthaya et al., 2022).

Ports and other large-scale coastal developments also present challenges and opportunities for shoreline management, as they can drastically affect coastal hydrodynamics and sediment distribution. The CDA plugin can be employed to study these impacts, facilitating the design of more sustainable port infrastructure and the mitigation of negative effects on surrounding shorelines. An example of this application is illustrated in recent research on the interaction between port structures and coastal erosion by Miranda et al., (2023), where the tool could be used to assess the long-term consequences of such developments.

Additionally, CDA is invaluable in the context of climate change adaptation. As sea levels rise and extreme weather events become more frequent, the plugin can aid in the planning of adaptive strategies that protect coastal areas from the increasing threats posed by climate change. By providing detailed analyses of shoreline behavior and the effectiveness of various interventions, CDA supports the development of resilient coastal management plans.

In summary, the CDA plugin is not just a tool for analyzing current shoreline conditions, but a comprehensive solution for a wide array of coastal management challenges. Its applications in assessing shoreline change, the impacts of coastal structures, and the effects of large-scale developments like ports demonstrate its utility in preserving and managing coastal environments in the face of both human-induced and natural changes. By leveraging the capabilities of CDA, stakeholders can make informed decisions that safeguard coastal regions for future generations.

6.6 Conclusion

The Coastal Dynamics Analyser (CDA) is a plugin for QGIS designed to provide versatile and intuitive analysis of coastal changes, focusing on key metrics such as End Point Rate (EPR), Net Shoreline Movement (NSM), Shoreline Change Envelope (SCE) and Linear Regression Rate (LRR). The adoption of transect-

based methods (TBA) makes CDA a powerful and accurate tool for assessing coastal dynamics.

The CDA plugin is an efficient and accurate solution for coastal change analysis, using the already widely discussed and validated methodology proposed by Manno et al 2022. Its functionalities allow the processing, analysis and visualisation of coastal transect data, providing fundamental information for understanding erosion processes and planning mitigation and adaptation measures. The ability to produce high-quality results with remarkable speed makes CDA particularly suitable for regional studies. The CDA plugin is currently under development and may undergo further enhancements. For more information and to download the plugin, you can visit the project website at the links provided in the *Code metadata* and *Software metadata* sections.

Upcoming versions of the plugin are expected to include the ability to calculate other analysis metrics (such as the Weighted Linear Regression Rate WLR) and to implement Area Based Analysis (ABA).

In summary, CDA offers a robust and affordable open-source alternative to traditional methods, thus supporting a wide range of coastal management studies and interventions.

Chapter VII

This chapter presents a new modelling approach for predicting coastal evolution. After analysing the limitations of currently available models and identifying the need for a balance between accuracy and computational efficiency, an innovative model, called COAST-PRO$_{SIM}$, is introduced that aims to improve the simulation capability of coastal dynamics. This model integrates several physical variables and interactions with defense works, offering an advanced solution for the study and management of coastal areas.

The topics and contents covered in the following chapter are taken from a conference abstract (Scala et al., 2024b) and part of the same chapter, as of the date of writing this thesis, is published as a scientific article to the journal Water, MDPI as Scala et al., (2025).

7.1 A new modeling approach for predicting shoreline movements

By this point in the thesis it is well known that shoreline evolution is a complex phenomenon, influenced by a wide range of physical processes acting on different temporal and spatial scales. Among these, sediment transport, wave action, currents, and interaction with coastal defense structures play a central role. Due to the non-linear and interconnected nature of these processes, there is still no comprehensive model that can accurately predict long-term coastal evolution (Alvarez-Cuesta et al., 2021; Toimil et al., 2020).

The currently available models analyzed in Section 2.5 for studying coastal evolution have significant limitations. On the one hand, detailed physical models manage to accurately capture local processes, but they require high computational resources and are often applicable only on a small scale. On the other hand, simplified models, based on empirical approaches or parameterizations of the physics of phenomena, require careful calibration to obtain reliable results, with the risk of losing the ability to represent the real complexity of the coastal system (Armenio et al., 2017).

This dichotomy between detailed but onerous models and simplified but potentially less accurate models has driven research toward the development of new approaches that can balance accuracy and efficiency. A key aspect of improving coastal evolution modeling is to integrate knowledge of local physical processes with techniques that allow consideration of the spatial and temporal

variability of the littoral system, without neglecting the impact of anthropogenic defense structures, such as breakwaters and groynes (Camus et al., 2014).

In response to these needs, the COAST-PRO$_{SIM}$ model, developed by the Department of Engineering of the University of Palermo, Coastal and Maritime Engineering Lab, was born. Officially presented at the XXXIX National Conference on Hydraulics and Hydraulic Engineering (IDRA) in September 2024 (Scala et al., 2024), the model is proposed as an integrated solution for the analysis and prediction of coastal dynamics. COAST-PRO$_{SIM}$ stands out for by its ability to combine the two-dimensional resolution of wave propagation and shoreline evolution, thus optimising the simulation of the effects of coastal protection works with reduced computation time.

The model requires wave height, direction and period data as input, and simulates the response effects of the coastline in relation to coastal protection works. In particular, the model can simulate the presence of one or more breakwaters, one or more groins, or the response of the shoreline following beach nourishment interventions, whether protected or not[4]. As an output, the model returns the evolution of the shoreline for each time interval, with limited computational time.

The model is based on two resolution processes:

1) a wave propagation routine to the shoreline using as input data obtained from a wave transformation module that exploits hybrid (statistical-numerical) propagation of the nearshore zone (Camus et al., 2013a).

2) a multi-process shoreline evolution equation that considers longshore and cross-shore contributions by accounting for the effects of coastal defense structures on the beach.

[4] Protected beach nourishment also involves the construction of coastal defence structures, such as breakwaters or groins, to protect the new sediments added by nourishment from erosion and increase the long-term stability of the beach.

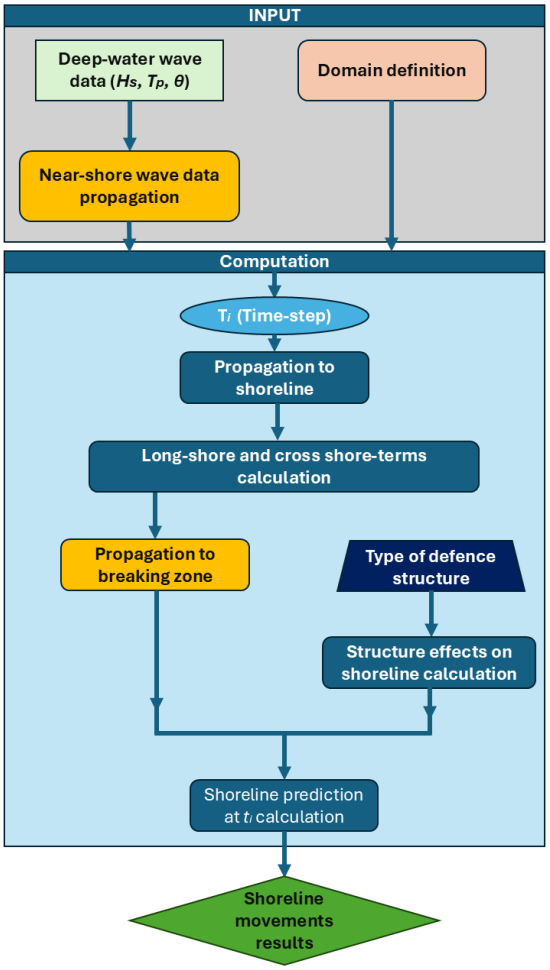

Figure 7.1.1 - COAST-PRO$_{SIM}$ model flowchart

In Figure 7.1.1 is presented the flowchart of the COAST-PRO$_{SIM}$ which highlights the steps that make up the execution and operational framework of the model.

The first step is to collect all the necessary inputs in the study area, such as bathymetry, sediment characteristics, shoreline observations, sediment exchange at the ends of the study area, and the schematisation of existing anthropogenic works. Once the input data has been collected, the calculation domain is defined, which consists of a computational grid for wave propagation in the near-shore

area and the discretization of the coastline based on transects, the number of which depends on the domain used and the desired resolution. Since the model does not compute propagation from offshore to the sub-coast, the data to be provided as input to the model were obtained through the nearshore hybrid downscaling technique (Camus et al., 2013b) which exploits SWAN propagation of spectral wave data. In order to exploit this method, marine magnitude data of significant wave height H_s, wave direction with respect to the shoreline θ and peak period T_p downloaded from the CMEMS database or nowadays CMS (Copernicus Marine Service) were used. The results are then propagated from COAST-PRO_{SIM} to the shoreline to solve the shoreline evolution equation.

In particular, the COAST-PROSIM model requires a set of input parameters that are fundamental for the accurate simulation of the shoreline evolution. Among these, the time series of wave motion characteristics output to the downscaling play a central role. These parameters must be provided as time series with hourly resolution, thus determining the simulation period: for example, twenty years of hourly data allow simulating a coastal evolution over an equivalent period. A second set of parameters concerns the initial morphological characteristics of the domain. The position of the shoreline is represented by a vector describing its initial configuration along the coastal domain, while a further vector indicates the slopes of the transects orthogonal to the shoreline. These slopes are calculated between the initial position of the shoreline and the closure depth, assuming that, in the propagation zone, the bathymetric lines are approximately parallel to the shoreline [71]. This hypothesis, supported by Snell's law (see section 2.2.2), links morphological changes to wave propagation, with the translation of the coastal profile indirectly represented by the variable orientation of the shoreline over time. To these parameters are added the median value of the sediment diameter (D_{50}), the closure depth (h_c) value, which is calculated by the model once the H_s time series data has been entered) and a vector of the berm height for each transect. Moreover, the hypothesis of the model is that sediment transport along the coast occurs up to the closure depth and no further.

For each structure to be simulated, it is necessary to specify the type, the position with respect to the shoreline, as well as the geometric characteristics such as length, height and, in the case of multiple configurations, the distance between the structures. Finally, it is necessary to indicate the values of solid flow entering or leaving the domain that will represent the rates of retreat or growth of the shoreline not due to wave-beach interaction (e.g. sediment sampling or inlets from basins) which is added or subtracted homogeneously over the entire domain.

The model offers flexibility in the output of results, allowing to choose between hourly, daily or monthly time resolutions. This feature makes the model suitable for simulations ranging from short-term studies to coastal evolution scenarios over periods of several decades.

COAST-PRO$_{SIM}$ utilizes a temporal discretization based on explicit methods that balance accuracy and computational stability, ensuring rapid convergence. The staggered spatial grid is defined on a domain divided by transects, allowing the integration of cross-shore and longshore processes. To solve the governing equations, the model adopts an explicit forward scheme for time and a finite difference scheme for spatial discretization.

The stability of the model is ensured by respecting the Courant-Friedrichs-Lewy (CFL) criterion, calculated as follow (Equation 7.1.1).

Equation 7.1.1 – Model stability, Courant condition

$$C = \frac{\Delta t}{h_c \, \Delta x^2} \cdot Q \leq 1$$

Where Δt represents the time step, Δx the spatial resolution between transects, and Q is the solid transport rate. This approach reduces calculation time while maintaining the accuracy required for engineering analysis.

7.2 Solving equation

The evolution equation of the multi-process coastline of the COAST-PRO$_{SIM}$ (Equation 7.2.1) considers the two components of long-shore and cross-shore coastal transport:

Equation 7.2.1 - Solving equation for the COAST-PRO$_{SIM}$ model

$$\frac{\partial Y_U}{\partial t} = \frac{\partial Y_{U1}}{\partial t} \pm \frac{\partial Y_{U2}}{\partial t} \pm \rho'$$

Y_U represents the shoreline displacement due to total transport (m) the derivative represents its temporal variation that depends on parameters that also vary spatially. Y_{U1} represents the shoreline displacement due to long-shore transport (m). Y_{U2} represents the shoreline displacement due to cross-shore transport (m). *t*

is the time (i.e. days) and ρ' represents the terms of loss and gain of sediment to and from the outside.

The numerical stability of the equation is guaranteed if the space between transects is less than half the shortest wavelength as suggested by (Alvarez-Cuesta et al., 2021).

7.3 How does COAST-PRO$_{SIM}$ model phenomena affecting propagation from offshore to near-shore

The main phenomena associated with wave motion during its propagation, schematised in Figure 7.3.1, are: shoaling, refraction, diffraction, breaking and reflection.

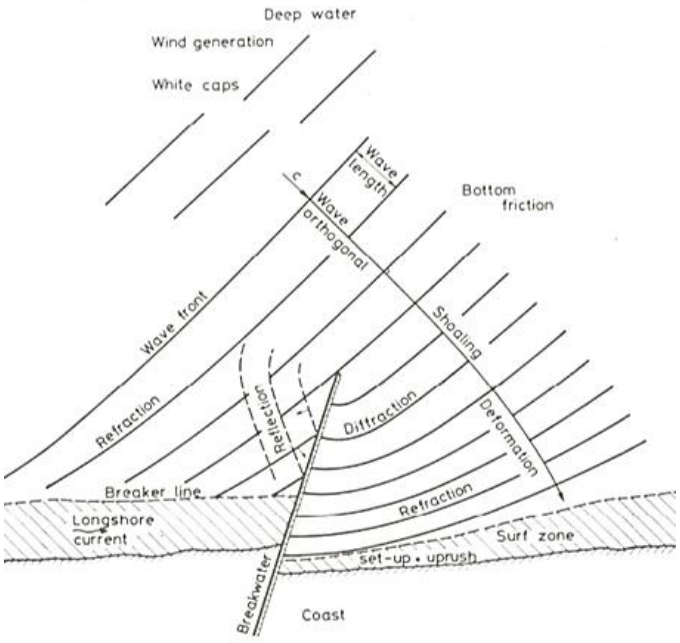

Figure 7.3.1 - Wave propagation phenomena (Svendsen 1976)

7.3.1 Shoaling

As already discussed in section 2.3.3, shoaling consists of an increase in the steepness of the wave due to the change in the depth of the seabed as it propagates from offshore towards the coast. And since the principle of conservation of

energy applies, a change in depth of the seabed corresponds to a change in wave height (Petti, 2021). The proposed model considers linear shoaling, which is a simplified approach to describe this phenomenon. In linear shoaling it is assumed that the wave energy is conserved and evenly distributed as the wave approaches the shore, resulting in a gradual and predictable increase in wave height in proportion to the decrease in water depth.

7.3.2 Refraction

Refraction (Figure 7.3.2)occurs when the wave rays propagating towards the shore form a non-zero angle with the perpendicular to the bathymetrics (i.e. they have an oblique attack). This causes the wavefronts to rotate as they move from deep to shallow water and causes them to lie parallel to the bathymetrics and the shoreline. This effect occurs because in the same wave front there are different depths and therefore different celerities; less as the seabed interacts with the wave (Foti, 2006; Petti, 2021).

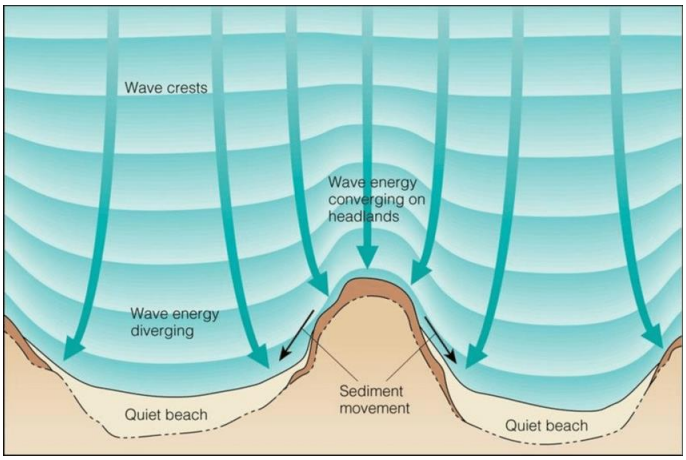

Figure 7.3.2 - Effects of refraction (Garrison, 2005)

To study refraction, the COAST-PRO$_{SIM}$ uses the simplified one-dimensional Snell treatment given in Equation 7.3.1 and the principle of conservation of wave energy along the wave rays (the lines along which waves propagate).

Equation 7.3.1 – Snell's refraction law

$$\frac{\sin\theta_b}{L_b} = \frac{\sin\theta_0}{L_0}$$

In which:

- θ_b e L_b are the angle and wave height at the break (m);
- θ_0 e L_0 are the angle and wave height offshore in deep water (m).

7.3.3 Diffraction

Diffraction is a phenomenon that occurs when sea waves encounter an obstacle, such as a reef, cliff, island or man-made structure. This obstacle causes a change in the direction and shape of the waves. Diffraction manifests itself as the ability of waves to bypass the obstacle and propagate laterally behind it, creating new wave fronts. When a wave crosses an obstacle, part of the wave energy is reflected, while another portion passes through the obstacle if it is partially permeable. In addition, some of the energy is diffracted, redistributing itself around the obstacle and curving the waves behind it. This phenomenon changes the wave regime behind the obstacle, making them weaker and less high than the direct waves, creating an area of relative calm. The diffracted waves form new fronts that can interfere with each other, leading to changes in the wave pattern and redistributing energy along an arc behind the obstacle. This can reduce erosion in some coastal areas and increase it in others.

Understanding diffraction is fundamental to designing harbours, jetties, breakwaters and other coastal structures. These structures must be correctly positioned and sized to minimise coastal erosion and protect beaches. Furthermore, diffraction affects the distribution of sediments along the coast, and thus the morphology of the beach. Knowing how waves spread behind an obstacle helps predict areas of accumulation or erosion, contributing to the protection of coastal infrastructure from wave force, especially in areas where wave energy can be reduced through natural or artificial obstacles (Foti, 2006; Petti, 2021).

The diffraction theory of wave motion can be studied with the Huygens principle, which can be seen in Figure 7.3.3: each wavefront point can be considered as the source of a small hemispherical wave propagating in the half-space forwards.

In Figure 7.3.4 examples of diffraction behind defence works can be seen.

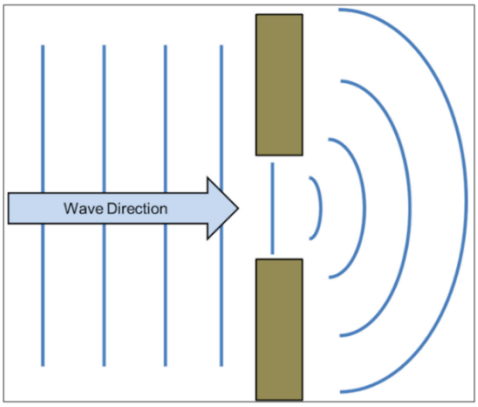

Figure 7.3.3 - Effects of diffraction on waves through an obstacle.

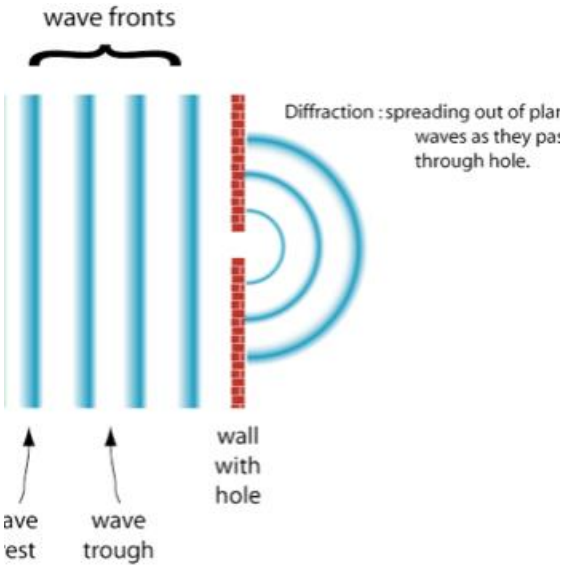

Figure 7.3.4 - Examples of diffraction using the Huygens principle. At the top the effect of a single barrier and at the bottom the effect of a barrier that is part of a series of barriers (Petti, 2021).

The COAST-PRO$_{SIM}$ uses empirical Kamphius diffraction laws to correct for breaking properties in the presence of detached groins and breakwaters. It also considers morphological changes influenced by wave propagation, which is controlled by the orientation of the shoreline, which varies over time and

influences refraction according to Snell's law in Equation 7.3.1. Consequently, the translation of the profile is indirectly explained by the evolution of the shoreline orientation.

Equation 7.3.2 – Transformation of significant wave height during propagation to nearshore

$$H_{s(b)} = H_s \sqrt{\frac{\cos(\theta_0)}{\cos(\theta_b)}} \sqrt{\frac{C_g}{\sqrt{g\ h_b}}}$$

In which:

- $H_{s(b)}$ is the transformed significant wave height (m);
- H_s is the significant wave height before transformation (m);
- θ_b is the wave angle at the break obtained from Snell's Law in Equation 7.3.1;
- θ_0 is the wave angle offshore in deep water;
- C_g is the group celerity (m/s) calculated as in Equation 7.3.3:

Equation 7.3.3 – Group celerity equation

$$C_g = 0.5\ C\ \left(1 + \frac{2kh}{\sinh(2kh)}\right)$$

In which:

- C is the celerity of the wave (m/s);
- h is the local depth (m);
- k is the wave number (m^{-1}) equal to $\frac{2\pi}{L}$ with L wavelength (m).

The formula for wave height diffraction at breakthrough, proposed by Kamphuis (2000) is given by the Equation 7.3.4:

Equation 7.3.4 - Kamphuis (2000) diffraction formula

$$H'_{s(b)} = \sigma_d\ H_{s(b)}$$

Where the diffraction coefficient σ_d is determined by the angle of attack θ and can be calculated using two different formulations depending on the value of θ. In particular, in Equation 7.3.5 the formulation for $-90 < \theta < 0$ and in Equation 7.3.6 that for $0 < \theta < \theta_r$ where θ_r is the maximum angle of diffraction:

Equation 7.3.5 - Value of the diffraction coefficient valid for -90 < θ < 0

$$\sigma_d = 0.71 - 0.0093\,\theta + 0.000025\theta^2$$

Equation 7.3.6 - Value of the diffraction coefficient valid for 0 < θ < θr

$$\sigma_d = 0.71 + 0.29\,\left[\sin\left(90\frac{\theta}{\theta_r}\right)\right]$$

That is, using the equations proposed by Kamphuis (2000), it is possible to calculate the height of the diffracted wave taking into account the angle of attack of the waves. This helps to predict the effectiveness of coastal defence works in reducing wave energy and protecting the coast from erosion.

7.3.4 Breaking

As already extensively discussed in the 2.3.3 section, *Breaking* occurs when the waves due to shoaling or refraction reach a critical height with a certain steepness, destabilise and lose their shape by breaking, with a more or less violent dissipation of energy, accompanied by strong turbulence and possible foam formation (Figure 7.3.5).

Let us briefly review the classification of breaking already discussed in Chapter II, adding some more information.

The breaking can have different effects depending on the slope of the seabed and the characteristics of the wave. Through the Iribarren parameter (Equation 7.3.7) the different types of breaking are identified.

Equation 7.3.7 – Iribarren parameter for different types of breaking

$$\beta = \frac{s}{\sqrt{\frac{Hb}{L0}}}$$

In which:

- *s* is the slope of the seabed;
- *Hb* is the wave height at the breaking (m);
- *L0* is the offshore wavelength (m).

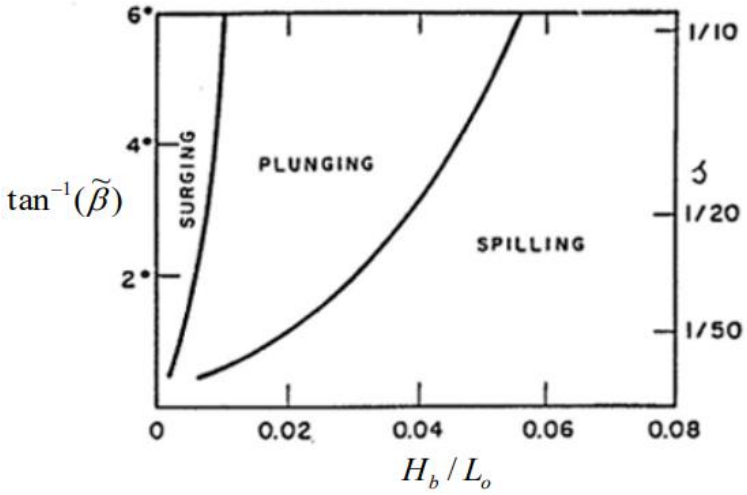

Figure 7.3.5 - Types of Iribarren's parameter fringing.

In particular, for:

- $\beta < 0.4$ *Spilling-type* breaker, characterised by a wave with a symmetrical crest. It presents foam on the side of the crest on the side of the wave propagation direction. It is found in horizontal or gently sloping bottoms and at wavelengths typical of the Mediterranean;
- $0.4 < \beta < 2.0$ *Plunging* type breaking, characterised by waves with a non-symmetrical crest with the presence of a 'jet' and a subsequent 'fall' on the side of the direction of wave propagation. It can be found in medium slope bottoms, waves of intermediate length and strong littoral currents;
- $\beta > 2.0$ *surging*, characterised by waves that cause the water surface to rise before breaking. It can be found in steeply sloping bottoms and very long waves.

In the COAST-PRO$_{SIM}$ a constant depth-induced breaking index of 0.78 was assumed according to Laitone's criterion (Petti, 2021).

7.3.5 Reflection

Wave reflection is a phenomenon that occurs when a wave train encounters a vertical obstacle, such as a steep cliff emerging from deep water or the wall of a pier. In this process, the waves reflect back on themselves with a modest loss of energy. When the period of the waves is regular, a standing wave system can be formed.

This process not only affects the morphology of the seabed but also the distribution of sediments. Reflection can increase erosion near the base of the obstacle, as refracted wave energy is concentrated in this area, thus causing an increase in wave height, pressure and causing resonances in closed basins (Foti, 2006; Petti, 2021). In the COAST-PRO$_{SIM}$ the effects of wave reflection were considered negligible.

7.4 Solid transport module

Normally, a beach is made up of sediments of various grain sizes, from the finest sands to gravel. These are mostly found in different positions: the coarser sediments typically have a diameter of more than 2 mm and are found close to the *swash* zone, in the steepest part of the profile; the medium and fine sands, with diameters varying between 0.063 mm and 2 mm, are found as one moves in the *offshore* direction, where they are distributed according to the *long-shore* current and *cross-shore* dynamics (J. W. Kamphuis, 2000).

Littorals are affected by a circulatory system determined by currents that can be:

- coastal: they are located offshore of the breakers zone and are independent of wave motion;
- littorals: these are wave-dependent and are located in the *surf zone* (Foti, 2006).

7.4.1 Modelling the long-shore component

Estimating the usual coastal transport is very complex as it depends on many different factors, such as:

- wave characteristics;

- type of breakage;
- sediment characteristics;
- slope of the beach;
- roughness of the seabed.

Two different approaches can be used to obtain estimates of sediment transport: total law or the distribution law. Only the first approach has been dealt with here, which refers to a methodology that estimates the total sediment transport along the coast, without distinguishing between the different contributions of the individual transport components, i.e. it focuses on the entire amount of sediment moved by wave motion and currents, considering the phenomenon in a global way.

The total approach is typical of the CERC-formula (Coastal Engineering Research Centre) in Section 2.3.3, which estimates the total transport in the breakwater zone and establishes a direct dependence between the energy flux associated with a wave in a direction parallel to the coast and the sediment transport in that direction.

Although the CERC formula is a frequently used method, it has some limitations that can lead to under- or over-estimates of sediment transport. The CERC formula assumes that sediment transport is dominated by waves breaking obliquely to the coastline, without considering in detail the effects of coastal currents and tides, which may play an important role in sediment transport. It also assumes a constant direction of transport along the coast, whereas in reality the direction of transport may vary depending on the local and temporal conditions of waves and currents. The constant K in the formula is empirical and can vary greatly depending on local conditions. The accurate determination of this value requires site-specific data and can be difficult to generalise. The formula is based on the wave height at the breaking point H_b, but offshore waves can vary considerably in height and period, affecting sediment transport in complex ways that the formula does not capture. Another limitation is the use of the angle of incidence of the waves φ_b with respect to the coastline. This angle can change rapidly with changes in meteorological and oceanographic conditions, making it difficult to accurately estimate sediment transport over time. The formula may underestimate sediment transport in areas where coastal currents and tides play a dominant role, or in situations where waves have a significant impact outside the

breaking zone. On the other hand, it may overestimate transport in conditions where waves are less energetic than expected or where sediments are less mobile, e.g. coarser sediments or cohesive conditions between sediments. Finally, the formula does not capture non-linearities and complex interactions between waves, currents and sediments over time, limiting its accuracy in long-term predictions (Foti, 2006). For all these reasons and in order to build a model that not necessarily require calibration of the coefficient K we decided to use another long-shore transport empirical formulation.

In fact, Kamphuis's (1991) formula, is an empirical method developed to estimate *long-shore* transport and considers various factors influencing sediment transport by providing a more accurate estimate of the volume of sediment transported per unit time. The formula is expressed by Equation 7.4.1 (same in Table 2.3-2):

Equation 7.4.1 - Long-shore transport (Kamphuis, 1991) equation

$$Q = 7.3\, H_b^4\, T_p^{1.5} s^{0.75} \left(\frac{D_{50}}{1000}\right)^{-0.25} \left(\sin\left(2\, rad(\varphi_b)\right)\right)^{0.6}$$

In which Q is the sediment flow rate (m^3 /s); H_b is the wave height at the breaking point (m). This term is raised to the fourth power, indicating that sediment transport is highly sensitive to wave height. Higher waves result in significantly greater sediment transport; T_p is the peak wave period (s). This term suggests that sediment transport increases as the period of the waves increases. Waves with longer periods tend to have more energy and thus greater capacity to transport sediment; *s* is the slope of the beach. The beach slope is elevated to the power of 0.75, indicating that beaches with steeper slopes favour greater sediment transport; D_{50} is the average diameter of the sediment granules (μm). This term shows that sediments with smaller granules (smaller diameter) tend to be transported more easily than those with larger granules. Finbally φ_b is the angle of incidence of the waves with respect to the coastline at the breaking point. This term indicates that the angle of incidence of waves has a significant effect on sediment transport. Waves that strike the coast at an oblique angle (as opposed to perpendicular) tend to transport more sediment along the coast.

Equation 7.4.1 represents an important evolution in coastal sediment transport estimation tools, providing a more detailed and specific estimate than the CERC formulation.

This COAST-PRO$_{SIM}$ is based on the mass continuity equation and a sediment transport equation along the coastline. Under the simplifying assumptions of a moderate shoreline gradient and small wave angle with respect to the shoreline, the first analytical solutions of the one-line model involve the concentration of the two equations into a single equation of diffusive type as shown in Equation 7.4.2 (Pelnard-Considère, 1957; Valsamidis and Reeve, 2020).

Equation 7.4.2 – Diffusive equation in one-line models

$$\frac{\partial Y_{U_1}}{\partial t} = \varepsilon \frac{\partial^2 Y}{\partial x^2}$$

In which Y_{U1} represents the displacement due to long-shore transport (m); *x* is the distance on an *X* axis parallel to the coastline (m); *y* is the position of the coastline on a vertical *Y-axis at X* (m); *t* is time (days) and ε is the diffusion coefficient (m^2 /s) given by the expression in Equation 7.4.3:

Equation 7.4.3 – Diffusion coefficient

$$\varepsilon = \frac{2Q}{d_b + h_c}$$

In which Q is the long-shore transport (m^3 /s) estimated with the expression in Equation 7.4.1; d_b is the height of the berm (m); h_c is the closure depth (m) calculated using Hallermeier's formula in 1981 given in section 2.3.3:

The solution to Equation 7.4.2 is expressed by Equation 7.4.4:

Equation 7.4.4 – Mathematical solution of the diffusive equation

$$Y_{U1}(t) = Y\ A - Y\ e^{rad(a_b)\frac{x}{Y} + rad(a_b)^2 * \frac{\varepsilon\ t\ 24}{Y^2}}\ B$$

Y is the length of the work considered (m).

The *A* term is defined as in Equation 7.4.5:

Equation 7.4.5 – A term of diffusive equation resolution

$$A = erfc\left(\frac{x}{2\sqrt{\varepsilon\ t\ 24}}\right)$$

The *B* term is expressed by Equation 7.4.6:

Equation 7.4.6 - B term of diffusive equation resolution

$$B = erfc(rad(a_b)\frac{\sqrt{(\varepsilon\ t\ 24)}}{Y} + \frac{x}{2\sqrt{\varepsilon\ t\ 24}}$$

The error function *erf(z)* is expressed as in Equation 7.4.7

Equation 7.4.7 – Error function

$$erf(z) = \frac{2}{\sqrt{\pi}} \int e^{-z^2}\ dz$$

Its complement *erfc(z)* is given by Equation 7.4.8*:*

Equation 7.4.8 – Error complement function

$$erfc(z) = 1 - \text{erf}\,(z)$$

To determine when the structure reaches its maximum capacity, the time t_f (s) is calculated in Equation 7.4.9 which is the time at which the structure can no longer support further accumulation, equal to:

Equation 7.4.9 – Time in maximum capacity of sediment retain

$$t_f = \frac{(Y^2\pi)}{4\ \varepsilon \tan^2 a_b}$$

Then under the condition that $t > tf$ the solution becomes Equation 7.4.10:

Equation 7.4.10 – Solution of diffusive equation when $t > t_f$

$$y = Y\ erfc\left(\frac{x}{2\ \sqrt{\varepsilon\ t_2}}\right) \quad per\ \ t > t_f$$

Valid with boundary conditions:

- $y=Y$ for $x=0$;
- y=0 for x=∞ for every $t > 0$.

7.4.2 Modelling the cross-shore component

The *cross-shore* sediment transport component is given by the Equation 7.4.11 which is derived from empirical and theoretical modelling studies of sediment transport in coastal environments (Miller & Dean, 2004). These studies often combine field observations, laboratory experiments and mathematical modelling to derive relationships that describe how sediments are transported by waves and currents. Equation 7.4.11 is particularly useful for predicting how sediments move during storm events, tides and other hydrodynamic forcing.

Equation 7.4.11 – Cross shore shoreline movement equation

$$Y_{U2} = -W\left(\frac{0.106\,H'_{s(b)}}{d_b + h_b}\right)$$

Y_{U2} represents the displacement due to *cross-shore* sediment transport (m); 0.106 is a coefficient derived from empirical adjustments based on data observed under different coastal conditions; $H'_{s(b)}$ represents the significant wave height at the breaking point (m) and h_b represents the depth at which the breaking occurs (m). Note that all these terms depend on time and space.

W (Equation 7.4.12) represents the width of the surf zone, i.e. the area where wave breaking occurs (m):

Equation 7.4.12 – Width of the surf zone equation

$$W = \frac{H'_{s(b)}}{0.55 * A}$$

Where A represents the scale parameter of Dean's (1977) equilibrium profile, which depends on the sedimentation rate *wf* of the sediment, and thus on characteristics such as size and density (Equation 7.4.13):

Equation 7.4.13 – Dean's profile scaling parameter

$$A = 0.5 * wf^{0.44}$$

Dean (1977) developed a theory for the equilibrium profile of beaches, which describes how beaches are shaped in response to wave-induced sediment transport processes. His theory includes parameters such as sedimentation velocity and sediment size, which are crucial for predicting how sediment is distributed along the coast.

The depth at which the breaking occurs can be expressed by the Equation 7.4.14:

Equation 7.4.14 – bathymetry depth at breaking

$$h_b = X_b\, i$$

In which i is the slope of the beach and X_b is the distance of the breaker line from the *surf-zone* (m) and can be expressed through the Equation 7.4.15:

Equation 7.4.15 – Distance of the breaker line estimation

$$X_b = \frac{h_c}{i}$$

7.5 Further considerations on the effects of structures

A tombolo (Figure 7.5.1) is formed when a barrier, such as a breakwater or groin, alters the natural movement of waves and sediment along the coast. Normally, sediments, such as sand and gravel, are transported along the coast by waves and currents, but when a barrier is placed in the sea, it interrupts this natural flow. The barrier acts as an obstacle that reduces the energy of the waves hitting the coast behind, thus decreasing the ability of the waves to transport sediment. As a result, sediment begins to settle in the area behind the barrier itself. The sand transported by the currents accumulates on the upstream side of the barrier, beginning to form a salient that, as it gradually increases, may become completely connected to the barrier, creating a land connection between the coast and the structure.

Once the tombolo is formed, it tends to stabilise as the waves behind the barrier are weaker and continue to deposit sediment instead of eroding it. However, the stability of the tombolo depends on the size and position of the barrier, as well as wave and sediment transport conditions.

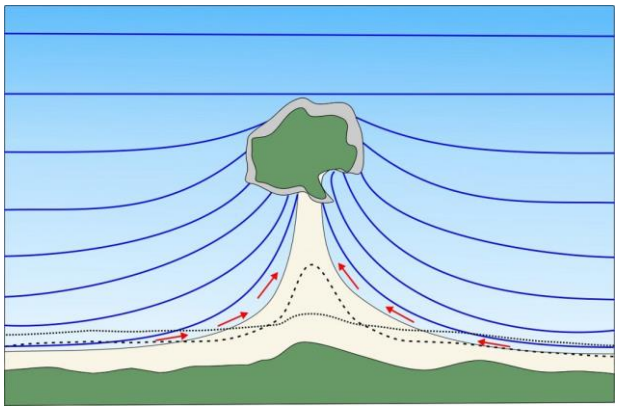

Figure 7.5.1 - Formation of a tombolo by converging sedimentary flows (red arrows) triggered by diffracted waves at the ends of the obstacle. The dotted and dashed lines mark two phases of tombolo development.

The COAST-PRO$_{SIM}$ is able to model and visualise the salient and tombolo formation at T-shaped groins and detached breakwaters. It is essential, to this end, to impose that the beach can reach the structure, but without crossing it or being carried beyond it. To this end, the model dictates that when a calculation cell (area between two consecutive transects) makes contact with the structure, the transport velocity in that cell is adjusted to allow excess sediment to remain in the ascending cells. The procedure for doing this must preserve the sediment volume and preserve the direction of its transport. The procedure is illustrated in Figure 7.5.2 in which a plan view of an idealised beach protected by a detached breakwater is shown at an arbitrary moment in time. In cell $i^{th}+1$, a tombolo was formed at a previous time step. In the adjacent cell i^{th}, by allowing the inflow from cell $i^{th}-1$, the shoreline would advance beyond the barrier, which is not permitted. Therefore, the initially calculated inflow velocity must be corrected so that the coastline advances to the barrier, but not beyond it.

The same reasoning applies in longitude for the groynes, the diagram of which is shown in Figure 7.5.3. When the maximum advance is reached at the back of the groin, the advance is stopped. The excess sediment is divided between the sediment that bypasses the structure and the excess to the adjacent cell, which then goes into accretion.

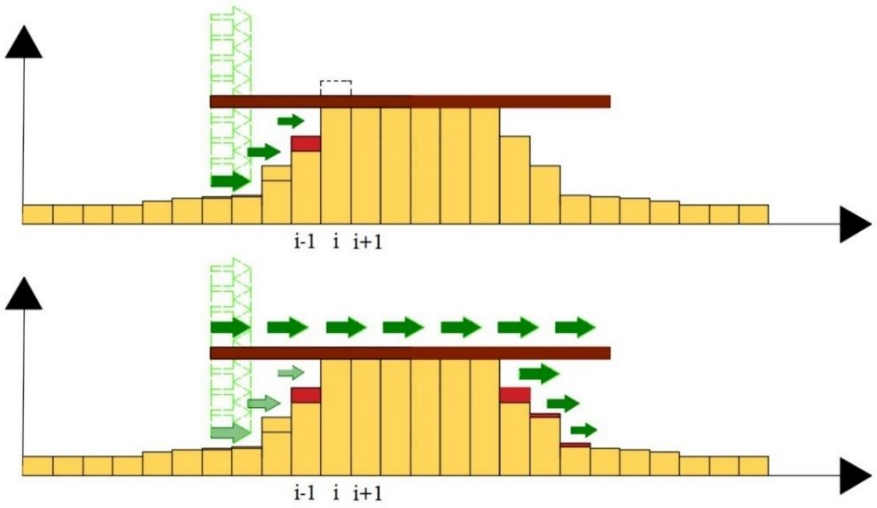

Figure 7.5.2 - Plan view of an idealised beach protected by a detached breakwater at an arbitrary point in time.

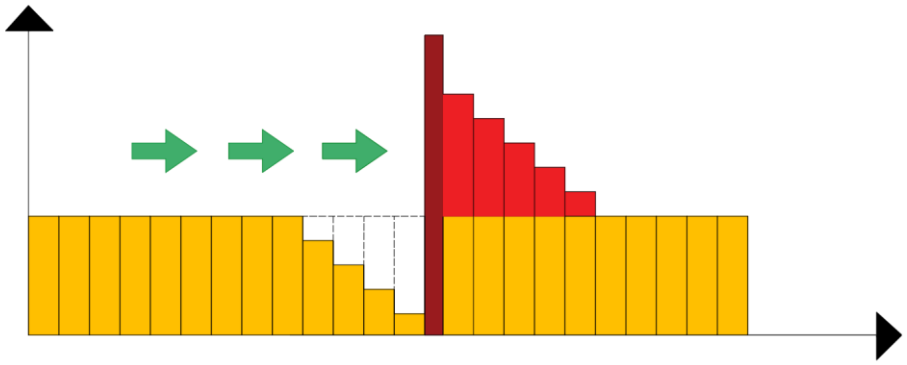

Figure 7.5.3 - Plan view of an idealised beach protected by a groin at an arbitrary moment in time.

7.6 Validation methods

The model COAST-PRO$_{SIM}$ is a one-line model that solves the Equation 7.2.1 in which it estimates the shoreline displacement due to total sediment transport

as the sum of the displacement terms due to *long-shore* and *cross-shore* transport, as well as any inputs and outputs to and from the outside. In particular, the application of the model in this thesis takes place within a physiographic unit, whereby exchanges with the outside can be considered zero.

The COAST-PRO$_{SIM}$ model adopts assumptions similar to those of one-line models already found in the literature (Valsamidis & Reeve, 2020):

- the beach profile is in equilibrium and does not change over time (this implies that the bathymetric contours are parallel to each other, so one contour is sufficient to predict the entire movement of the beach);
- sediment transport along the coast occurs up to the closure depth and no further.

For the validation of the model, a preliminary analysis of the model was carried out on synthetic cases of linear shoreline, oriented northwards with a normal at 0°N, under conditions of constant and synthetic meteorological and sea forcing, simulating the variation of the beach line with the effect of the presence of:

- a semi-permeable detached breakwater;
- a semi-permeable groyn.

We would like to specify that, while the first analytical solutions in the literature dealt with the case of groins and impermeable barriers of infinite length, the present one aims to describe a condition that more closely reflects the actual conditions that allow the transport of sediment through and around such works, which are therefore semi-permeable and of finite length.

7.6.1 Validation metrics

For the validation of the COAST-PROSIM model and its ability to predict the coastline in the presence of protective works, reference is made to established methodologies in literature. The results obtained are compared using specific validation metrics. The metrics chosen for this analysis are the correlation coefficient CC; the mean error BIAS; the mean square error RMSE; the normalised mean square error NMSE and the coefficient of determination R^2.

The equations of the coefficients are the same as in the previous chapters. They are given again for easier reading characterising them on the model and validation methods.

7.6.1.1 Correlation coefficient CC

The Correlation Coefficient *(CC)*, or Pearson's coefficient is expressed by Equation 3.3.6 and is used to quantify the strength of the linear relationship between the two predictions ("Pearson correlation index," 2024):

$$CC = \frac{\sum_{i=1}^{n}(\hat{y}_i - \bar{\bar{y}})(y_i - \bar{y})}{\sqrt{\sum_{i=1}^{n}(\hat{y}_i - \bar{\bar{y}})^2} * \sqrt{\sum_{i=1}^{n}(y_i - \bar{y})^2}}$$

where, *n* is the number of available values; $\hat{y}_i$ are the values provided by COAST-PRO$_{SIM}$; y_i are the values predicted by the Silvester - Hsu method; $\bar{\bar{y}}$ is the mean of the values predicted by COAST-PRO$_{SIM}$ and $\bar{y}$ is the average of the values predicted by the Silvester - Hsu method.

This coefficient takes values varying between -1 and 1 and the result can be interpreted respectively as perfect negative correlation, data perfectly aligned on a decreasing line (bisector of the second and fourth quadrants) and perfect positive correlation, data perfectly aligned on an increasing line (bisector of the first and third quadrants).

In the case of a value equal to or close to 0, the metric suggests no linear correlation, the data are randomly distributed with no obvious linear pattern.

7.6.1.2 Mean error BIAS

BIAS (*mean error*) measures the tendency of the model to overestimate or underestimate the values predicted by the reference model. It measures the average difference between the values predicted by the COAST-PRO$_{SIM}$ and the values obtained by the Silvester - Hsu technique:

$$BIAS = \frac{1}{n}\sum_{i=1}^{n}(\hat{y}_i - y_i)$$

where *n* is the number of available values; $\hat{y}_i$ are the values provided by COAST-PRO$_{SIM}$ and y_i are the values predicted by the Silvester - Hsu method.

The BIAS can take on any real value, positive or negative. The magnitude and sign provide information on the direction and magnitude of the model's systematic error ("Bias", 2024). When the BIAS is zero, it means that, on average, the model does not show a tendency to overestimate or underestimate the comparison data, indicating a good balance in the predictions. Conversely, a positive BIAS suggests that the model tends to overestimate the comparison

values - i.e. its predictions are generally higher than the observed data. If the BIAS is negative, it means that the model tends to underestimate the actual values, with predictions that are, on average, lower than what has been observed.

7.6.1.3 RMSE mean square error

The RMSE (*Root Mean Square Error*) provides a measure of the *root* mean square deviation between the values of the two models. It therefore provides a measure of the dispersion of the predictions from the observed values, penalising larger errors more heavily. The lower the RMSE, the better the performance of the model.

$$RMSE = \sqrt{\frac{1}{n}\sum_{i=1}^{n}(\hat{y}_i - y_i)^2}$$

where *n* is the number of available values; $\hat{y}_i$ are the values provided by COAST-PRO$_{SIM}$ and y_i are the values predicted by the Silvester - Hsu method.

The RMSE can take values between 0 and ∞. An RMSE value of zero indicates a perfect match between the model's predicted and observed values, suggesting that the predictions are accurate. When the RMSE is greater than zero, it means that errors exist between the predictions and the actual values. A higher RMSE indicates a larger averege error in the forecasts. There is no theoretical upper limit for the RMSE, as it can increase indefinitely in the presence of very large errors.

7.6.1.4 Normalised root mean square error NMSE

The NMSE is a normalised version of the MSE (*Mean Square Error*), which facilitates comparisons between models on different scales. It is usually normalised with respect to the variance of the observed data.

$$NMSE = \frac{\sum_{i=1}^{n}(\hat{y}_i - y_i)^2}{\sum_{i=1}^{n}(\hat{y}_i - \bar{y})^2}$$

where *n* is the number of available values; $\hat{y}_i$ are the values provided by COAST-PRO$_{SIM}$; y_i are the values predicted by the Silvester - Hsu method and $\bar{y}$ is the mean value of the values predicted by the Silvester - Hsu method.

The Mean Square Error (MSE) can be expressed as follow:

$$MSE = \frac{1}{n}\sum_{i=1}^{n}(\hat{y}_i - y_i)^2$$

where n is the total number of observations; $\hat{y}_i$ represents the model-predicted value from COAST-PRO$_{SIM}$ for the i-th observation; and y_i represents the value predicted by the Silvester - Hsu method for the i-th observation.

Since the errors between the values predicted by the two models are squared, the MSE is sensitive to outliers, i.e. very large prediction errors, which can have a significant impact on the overall measurement. For this reason, the MSE is used in combination with other metrics (such as RMSE, NMSE and R^2) to provide a more comprehensive assessment of a model's performance.

Variance is a statistical measure that quantifies the dispersion of data with respect to their mean. In other words, variance indicates how far the values of a set of data deviate, on average, from the arithmetic mean of that set. It is one of the most common measures of variability and is used to understand the distribution of data within a sample or population. For a population, variance is expressed by Equation 7.6.1:

Equation 7.6.1 – Variance equation

$$\sigma^2 = \frac{1}{n}\sum_{i=1}^{n}(x_i - \mu)^2$$

where n is the total number of data in the population; x_i is the value of the i^{th} data μ is the population mean.

An NMSE of zero indicates that the model perfectly predicts all values according to this reference method. When the NMSE is less than one, it means that the model is more accurate than using the average of the values predicted by the Silvester-Hsu method. An NMSE equal to one suggests that the accuracy of the model is equivalent to that obtained using the average of the values of the reference method. If the NMSE is greater than one, the model is less accurate than using the average of the values provided by the Silvester-Hsu method.

7.6.1.5 Coefficient of determination R^2

The coefficient of determination R^2 represents the proportion of the variance in the data predicted by the reference method that is explained by the model. It is

commonly used to assess the accuracy of a regression model, indicating how well the predicted data matches with the reference data. It can be calculated using the following equation:

$$R^2 = 1 - \frac{\sum_{i=1}^{n}(\hat{y}_i - y_i)^2}{\sum_{i=1}^{n}(y_i - \bar{y})^2}$$

where n is the number of available values; $\hat{y}_i$ are the i-th values provided by COAST-PRO$_{SIM}$; y_i are the i-th values predicted by the Silvester - Hsu method and $\bar{y}$ is the average of the values predicted by the Silvester - Hsu method.

An R^2 value of 1 indicates that the model perfectly explains the variance in the data, showing an ideal match between predictions and observations. Conversely, an R^2 of 0 means that the model cannot explain the variance in the data, being useless as a forecasting tool. When R^2 lies between 0 and 1, the model can only explain part of the variance in the data. Finally, a negative R^2 can occur if the predictive model is even worse than using the mean of the data from the Silvester-Hsu reference method.

7.6.2 Validation of semi-permeable detached breakwater barrier

For the validation of the COAST-PRO$_{SIM}$ and its ability to predict the coastline due to the effect of a semi-permeable detached breakwater, reference is made to Silvester and Hsu's methodology proposed in 1997 by comparing the results obtained through the use of the chosen validation metrics (section 7.6).

The method proposed by Silvester and Hsu in 1997, also known as the parabolic bay shape method, is used to predict the evolution of the shoreline following the insertion of a breakwater. This method is based on the geometric configuration of the bay that is formed as a result of wave interaction with the barrier (Silvester and Hsu, 1997).

With reference to the diagram shown in Figure 7.6.1, the diagram shows a parabolic bay developing behind a breakwater, with an initially straight beach.

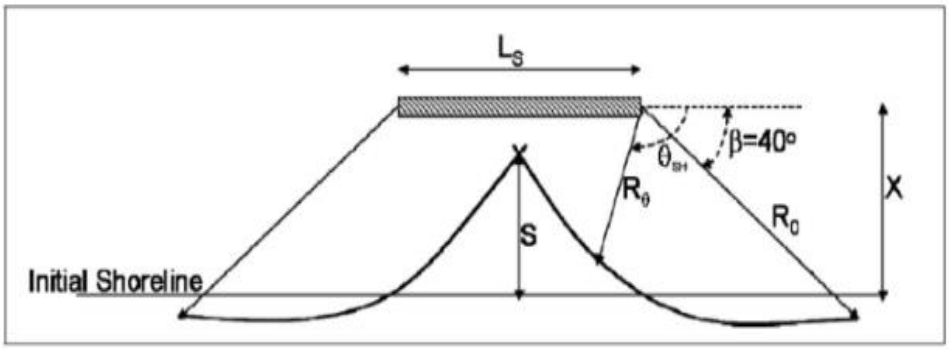

Figure 7.6.1 - Simplified diagram Silvester & Hsu (1997)

In which L_s represents the length of the breakwater barrier (m); *X* represents the distance of the shoreline from the horizontal axis of the barrier (m); R_0 represents the length of the parabolic bay (m) and θ_{SH} is the angle of attack of the wave on the breakwater.

The formula for predicting the shoreline R_0/L_s is given by Equation 7.6.2:

Equation 7.6.2 - Formula for shoreline position prediction using Silvester & Hsu (1997) method

$$\frac{R_0}{L_S} = C_0 + C_1\left(\frac{\beta}{\theta_{SH}}\right) + C_2\left(\frac{\beta}{\theta_{SH}}\right)^2$$

In which β is the angle between the wave crest at the point of diffraction and the control line and C_0, C_1 *e* C_2 are coefficients that depend on the angle β.

The relationship between R_0/L_s e L_s/X is expressed by Equation 7.6.3:

Equation 7.6.3 - Equation to determine the specific shape of the bay using Silvester & Hsu (1997) method

$$\frac{R_0}{L_S} = 0.1737 + \frac{1.683}{L_s/X}$$

This equation helps determine the specific shape of the bay based on the geometric parameters of the configuration. In particular, for an angle $\beta = 10°$ and for the configuration with a single breakwater on a straight beach, the coefficients take the values $C_0 = 0$; $C_1 = 1.32$ and $C_2 = -0.33$.

7.6.3 Semi-permeable groin validation

For the validation of the COAST-PRO$_{SIM}$ and its ability to predict the coastline influenced by a semi-permeable shoreline, we refer to the studies by A. Valsamidis and D. E. Reeve from 2020 (Valsamidis and Reeve, 2020), in which analytical solutions are applied with satisfactory results in simple situations, such as a single permeable groin or for a compartment of groins.

The method proposed by Valsamidis and Reeve consists of combining the semi-analytical solution for predicting the evolution of the shoreline in the vicinity of a single groove (Reeve & Valsamidis, 2014) to that derived by Zacharioudaki and Reeve (Zacharioudaki & Reeve, 2008) for a complex of groynes, using appropriate boundary conditions so that a model can be developed that is suitable for describing a field of several groynes positioned in succession.

Concerning the semi-analytical solution for the prediction of shoreline evolution in the vicinity of a single groin (Reeve & Valsamidis, 2014), a Fourier cosine transform is used to develop the solution to the diffusive equation (Equation 7.4.2). This solution is given by the sum of the following three terms in Equation 7.6.4:

Equation 7.6.4 - Solution to the diffusive equation proposed by Reeve and Valsamidis (2014)

$$Y^G = Y_1^G + Y_2^G + Y_3^G$$

In which Y^G is the position of the coastline and Y_1^G is expressed by Equation 7.6.5:

Equation 7.6.5 - First term of the solution to the diffusive equation proposed by Reeve and Valsamidis (2014)

$$Y_1^G = \frac{1}{\pi}\left(\pi \int_0^t \varepsilon(u)du\right)^{-\frac{1}{2}} \int_0^{+\infty} g(\xi)\left[exp\left(-\frac{(x-\xi)^2}{4\int_0^t \varepsilon\,(u)du}\right) + exp\left(-\frac{(x+\xi)^2}{4\int_0^t \varepsilon\,(u)du}\right)\right]d\xi$$

Y_2^G is expressed by Equation 7.6.6:

Equation 7.6.6 - Second term of the solution to the diffusive equation proposed by Reeve and Valsamidis (2014)

$$Y_2^G = \frac{2}{\pi}\int_0^{+\infty}\left(\int_0^t \exp\left(-\int_w^t [\omega^2\ \varepsilon(u)]du\right)\tilde{q}(\omega,w)dw\right)cos(\omega x)d\omega$$

Also, Y_3^G is expressed by Equation 7.6.7:

Equation 7.6.7 - Third term of the solution to the diffusive equation proposed by Reeve and Valsamidis (2014)

$$Y_3^G = \frac{1}{\sqrt{\pi}}\int_0^t \varepsilon(w)j(w)\left(\frac{1}{\sqrt{\pi\ \int_w^t \varepsilon\ (u)du}}\exp\left(-\frac{x^2}{4\ \int_w^t \varepsilon\ (u)du}\right)\right)dw$$

where, $g(\xi)$ is the initial position of the coastline; ξ is a dummy variable used in the integration process ω is the transformation variable used in the Fourier cosine transform operation, $\tilde{q}$ is the Fourier cosine transformed variable of q, a parameter describing the flow of sediment from a sediment source or sink; w is a time-related variable and finally *j(w)* is a groin boundary condition.

On the other hand, as regards the semi-analytical solution for predicting shoreline evolution in the vicinity of a groin compartment (Zacharioudaki & Reeve, 2008) a solution to the diffusive equation is used (Equation 7.4.4), derived via finite Fourier cosine transforms. This solution is given by the sum of the following four terms in Equation 7.6.8:

Equation 7.6.8 - Solution to the diffusive equation proposed by Reeve and Zacharioudaki (2008)

$$y^{GC} = y_1^{GC} + y_2^{GC} + y_3^{GC} + y_4^{GC}$$

y^{GC} is the position of the coastline while y_1^{GC} is expressed by Equation 7.6.9:

Equation 7.6.9 - First term of the solution to the diffusive equation proposed by Reeve and Zacharioudaki (2008)

$$y_1^{GC} = \frac{1}{a}\ \bar{g}(0) + \frac{1}{a}\int_0^t \varepsilon(w)\big(j(w) -\ \ k(w) +\ \hat{s}(0,w)\big)dw$$

y_2^{GC} is expressed by Equation 7.6.10:

Equation 7.6.10 - Second term of the solution to the diffusive equation proposed by Reeve and Zacharioudaki (2008)

$$y_2^{GC} = \frac{2}{a}\sum_{\psi=1}^{+\infty} \cos\left(\frac{\psi\pi x}{a}\right) \hat{g}\,(\psi) \exp\left(-\int_0^t \frac{\pi^2\psi^2}{a^2}\varepsilon(u)du\right)$$

y_3^{GC} is expressed by Equation 7.6.11:

Equation 7.6.11 - Third term of the solution to the diffusive equation proposed by Reeve and Zacharioudaki (2008)

$$y_3^{GC} = \frac{2}{a}\sum_{\psi=1}^{+\infty} \cos\left(\frac{\psi\pi x}{a}\right) \int_0^t \exp\left(-\int_w^t \varepsilon(u)\left(\frac{\psi\pi}{a}\right)^2 du\right)(\varepsilon(u)\left((-1)^{\psi} j(w) - k(w)\right)dw$$

y_4^{GC} is expressed by Equation 7.6.12 :

Equation 7.6.12 - Fourth term of the solution to the diffusive equation proposed by Reeve and Zacharioudaki (2008)

$$y_4^{GC} = \frac{2}{a}\sum_{\psi=1}^{+\infty} \cos\left(\frac{\psi\pi x}{a}\right) \int_0^t \exp\left(-\int_w^t \varepsilon(u)\left(\frac{\psi\pi}{a}\right)^2 du\right) \hat{s}\,(\psi, w)dw$$

In the equation $g(x)$ represent the initial position of the coastline expressed as Equation 7.6.13:

Equation 7.6.13 - Formula for the initial position of the coastline g(x)

$$\hat{g}\,(\psi) = \int_0^a g(x)\cos\left(\frac{\psi\pi x}{a}\right)dx \;\; per\; cui \;\; \hat{g}\,(0) = \int_0^a g(x)dx$$

a is the length of the barrier compartment; $\hat{g}\,(\psi)$ is the finite cosine Fourier transform of *g(x);* ψ is an integer transformation variable; *j(w)* is the time-varying boundary condition on the left side of the groin compartment; *k(w)* is the boundary condition corresponding to the right-hand side of the groin compartment; *w* is a dummy variable of integration and $\hat{s}$ is the source term given by the expression in Equation 7.6.14:

Equation 7.6.14 - Source term formula

$$\hat{s}(0,\mathrm{w}) = \int_0^a s(x,w)dx$$

For validation, the input data shown in Table *7.6-1*.

Table 7.6-1 – Validation input data

Input data	**Values**
Groin length (*Y*) [m].	15
Wave height at break? (H_b) [m].	1
Beach slope (*s*) [-]	0.01
Closing depth (h_c) [m].	7.5
Significant sediment diameter (D_{50}) [mm].	0.5
Breaking angle (*ab*) [°].	10
Berm height (*db*) [m].	1
Peak period (T_p) [s].	6

7.7 Areas of real application and validation

To assess the reliability of the COAST-PRO$_{SIM}$ in predicting the evolution of the coastline in the presence of coastal works, such as barriers and groins, three pilot sites characterised by different environmental conditions were selected: San Leone (Ag), Porto Empedocle (Ag) and Villafranca Tirrena (Me).

These locations were selected for their geographical relevance and the diversity of coastal conditions present, which allow the model to be tested in varied and complex scenarios. San Leone is a seaside resort characterised by high coastal dynamics and significant erosion phenomena. The presence of anthropogenic structures makes this site particularly interesting for assessing the model's effectiveness in predicting interactions between infrastructure and coastlines. Porto Empedocle, known for its commercial port, represents a different context in which port works and human activities greatly influence coastal morphology.

Studying this area makes it possible to verify the model's ability to adapt to an environment strongly modified by human activities and to predict the evolution of the coastline in the presence of intense port activities. Finally, Villafranca Tirrena offers an opportunity for analysis in a natural coastal context with a lesser presence of artificial structures. This location is characterised by erosional and depositional processes typical of sandy coasts, providing a test bed for the model under more natural conditions and less influenced by human intervention.

Model results in the last configuration in December 2023 were compared with observations from satellite images acquired at different times temporally close to the simulation end date (December 2023), in particular: Bing Satellite in October 2023; ESRI Satellite in July 2023; Google Satellite in May 2023 and Google Satellite in March 2024. The shorelines were detected using the methodology reported in Chapter 4. The obtained shorelines (for each case study area) were processed using the CDA plugin (Chapter 6) in order to conduct a transect based comparison between detected shorelines and COAST-PRO$_{SIM}$ results.

The comparative analysis of these three case studies made it possible to assess the reliability and versatility of the forecasting model developed, providing valuable indications for its use in real contexts and for sustainable coastal management.

7.7.1 Case Study 1: San Leone

San Leone beach is located along the southern coast of Sicily, in the municipality of Agrigento, and is part of physiographic unit No. 6.1 (refer to Section 5.2.1, Chapter 5) described by the Hydrogeological Structure Plan (PAI). According to the information reported by the PAI, this coastal area is characterised by a low and sandy beach that extends for several kilometres, interrupted by rocky outcrops and small promontories and by slight slopes towards the sea. The sediments present vary in grain size, but are predominantly fine, with coarser materials present near the mouths of minor watercourses. The morphology of the area is characterised by small hills with peaks of robust lithologies, generally limestone, that emerge as islands in the surrounding landscape. These hills are often inclined and furrowed by watercourses that cross them perpendicularly. The main geomorphological phenomena include slope modelling, which is closely linked to intense erosive phenomena, mainly due to the presence of clayey, marly and silty-sandy sediments, which are exposed and lack adequate vegetation cover.

Since the 1970s, the San Leone beach has undergone major changes as a result of intense human activity in the area and this has led to imbalances in coastal dynamics over the years. The effect of these imbalances has been advances and/or retreats of the shoreline and the effect is that, like most Sicilian coastal areas, San Leone is subject to coastal erosion phenomena, which are particularly accentuated during winter periods.

Several key elements can be mentioned on the coast of San Leone. Along the coast, there are jetties and groynes extending perpendicularly to the shoreline. In some sections, breakwaters have been installed parallel to the shoreline, built with large boulders. In addition, various coastal defence works have been built, including retaining walls and artificial beach nourishments. A significant element of the coastal configuration is the marina of San Leone. The harbour, equipped with breakwaters, alters local currents and sediment flows, influencing coastal dynamics. These works, although necessary to protect the coast and infrastructure, have a significant impact on the morphodynamics of the beach, altering the natural processes of sediment transport and deposition (PAI, s.d.).

7.7.2 Case Study 2: Porto Empedocle

The Porto Empedocle beach is located along the southern coast of Sicily, in the municipality of the same name, and is part of physiographic unit No. 6.1 described by the Hydrogeological Structure Plan (PAI) and extensively described from a morphological point of view in the previous paragraph regarding the San Leone beach.

In the course of this thesis, the COAST-PRO$_{SIM}$ was applied for the prediction of the shoreline following the construction of the harbour, the inner arm of which is treated as a long groin, shown in Figure 7.9.4 and its results were subsequently compared with observations from satellite images.

7.7.3 Case Study 3: Villafranca Tirrena

The beach of Villafranca Tirrena is located along the north-east coast of Sicily, in the municipality of the same name, overlooking the Tyrrhenian Sea a few kilometres north-west of Messina and is part of physiographic unit No. 1.1. From the information reported by the PAI, this stretch of the coastline is characterised by low beaches with fine, golden sand extending for several kilometres. The sediments present are mainly sandy, and the presence of gravel and pebbles is sporadic and tends to increase towards the mouths of the streams that flow into

the sea, carrying coarse materials. The area is also characterised by coastal dunes, which help protect the hinterland from storm surges.

Over the years, the Villafranca Tirrena beach has experienced alternating phases of erosion and accumulation, with a predominant tendency towards erosion in the current period, a condition typical of most Sicilian coastal areas. Today's erosion is mainly attributable to a reduction in natural sedimentary inputs, following the regulation of local torrents, and to the presence of obstacles, both natural, such as rock heads and promontories, and artificial, such as the port of Villafranca Tirrena and coastal protection structures, as well as urban expansion that has modified the normal sedimentation processes. As a result, the beach, despite the presence of 14 breakwaters, is extremely reduced in width and, in some areas, has practically disappeared. In addition, the presence of coastal roads and urban infrastructure that come very close to the shore has reduced the space available for the beach, accelerating erosion processes. Tourist facilities, such as bathing establishments and beach access walkways, while improving access and enjoyment of the shoreline, may further contribute to erosion and the complexity of coastal management.

7.7.4 Wave data

For the three case studies under consideration, namely San Leone, Porto Empedocle and Villafranca, reanalysis data obtained free of charge through the Copernicus Marine Environment Monitoring Service (CMEMS or Copernicus Marine Service CMS) portal (https://data.marine.copernicus.eu/products - last access 28 oct 2024) were used to characterise the meteorological climate. These data are hourly averages of: Significant wave height [m]; Wave direction of significant height [°]; Wave period at maximum spectral density [s]. The acquired data, calculated on an hourly basis, cover a time interval of 29½ years, from 01/01/1993 at 00:00 to 30/07/2022 at 23:00.

For each of the three case studies, the wave rose (Figure 7.7.1) is shown for the meteomarine characterisation. In each wave rose, the sectors are described by a length indicating the number of elements within specific percentage thresholds and a colour gradation representing the intensity of the variable - i.e. the significant wave height. The distribution of the waves is a function of the frequency of occurrence (%), represented by concentric circles.

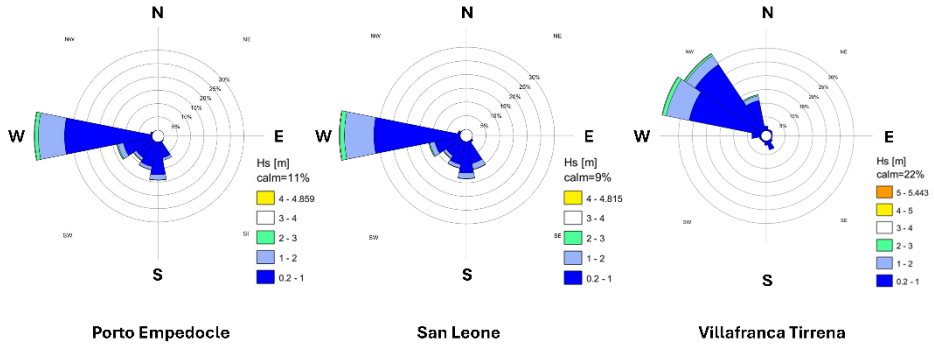

Figure 7.7.1 - Wave roses for the three application study sites

The analysis of the wave roses for the three sites shows that the most frequent and intense waves come from quadrant IV, particularly from the west and northwest (especially for Villafranca). In all cases, the highest value of significant height is recorded in the direction of approximately 270-290° N, with a frequency of over 30%. The calm condition, associated with significant heights of less than 0.2 m, occurs with an occurrence rate of about 11%, 9% and 22% of the total for San Leone, Porto Empedocle and Villafranca Tirrena, respectively.

The wave height, direction and period data described above were subsequently used as input for the nearshore hybrid downscaling (Camus et al., 2013b), the results of which were used as input for the COAST-PRO$_{SIM}$ model.

7.8 Validation results

7.8.1 Breackwater test

In the evaluation of predictive models, the use of validation metrics is crucial to quantify the accuracy of the predictions of one model compared to another. Such metrics not only provide a measure of the error committed by the model, but also allow one to compare the effectiveness of different models or approaches, as in the case of the comparison between the proposed COAST-PRO$_{SIM}$ and the Silvester - Hsu technique for shoreline prediction.

In the outline of this validation L is the length of the barrier (m) and S *is* the distance of the shoreline from the horizontal axis of the barrier (m).

Simulations were carried out for 33 configurations differing in S length but maintaining a constant L value of 100 m and considering the shoreline

discretization based on 600 transects with 1 m resolution spacing. The configurations are shown in Table 7.8-1.

Table 7.8-1 - Values used for simulation with barrier

Conf. [n°]	L [m]	S [m]	Conf. [n°]	L [m]	S [m]	Conf. [n°]	L [m]	S [m]
1	100	175	**12**	100	120	**23**	100	65
2	100	170	**13**	100	115	**24**	100	60
3	100	165	**14**	100	110	**25**	100	55
4	100	160	**15**	100	105	**26**	100	50
5	100	155	**16**	100	100	**27**	100	45
6	100	150	**17**	100	95	**28**	100	40
7	100	145	**18**	100	90	**29**	100	35
8	100	140	**19**	100	85	**30**	100	30
9	100	135	**20**	100	80	**31**	100	25
10	100	130	**21**	100	75	**32**	100	20
11	100	125	**22**	100	70	**33**	100	15

Figure 7.8.1 shows the comparison between the results obtained using the COAST-PRO$_{SIM}$, shown as blue dots, and those obtained using the method proposed by Silevster & Hsu (1997), used in this thesis as a reference method, shown as a red dashed line. An initial graphical analysis shows a high degree of closeness between the values of the two methods. For analytical comparison, the relative values of the chosen validation metrics are also shown (Figure 7.8.1).

From what was highlighted in the previous paragraph on the interpretation of the results of the validation metrics, the values obtained indicate that the COAST-PRO$_{SIM}$ is suitable for the prediction of the shoreline following the insertion of a breakwater. In particular, the correlation coefficient is very close to the value 1, the BIAS does not show large overestimates or underestimates, the RMSE value is low, suggesting high accuracy, the NMSE value is very close to the value 0, and finally the coefficient of determination R^2 is high.

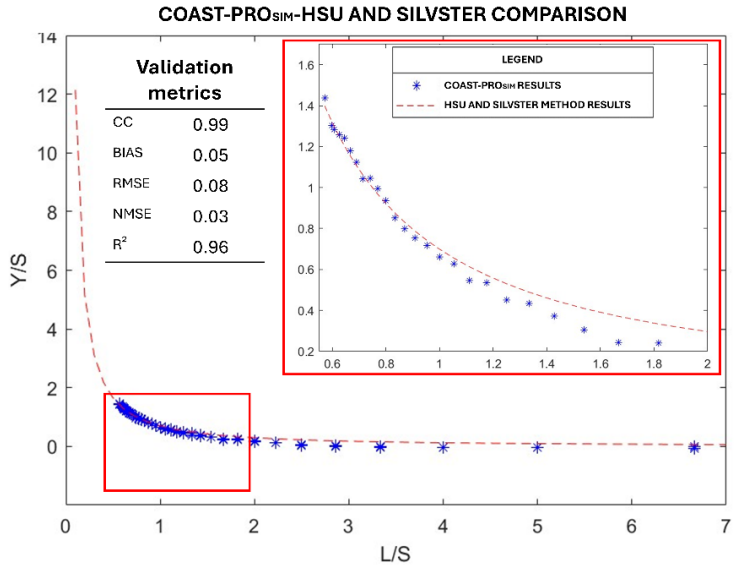

Figure 7.8.1 - Comparison of the results obtained with the COAST-PRO$_{SIM}$ and the Silevster & Hsu (1997) method with relative values of the validation metrics: Correlation Coefficient, BIAS, RMSE, NMSE, Coefficient of Determination R^2

After comparing the validation metrics, simulations were carried out to predict shoreline displacement by solving the Equation 7.2.1for a time span of 20 years, with a daily simulation.

Of the 33 configurations shown in Table 7.8-1 six representatives were chosen and are shown in Table 7.8-2. The graphical results of shoreline displacement with the final configuration on simulation day 7,201 are shown in Figure 7.8.2.

Table 7.8-2 - Configurations shown graphically

Conf. [n°] and Subplot ID	L [m]	S [m]
1-A	100	175
15-B	100	105
20-C	100	80
27-D	100	45

30-E	100	30
33-F	100	15

In Figure 7.8.2 it is possible to observe the position of three selected transects, named Transect -100, Transect 0 and Transect 100 on simulation day 7,201, the time when the structure is fully operational, for the six chosen configurations. Note that in the graph of configuration 1, the three transects are represented as follows: Transect -100 in red; Transect 0 in magenta and Transect 100 in blue.

This colour coding is also kept constant in the graphs of subsequent configurations. The barrier, highlighted in grey, has a constant length of 100 metres.

The analysis of the results clearly shows how the presence of the barrier constitutes an obstacle that induces a dissipation of wave energy and, consequently, a reduction in the sediment transport capacity along the coast. The sediment, deprived of its kinetic energy, tends to settle upstream of the structure, giving rise to a salient that, as the simulation progresses, gradually increases until it joins the barrier itself, forming a tombolo. This phenomenon can be observed from configuration 30 onwards. This occurs because, as mentioned in the presentation phase, COAST-PRO$_{SIM}$ is able to model and visualise the formation of the salient and the tombolo at the structure, taking into account that the sediments can only reach the structure without crossing it or being transported beyond it.

The quantitative analysis of the results indicates that the distance from the shoreline significantly influences the morphology of the tombolo. In particular, for distances greater than 40 metres, the barrier is too far from the shoreline to favour the formation of a complete tombolo. On the contrary, for distances of less than 30 metres, as in the case of configuration 30, a clear morphological evolution is observed with the formation of a well-defined tombolo.

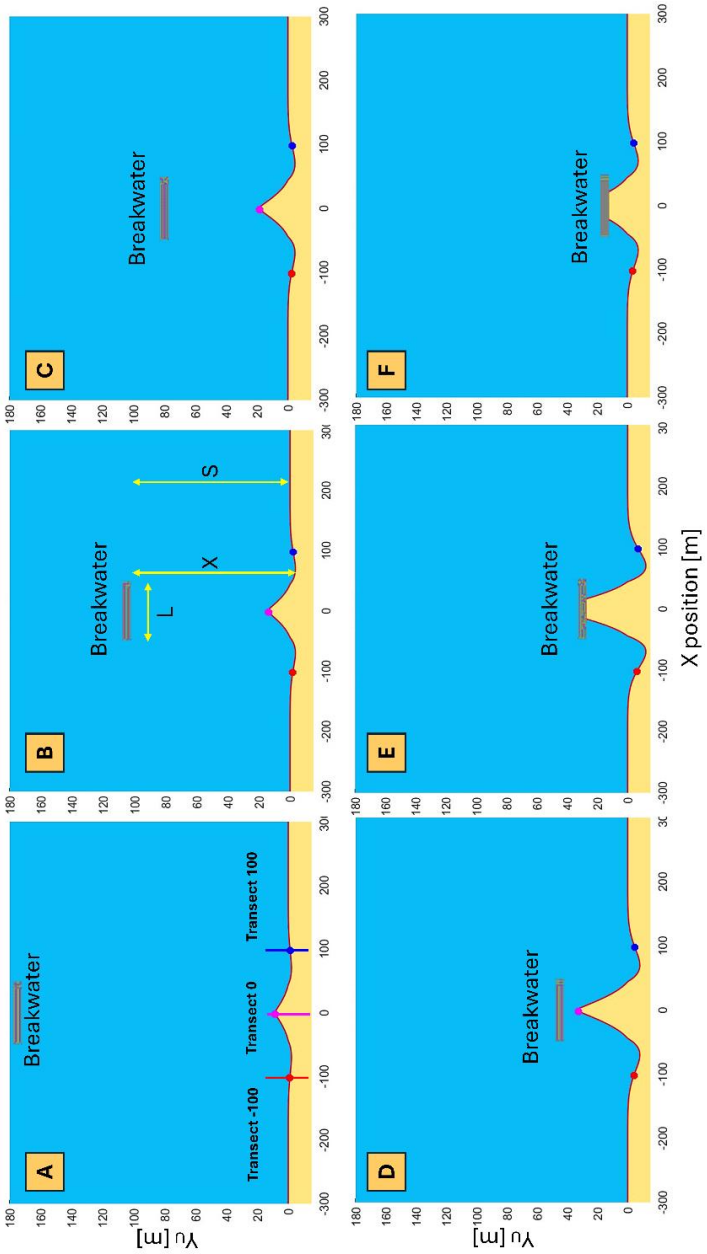

Figure 7.8.2 - Trend of Yu on simulation day 7201 for the six configurations selected in Table 7.8-2 considering a 20-year simulation.

In Figure 7.8.3 shows the time course of the shoreline displacement due to the total transport of the Equation 7.2.1, Y_U, for the selected transects in the six configurations shown in Table 7.8-2. It is observed that the -100 and 100 transects undergo negative positional changes, indicating a modest erosion. Transect 0 shows positive and larger changes in position, indicating significant accumulation.

This evidence is consistent with the observations of Figure 7.8.2.

Interestingly, in configurations 30 and 33, transect 0 reaches a condition of dynamic equilibrium. This is attributable to the formation of the tombolo, when the sediment reaches the barrier and becomes trapped, unable to cross it. In fact, the barrier constitutes an obstacle for sediment accumulation. Specifically, Transect 0 reaches equilibrium for configuration 30, in wich $Y_u = 30\ m$ on day 1604 of the simulation and for configuration 33, in wich $Y_u = 15\ m$ on day 1143 of the simulation.

In contrast, the -100 and 100 transects do not reach a dynamic equilibrium condition over the simulation period considered, showing continuous fluctuations in the Y_u. These variations are mainly attributable to the cross-shore transport-related shoreline displacement component. The quantitative analysis indicates that the amplitude of the oscillations varies from a few centimetres to approximately 5 m between the beginning and end of the simulation between the various configurations. In order for these transects to also reach a stable equilibrium condition, it would be necessary to increase the length of the barrier. This would limit the influence of the cross-shore transport, favouring greater morphological stability.

Figure 7.8.3 shows the results of an annual simulation, displaying the temporal evolution of shoreline position for two configurations (1 and 33) shown in Table 7.8-2. The profiles are shown at all simulation days. It can be seen that the distance of the reef from the coastline exerts a significant control on the morphological dynamics.

For configuration 1, characterised by the greatest distance from the barrier, there is an average variation in the mean elevation of the central transect of approximately 4 m, indicating an almost static equilibrium. On the contrary, for the configurations with barriers closer to the coast (n° 33), the average variations

of the central transect reach values of about 8 m, highlighting a more pronounced morphological dynamic, characterised by significant oscillations due to wave diffraction and reflection. The implications of these results are relevant for the design of coastal defence works, as they highlight the need for an accurate assessment of local conditions and an optimal choice of barrier position.

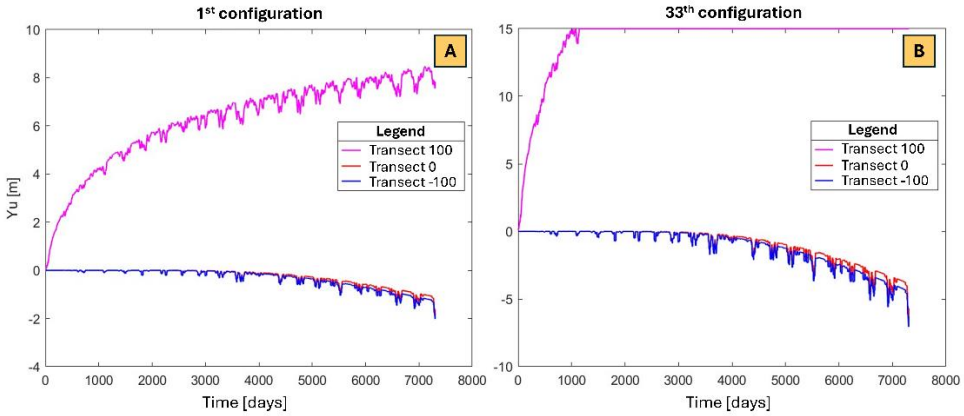

Figure 7.8.3 - Development of Yu over time at the three selected transects, for the six selected configurations considering a 20-year simulation.

7.8.2 Groin test

After carrying out a one-year simulation, in Figure 7.8.4 shows the comparison of the results obtained with the COAST-PRO$_{SIM}$, shown as a red dashed line in the graph below, with those obtained through the method proposed by A. Valsamidis and D. E. Reeve of 2020, used in this thesis as a reference method, shown as blue dots.

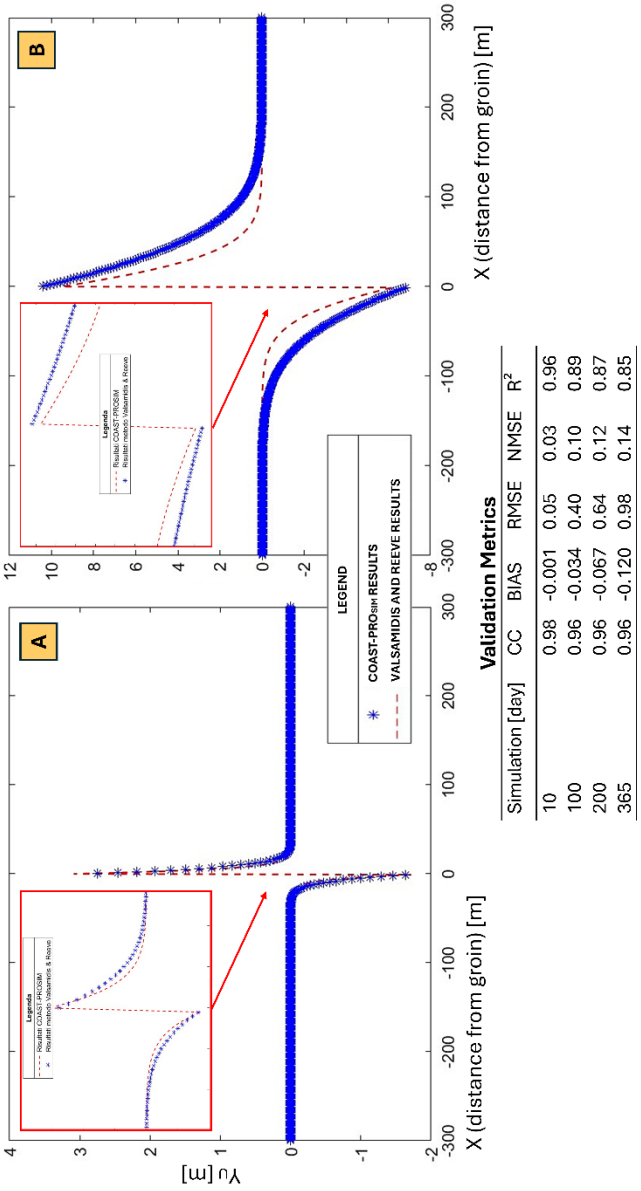

Validation Metrics

Simulation [day]	CC	BIAS	RMSE	NMSE	R^2
10	0.98	-0.001	0.05	0.03	0.96
100	0.96	-0.034	0.40	0.10	0.89
200	0.96	-0.067	0.64	0.12	0.87
365	0.96	-0.120	0.98	0.14	0.85

Figure 7.8.4 - Comparison of results obtained with the COAST-PRO$_{SIM}$ and the method proposed by A. Valsamidis and D. E. Reeve (2020) on different simulation days considering a total simulation duration of 1 year.

The first analysis shows a remarkable concordance between the values obtained from the two methods, particularly in the first 10 days of simulation, then deviating slightly as time progresses (Subplot A of Figure 7.8.4).

For an analytical comparison, see Table reported at the bottom of Figure 7.8.4, the relative values of the chosen validation metrics, calculated for several arbitrarily chosen time instants and considered representative, in particular, after 10, 100, 200 and 365 days;

From the comparative analysis, the values obtained indicate that the COAST-PRO_{SIM} is adequate for the prediction of the shoreline following the insertion of a semi-permeable groin. Although the results vary negligibly as the number of simulation days increases, they remain consistent.

The correlation coefficient approaches the value 1 already after a few days of simulation, deviating by only about 2% after one year. The BIAS remains negative, showing no significant over- or underestimates. The RMSE value remains low, suggesting good accuracy. The NMSE value is very close to 0, while the coefficient of determination R^2 is at a rather high level.

The shoreline displacement simulation, obtained by solving the Equation 7.2.1 was further conducted over a period of 20 years, with daily simulations. For illustrative purposes, in Figure 7.8.5 presents the solution for 12 arbitrarily chosen simulation days. In particular Day 1; Day 100; Day 200; Day 365, corresponding to one year from the simulation; Day 500, representing the middle of the second year, useful for observing changes after another annual cycle; Day 1000, to analyze how the dynamics change on a multi-year scale; Day 1,500, about four and a half years, representing an intermediate point in the long-term simulation; Day 2,000; Day 3,000, about eight and a half years, showing longer-term changes; Day 5,000, after some 13 and a half years of simulation and finally Day 7305, representing the final situation after 20 years of simulation.

In Figure 7.8.5 can be seen, highlighted as a red line, the evolution of the shoreline as the number of simulation days increases; in grey is the groin, which, as shown in Table 7.6-1, has a length of 15 m. Note that the following three transects are highlighted in the graph for simulation day 1. In particular Transect -100 in red; Transect 0 in magenta and Transect 100 in blue.

This colour coding is also kept constant in the graphs of subsequent configurations.

The results of the numerical simulation show a significant shoreline evolution in response to the presence of the groin. In the first 100 days, a shoreline retreat of about 5 metres is observed to the left of the groyn (in the upwind zone), due to the interruption of sediment transport along the coast. At the same time, there is an advancement of an equal magnitude to the right of the breakwater (in the under-billow zone), due to the accumulation of sediment diverted by the breakwater, which allows a partial passage of sediment, but limits erosion in the area above the breakwater. At full regime, after 20 years, the advancement of the shoreline reaches a maximum of 12 m, while the retreat is about -9 m. This difference between advancement and retreat results from the semi-permeable nature of the groin. The analysis of erosion and accretion rates indicates that the most significant variations occur during the first year of the simulation, with a progressive decrease over time.

Figure 7.8.6 confirms this trend, showing how the changes in the position of the shoreline are more pronounced in the early days of the simulation. This figure shows the trend of the shoreline Y_U as time changes for seven selected simulation days (subplot A), from Day 1 to Day 7305 (same as previous).

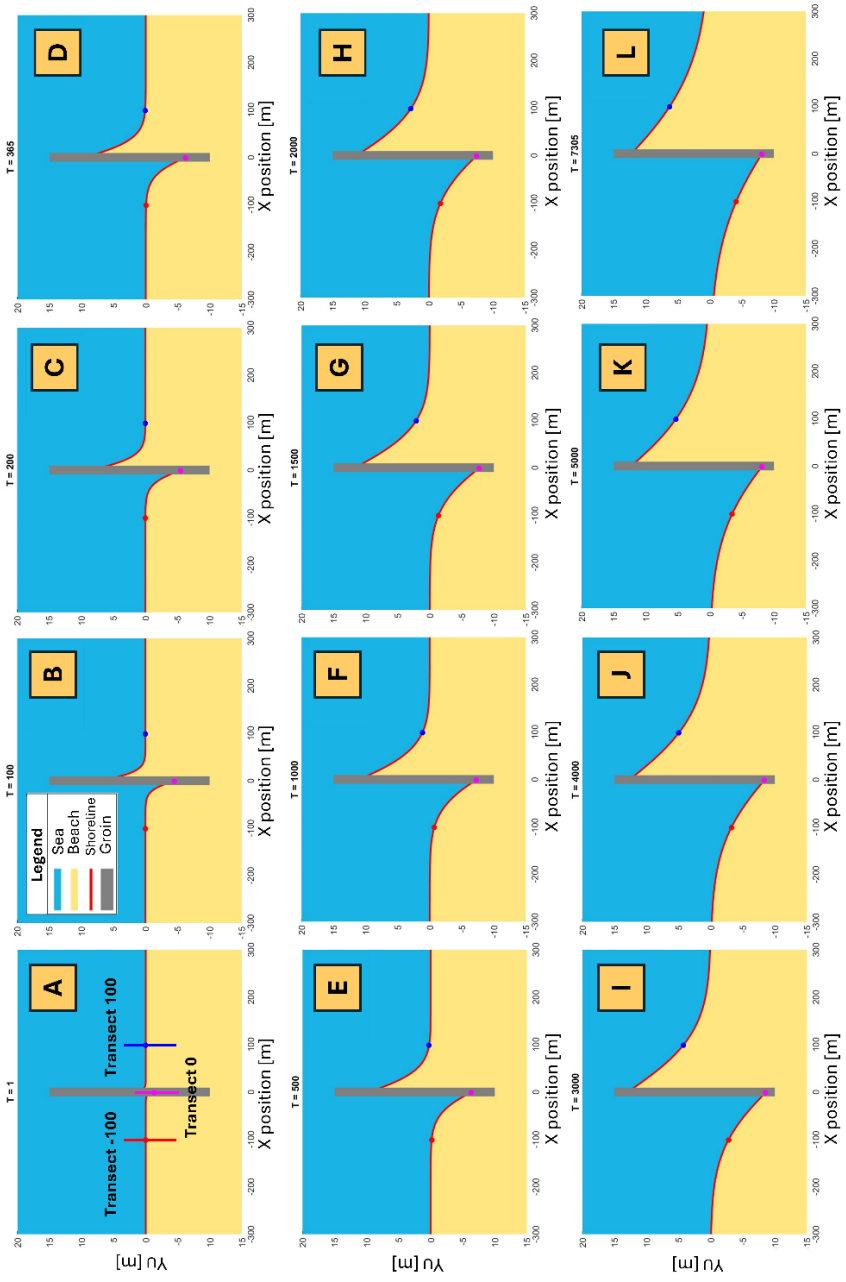

Figure 7.8.5 - Trend of Yu for 12 selected simulation days considering an overall simulation of 20 years.

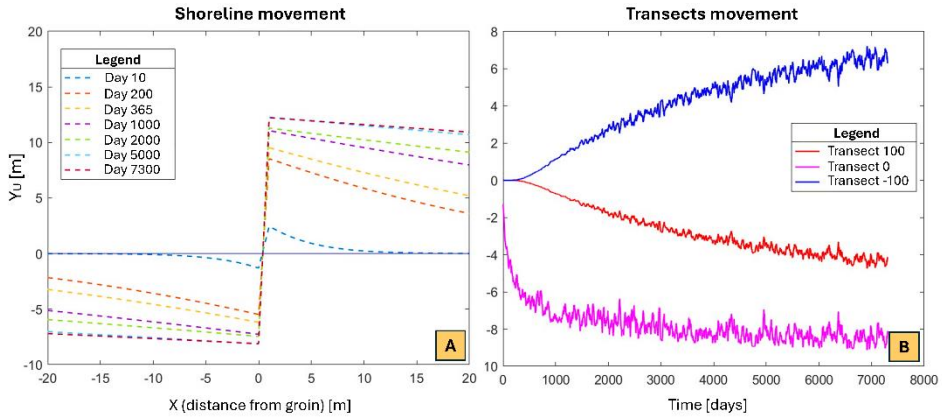

Figure 7.8.6 - Development of Yu as time changes for seven selected simulation days, considering a total simulation period of 20 years.

Figure 7.8.6 shows also (subplot B) the evolution over time of the shoreline Y_U at the three selected transects (-100, 0 and 100).

It can be noted that the transects -100 and 0 show a general decreasing trend over time, indicating progressive erosion. Erosion is particularly pronounced in the transect 0, suggesting that the area near the groin is subject to greater erosion. In contrast, transect 100 shows an upward trend, indicating an accumulation of sediment.

In addition, all three curves show oscillations around the general trend. These oscillations are due to the interaction between wave motion and sedimentary dynamics, which the COAST-PRO$_{SIM}$ takes into account. The oscillations become more pronounced as time passes. This could be because, initially, the system is dominated by processes of adaptation to the new condition imposed by the groin, while later more complex mechanisms related to the interaction between wave motion and bottom morphology come into play. These observations are in line with the idea that cross-shore transport plays an important role in sedimentary dynamics. Wave motion suspends sediments, which are then transported along the profile under the action of wave-induced currents. This process generates fluctuations in the amount of sediment present at a given point, which are reflected in the fluctuations of the parameter considered.

7.9 Real case study results

7.9.1 San Leone

In the course of this thesis, the COAST-PRO$_{SIM}$ was applied for the prediction of the shoreline following the construction of six breakwaters, shown in Figure 7.9.1 and its results were subsequently compared with shoreline observations detected from satellite images.

Considering a horizontal shoreline development, in Figure 7.9.2 above shows the shoreline simulated by the model and the four shorelines detected from satellite images, and below shows the deviation between the model results and the comparison observations. From a first visual analysis, it is possible to see an overestimation of advancement at reef No. 4 where the observations report a lesser advancement, probably due to the fact that the drift in the opposite direction was interrupted due to the deposition caused by the presence of the structures.

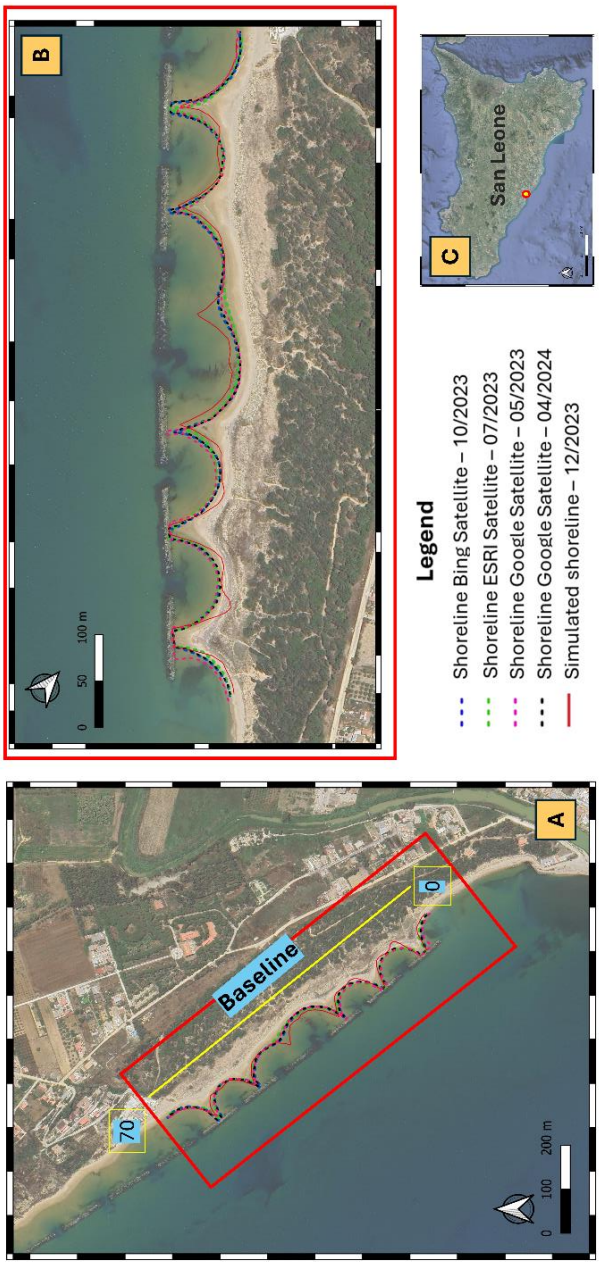

Figure 7.9.1 - San Leone study area. SR: WGS84 UTM 33N - 32633

From the analysis of the deviations, however, the greatest difference between the model and observations is evident at barrier No. 6, where the model does not predict the formation of a tombolo on the last day of the simulation (December 2023), which is instead found in the observations of the satellite images. Quantitatively, the observations between simulated and observed reach the maximum negative value of -47 m compared to the Google Satellite images on May 2023 and the maximum positive difference of +31 m compared to the ESRI Satellite images on July 2023 precisely at barrier No. 3.

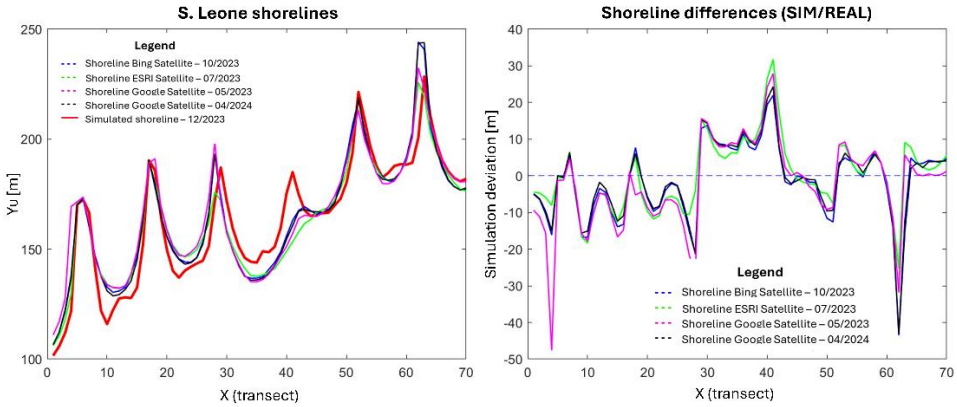

Figure 7.9.2 - Top: the shoreline simulated by the model and the four shorelines observed from satellite images; bottom: the deviation between the model results and the St. Leo comparison observations. Inserire Subplot A e B

The comparative analysis between the model results and satellite observations shows a high accuracy in predicting the coastline. With a tolerance of 10, 15 and 20 metres, the model has an accurate prediction rate of 68% to 77%, 85% to 90% and 92% to 96% respectively (*Table 7.9-1*). These results indicate that the model is able to capture the coastal dynamics of the studied sites with good approximation.

Table 7.9-1 - Percentage of accurate predictions of the COAST-PRO$_{SIM}$ for different tolerances and satellite image acquisition periods for San Leone beach.

Tolerance (m)	Bing (October 2023)	ESRI (July 2023)	Google (May 2023)	Google (March 2024)
10	73%	77%	68%	76%
15	89%	90%	85%	89%
20	96%	96%	95%	92%

Table 7.9-2 shows the values of the chosen validation metrics for the comparison between simulated data from the COAST-PRO$_{SIM}$ and observations from satellite imagery.

Table 7.9-2 - Analytical comparison between the results obtained with the COAST-PRO$_{SIM}$ model and observations from satellite images with relative values of the chosen validation metrics: Correlation Coefficient, BIAS, RMSE, NMSE, Coefficient of Determination R^2 for the San Leone beach.

Validation metrics between simulated and observed data

	Bing (October 2023)	ESRI (July 2023)	Google (May 2023)	Google (March 2024)
CC	0.93	0.94	0.90	0.93
BIAS	-1.39	0.17	-2.01	-0.84
RMSE	10.35	9.63	12.25	10.23
NMSE	0.14	0.14	0.23	0.13
R^2	0.85	0.85	0.77	0.86

Analytical comparison of the values obtained indicate that the COAST-PROs$_{SIM}$ is suitable for predicting the shoreline for San Leone beach following the insertion of the six breakwaters.

The statistical analysis showed a high correlation between the model results and the observed data, with a correlation coefficient close to 1. The BIAS, slightly negative for the Bing Satellite (October 2023), Google Satellite (May 2023 and March 2024) images, indicates a slight tendency for the model to underestimate erosion. The RMSE and NMSE confirm the good accuracy of the predictions, and the coefficient of determination R^2 is quite high.

The results show the model's ability to reproduce the formation of tombolos at the first barrier, after approximately day 3,000 of simulation, and at the second barrier at the end of the simulation, as well as the formation of salients for the others. Furthermore, the model reproduces the oscillations of the coastline due to the interaction with wave motion. In particular, it can be observed that the oscillations are less pronounced in the early stages of the simulation, to become more pronounced later on due to the greater amount of sediment placed in suspension. An example of this behavior is presented in Figure 7.9.3 (bottom subplot).

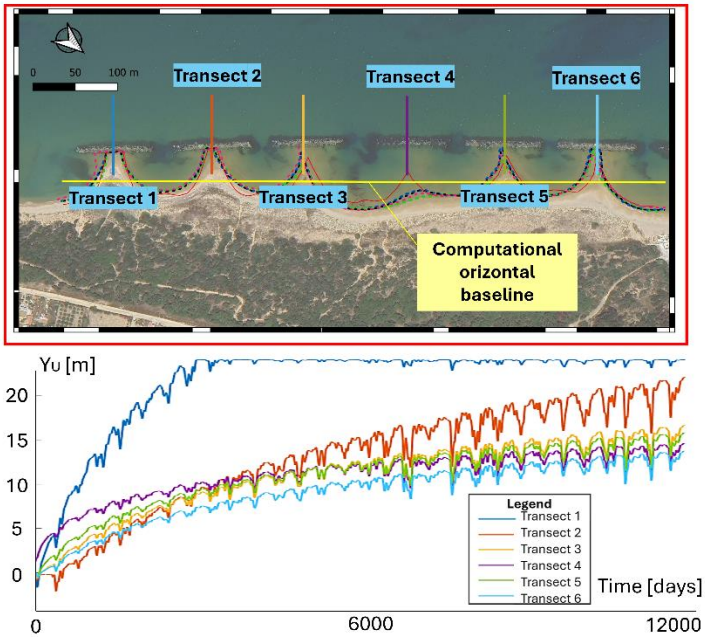

Figure 7.9.3 - On the left the shoreline simulated with the COAST-PRO$_{SIM}$. for San Leone beach in its final configuration in December 2023, and on the right the trend at the transects.

7.9.2 Porto Empedocle

As already anticipated COAST-PRO$_{SIM}$ was applied for the prediction of the shoreline following the construction of the harbour, the inner arm of which is treated as a long impermeable groin, shown in Figure 7.9.4 and its results were subsequently compared with shoreline observations from satellite images. It should be noted that only the under-billow zone of the harbour, characterised by sediment accumulation, has been dealt with. The area above the groin, which is characterised by erosion, is omitted here because, to the left of the harbour, there is no more beach, but only the harbour itself, making the erosion phenomenon irrelevant for this specific area.

Figure 7.9.4 - Porto Empedocle study area with shorelines.

The same procedure described in the case study for the San Leone beach was used to characterise the meteo-marine climate.

Considering a horizontal shoreline development, in Figure 7.9.5 above shows the shoreline simulated by the model and the four shorelines observed from satellite images, and below shows the deviation between the model results and the comparison observations. From a first visual analysis, it is possible to see how the five shorelines do not overlap, with differences between the various observations as well.

From the analysis of the deviations, on the other hand, the greatest difference between model and observations is evident in the area immediately behind the harbour arm. Quantitatively, the observations between simulated and observed reach the maximum negative value of -21 m compared to the Google Satellite images in March 2024 and the maximum positive difference of +22 m compared to the Bing Satellite images on October 2023.

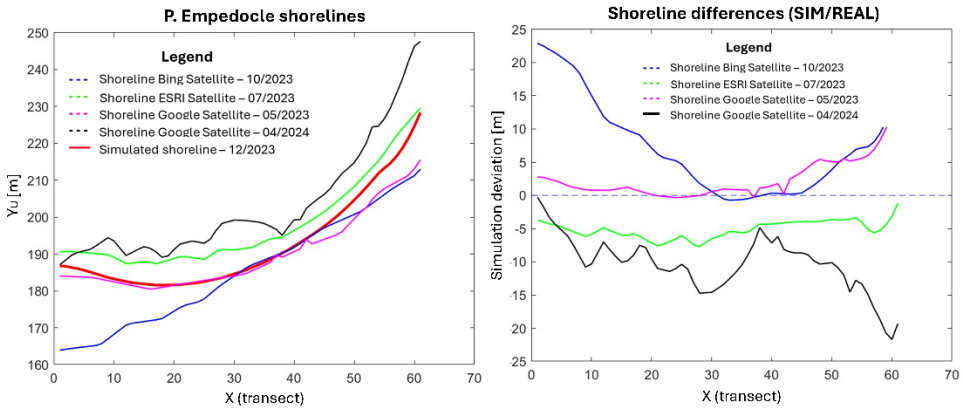

Figure 7.9.5 - Top: the shoreline simulated by the model and the four shorelines observed from satellite images; bottom: the deviation between the model results and the comparison observations.

The comparative analysis of the results for Porto Empedocle showed greater accuracy in the model's ability to predict the coastline than for San Leone (7.7.1). In particular, with tolerances of 20 metres there is always an accuracy above 90%

and for a tolerance of 10 metres, the accuracy is never less than 70% (Table 7.9-3).

Table 7.9-3 - Percentage of accurate predictions of the COAST-PRO$_{SIM}$ for different tolerances and satellite image acquisition periods for the Porto Empedocle beach.

Tolerance [m]	**Bing (October 2023)**	**ESRI (July 2023)**	**Google (May 2023)**	**Google (March 2024)**
10	70%	100%	50%	96%
15	82%	100%	92%	100%
20	90%	100%	97%	100%

In Table 7.9-4 shows the values of the chosen validation metrics for the comparison between simulated data from the COAST-PRO$_{SIM}$ model and observations from satellite imagery.

Table 7.9-4 - Analytical comparison between the results obtained with the COAST-PRO$_{SIM}$ model and observations from satellite images with relative values of the validation metrics: Correlation Coefficient, BIAS, RMSE, NMSE, Coefficient of Determination R^2 for the Porto Empedocle beach.

Validation metrics between simulated and observed data

	Bing (October 2023)	**ESRI (July 2023)**	**Google (May 2023)**	**Google (March 2024)**
CC	0.88	0.99	0.99	0.98
BIAS	7.24	-5.13	2.47	-10.35
RMSE	10.09	5.30	3.84	11.14
NMSE	0.46	0.20	0.15	0.51

R^2	0.53	0.80	0.85	0.48

Analytical comparison of the values obtained indicate that the COAST-PRO$_{SIM}$ is suitable for the prediction of the shoreline for the Porto Empedocle beach following the insertion of a groin.

The correlation coefficient is very close to value 1, the lowest value being for the Bing Satellite observation dated October 2023. The BIAS has slightly different values; it is positive when comparing the Bing Satellite images from October 2023 and the Google Satellite images from May 2023, indicating an, albeit negligible, overestimation of the model. In contrast, it remains negative for ESRI Satellite's July 2023 and Google Satellite's March 2024 images. The RMSE value remains within the same order of magnitude for all four comparison images, indicating no substantial differences. The value of NMSE is close to 0, and finally, the coefficient of determination R^2 is quite high when comparing the 2023 images for ESRI Satellite and Google Satellite.

Again, the results of the simulation reveal model's ability to reproduce the position of the shoreline at a groin and the graph on the right shows that the model reproduces the oscillations of the shoreline due to interaction with wave motion. As in the previous case concerning the San Leone beach, the oscillations are less pronounced in the early stages of the simulation, becoming more pronounced later.

7.9.3 Villafranca Tirrena

In the course of this thesis, the COAST-PRO $_{SIM}$ was applied for the prediction of the shoreline following the construction of five groins, shown in Figure 7.9.6 and its results were subsequently compared with observations from satellite images.

Figure 7.9.6 - Villafranca Tirrena study area. Same SR of previous figures.

Considering a horizontal shoreline development, in Figure 7.9.7 above shows the shoreline simulated by the model and the four shorelines observed from satellite images, and below shows the deviation between the model results and the comparison observations. From a first visual analysis, it is possible to see the absence of any particular areas of overestimation or underestimation of the model compared to the observations.

On the other hand, the analysis of the deviations shows the negative deviation from the observations of the Google Satellite images dated May 2023 and the positive deviation from the Google Satellite images dated March 2024. Quantitatively, the observations between simulated and observed reach the maximum negative value of -21 m compared to the Bing Satellite images dated October 2023 and the maximum positive difference of +10 m compared to the same satellite images.

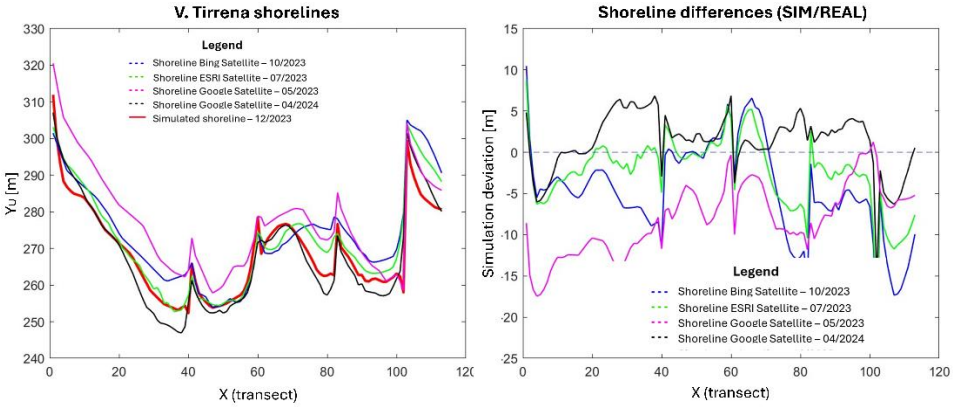

Figure 7.9.7 - Top: the shoreline simulated by the model and the four shorelines observed from satellite images; bottom: the deviation between the model results and the Villafranca Tirrena comparison observations. Subplot A e B

Analysing the comparison with satellite image observations, it appears that the model is able to accurately predict the position of the shoreline. Specifically, with a tolerance of 10 m deviation between simulated and actual, the results are:

The comparative analysis of the results for Villafranca Tirrena showed excellent accuracy in the model's ability to predict the coastline. In particular, with tolerances of 20 metres, there is always an accuracy of over 99% and for a

tolerance of 10 metres, while reaching an accuracy of less than 70% for the year 2024, this exceeds 80% for the observations of the year 2023 (Table 7.9-5).

Table 7.9-5 - Percentage of accurate predictions of the COAST-PRO$_{SIM}$ for different tolerances and satellite image acquisition periods for Villafranca Tirrena beach.

Tolerance (m)	**Bing (October 2023)**	**ESRI (July 2023)**	**Google (May 2023)**	**Google (March 2024)**
10	83%	93%	99%	67%
15	94%	99%	99%	96%
20	99%	99%	100%	100%

Table 7.9-6 shows the values of the chosen validation metrics for the comparison between simulated data from the COAST-PRO$_{SIM}$ model and observations from satellite imagery.

Table 7.9-6 - Analytical comparison between the results obtained with the COAST-PRO$_{SIM}$ model and observations from satellite images with relative values of the validation metrics: Correlation Coefficient, BIAS, RMSE, NMSE, Coefficient of Determination R^2 for the Villafranca Tirrena beach.

Validation metrics between simulated and observed data

	Bing (October 2023)	**ESRI (July 2023)**	**Google (May 2023)**	**Google (March 2024)**
CC	0.90	0.95	0.95	0.98
BIAS	-4.64	-2.46	-8.12	1.30
RMSE	7.41	4.99	9.12	3.81
NMSE	0.31	0.13	0.45	0.07
R^2	0.68	0.86	0.54	0.93

Analytical comparison of the values obtained indicate that the COAST-PRO$_{SIM}$ is suitable for predicting the shoreline for the beach of Villafranca Tirrena following the construction of five groins.

The correlation coefficient is very close to a value of 1, reaching maximum values when compared to the Google Satellite images of March 2024. The BIAS is negative when comparing Bing Satellite images from October 2023, ESRI Satellite images from July 2023 and Google Satellite images from May 2023, indicating a slight underestimation of the model. However, the BIAS is positive for the Google Satellite images of March 2024. The RMSE value is similar for all four comparison images, suggesting no substantial differences between them. The value of NMSE is close to 0, with better performance for the Google Satellite images of March 2024. Finally, the coefficient of determination R^2 is relatively high, with optimal results again for the March 2024 Google Satellite images. These results indicate that the Google Satellite images are the most accurate in representing the simulated shoreline.

7.10 Computation time

All simulations were run on a powerful desktop computer equipped with a Windows 10 operating system, a 3.00 GHz Intel Core i9-13900K processor and 32 GB RAM.

The case study of Porto Empedocle, characterised by a relatively simple geometry and a limited study area, took approximately five minutes to calculate. The case studies of San Leone and Villafranca Tirrena, with more complex geometries and larger study areas, took approximately 30 minutes and 20 minutes of calculation time respectively.

These results highlight one of the main strengths of the model: its ability to provide accurate results in extremely fast calculation times, making it an ideal tool for scenario analysis and decision making in coastal engineering.

7.11 Final considerations

This chapter has tackled the problem of coastal erosion in depth, proposing an innovative simulation model for evaluating the effectiveness of coastal protection structures. It stands out for its ability to integrate a variety of variables and phenomena that influence shoreline evolution, making it a versatile tool for analysing coastal dynamics.

The simulations carried out on real case studies, including San Leone, Porto Empedocle and Villafranca Tirrena, highlighted the model's ability to provide detailed and reliable predictions of the evolution of the coastline in the presence of protection structures day by day. The results obtained show that the model can be used effectively as a support tool for coastal planning, adapting to the geographical and environmental specificities of different contexts. This flexibility allows its application to a wider range of coastal environments possible, making a significant contribution to the sustainable management of coastal resources.

The main conclusion of this research is the obvious utility of advanced numerical models for coastal management and protection. Although the use of such models requires the availability of high-quality data and access to adequate computational resources, they are an indispensable tool for understanding the complex dynamics of erosion and sedimentation, as well as for assessing the impact of natural phenomena and anthropogenic interventions. Indeed, the ability to simulate future scenarios related to climate change, extreme events and variations in sediment transport makes it possible to anticipate the potential consequences of human actions and natural phenomena. This is particulary important in the context of the increasing vulnerability of coastal areas, where threats associated with climate change, such as sea level rise and increased frequency of extreme weather and sea events, make the adoption of adaptation and mitigation strategies urgent. For example, using forcings input data that consider more extreme meteorological and marine climate scenarios (obtained through the application of the model presented in Chapter 3) allows, from a management and analysis perspective, to simulate the behavior of structures on coastal dynamics, allowing timely action.

Despite the promising results, it is crucial to emphasize that the accuracy of predictions is highly dependent on the quality of the input data used to feed the model. In many cases, there is a need to improve data collection and analysis practices to reduce the uncertainty associated with simulations and provide more reliable indications to decision-makers. Furthermore, in order to ensure that the model can meet the specific needs of different geographical areas, it is essential that it continues to be refined and validated in an increasing number of coastal contexts.

Conclusions and future developments

The conclusions of this Doctoral Thesis summarise an in-depth research course aimed at exploring the evolution of coastal areas, with a particular focus on the combined impacts of natural dynamics and human activities, and the application of advanced tools and methodologies for coastal monitoring and management. This multidisciplinary work has integrated innovative techniques, such as artificial intelligence models and spatial analysis, to develop more accurate and reliable prediction and management tools for coastal areas, contributing to a comprehensive and detailed perspective on coastal issues.

A distinctive contribution of this research is the use of advanced predictive models, such as Conv-LSTM and the U-net network for semantic image segmentation. The application of artificial intelligence has shown significant potential in refining marine condition predictions and accurately mapping shoreline changes. The simulations carried out demonstrated the importance of including geographic, atmospheric, and oceanographic variables to ensure more reliable predictions, which are particularly relevant in complex contexts like the Mediterranean basin, characterised by high spatial and temporal variability.

From a methodological perspective, the thesis highlighted the value of using semantic segmentation techniques for large-scale monitoring of coastal changes, achieving accurate classifications of coastal areas and tracing long-term landscape evolution. The segmentation results, integrated with detailed spatial analysis of different land-use types, revealed how urbanisation and other human pressures are transforming coastal landscapes, contributing to beach loss and changes in natural vegetation.

Additionally, a fundamental aspect of this work was the development of the Coastal Dynamics Analyser (CDA) plugin for QGIS, an innovative tool that provides a highly efficient open-source alternative for analyzing coastal dynamics. This plugin represents a significant advancement in coastal dynamics analysis due to its speed and efficiency in handling transect data, making it particularly useful for regional studies as a fully user-friendly and free-source tool. Its features offer a practical solution for understanding erosion processes and planning adaptation measures, with future potential including additional metrics and Area Based Analysis (ABA), which is currently nearing completion. The integration of CDA within an open-source system like QGIS expands access to its capabilities for researchers and professionals in coastal management.

Finally in the context of coastal protection, this thesis also developed an innovative model to evaluate the effectiveness of defense structures against erosion, emphasizing the need for sophisticated numerical models to thoroughly understand erosional and sedimentary phenomena. These models not only support critical coastal planning decisions but also enable the anticipation of climate change impacts, facilitating the development of more targeted adaptation and mitigation strategies. It became clear that an integrated approach, combining meteorological and marine data with numerical modeling, can improve prediction accuracy, reducing uncertainties linked to the quality of the input data.

At the time of writing this Thesis, a study is being developed to understand and assess coastal vulnerability along the Tuscan coastline, through the combined application of the Coastal Vulnerability Index (CeVI) and the analysis of Net Shoreline Movement (NSM) and in which all topics covered during the chapters of this Thesis are used to provide up-to-date coastal vulnerability maps. This approach aims to build a model that integrates a wide range of physical, morphological and hydraulic parameters, including geomorphological characteristics, resilience of coastal areas and factors related to the energy of erosive agents. The work is carrying out together with colleagues from the CNR Pisa and the Department of Geological Sciences of the University of Palermo, in a research article entitled “Application of the validated CeVI methodology to the Tuscany coastline, Italy”.
The choice of the Tuscan coast as the study area is motivated by its geomorphological complexity and the variety of natural and anthropic pressures that characterise it, making it an ideal laboratory for analysing the dynamics of coastal vulnerability. This region presents a delicate balance between highly urbanised stretches of coastline, protected natural areas and strategic river mouths, offering a diverse context for testing risk assessment models and identifying integrated management solutions.
The aim of the work is to identify the areas most at risk of erosion, distinguishing coastal stretches subject to increased exposure from those characterised by relative stability. Through targeted analysis, the intention is to isolate intrinsic vulnerability factors in order to better understand the processes influencing coastal dynamics, separating them from actual changes in the coastline. The latter, rather than being used as inputs to the model, will be used as validation tools to confirm the accuracy of the risk classifications.
In particular, the study plans to examine the degree of morphodynamic connectivity between catchment areas, river mouths and adjacent coastal cells, with a specific focus on sediment transport and availability along the coastline. The role of hydraulic infrastructures and port works in modifying sediment transport capacity and sediment distribution is also expected to be investigated,

integrating high-resolution data on meteo-marine conditions and seabed morphology.
Finally, the work aims to provide an updated regional map of coastal vulnerability as an operational tool to identify critical areas and plan targeted mitigation and protection interventions. This innovative approach intends to offer a complete and reliable picture of the risk conditions, contributing to a sustainable and proactive management of the Tuscan coastline.

In conclusion, the research period, of which this Thesis is the summary, has made a significant contribution to the understanding of coastal dynamics, proposing innovative tools for monitoring, forecasting, and managing vulnerable areas. The integrated approach that combines numerical models, remote sensing, and vulnerability analysis enables a multidimensional and comprehensive view of coasts, essential to addressing future challenges posed by climate change, urbanization, and erosion. The results obtained from a solid foundation for the development of more targeted and sustainable coastal management policies, guiding territorial planning towards adaptive and proactive solutions essential for the protection and preservation of natural heritage. This thesis therefore aims to lay the groundwork for future research, reaffirming the importance of continuous monitoring, high-quality data collection, and the use of increasingly sophisticated models to effectively to address coastal challenges effectively and in a timely manner.

Bibliography

A. k, P., M, M., Rajamanickam, S., Sivarethinamohan, S., Gaddam, M. K. R., Velusamy, P., R, G., Ravindiran, G., Gurugubelli, T. R., & Muniasamy, S. K. (2023). Impact of climate change and anthropogenic activities on aquatic ecosystem – A review. *Environmental Research*, *238*, 117233. https://doi.org/10.1016/j.envres.2023.117233

Abd-Elhamid, H. F., Zeleňáková, M., Barańczuk, J., Gergelova, M. B., & Mahdy, M. (2023). Historical trend analysis and forecasting of shoreline change at the Nile Delta using RS data and GIS with the DSAS tool. *Remote Sensing*, *15*(7), 1737.

Abdullah, A. Y. M., Masrur, A., Adnan, M. S. G., Baky, Md. A. A., Hassan, Q. K., & Dewan, A. (2019). Spatio-temporal Patterns of Land Use/Land Cover Change in the Heterogeneous Coastal Region of Bangladesh between 1990 and 2017. *Remote Sensing*, *11*(7), Articolo 7. https://doi.org/10.3390/rs11070790

Abuzahrah, S. S., Akhdhar, A., & Baeshen, M. N. (2023). Studying The Impact Of Physicochemical Parameters In Marine Sediments. *Journal of Pharmaceutical Negative Results*, 539–558. https://doi.org/10.47750/pnr.2023.14.S02.67

Aghdami-Nia, M., Shah-Hosseini, R., Rostami, A., & Homayouni, S. (2022). Automatic coastline extraction through enhanced sea-land segmentation by modifying Standard U-Net. *International Journal of Applied Earth Observation and Geoinformation*, *109*, 102785. https://doi.org/10.1016/j.jag.2022.102785

Albon, C. (s.d.). *Machine Learning with Python Cookbook: Practical Solutions From Preprocessing to Deep Learning*.

Albuquerque, M., Espinoza, J., Teixeira, P., De Oliveira, A., Corrêa, I., & Calliari, L. (2013). Erosion or Coastal Variability: An Evaluation of the DSAS and the Change Polygon Methods for the Determination of Erosive Processes on Sandy Beaches. *Journal of Coastal Research*, *165*, 1710–1714. https://doi.org/10.2112/SI65-289.1

Alvarez-Cuesta, M., Toimil, A., & Losada, I. J. (2021). Modelling long-term shoreline evolution in highly anthropized coastal areas. Part 1: Model description and validation. *Coastal Engineering*, *169*, 103960. https://doi.org/10.1016/j.coastaleng.2021.103960

Analytical Solutions of One-Line Model for Shoreline Change near Coastal Structures | Journal of Waterway, Port, Coastal, and Ocean Engineering | Vol 123, No 4. (s.d.). Recuperato 5 novembre 2024, da https://ascelibrary.org/doi/abs/10.1061/(ASCE)0733-950X(1997)123:4(180)

Anfuso, G., Bowman, D., Danese, C., & Pranzini, E. (2016). Transect based analysis versus area based analysis to quantify shoreline displacement: Spatial resolution issues. *Environmental monitoring and assessment*, *188*, 1–14.

Anfuso, G., & Martínez Del Pozo, J. Á. (2009). Assessment of Coastal Vulnerability Through the Use of GIS Tools in South Sicily (Italy). *Environmental Management*, *43*(3), 533–545. https://doi.org/10.1007/s00267-008-9238-8

Anfuso, G., Martínez-del-Pozo, J. Á., & Rangel-Buitrago, N. (2012). Bad Practice in Erosion Management: The Southern Sicily Case Study. In J. A. G. Cooper & O. H. Pilkey (A c. Di), *Pitfalls of Shoreline Stabilization* (Vol. 3, pp. 215–233). Springer Netherlands. https://doi.org/10.1007/978-94-007-4123-2_13

Anfuso, G., Martínez-del-Pozo, J. Á., & Rangel-Buitrago, N. (2013). Morphological cells in the Ragusa littoral (Sicily, Italy). *Journal of Coastal Conservation*, *17*(3), 369–377. https://doi.org/10.1007/s11852-013-0233-8

Anfuso, G., Pranzini, E., & Vitale, G. (2011). An integrated approach to coastal erosion problems in northern Tuscany (Italy): Littoral morphological evolution and cell distribution. *Geomorphology*, *129*(3–4), 204–214. https://doi.org/10.1016/j.geomorph.2011.01.023

Angeli, F. (2019). *The injured coast: The degradation of the Italian coastal landscape between unauthorized development, eco-mafia and regulations*.

Armenio, E., De Serio, F., Mossa, M., Nobile, B., & Petrillo, A. F. (2017). *Investigation on coastline evolution using long-term observations and numerical modelling*. ISOPE-I.

Armenio, E., De Serio, F., Mossa, M., & Petrillo, A. F. (2019). Coastline evolution based on statistical analysis and modeling. *Natural Hazards and Earth System Sciences*, *19*(9), 1937–1953.

Azzopardi, B., Balzan, M. V., Cherif, S., Doblas-Miranda, E., dos Santos, M., Dobrinski, P., Falder, M., Hassoun, A. E. R., Giupponi, C., & Koubi, V. V. (2020). *Climate and environmental*

change in the Mediterranean basin–Current situation and risks for the future. First Mediterranean assessment report.

Bai, X., Jia, X., Jia, Y., & Hu, W. (2020). Modeling long-term soil water dynamics in response to land-use change in a semi-arid area. *Journal of Hydrology*, *585*, 124824.

Bailard, J. A. (1981). An energetics total load sediment transport model for a plane sloping beach. *Journal of Geophysical Research: Oceans*, *86*(C11), 10938–10954. https://doi.org/10.1029/JC086iC11p10938

Ballesteros, C., & Esteves, L. S. (2021). Integrated Assessment of Coastal Exposure and Social Vulnerability to Coastal Hazards in East Africa. *Estuaries and Coasts*, *44*(8), 2056–2072. https://doi.org/10.1007/s12237-021-00930-5

Behera, R., Kar, A., Das, M. R., & Panda, P. P. (2019). GIS-based vulnerability mapping of the coastal stretch from Puri to Konark in Odisha using analytical hierarchy process. *Natural Hazards*, *96*(2), 731–751. https://doi.org/10.1007/s11069-018-03566-0

Benassai, G. (2006). *Introduction to Coastal Dynamics and Shoreline Protection*.

Bengio, Y. (2012). Practical recommendations for gradient-based training of deep architectures. In *Neural networks: Tricks of the trade: Second edition* (pp. 437–478). Springer.

Bento, P., Pombo, J., Mendes, R., Calado, M., & Mariano, S. (2021). Ocean wave energy forecasting using optimised deep learning neural networks. *Ocean Engineering*, *219*, 108372.

Bias (statistica). (2024). In *Wikipedia*. https://it.wikipedia.org/w/index.php?title=Bias_(statistica)&oldid=139619189

Boak, E. H., & Turner, I. L. (2005a). Shoreline Definition and Detection: A Review. *Journal of Coastal Research*, *214*, 688–703. https://doi.org/10.2112/03-0071.1

Boak, E. H., & Turner, I. L. (2005b). Shoreline Definition and Detection: A Review. *Journal of Coastal Research*, *214*, 688–703. https://doi.org/10.2112/03-0071.1

Boak, E. H., & Turner, I. L. (2005c). Shoreline Definition and Detection: A Review. *Journal of Coastal Research*, *214*, 688–703. https://doi.org/10.2112/03-0071.1

Bolaños-Sanchez, R., Sanchez-Arcilla, A., & Cateura, J. (2007). Evaluation of two atmospheric models for wind–wave modelling in the NW Mediterranean. *Journal of Marine Systems*, *65*(1–4), 336–353.

Booij, N., Ris, R. C., & Holthuijsen, L. H. (1999). A third-generation wave model for coastal regions: 1. Model description and validation. *Journal of geophysical research: Oceans*, *104*(C4), 7649–7666.

Borrelli, P., Robinson, D. A., Panagos, P., Lugato, E., Yang, J. E., Alewell, C., Wuepper, D., Montanarella, L., & Ballabio, C. (2020). Land use and climate change impacts on global soil erosion by water (2015-2070). *Proceedings of the National Academy of Sciences*, *117*(36), 21994–22001.

Borzì, L., Anfuso, G., Manno, G., Distefano, S., Urso, S., Chiarella, D., & Di Stefano, A. (2021). Shoreline Evolution and Environmental Changes at the NW Area of the Gulf of Gela (Sicily, Italy). *Land*, *10*(10), 1034. https://doi.org/10.3390/land10101034

Boumboulis, V., Apostolopoulos, D., Depountis, N., & Nikolakopoulos, K. (2021). The importance of geotechnical evaluation and shoreline evolution in coastal vulnerability index calculations. *Journal of Marine Science and Engineering*, *9*(4), 423.

Briassoulis, H. (2009). Factors influencing land-use and land-cover change. *Land cover, land use and the global change, encyclopaedia of life support systems (EOLSS)*, *1*, 126–146.

Brownlee, A. E. I., Adair, J., Haraldsson, S. O., & Jabbo, J. (2021a). Exploring the Accuracy – Energy Trade-off in Machine Learning. *2021 IEEE/ACM International Workshop on Genetic Improvement (GI)*, 11–18. https://doi.org/10.1109/GI52543.2021.00011

Brownlee, A. E. I., Adair, J., Haraldsson, S. O., & Jabbo, J. (2021b). Exploring the Accuracy – Energy Trade-off in Machine Learning. *2021 IEEE/ACM International Workshop on Genetic Improvement (GI)*, 11–18. https://doi.org/10.1109/GI52543.2021.00011

Bruun, P. (1962). Sea-Level Rise as a Cause of Shore Erosion. *Journal of the Waterways and Harbors Division*, *88*(1), 117–130. https://doi.org/10.1061/JWHEAU.0000252

Bruun, P. (1983). Review of conditions for uses of the Bruun rule of erosion. *Coastal Engineering*, *7*(1), 77–89. https://doi.org/10.1016/0378-3839(83)90028-5

Bruun, P. (1988). The Bruun Rule of Erosion by Sea-Level Rise: A Discussion on Large-Scale Two- and Three-Dimensional Usages. *Journal of Coastal Research*, *4*(4), 627–648.

Burningham, H., & Fernandez-Nunez, M. (2020). Shoreline change analysis. In *Sandy beach morphodynamics* (pp. 439–460). Elsevier.

Buscombe, D., Wernette, P., Fitzpatrick, S., Favela, J., Goldstein, E. B., & Enwright, N. M. (2023a). A 1.2 Billion Pixel Human-Labeled Dataset for Data-Driven Classification of Coastal Environments. *Scientific Data*, *10*(1), 46. https://doi.org/10.1038/s41597-023-01929-2

Buscombe, D., Wernette, P., Fitzpatrick, S., Favela, J., Goldstein, E. B., & Enwright, N. M. (2023b). A 1.2 Billion Pixel Human-Labeled Dataset for Data-Driven Classification of Coastal Environments. *Scientific Data*, *10*(1), Articolo 1. https://doi.org/10.1038/s41597-023-01929-2

Buslaev, A., Iglovikov, V. I., Khvedchenya, E., Parinov, A., Druzhinin, M., & Kalinin, A. A. (2020). Albumentations: Fast and Flexible Image Augmentations. *Information*, *11*(2), 125. https://doi.org/10.3390/info11020125

Camus, P., Mendez, F. J., Medina, R., Tomas, A., & Izaguirre, C. (2013a). High resolution downscaled ocean waves (DOW) reanalysis in coastal areas. *Coastal Engineering*, *72*, 56–68.

Camus, P., Mendez, F., Medina, R., Tomas, A., & Izaguirre, C. (2013b). High resolution downscaled ocean waves (DOW) reanalysis in coastal areas. *Coastal Engineering*, *72*, 56–68. https://doi.org/10.1016/j.coastaleng.2012.09.002

Cañellas, B., Orfila, A., Méndez, F. J., Menéndez, M., Gómez-Pujol, L., & Tintoré, J. (2024). Application of a POT model to estimate the extreme significant wave height levels around

the Balearic Sea (Western Mediterranean). *Journal of Coastal Research*, *50*(sp1), 329–333.

Cao, W., Zhou, Y., Li, R., & Li, X. (2020). Mapping changes in coastlines and tidal flats in developing islands using the full time series of Landsat images. *Remote Sensing of Environment*, *239*, 111665. https://doi.org/10.1016/j.rse.2020.111665

Carranza-García, M., García-Gutiérrez, J., & Riquelme, J. C. (2019). A framework for evaluating land use and land cover classification using convolutional neural networks. *Remote Sensing*, *11*(3), 274.

Casaioli, M., Catini, F., Inghilesi, R., Lanucara, P., Malguzzi, P., Mariani, S., & Orasi, A. (2014). An operational forecasting system for the meteorological and marine conditions in Mediterranean regional and coastal areas. *Advances in Science and Research*, *11*(1), 11–23.

Casamayor, M., Alonso, I., Valiente, N. G., & Sánchez-García, M. J. (2022). Seasonal response of a composite beach in relation to wave climate. *Geomorphology*, *408*, 108245. https://doi.org/10.1016/j.geomorph.2022.108245

Castelle, B., & Masselink, G. (2023). Morphodynamics of wave-dominated beaches. *Cambridge Prisms: Coastal Futures*, *1*, e1. https://doi.org/10.1017/cft.2022.2

Cavaleri, L., Abdalla, S., Benetazzo, A., Bertotti, L., Bidlot, J.-R., Breivik, Ø., Carniel, S., Jensen, R. E., Portilla-Yandun, J., & Rogers, W. E. (2018). Wave modelling in coastal and inner seas. *Progress in oceanography*, *167*, 164–233.

Cavaleri, L., Bertotti, L., Buizza, R., Buzzi, A., Masato, V., Umgiesser, G., & Zampieri, M. (2010). Predictability of extreme meteo-oceanographic events in the Adriatic Sea. *Quarterly Journal of the Royal Meteorological Society: A journal of the atmospheric sciences, applied meteorology and physical oceanography*, *136*(647), 400–413.

Cavaleri, L., Fox-Kemper, B., & Hemer, M. (2012). Wind waves in the coupled climate system. *Bulletin of the American Meteorological Society*, *93*(11), 1651–1661.

Celata, F., & Gioia, E. (2024). Resist or retreat? Beach erosion and the climate crisis in Italy: Scenarios, impacts and challenges. *Applied Geography*, *169*, 103335. https://doi.org/10.1016/j.apgeog.2024.103335

Chachondhia, P., Shakya, A., & Kumar, G. (2021). Performance evaluation of machine learning algorithms using optical and microwave data for LULC classification. *Remote Sensing Applications: Society and Environment*, *23*, 100599. https://doi.org/10.1016/j.rsase.2021.100599

Chang, L., Chen, Y.-T., Wu, M.-C., Alkhaleefah, M., & Chang, Y.-L. (2022). U-Net for Taiwan Shoreline Detection from SAR Images. *Remote Sensing*, *14*(20), 5135. https://doi.org/10.3390/rs14205135

Chapman, V. J. (2016). *Coastal Vegetation*. Elsevier.

Chen, L.-C., Papandreou, G., Schroff, F., & Adam, H. (2017). Rethinking atrous convolution for semantic image segmentation. *arXiv preprint arXiv:1706.05587*.

Chen, X., Yu, R., Ullah, S., Wu, D., Li, Z., Li, Q., Qi, H., Liu, J., Liu, M., & Zhang, Y. (2022). A novel loss function of deep learning in wind speed forecasting. *Energy*, *238*, 121808.

Cherneva, Z., Petrova, P., Andreeva, N., & Soares, C. G. (2005). Probability distributions of peaks, troughs and heights of wind waves measured in the black sea coastal zone. *Coastal Engineering*, *52*(7), 599–615.

Cirelli, C., Mercatanti, L., & Porto, C. M. (2003). *Sustainable development of Sicily east coast area*.

Ciro Aucelli, P. P., Di Paola, G., Incontri, P., Rizzo, A., Vilardo, G., Benassai, G., Buonocore, B., & Pappone, G. (2017). Coastal inundation risk assessment due to subsidence and sea level rise in a Mediterranean alluvial plain (Volturno coastal plain – southern Italy). *Estuarine, Coastal and Shelf Science*, *198*, 597–609. https://doi.org/10.1016/j.ecss.2016.06.017

Clemente, M. F., D'Ambrosio, V., & Focareta, M. (2022). The proposal of the Coast-RiskBySea: COASTal zones RISK assessment for Built environment bY extreme SEA level, based on the new Copernicus Coastal Zones data. *International Journal of Disaster Risk Reduction*, *75*, 102947.

Cohen, I., Huang, Y., Chen, J., Benesty, J., Benesty, J., Chen, J., Huang, Y., & Cohen, I. (2009). Pearson correlation coefficient. *Noise reduction in speech processing*, 1–4.

Cohen, J. (1960). A coefficient of agreement for nominal scales. *Educational and psychological measurement*, *20*(1), 37–46.

Cooper, J. A. G., O'Connor, M. C., & McIvor, S. (2020). Coastal defences versus coastal ecosystems: A regional appraisal. *Marine Policy*, *111*, 102332. https://doi.org/10.1016/j.marpol.2016.02.021

Crain, C. M., Halpern, B. S., Beck, M. W., & Kappel, C. V. (2009). Understanding and managing human threats to the coastal marine environment. *Annals of the New York Academy of Sciences*, *1162*(1), 39–62.

Cunha, J., Cardona, F. S., Bio, A., & Ramos, S. (2021). Importance of Protection Service Against Erosion and Storm Events Provided by Coastal Ecosystems Under Climate Change Scenarios. *Frontiers in Marine Science*, *8*. https://doi.org/10.3389/fmars.2021.726145

Dang, K. B., Dang, V. B., Ngo, V. L., Vu, K. C., Nguyen, H., Nguyen, D. A., Nguyen, T. D. L., Pham, T. P. N., Giang, T. L., Nguyen, H. D., & Hieu Do, T. (2022). Application of deep learning models to detect coastlines and shorelines. *Journal of Environmental Management*, *320*, 115732. https://doi.org/10.1016/j.jenvman.2022.115732

D'Anna, M., Idier, D., Castelle, B., Vitousek, S., & Le Cozannet, G. (2021). Reinterpreting the Bruun Rule in the Context of Equilibrium Shoreline Models. *Journal of Marine Science and Engineering*, *9*(9), Articolo 9. https://doi.org/10.3390/jmse9090974

Danovaro, R., Fanelli, E., Canals, M., Ciuffardi, T., Fabri, M.-C., Taviani, M., Argyrou, M., Azzurro, E., Bianchelli, S., & Cantafaro, A. (2020). Towards a marine strategy for the deep Mediterranean Sea: Analysis of current ecological status. *Marine Policy*, *112*, 103781.

de Oliveira Dias, L. S., Assunção, A. F., & de Jesus, F. A. N. (2024). *Free Geospatial Software and Applications*.

Dean, R. G., & Dalrymple, R. A. (2004). *Coastal Processes with Engineering Applications*. Cambridge University Press.

Del Río, L., Gracia, F. J., & Benavente, J. (2013). Shoreline change patterns in sandy coasts. A case study in SW Spain. *Geomorphology*, *196*, 252–266.

Desmet, K., Kopp, R. E., Kulp, S. A., Nagy, D. K., Oppenheimer, M., Rossi-Hansberg, E., & Strauss, B. H. (2018). *Evaluating the economic cost of coastal flooding*. National Bureau of Economic Research.

Dhingra, N., Chogovadze, G., & Kunz, A. (2021). Border-SegGCN: Improving Semantic Segmentation by Refining the Border Outline using Graph Convolutional Network. *2021 IEEE/CVF International Conference on Computer Vision Workshops (ICCVW)*, 865–875. https://doi.org/10.1109/ICCVW54120.2021.00102

Di Paola, G., Minervino Amodio, A., Dilauro, G., Rodriguez, G., & Rosskopf, C. M. (2022). Shoreline evolution and erosion vulnerability assessment along the Central Adriatic coast with the contribution of UAV beach monitoring. *Geosciences*, *12*(10), 353.

Ding, J., Deng, F., Liu, Q., & Wang, J. (2023). Regional forecasting of significant wave height and mean wave period using EOF-EEMD-SCINet hybrid model. *Applied Ocean Research*, *136*, 103582.

Dolan, R., Hayden, B., & Heywood, J. (1978). A new photogrammetric method for determining shoreline erosion. *Coastal Engineering*, *2*, 21–39.

Dong, W. S., Ariffin, E. H., Saengsupavanich, C., Rashid, M. A. M., Shukri, M. H. M., Ramli, M. Z., Miskon, M. F., Jeofry, M. H., Yunus, K., & Ghazali, N. H. M. (2023). Adaptation of coastal defence structure as a mechanism to alleviate coastal erosion in monsoon dominated coast of Peninsular Malaysia. *Journal of Environmental Management*, *333*, 117391.

Donnelly, J., Daneshkhah, A., & Abolfathi, S. (2024). Forecasting global climate drivers using Gaussian processes and convolutional autoencoders. *Engineering Applications of Artificial Intelligence*, *128*, 107536.

Du, J., & Hesp, P. A. (2020). Salt Spray Distribution and Its Impact on Vegetation Zonation on Coastal Dunes: A Review. *Estuaries and Coasts*, *43*(8), 1885–1907. https://doi.org/10.1007/s12237-020-00820-2

Earth Observations for Monitoring Marine Coastal Hazards and Their Drivers | Surveys in Geophysics. (s.d.). Recuperato 5 novembre 2024, da https://link.springer.com/article/10.1007/s10712-020-09594-5

Eea, F. (s.d.). *Pkz048-99-v0 Massimo Zotti Claudio La Mantia*.

Feng, Q., Yang, J., Zhu, D., Liu, J., Guo, H., Bayartungalag, B., & Li, B. (2019). Integrating Multitemporal Sentinel-1/2 Data for Coastal Land Cover Classification Using a

Multibranch Convolutional Neural Network: A Case of the Yellow River Delta. *Remote Sensing*, *11*(9), Articolo 9. https://doi.org/10.3390/rs11091006

Feng, Y., Zeng, Z., Searchinger, T. D., Ziegler, A. D., Wu, J., Wang, D., He, X., Elsen, P. R., Ciais, P., Xu, R., Guo, Z., Peng, L., Tao, Y., Spracklen, D. V., Holden, J., Liu, X., Zheng, Y., Xu, P., Chen, J., … Zheng, C. (2022). Doubling of annual forest carbon loss over the tropics during the early twenty-first century. *Nature Sustainability*, *5*(5), Articolo 5. https://doi.org/10.1038/s41893-022-00854-3

Feng, Z., Hu, P., Li, S., & Mo, D. (2022). Prediction of significant wave height in offshore China based on the machine learning method. *Journal of Marine Science and Engineering*, *10*(6), 836.

Fernando, K. R. M., & Tsokos, C. P. (2021). Dynamically weighted balanced loss: Class imbalanced learning and confidence calibration of deep neural networks. *IEEE Transactions on Neural Networks and Learning Systems*, *33*(7), 2940–2951.

Findell, K. L., Berg, A., Gentine, P., Krasting, J. P., Lintner, B. R., Malyshev, S., Santanello, J. A., & Shevliakova, E. (2017). The impact of anthropogenic land use and land cover change on regional climate extremes. *Nature Communications*, *8*(1), 989. https://doi.org/10.1038/s41467-017-01038-w

Foody, G. M. (2002). Status of land cover classification accuracy assessment. *Remote sensing of environment*, *80*(1), 185–201.

Foti, E. (2006). *Note di Idraulica Marittima e Ingegneria Costiera*.

Foti, E., Musumeci, R. E., & Stagnitti, M. (2020). Coastal defence techniques and climate change: A review. *Rendiconti Lincei. Scienze Fisiche e Naturali*, *31*(1), 123–138. https://doi.org/10.1007/s12210-020-00877-y

Franzen, M. O., Fernandes, E. H. L., & Siegle, E. (2021). Impacts of coastal structures on hydro-morphodynamic patterns and guidelines towards sustainable coastal development: A case studies review. *Regional Studies in Marine Science*, *44*, 101800. https://doi.org/10.1016/j.rsma.2021.101800

Frihy, O. E., Hassan, M. S., Deabes, E. A., & Badr, A. E. M. A. (2008). Seasonal wave changes and the morphodynamic response of the beach–inner shelf of Abu Qir Bay, Mediterranean coast, Egypt. *Marine Geology*, *247*(3), 145–158. https://doi.org/10.1016/j.margeo.2007.09.001

Froese, R., & Schilling, J. (2019). The nexus of climate change, land use, and conflicts. *Current climate change reports*, *5*, 24–35.

Fu, E., Zhang, Y., Yang, F., & Wang, S. (2022). Temporal self-attention-based Conv-LSTM network for multivariate time series prediction. *Neurocomputing*, *501*, 162–173.

Galeone, P. (2019). *Hands-On Neural Networks with TensorFlow 2.0: Understand TensorFlow, from static graph to eager execution, and design neural networks.*

Gao, J., Kennedy, D. M., & Konlechner, T. M. (2020). Coastal dune mobility over the past century: A global review. *Progress in Physical Geography: Earth and Environment*, *44*(6), 814–836. https://doi.org/10.1177/0309133320919612

García-Nieto, A. P., Geijzendorffer, I. R., Baró, F., Roche, P. K., Bondeau, A., & Cramer, W. (2018). Impacts of urbanization around Mediterranean cities: Changes in ecosystem service supply. *Ecological Indicators*, *91*, 589–606. https://doi.org/10.1016/j.ecolind.2018.03.082

Ghasemirahni, H., Farshin, A., Scazzariello, M., Chiesa, M., & Kostić, D. (2024). *Deploying Stateful Network Functions Efficiently using Large Language Models*. 28–38.

Ghoussein, Y., Mhawej, M., Jaffal, A., Fadel, A., El Hourany, R., & Faour, G. (2018). Vulnerability assessment of the South-Lebanese coast: A GIS-based approach. *Ocean & Coastal Management*, *158*, 56–63. https://doi.org/10.1016/j.ocecoaman.2018.03.028

Gibbard, S., Caldeira, K., Bala, G., Phillips, T. J., & Wickett, M. (2005). Climate effects of global land cover change. *Geophysical Research Letters*, *32*(23), 2005GL024550. https://doi.org/10.1029/2005GL024550

Girshick, R., Donahue, J., Darrell, T., & Malik, J. (2014). *Rich feature hierarchies for accurate object detection and semantic segmentation* (No. arXiv:1311.2524). arXiv. http://arxiv.org/abs/1311.2524

Gonzalez-Perez, A., Abd-Elrahman, A., Wilkinson, B., Johnson, D. J., & Carthy, R. R. (2022). Deep and machine learning image classification of coastal wetlands using unpiloted aircraft system multispectral images and lidar datasets. *Remote Sensing*, *14*(16), 3937.

Gracia, A. de, Rangel-Buitrago, N., Oakley, J. A., & Williams, A. (2018a). Use of ecosystems in coastal erosion management. *Ocean & coastal management*, *156*, 277–289.

Gracia, A. de, Rangel-Buitrago, N., Oakley, J. A., & Williams, A. (2018b). Use of ecosystems in coastal erosion management. *Ocean & coastal management*, *156*, 277–289.

Grasmeijer, B. T., & Kleinhans, M. G. (2004). Observed and predicted bed forms and their effect on suspended sand concentrations. *Coastal Engineering*, *51*(5), 351–371. https://doi.org/10.1016/j.coastaleng.2004.05.001

Graves, A. (2013). Generating sequences with recurrent neural networks. *arXiv preprint arXiv:1308.0850*.

Grimes, M., Carrivick, J. L., Smith, M. W., & Comber, A. J. (2024). Land cover changes across Greenland dominated by a doubling of vegetation in three decades. *Scientific Reports*, *14*(1), 3120. https://doi.org/10.1038/s41598-024-52124-1

Group, T. W. (1988). The WAM model—A third generation ocean wave prediction model. *Journal of physical oceanography*, *18*(12), 1775–1810.

Guimarães, A., Lima, M., Coelho, C., Silva, R., & Veloso-Gomes, F. (2016). Groin impacts on updrift morphology: Physical and numerical study. *Coastal Engineering*, *109*, 63–75. https://doi.org/10.1016/j.coastaleng.2015.12.003

Habib, M. A., & Zarillo, G. A. (2024). Construction of a Real-Time Forecast Model with Deep Learning Techniques for Coastal Engineering and Processes: Nested in a Basin Scale Suite of Models. *Journal of Marine Science and Engineering*, *12*(7), 1152.

Hallermeier, R. J. (1980). A profile zonation for seasonal sand beaches from wave climate. *Coastal Engineering*, *4*, 253–277. https://doi.org/10.1016/0378-3839(80)90022-8

Hanson, H., Kraus, N. C., & Nakashima, L. D. (1989). *Shoreline change behind transmissive detached breakwaters*. *1*(pt1), 568–582. Scopus.

Harley, C. D., Randall Hughes, A., Hultgren, K. M., Miner, B. G., Sorte, C. J., Thornber, C. S., Rodriguez, L. F., Tomanek, L., & Williams, S. L. (2006). The impacts of climate change in coastal marine systems. *Ecology letters*, *9*(2), 228–241.

Hashmi, M. F., Ashish, B. K. K., Keskar, A. G., Bokde, N. D., Yoon, J. H., & Geem, Z. W. (2020). An exploratory analysis on visual counterfeits using conv-lstm hybrid architecture. *IEEE Access*, *8*, 101293–101308.

Hauer, M. E., Hardy, D., Kulp, S. A., Mueller, V., Wrathall, D. J., & Clark, P. U. (2021). Assessing population exposure to coastal flooding due to sea level rise. *Nature Communications*, *12*(1), 6900. https://doi.org/10.1038/s41467-021-27260-1

He, K., Gkioxari, G., Dollár, P., & Girshick, R. (2018). *Mask R-CNN* (No. arXiv:1703.06870). arXiv. http://arxiv.org/abs/1703.06870

Hernández-Delgado, E. A. (2024). Coastal Restoration Challenges and Strategies for Small Island Developing States in the Face of Sea Level Rise and Climate Change. *Coasts*, *4*(2), Articolo 2. https://doi.org/10.3390/coasts4020014

Hewitt, H. T., Bell, M. J., Chassignet, E. P., Czaja, A., Ferreira, D., Griffies, S. M., Hyder, P., McClean, J. L., New, A. L., & Roberts, M. J. (2017). Will high-resolution global ocean models benefit coupled predictions on short-range to climate timescales? *Ocean Modelling*, *120*, 120–136.

Himmelstoss, E., Henderson, R. E., Kratzmann, M. G., & Farris, A. S. (2021). *Digital shoreline analysis system (DSAS) version 5.1 user guide* (Nos. 2331–1258). US Geological Survey.

Hirahara, D., Takaya, E., Kadowaki, M., Kobayashi, Y., & Ueda, T. (2021). Effect of the pixel interpolation method for downsampling medical images on deep learning accuracy. *Journal of Computer and Communications*, *9*(11), 150–156.

Hoptsii, D., Siedov, A., Anopriienko, T., Khainus, D., & Yaremko, D. (2023). *Advantages of using QGIS to solve spatial planning tasks*.

Hu, P., Cheng, W., Xu, G., Han, Y., Yan, N., & Wang, N. (2023). Prediction of buffeting responses of the thin plate under joint action of wave and wind using LSTM and transfer learning. *Applied Ocean Research*, *134*, 103514.

Hussein, K., Alkaabi, K., Ghebreyesus, D., Liaqat, M. U., & Sharif, H. O. (2020). Land use/land cover change along the Eastern Coast of the UAE and its impact on flooding risk. *Geomatics, Natural Hazards and Risk*, *11*(1), Articolo 1.

Indice di correlazione di Pearson. (2024). In *Wikipedia*. https://it.wikipedia.org/w/index.php?title=Indice_di_correlazione_di_Pearson&oldid=137580649

Intergovernmental Panel On Climate Change (Ipcc). (2022). *The Ocean and Cryosphere in a Changing Climate: Special Report of the Intergovernmental Panel on Climate Change* (1ª ed.). Cambridge University Press. https://doi.org/10.1017/9781009157964

Isaacson, M. de S. Q., & MacKenzie, N. G. (1981). Long-term distributions of ocean waves: A review. *Journal of the Waterway, Port, Coastal and Ocean Division*, *107*(2), 93–109.

Iuppa, C., Cavallaro, L., Vicinanza, D., & Foti, E. (2015). Investigation of suitable sites for wave energy converters around Sicily (Italy). *Ocean Science*, *11*(4), 543–557.

Jackson Jr, C. W., Alexander, C. R., & Bush, D. M. (2012). Application of the AMBUR R package for spatio-temporal analysis of shoreline change: Jekyll Island, Georgia, USA. *Computers & Geosciences*, *41*, 199–207.

Jacquez, G. M. (1998). GIS as an Enabling Technology. In *GIS And Health*. CRC Press.

Jamali, A., & Mahdianpari, M. (2022). Swin transformer and deep convolutional neural networks for coastal wetland classification using sentinel-1, sentinel-2, and LiDAR data. *Remote Sensing*, *14*(2), Articolo 2.

James, O. C., Schillereff, D. N., Grieve, S. W., & Baas, A. C. (2024). PyShoreVolume 1.0. 0: A Python based Shoreline Change and beach Volumetric Change Analysis tool. *Computers & Geosciences*, *187*, 105591.

Jordan, P., & Fröhle, P. (2022). Bridging the gap between coastal engineering and nature conservation? *Journal of Coastal Conservation*, *26*(2), 4. https://doi.org/10.1007/s11852-021-00848-x

Jörges, C., Berkenbrink, C., Gottschalk, H., & Stumpe, B. (2023). Spatial ocean wave height prediction with CNN mixed-data deep neural networks using random field simulated bathymetry. *Ocean Engineering*, *271*, 113699.

Kamphuis, J. (1996). Physical modelling of coastal processes. *Advances in coastal and ocean engineering*, *2*, 79–114.

Kamphuis, J. W. (2000). *Introduction to coastal engineering and management* (Vol. 6).

Kandel, I., & Castelli, M. (2020). The effect of batch size on the generalizability of the convolutional neural networks on a histopathology dataset. *ICT express*, *6*(4), 312–315.

Kattenborn, T., Leitloff, J., Schiefer, F., & Hinz, S. (2021). Review on Convolutional Neural Networks (CNN) in vegetation remote sensing. *ISPRS Journal of Photogrammetry and Remote Sensing*, *173*, 24–49. https://doi.org/10.1016/j.isprsjprs.2020.12.010

Khan, M. A., Karim, M. R., & Kim, Y. (2019). A scalable and hybrid intrusion detection system based on the convolutional-LSTM network. *Symmetry*, *11*(4), 583.

Kim, D., Sexton, J. O., & Townshend, J. R. (2015). Accelerated deforestation in the humid tropics from the 1990s to the 2000s. *Geophysical Research Letters*, *42*(9), Articolo 9. https://doi.org/10.1002/2014GL062777

Kim, G. S., Chun, J., Kim, Y., & Kim, C.-K. (2021). Coastal Tourism Spatial Planning at the Regional Unit: Identifying Coastal Tourism Hotspots Based on Social Media Data. *ISPRS International Journal of Geo-Information*, *10*(3), Articolo 3. https://doi.org/10.3390/ijgi10030167

Kingma, D. P. (2014). Adam: A method for stochastic optimization. *arXiv preprint arXiv:1412.6980*.

Kirwan, M. L., & Megonigal, J. P. (2013). Tidal wetland stability in the face of human impacts and sea-level rise. *Nature*, *504*(7478), 53–60. https://doi.org/10.1038/nature12856

Kokkos, N., Zoidou, M., Zachopoulos, K., Nezhad, M. M., Garcia, D. A., & Sylaios, G. (2021). Wind climate and wind power resource assessment based on gridded scatterometer data: A Thracian Sea case study. *Energies*, *14*(12), 3448.

Komen, G. (1986). *Activities of the WAM (Wave Modelling) Group*. SUT-AUTOE.

Kummu, M., De Moel, H., Salvucci, G., Viviroli, D., Ward, P. J., & Varis, O. (2016). Over the hills and further away from coast: Global geospatial patterns of human and environment over the 20th–21st centuries. *Environmental Research Letters*, *11*(3), 034010.

Kuschnerus, T., Redenbach, C., Schladitz, K., Wagner, T., & Zerling, F. (s.d.). *IN-SITU TESTING WITH DIFFEOMORPHIC MAPPING*.

LeBlond, P. H. (1979). An explanation of the logarithmic spiral plan shape of headland-bay beaches. *Journal of Sedimentary Research*, *49*(4), 1093–1100.

Lee, Y., Sim, W., Park, J., & Lee, J. (2022). Evaluation of Hyperparameter Combinations of the U-Net Model for Land Cover Classification. *Forests*, *13*(11), 1813.

Lesser, G. R., Roelvink, J. A., van Kester, J. A. T. M., & Stelling, G. S. (2004). Development and validation of a three-dimensional morphological model. *Coastal Engineering*, *51*(8), 883–915. https://doi.org/10.1016/j.coastaleng.2004.07.014

Li, G., Zhang, H., Lyu, T., & Zhang, H. (2024). Regional significant wave height forecast in the East China Sea based on the Self-Attention ConvLSTM with SWAN model. *Ocean Engineering*, *312*, 119064.

Lim, C., Hsu, J. R. C., & Lee, J. L. (2022). MeePaSoL: A MATLAB-based GUI software tool for shoreline management. *Computers & Geosciences*, *161*, 105059. https://doi.org/10.1016/j.cageo.2022.105059

Lin, G., Milan, A., Shen, C., & Reid, I. (2017). RefineNet: Multi-path Refinement Networks for High-Resolution Semantic Segmentation. *2017 IEEE Conference on Computer Vision and Pattern Recognition (CVPR)*, 5168–5177. https://doi.org/10.1109/CVPR.2017.549

Lin, K., Gong, L., Huang, Y., Liu, C., & Pan, J. (2019). Deep Learning-Based Segmentation and Quantification of Cucumber Powdery Mildew Using Convolutional Neural Network. *Frontiers in Plant Science*, *10*, 155. https://doi.org/10.3389/fpls.2019.00155

Lionello, P., Malanotte-Rizzoli, P., & Boscolo, R. (2006). *Mediterranean climate variability*. Elsevier.

Liu, H., & Jezek, K. C. (2004). *Automated extraction of coastline from satellite imagery by integrating Canny edge detection and locally adaptive thresholding methods.*

Liu, P., Jia, S., Han, R., Liu, Y., Lu, X., & Zhang, H. (2020). RS and GIS Supported Urban LULC and UHI Change Simulation and Assessment. *Journal of Sensors*, *2020*, 1–17. https://doi.org/10.1155/2020/5863164

Liu, X., Huang, Y., Xu, X., Li, X., Li, X., Ciais, P., Lin, P., Gong, K., Ziegler, A. D., Chen, A., Gong, P., Chen, J., Hu, G., Chen, Y., Wang, S., Wu, Q., Huang, K., Estes, L., & Zeng, Z. (2020). High-spatiotemporal-resolution mapping of global urban change from 1985 to 2015. *Nature Sustainability*, *3*(7), Articolo 7. https://doi.org/10.1038/s41893-020-0521-x

Liu, X., Luo, X., Lu, C., Zhang, G., & Ding, W. (2024). The Impact of Foreshore Slope on Cross-Shore Sediment Transport and Sandbar Formation in Beach Berm Nourishment. *Water*, *16*(15), Articolo 15. https://doi.org/10.3390/w16152212

Liu, Y., Huang, L., Ma, X., Zhang, L., Fan, J., & Jing, Y. (2023). A fast, high-precision deep learning model for regional wave prediction. *Ocean Engineering*, *288*, 115949.

Liu, Y., Wang, X., Ling, F., Xu, S., & Wang, C. (2017). Analysis of Coastline Extraction from Landsat-8 OLI Imagery. *Water*, *9*(11), 816. https://doi.org/10.3390/w9110816

Liu, Z., & Balk, D. (2020). Urbanisation and differential vulnerability to coastal flooding among migrants and nonmigrants in Bangladesh. *Population, Space and Place*, *26*(7), e2334. https://doi.org/10.1002/psp.2334

Lloret, J., Turiel, A., Solé, J., Berdalet, E., Sabatés, A., Olivares, A., Gili, J.-M., Vila-Subirós, J., & Sardá, R. (2022). Unravelling the ecological impacts of large-scale offshore wind farms in the Mediterranean Sea. *Science of the Total Environment*, *824*, 153803.

Lo Re, C., Manno, G., Ciraolo, G., & Besio, G. (2019a). Wave energy assessment around the Aegadian Islands (Sicily). *Energies*, *12*(3), Articolo 3.

Lo Re, C., Manno, G., Ciraolo, G., & Besio, G. (2019b). Wave energy assessment around the Aegadian Islands (Sicily). *Energies*, *12*(3), 333.

López Royo, M., Ranasinghe, R., & Jiménez, J. A. (2016). A Rapid, Low-Cost Approach to Coastal Vulnerability Assessment at a National Level. *Journal of Coastal Research*, *320*, 932–945. https://doi.org/10.2112/JCOASTRES-D-14-00217.1

Losada, M. A., & Gimenez-Curto, L. A. (1979). The joint effect of the wave height and period on the stability of rubble mound breakwaters using Iribarren's number. *Coastal Engineering*, *3*, 77–96. https://doi.org/10.1016/0378-3839(79)90011-5

Luijendijk, A., Hagenaars, G., Ranasinghe, R., Baart, F., Donchyts, G., & Aarninkhof, S. (2018). The state of the world's beaches. *Scientific reports*, *8*(1), 1–11.

Luque, P., Gómez-Pujol, L., Marcos, M., & Orfila, A. (2021). Coastal Flooding in the Balearic Islands During the Twenty-First Century Caused by Sea-Level Rise and Extreme Events. *Frontiers in Marine Science*, *8*. https://doi.org/10.3389/fmars.2021.676452

Mahapatra, M., Ramakrishnan, R., & Rajawat, A. S. (2015). Coastal vulnerability assessment using analytical hierarchical process for South Gujarat coast, India. *Natural Hazards*, *76*(1), 139–159. https://doi.org/10.1007/s11069-014-1491-y

Mandal, S., & Chaudhuri, S. (2023). Identification of littoral cell and its impact on shoreline dynamics along the Purba Medinipur–Balasore coastal stretch, Bay of Bengal, India: A numerical modelling and geospatial study. *Regional Studies in Marine Science*, *57*, 102740. https://doi.org/10.1016/j.rsma.2022.102740

Mani Murali, R., Ankita, M., Amrita, S., & Vethamony, P. (2013). Coastal vulnerability assessment of Puducherry coast, India, using the analytical hierarchical process. *Natural Hazards and Earth System Sciences*, *13*(12), 3291–3311. https://doi.org/10.5194/nhess-13-3291-2013

Manno, G., Azzara, G., Lo Re, C., Martinello, C., Basile, M., Rotigliano, E., & Ciraolo, G. (2022a). An Approach for the Validation of a Coastal Erosion Vulnerability Index: An Application in Sicily. *Journal of Marine Science and Engineering*, *11*(1), 23. https://doi.org/10.3390/jmse11010023

Manno, G., Azzara, G., Lo Re, C., Martinello, C., Basile, M., Rotigliano, E., & Ciraolo, G. (2022b). An Approach for the Validation of a Coastal Erosion Vulnerability Index: An Application in Sicily. *Journal of Marine Science and Engineering*, *11*(1), Articolo 1. https://doi.org/10.3390/jmse11010023

Manno, G., Azzara, G., Lo Re, C., Martinello, C., Basile, M., Rotigliano, E., & Ciraolo, G. (2022c). An Approach for the Validation of a Coastal Erosion Vulnerability Index: An Application in Sicily. *Journal of Marine Science and Engineering*, *11*(1), Articolo 1. https://doi.org/10.3390/jmse11010023

Manno, G., Azzara, G., Lo Re, C., Martinello, C., Basile, M., Rotigliano, E., & Ciraolo, G. (2022d). An Approach for the Validation of a Coastal Erosion Vulnerability Index: An Application in Sicily. *Journal of Marine Science and Engineering*, *11*(1), Articolo 1. https://doi.org/10.3390/jmse11010023

Manno, G., & Ciraolo, G. (2015). Diachronic analysis of the shoreline in San Leone beach (Agrigento-Sicily). In *Establishment of an integrated Italy-Malta cross-border system of civil protection-geological aspects* (Vol. 1, pp. 117–136). Aracne.

Manno, G., Lo Re, C., Basile, M., & Ciraolo, G. (2022a). A new shoreline change assessment approach for erosion management strategies. *Ocean & Coastal Management*, *225*, 106226. https://doi.org/10.1016/j.ocecoaman.2022.106226

Manno, G., Lo Re, C., Basile, M., & Ciraolo, G. (2022b). A new shoreline change assessment approach for erosion management strategies. *Ocean & Coastal Management*, *225*, 106226. https://doi.org/10.1016/j.ocecoaman.2022.106226

Manno, G., Lo Re, C., Basile, M., & Ciraolo, G. (2022c). A new shoreline change assessment approach for erosion management strategies. *Ocean & Coastal Management*, *225*, 106226. https://doi.org/10.1016/j.ocecoaman.2022.106226

Mansour, S., Ghoneim, E., El-Kersh, A., Said, S., & Abdelnaby, S. (2023). Spatiotemporal Monitoring of Urban Sprawl in a Coastal City Using GIS-Based Markov Chain and Artificial Neural Network (ANN). *Remote Sensing*, *15*(3), 601.

Martin-Donas, J. M., Gomez, A. M., Gonzalez, J. A., & Peinado, A. M. (2018). A deep learning loss function based on the perceptual evaluation of the speech quality. *IEEE Signal processing letters*, *25*(11), 1680–1684.

Martins, V. N., Pires, R., & Cabral, P. (2012). Modelling of coastal vulnerability in the stretch between the beaches of Porto de Mós and Falésia, Algarve (Portugal). *Journal of Coastal Conservation*, *16*(4), 503–510. https://doi.org/10.1007/s11852-012-0191-6

McCarroll, R. J., Kennedy, D. M., Liu, J., Allan, B., & Ierodiaconou, D. (2024). Design and application of coastal erosion indicators using satellite and drone data for a regional monitoring program. *Ocean & Coastal Management*, *253*, 107146. https://doi.org/10.1016/j.ocecoaman.2024.107146

McGranahan, G., Balk, D., & Anderson, B. (2007). The rising tide: Assessing the risks of climate change and human settlements in low elevation coastal zones. *Environment and urbanization*, *19*(1), 17–37.

McLeod, A. I. (2005). Kendall rank correlation and Mann-Kendall trend test. *R package Kendall*, *602*, 1–10.

Mejjad, N., Laissaoui, A., Fekri, A., & Hammoumi, O. E. (2023). Marine plastic pollution in Morocco: State of the knowledge on origin, occurrence, fate, and management. *Environmental Science and Pollution Research*, *30*(49), 107371–107389. https://doi.org/10.1007/s11356-023-26973-8

Mejjad, N., Rossi, A., & Pavel, A. B. (2022). The coastal tourism industry in the Mediterranean: A critical review of the socio-economic and environmental pressures & impacts. *Tourism Management Perspectives*, *44*, 101007. https://doi.org/10.1016/j.tmp.2022.101007

Menna, M., Poulain, P.-M., Ciani, D., Doglioli, A., Notarstefano, G., Gerin, R., Rio, M.-H., Santoleri, R., Gauci, A., & Drago, A. (2019). New insights of the Sicily Channel and southern Tyrrhenian Sea variability. *Water*, *11*(7), 1355.

Miller, J. K., & Dean, R. G. (2004). A simple new shoreline change model. *Coastal Engineering*, *51*(7), 531–556. https://doi.org/10.1016/j.coastaleng.2004.05.006

Miranda, N. A., Bintoro, R. S., & Prasita, V. D. (2023). The Pattern of Coastline Changes and Wave Modelling around the Expansion of PPI Popoh Tulung Agung, East Java. *Maritime Technology and Research*, *5*(4), 262926–262926.

Molina, R., Manno, G., Lo Re, C., Anfuso, G., & Ciraolo, G. (2020a). A Methodological Approach to Determine Sound Response Modalities to Coastal Erosion Processes in Mediterranean Andalusia (Spain). *Journal of Marine Science and Engineering*, *8*(3), Articolo 3. https://doi.org/10.3390/jmse8030154

Molina, R., Manno, G., Lo Re, C., Anfuso, G., & Ciraolo, G. (2020b). A Methodological Approach to Determine Sound Response Modalities to Coastal Erosion Processes in Mediterranean Andalusia (Spain). *Journal of Marine Science and Engineering*, *8*(3), 154. https://doi.org/10.3390/jmse8030154

Monteforte, M., Re, C. L., & Ferreri, G. (2015). Wave energy assessment in Sicily (Italy). *Renewable Energy*, *78*, 276–287.

Morris, R. L., Bilkovic, D. M., Walles, B., & Strain, E. M. A. (2022). Nature-based coastal defence: Developing the knowledge needed for wider implementation of living shorelines. *Ecological Engineering*, *185*, 106798. https://doi.org/10.1016/j.ecoleng.2022.106798

Mucerino, L., Besio, G., Casella, E., Rovere, A., Ferrari, M., & Firpo, M. (2014, settembre 8). *Validazione del software Xbeach attraverso l'utilizzo di immagini da webcam.*

Muraleedharan, G., Lucas, C., Martins, D., Soares, C. G., & Kurup, P. (2015). On the distribution of significant wave height and associated peak periods. *Coastal Engineering*, *103*, 42–51.

N. Apostolopoulos, D., & G. Nikolakopoulos, K. (2020). Assessment and quantification of the accuracy of low-and high-resolution remote sensing data for shoreline monitoring. *ISPRS International Journal of Geo-Information*, *9*(6), 391.

Nath, A., Koley, B., Choudhury, T., Saraswati, S., Ray, B. C., Um, J.-S., & Sharma, A. (2023). Assessing Coastal Land-Use and Land-Cover Change Dynamics Using Geospatial Techniques. *Sustainability*, *15*(9), Articolo 9. https://doi.org/10.3390/su15097398

Nekrasov, V., Shen, C., & Reid, I. (2018). *Light-Weight RefineNet for Real-Time Semantic Segmentation* (No. arXiv:1810.03272). arXiv. http://arxiv.org/abs/1810.03272

Ngondo, J., Mango, J., Liu, R., Nobert, J., Dubi, A., & Cheng, H. (2021). Land-Use and Land-Cover (LULC) Change Detection and the Implications for Coastal Water Resource Management in the Wami–Ruvu Basin, Tanzania. *Sustainability*, *13*(8), Articolo 8. https://doi.org/10.3390/su13084092

Nguyen, T. T. X., Bonetti, J., Rogers, K., & Woodroffe, C. D. (2016). Indicator-based assessment of climate-change impacts on coasts: A review of concepts, methodological approaches and vulnerability indices. *Ocean & Coastal Management*, *123*, 18–43. https://doi.org/10.1016/j.ocecoaman.2015.11.022

O'Connor, C. S., & Mieras, R. S. (2022). Beach Profile, Water Level, and Wave Runup Measurements Using a Standalone Line-Scanning, Low-Cost (LLC) LiDAR System. *Remote Sensing*, *14*(19), Articolo 19. https://doi.org/10.3390/rs14194968

O'Donncha, F., Hu, Y., Palmes, P., Burke, M., Filgueira, R., & Grant, J. (2022). A spatio-temporal LSTM model to forecast across multiple temporal and spatial scales. *Ecological Informatics*, *69*, 101687.

Oliveira, F. S. B. F., Fortunato, A. B., & Freire, P. (2024). Beach Nourishment Protection against Storms for Contrasting Backshore Typologies. *Journal of Marine Science and Engineering*, *12*(9), Articolo 9. https://doi.org/10.3390/jmse12091465

Ouyang, L., Ling, F., Li, Y., Bai, L., & Luo, J.-J. (2023). Wave forecast in the Atlantic Ocean using a double-stage ConvLSTM network. *Atmospheric and Oceanic Science Letters*, *16*(4), 100347.

Oyedotun, T. D. (2014). Shoreline geometry: DSAS as a tool for historical trend analysis. *Geomorphological techniques*, *3*(2.2), 1–12.

PAI. (s.d.). *PAI – Unità Fisiografiche – S.I.T.R – Sistema Informativo Territoriale Regionale*. Recuperato 8 settembre 2024, da https://www.sitr.regione.sicilia.it/pai/pai-unita-fisiografiche/

Pan, Y., Kuang, C. P., Chen, Y. P., Yin, S., Yang, Y. B., Yang, Y. X., Zhang, J. B., Qiu, R. F., & Zhang, Y. (2018). A comparison of the performance of submerged and detached artificial headlands in a beach nourishment project. *Ocean Engineering*, *159*, 295–304. https://doi.org/10.1016/j.oceaneng.2018.04.038

Paravolidakis, V., Ragia, L., Moirogiorgou, K., & Zervakis, M. (2018). Automatic Coastline Extraction Using Edge Detection and Optimization Procedures. *Geosciences*, *8*(11), 407. https://doi.org/10.3390/geosciences8110407

Pelnard-Considère, R. (1957). *Essai de théorie de l'évolution des formes de rivage en plages de sable et de galets*. https://www.persee.fr/doc/jhydr_0000-0001_1957_act_4_1_3370

Pepe, M., Costantino, D., & Alfio, V. S. (2023). A GIS Procedure to Assess Shoreline Changes over Time Using Multi-temporal Maps: An Analysis of a Sandy Shoreline in Southern Italy over the Last 100 Years. *Geomatics and Environmental Engineering*, *17*(3).

Perugini, L., Caporaso, L., Marconi, S., Cescatti, A., Quesada, B., De Noblet-Ducoudré, N., House, J. I., & Arneth, A. (2017). Biophysical effects on temperature and precipitation due to land cover change. *Environmental Research Letters*, *12*(5), 053002. https://doi.org/10.1088/1748-9326/aa6b3f

Petruzzelli, V. (2012). *Utilizzo di materiali innovativi per lo studio della morfodinamica di spiaggia mediante modelli fisici*.

Petti, M. (2021). *Fondamenti di idraulica marittima e costiera*.

Phiri, D., & Morgenroth, J. (2017). Developments in Landsat land cover classification methods: A review. *Remote Sensing*, *9*(9), 967.

Pinardi, N., & Masetti, E. (2000). Variability of the large scale general circulation of the Mediterranean Sea from observations and modelling: A review. *Palaeogeography, Palaeoclimatology, Palaeoecology*, *158*(3–4), 153–173.

Pollard, J. A., Spencer, T., Brooks, S. M., Christie, E. K., & Möller, I. (2020). Understanding spatio-temporal barrier dynamics through the use of multiple shoreline proxies. *Geomorphology*, *354*, 107058. https://doi.org/10.1016/j.geomorph.2020.107058

Pombo, R., Fernández-Fernández, S., Baptista, P., Coelho, C., & Bernardes, C. (2022). Old forecasts vs actual shoreline evolution: Assessing model's performance and projections accuracy. *Coastal Engineering*, *175*, 104143. https://doi.org/10.1016/j.coastaleng.2022.104143

Pomianowski, A., & Doburzynski, S. (2021). The Importance of Coastal Cities and Regions in Selected European Countries. *EUROPEAN RESEARCH STUDIES JOURNAL*, *XXIV*(Issue 4), 578–589. https://doi.org/10.35808/ersj/2608

Port, D., & Korte, M. (2008). *Comparative studies of the model evaluation criterions MMRE and PRED in software cost estimation research*. 51–60.

Pranzini, E. (1992). *La difesa dei litorali in Italia. L'erosione delle coste. Le opere di difesa. Il ripascimento artificiale. Gli interventi di difesa realizzati in Italia. La valutazione dell'efficacia*.

Pranzini, E. (2004a). *La forma delle coste. Geomorfologia costiera, impatto antropico e difesa dei litorali*.

Pranzini, E. (2004b). *La forma delle coste. Geomorfologia costiera, impatto antropico e difesa dei litorali*.

Pranzini, E., Anfuso, G., Cinelli, I., Piccardi, M., & Vitale, G. (2018). Shore Protection Structures Increase and Evolution on the Northern Tuscany Coast (Italy): Influence of Tourism Industry. *Water*, *10*(11), 1647. https://doi.org/10.3390/w10111647

Pranzini, E., Cinelli, I., Cipriani, L. E., & Anfuso, G. (2020). An Integrated Coastal Sediment Management Plan: The Example of the Tuscany Region (Italy). *Journal of Marine Science and Engineering*, *8*(1), 33. https://doi.org/10.3390/jmse8010033

Pranzini, E., & Williams, A. T. (2021a). The Equilibrium Concept, or…(Mis)concept in Beaches. *Geosciences*, *11*(2), Articolo 2. https://doi.org/10.3390/geosciences11020059

Pranzini, E., & Williams, A. T. (2021b). The Equilibrium Concept, or…(Mis)concept in Beaches. *Geosciences*, *11*(2), Articolo 2. https://doi.org/10.3390/geosciences11020059

Rangel-Buitrago, N., de Jonge, V. N., & Neal, W. (2018a). How to make integrated coastal erosion management a reality. *Ocean & Coastal Management*, *156*, 290–299.

Rangel-Buitrago, N., de Jonge, V. N., & Neal, W. (2018b). How to make integrated coastal erosion management a reality. *Ocean & Coastal Management*, *156*, 290–299.

Reeve, D. E., & Valsamidis, A. (2014). On the stability of a class of shoreline planform models. *Coastal Engineering*, *91*, 76–83. https://doi.org/10.1016/j.coastaleng.2014.05.005

Robinson, A., Golnaraghi, M., Leslie, W., Artegiani, A., Hecht, A., Lazzoni, E., Michelato, A., Sansone, E., Theocharis, A., & Ünlüata, Ü. (1991). The eastern Mediterranean general circulation: Features, structure and variability. *Dynamics of Atmospheres and Oceans*, *15*(3–5), 215–240.

Rocha, C., Antunes, C., & Catita, C. (2023). Coastal indices to assess sea-level rise impacts—A brief review of the last decade. *Ocean & Coastal Management*, *237*, 106536. https://doi.org/10.1016/j.ocecoaman.2023.106536

Rodriguez-Delgado, C., Bergillos, R. J., & Iglesias, G. (2019). An artificial neural network model of coastal erosion mitigation through wave farms. *Environmental Modelling & Software*, *119*, 390–399. https://doi.org/10.1016/j.envsoft.2019.07.010

Roelvink, D., Reniers, A., van Dongeren, A., van Thiel de Vries, J., McCall, R., & Lescinski, J. (2009). Modelling storm impacts on beaches, dunes and barrier islands. *Coastal Engineering*, *56*(11), 1133–1152. https://doi.org/10.1016/j.coastaleng.2009.08.006

Romano, B., Zullo, F., Fiorini, L., & Marucci, A. (2021). Illegal building in Italy: Too complex a problem for national land policy? *Cities*, *112*, 103159.

Ronneberger, O., Fischer, P., & Brox, T. (2015). *U-Net: Convolutional Networks for Biomedical Image Segmentation* (No. arXiv:1505.04597). arXiv. http://arxiv.org/abs/1505.04597

Rosas-Chavoya, M., Gallardo-Salazar, J. L., López-Serrano, P. M., Alcántara-Concepción, P. C., & León-Miranda, A. K. (2022). QGIS a constantly growing free and open-source geospatial software contributing to scientific development. *Cuadernos de Investigación Geográfica*, *48*(1), 197–213.

Saengsupavanich, C. (2021). Morphological evolution of sand spits in Thailand. *Marine Geodesy*, *44*(5), 432–453.

Saengsupavanich, C., Yun, L. S., Lee, L. H., & Sanitwong-Na-Ayutthaya, S. (2022). Intertidal intercepted sediment at jetties along the Gulf of Thailand. *Frontiers in Marine Science*, *9*, 970592.

Salhi, A., Benabdelouahab, S., Bouayad, E. O., Benabdelouahab, T., Larifi, I., El Mousaoui, M., Acharrat, N., Himi, M., & Ponsati, A. C. (2021). Impacts and social implications of landuse-environment conflicts in a typical Mediterranean watershed. *Science of the Total Environment*, *764*, 142853.

Salvati, L., Smiraglia, D., Bajocco, S., & Munafò, M. (2014). *Land Use Changes in Two Mediterranean Coastal Regions: Do Urban Areas Matter?* (No. 9). *8*(9), Articolo 9.

Sanhory, A., El-Tahan, M., Moghazy, H. M., & Reda, W. (2022). Natural and manmade impact on Rosetta eastern shoreline using satellite Image processing technique. *Alexandria Engineering Journal*, *61*(8), 6247–6260. https://doi.org/10.1016/j.aej.2021.11.053

Sanitwong-Na-Ayutthaya, S., Saengsupavanich, C., Ariffin, E. H., Buayam, S., Wiramitchai, L., Kayunha, K., & Charuseiam, Y. (2022). Coastal protection by a stepped concrete revetment in Thailand. *J. Sustainability Sci. Manage.*, *17*, 28–45.

Sapkota, Y., & White, J. R. (2019). Marsh edge erosion and associated carbon dynamics in coastal Louisiana: A proxy for future wetland-dominated coastlines world-wide. *Estuarine, Coastal and Shelf Science*, *226*, 106289. https://doi.org/10.1016/j.ecss.2019.106289

Sartini, L., Besio, G., & Cassola, F. (2017). Spatio-temporal modelling of extreme wave heights in the Mediterranean Sea. *Ocean Modelling*, *117*, 52–69.

Satta, A., Puddu, M., Venturini, S., & Giupponi, C. (2017). Assessment of coastal risks to climate change related impacts at the regional scale: The case of the Mediterranean region. *International Journal of Disaster Risk Reduction*, *24*, 284–296. https://doi.org/10.1016/j.ijdrr.2017.06.018

Scala, P., Manno, G., & Ciraolo, G. (2024a). Coastal dynamics analyzer (CDA): A QGIS plugin for transect based analysis of coastal erosion. *SoftwareX*, *28*, 101894. https://doi.org/10.1016/j.softx.2024.101894

Scala, P., Manno, G., & Ciraolo, G. (2024b). *COAST-PROSIM: UN MODELLO DI SIMULAZIONE DEGLI EFFETTI DELLE OPERE DI DIFESA COSTIERA SULLA LINEA DI RIVA*. IT. https://iris.unipa.it/handle/10447/655533

Scala, P., Manno, G., & Ciraolo, G. (2024c). Semantic segmentation of coastal aerial/satellite images using Deep Learning techniques: An application to coastline detection. *Computers & Geosciences*, 105704.

Scala, P., Manno, G., & Ciraolo, G. (2024d). Semantic segmentation of coastal aerial/satellite images using Deep Learning techniques: An application to coastline detection. *Computers & Geosciences*, 105704.

Scala, P., Toimil, A., Álvarez-Cuesta, M., Manno, G., & Ciraolo, G. (2024). Mapping decadal land cover dynamics in Sicily's coastal regions. *Scientific Reports*, *14*(1), 22222. https://doi.org/10.1038/s41598-024-73085-5

Scala, P., Manno, G., Cozar, L. C., & Ciraolo, G. (2025). COAST-PROSIM: A Model for Predicting Shoreline Evolution and Assessing the Impacts of Coastal Defence Structures. Water, 17(2), 269, https://doi.org/10.3390/w17020269

Scardino, G., Scicchitano, G., Chirivì, M., Costa, P. J. M., Luparelli, A., & Mastronuzzi, G. (2022a). Convolutional Neural Network and Optical Flow for the Assessment of Wave and Tide Parameters from Video Analysis (LEUCOTEA): An Innovative Tool for Coastal Monitoring. *Remote Sensing*, *14*(13), Articolo 13. https://doi.org/10.3390/rs14132994

Scardino, G., Scicchitano, G., Chirivì, M., Costa, P. J. M., Luparelli, A., & Mastronuzzi, G. (2022b). Convolutional Neural Network and Optical Flow for the Assessment of Wave and Tide Parameters from Video Analysis (LEUCOTEA): An Innovative Tool for Coastal Monitoring. *Remote Sensing*, *14*(13), 2994. https://doi.org/10.3390/rs14132994

Scepan, J. (1999). Thematic validation of high-resolution global land-cover data sets. *Photogrammetric engineering and remote sensing*, *65*, 1051–1060.

Seale, C., Redfern, T., Chatfield, P., Luo, C., & Dempsey, K. (2022). Coastline detection in satellite imagery: A deep learning approach on new benchmark data. *Remote Sensing of Environment*, *278*, 113044. https://doi.org/10.1016/j.rse.2022.113044

Setiyanto, I., Wijayanto, D., Wibowo, B., & Dewi, D. A. (2022). Important-performance analysis of marine tourism development in Karimunjawa Island. *AACL Bioflux*, *16*, 2912–2922.

Sherwood, C. R., Van Dongeren, A., Doyle, J., Hegermiller, C. A., Hsu, T.-J., Kalra, T. S., Olabarrieta, M., Penko, A. M., Rafati, Y., & Roelvink, D. (2022). Modeling the morphodynamics of coastal responses to extreme events: What shape are we in? *Annual review of marine science*, *14*(1), 457–492.

Shetty, S. (s.d.). *Analysis of Machine Learning Classifiers for LULC Classification on Google Earth Engine*.

Shi, J., Dang, J., Cui, M., Zuo, R., Shimizu, K., Tsunoda, A., & Suzuki, Y. (2021). Improvement of Damage Segmentation Based on Pixel-Level Data Balance Using VGG-Unet. *Applied Sciences*, *11*(2), 518. https://doi.org/10.3390/app11020518

Shi, X., Chen, Z., Wang, H., Yeung, D.-Y., Wong, W.-K., & Woo, W. (2015). Convolutional LSTM network: A machine learning approach for precipitation nowcasting. *Advances in neural information processing systems*, *28*.

Shilland, R., Grimsditch, G., Ahmed, M., Bandeira, S., Kennedy, H., Potouroglou, M., & Huxham, M. (2021). A question of standards: Adapting carbon and other PES markets to work for community seagrass conservation. *Marine Policy*, *129*, 104574. https://doi.org/10.1016/j.marpol.2021.104574

Silva, A. N., Taborda, R., Andrade, C., & Ribeiro, M. (2019). The future of insular beaches: Insights from a past-to-future sediment budget approach. *Science of The Total Environment*, *676*, 692–705. https://doi.org/10.1016/j.scitotenv.2019.04.228

Silvester, R., & Hsu, J. R. C. (1997). *Coastal Stabilization. Advanced Series on Ocean Engineering: Volume 14* (Vol. 14).

Smith, K. E. L., Terrano, J. F., Pitchford, J. L., & Archer, M. J. (2021). Coastal Wetland Shoreline Change Monitoring: A Comparison of Shorelines from High-Resolution WorldView Satellite Imagery, Aerial Imagery, and Field Surveys. *Remote Sensing*, *13*(15), Articolo 15. https://doi.org/10.3390/rs13153030

Smith, M. J., & Cromley, R. G. (2012). Measuring Historical Coastal Change using GIS and the Change Polygon Approach. *Transactions in GIS*, *16*(1), 3–15. https://doi.org/10.1111/j.1467-9671.2011.01292.x

Song, T., Han, R., Meng, F., Wang, J., Wei, W., & Peng, S. (2022). A significant wave height prediction method based on deep learning combining the correlation between wind and wind waves. *Frontiers in Marine Science*, *9*, 983007.

Spalding, M. D., Ruffo, S., Lacambra, C., Meliane, I., Hale, L. Z., Shepard, C. C., & Beck, M. W. (2014). The role of ecosystems in coastal protection: Adapting to climate change and coastal hazards. *Ocean & Coastal Management*, *90*, 50–57. https://doi.org/10.1016/j.ocecoaman.2013.09.007

Srivastava, N., Hinton, G., Krizhevsky, A., Sutskever, I., & Salakhutdinov, R. (2014). Dropout: A simple way to prevent neural networks from overfitting. *The journal of machine learning research*, *15*(1), 1929–1958.

Stocker, T., & Qin, D. (A c. Di). (2013). *Climate change 2013: The physical science basis: summary for policymakers, a report of working group I of the IPCC: technical summary, a report accepted by working group I of the IPCC but not approved in detail: and frequently asked questions: part of the working group I contribution to the fifth assessment report of the intergovernmental panel on climate change*. WMO, UNEP.

Sultan, A. S., Elgharib, M. A., Tavares, T., Jessri, M., & Basile, J. R. (2020). The use of artificial intelligence, machine learning and deep learning in oncologic histopathology. *Journal of Oral Pathology & Medicine*, *49*(9), 849–856. https://doi.org/10.1111/jop.13042

Syvitski, J. P. M., Kettner, A. J., Overeem, I., Hutton, E. W. H., Hannon, M. T., Brakenridge, G. R., Day, J., Vörösmarty, C., Saito, Y., Giosan, L., & Nicholls, R. J. (2009). Sinking deltas due to human activities. *Nature Geoscience*, *2*(10), Articolo 10. https://doi.org/10.1038/ngeo629

Tackley, H. A., Kurylyk, B. L., Lake, C. B., Lapen, D. R., & van Proosdij, D. (2023). Impacts of repeated coastal flooding on soil and groundwater following managed dike realignment. *Science of The Total Environment*, *893*, 164957. https://doi.org/10.1016/j.scitotenv.2023.164957

Tanveer, M., Kim, B., Hong, J., Sim, S.-H., & Cho, S. (2022). Comparative Study of Lightweight Deep Semantic Segmentation Models for Concrete Damage Detection. *Applied Sciences*, *12*(24), 12786. https://doi.org/10.3390/app122412786

Tassi, A., & Vizzari, M. (2020). Object-Oriented LULC Classification in Google Earth Engine Combining SNIC, GLCM, and Machine Learning Algorithms. *Remote Sensing*, *12*(22), 3776. https://doi.org/10.3390/rs12223776

Terres de Lima, L., Fernández-Fernández, S., Marcel de Almeida Espinoza, J., da Guia Albuquerque, M., & Bernardes, C. (2021). End Point Rate tool for QGIS (EPR4Q): Validation using DSAS and AMBUR. *ISPRS International Journal of Geo-Information*, *10*(3), 162.

Thanh Doan, N. (2021). Improving the efficiency of using deep learning model to determine shoreline position in high-resolution satellite imagery. *E3S Web of Conferences*, *310*, 04002. https://doi.org/10.1051/e3sconf/202131004002

Thanh Noi, P., & Kappas, M. (2018). Comparison of random forest, k-nearest neighbor, and support vector machine classifiers for land cover classification using Sentinel-2 imagery. *Sensors*, *18*(1), Articolo 1.

Thornton, E. B., MacMahan, J., & Sallenger, A. H. (2007). Rip currents, mega-cusps, and eroding dunes. *Marine Geology*, *240*(1), 151–167. https://doi.org/10.1016/j.margeo.2007.02.018

Toimil, A., Camus, P., Losada, I. J., Le Cozannet, G., Nicholls, R. J., Idier, D., & Maspataud, A. (2020). Climate change-driven coastal erosion modelling in temperate sandy beaches: Methods and uncertainty treatment. *Earth-Science Reviews*, *202*, 103110. https://doi.org/10.1016/j.earscirev.2020.103110

Toimil, A., Losada, I. J., Nicholls, R. J., Dalrymple, R. A., & Stive, M. J. F. (2020a). Addressing the challenges of climate change risks and adaptation in coastal areas: A review. *Coastal Engineering*, *156*, 103611. https://doi.org/10.1016/j.coastaleng.2019.103611

Toimil, A., Losada, I. J., Nicholls, R. J., Dalrymple, R. A., & Stive, M. J. F. (2020b). Addressing the challenges of climate change risks and adaptation in coastal areas: A review. *Coastal Engineering*, *156*, 103611. https://doi.org/10.1016/j.coastaleng.2019.103611

Toimil, A., Losada, I. J., Nicholls, R. J., Dalrymple, R. A., & Stive, M. J. F. (2020c). Addressing the challenges of climate change risks and adaptation in coastal areas: A review. *Coastal Engineering*, *156*, 103611. https://doi.org/10.1016/j.coastaleng.2019.103611

Tolman, H. L. (1991). A third-generation model for wind waves on slowly varying, unsteady, and inhomogeneous depths and currents. *Journal of Physical Oceanography*, *21*(6), 782–797.

Torresan, S., Critto, A., Dalla Valle, M., Harvey, N., & Marcomini, A. (2008). Assessing coastal vulnerability to climate change: Comparing segmentation at global and regional scales. *Sustainability Science*, *3*(1), 45–65. https://doi.org/10.1007/s11625-008-0045-1

Toure, S., Diop, O., Kpalma, K., & Maiga, A. (2019a). Shoreline Detection using Optical Remote Sensing: A Review. *ISPRS International Journal of Geo-Information*, *8*(2), Articolo 2. https://doi.org/10.3390/ijgi8020075

Toure, S., Diop, O., Kpalma, K., & Maiga, A. (2019b). Shoreline Detection using Optical Remote Sensing: A Review. *ISPRS International Journal of Geo-Information*, *8*(2), 75. https://doi.org/10.3390/ijgi8020075

Trends and Composition—A Sedimentological-Chemical-Mineralogical Approach to Constrain the Origin of Quaternary Deposits and Landforms—From a Review to a Manual. (s.d.). Recuperato 5 novembre 2024, da https://www.mdpi.com/2076-3263/12/1/24

Truong, V. T., Hirayama, S., Phan, D. C., Hoang, T. T., Tadono, T., & Nasahara, K. N. (2024). JAXA's new high-resolution land use land cover map for Vietnam using a time-feature convolutional neural network. *Scientific Reports*, *14*(1), 3926. https://doi.org/10.1038/s41598-024-54308-1

Tyagi, S., & Mittal, S. (2020). *Sampling approaches for imbalanced data classification problem in machine learning*. 209–221.

Uda, T. (2022). Fundamental issues in Japan's coastal management system for the prevention of beach erosion. *Maritime Technology and Research*, *4*(1), 251788–251788.

Upreti, K., Arora, S., Sharma, A. K., Pandey, A. K., Sharma, K. K., & Dayal, M. (2023). Wave height forecasting over ocean of things based on machine learning techniques: An

application for ocean renewable energy generation. *IEEE Journal of Oceanic Engineering*.

Valsamidis, A., & Reeve, D. E. (2020). A new approach to analytical modelling of groyne fields. *Continental Shelf Research*, *211*, 104288. https://doi.org/10.1016/j.csr.2020.104288

van Rijn, L. C. (2011). Coastal erosion and control. *Ocean & Coastal Management*, *54*(12), Articolo 12. https://doi.org/10.1016/j.ocecoaman.2011.05.004

van Vliet, J., Bregt, A. K., & Hagen-Zanker, A. (2011). Revisiting Kappa to account for change in the accuracy assessment of land-use change models. *Ecological modelling*, *222*(8), 1367–1375.

Vasarmidis, P., Klonaris, G., Zijlema, M., Stratigaki, V., & Troch, P. (2024). A study of the non-linear properties and wave generation of the multi-layer non-hydrostatic wave model SWASH. *Ocean Engineering*, *302*, 117633. https://doi.org/10.1016/j.oceaneng.2024.117633

Venter, Z. S., Barton, D. N., Chakraborty, T., Simensen, T., & Singh, G. (2022). Global 10 m Land Use Land Cover Datasets: A Comparison of Dynamic World, World Cover and Esri Land Cover. *Remote Sensing*, *14*(16), Articolo 16.

Vincent, O., & Folorunso, O. (2009). *A Descriptive Algorithm for Sobel Image Edge Detection*. InSITE 2009: Informing Science + IT Education Conference. https://doi.org/10.28945/3351

Vivas, E., Allende-Cid, H., & Salas, R. (2020). A systematic review of statistical and machine learning methods for electrical power forecasting with reported mape score. *Entropy*, *22*(12), 1412.

Wahl, T., & Plant, N. G. (2015). Changes in erosion and flooding risk due to long-term and cyclic oceanographic trends. *Geophysical Research Letters*, *42*(8), 2943–2950. https://doi.org/10.1002/2015GL063876

Wang, M., She, A., Chang, H., Cheng, F., & Yang, H. (2024). A deep inverse convolutional neural network-based semantic classification method for land cover remote sensing images. *Scientific Reports*, *14*(1), 7313. https://doi.org/10.1038/s41598-024-57408-0

Wang, N., Wang, Y., & Er, M. J. (2022). Review on deep learning techniques for marine object recognition: Architectures and algorithms. *Control Engineering Practice*, *118*, 104458.

Wang, P., & Beck, T. M. (2022). *Beach-Inlet Interaction and Sediment Management*. Cambridge University Press.

Wang, Y., Sun, Y., Cao, X., Wang, Y., Zhang, W., & Cheng, X. (2023). A review of regional and Global scale Land Use/Land Cover (LULC) mapping products generated from satellite remote sensing. *ISPRS Journal of Photogrammetry and Remote Sensing*, *206*, 311–334.

Wang, Y., Wang, H., Zhou, B., & Fu, H. (2021). Multi-dimensional prediction method based on Bi-LSTMC for ship roll. *Ocean Engineering*, *242*, 110106.

Warren, I. R., & Bach, H. K. (1992). MIKE 21: A modelling system for estuaries, coastal waters and seas. *Environmental Software*, *7*(4), 229–240. https://doi.org/10.1016/0266-9838(92)90006-P

Wells, J. T. (1995). Effects of Sea Level Rise on Coastal Sedimention and Erosion. In *Climate ChangeImpact on Coastal Habitation*. CRC Press.

Wernette, P. A., Buscombe, D. D., & Favela, J., Fitzpatrick, S., and Goldstein E. (2022). *Coast Train—Labeled imagery for training and evaluation of data-driven models for image segmentation: U.S. Geological Survey data release*. https://doi.org/10.5066/P91NP87I.

Winkler, K., Fuchs, R., Rounsevell, M., & Herold, M. (2021). Global land use changes are four times greater than previously estimated. *Nature Communications*, *12*(1), Articolo 1. https://doi.org/10.1038/s41467-021-22702-2

Witjes, M., Parente, L., van Diemen, C. J., Hengl, T., Landa, M., Brodský, L., Halounova, L., Križan, J., Antonić, L., & Ilie, C. M. (2022a). A spatiotemporal ensemble machine learning framework for generating land use/land cover time-series maps for Europe (2000–2019) based on LUCAS, CORINE and GLAD Landsat. *PeerJ*, *10*, e13573.

Witjes, M., Parente, L., van Diemen, C. J., Hengl, T., Landa, M., Brodský, L., Halounova, L., Križan, J., Antonić, L., & Ilie, C. M. (2022b). A spatiotemporal ensemble machine learning framework for generating land use/land cover time-series maps for Europe (2000–2019) based on LUCAS, CORINE and GLAD Landsat. *PeerJ*, *10*, e13573.

Wu, L., Tajima, Y., Yamanaka, Y., Shimozono, T., & Sato, S. (2019). Study on characteristics of SAR imagery around the coast for shoreline detection. *Coastal Engineering Journal*, *61*(2), 152–170. https://doi.org/10.1080/21664250.2018.1560685

Yin, K., Xu, S., Gong, S., Chen, J., Wang, Y., & Li, M. (2022a). Modeling wave attenuation by submerged flexible vegetation with XBeach phase-averaged model. *Ocean Engineering*, *257*, 111646. https://doi.org/10.1016/j.oceaneng.2022.111646

Yin, K., Xu, S., Gong, S., Chen, J., Wang, Y., & Li, M. (2022b). Modeling wave attenuation by submerged flexible vegetation with XBeach phase-averaged model. *Ocean Engineering*, *257*, 111646. https://doi.org/10.1016/j.oceaneng.2022.111646

Yun, L. S., Saengsupavanich, C., Ariffin, E. H., & Rashidi, A. H. M. (2023). The morphodynamics of wave on a monsoon-dominated coasts: West coast of GoT. *Regional Studies in Marine Science*, *57*, 102729.

Zacharioudaki, A., & Reeve, D. E. (2008). *Semianalytical Solutions of Shoreline Response to Time-Varying Wave Conditions | Journal of Waterway, Port, Coastal, and Ocean Engineering | Vol 134, No 5*. https://ascelibrary.org/doi/abs/10.1061/(ASCE)0733-950X(2008)134:5(265)

Zanfi, F. (2013). The Città Abusiva in Contemporary Southern Italy: Illegal Building and Prospects for Change. *Urban Studies*, *50*(16), 3428–3445. https://doi.org/10.1177/0042098013484542

Zhai, T., Wang, J., Fang, Y., Qin, Y., Huang, L., & Chen, Y. (2020). Assessing ecological risks caused by human activities in rapid urbanization coastal areas: Towards an integrated approach to determining key areas of terrestrial-oceanic ecosystems preservation and restoration. *Science of The Total Environment*, *708*, 135153. https://doi.org/10.1016/j.scitotenv.2019.135153

Zhang, X., & Li, X. (2020). Combination of satellite observations and machine learning method for internal wave forecast in the Sulu and Celebes seas. *IEEE Transactions on Geoscience and Remote Sensing*, *59*(4), 2822–2832.

Zhang, Y., Zhao, D., Zhang, J., Xiong, R., & Gao, W. (2011). Interpolation-dependent image downsampling. *IEEE Transactions on Image Processing*, *20*(11), 3291–3296.

Zhao, Q., Pepe, A., Devlin, A., Zhang, S., Falabella, F., Zeni, G., Wang, Q., Ding, J., Dong, D., & Liu, M. (2021). Impact of sea-level-rise and human activities in coastal regions: An overview. *Journal of Geodesy and Geoinformation Science*, *4*(1), Articolo 1.

Zheng, G., Li, X., Zhang, R.-H., & Liu, B. (2020). Purely satellite data–driven deep learning forecast of complicated tropical instability waves. *Science advances*, *6*(29), eaba1482.

Zheng, Q.-H., Chen, W., Li, S.-L., Yu, L., Zhang, X., Liu, L.-F., Singh, R. P., & Liu, C.-Q. (2021). Accuracy comparison and driving factor analysis of LULC changes using multi-source time-series remote sensing data in a coastal area. *Ecological Informatics*, *66*, 101457. https://doi.org/10.1016/j.ecoinf.2021.101457

Zheng, Z., Ali, M., Jamei, M., Xiang, Y., Abdulla, S., Yaseen, Z. M., & Farooque, A. A. (2023). Multivariate data decomposition based deep learning approach to forecast one-day ahead significant wave height for ocean energy generation. *Renewable and Sustainable Energy Reviews*, *185*, 113645.

Zheng, Z., Wu, Z., Chen, Y., Yang, Z., & Marinello, F. (2020). Exploration of eco-environment and urbanization changes in coastal zones: A case study in China over the past 20 years. *Ecological Indicators*, *119*, 106847. https://doi.org/10.1016/j.ecolind.2020.106847

Zhou, H., & Liu, Y. (2008). Accurate integration of multi-view range images using k-means clustering. *Pattern Recognition*, *41*(1), Articolo 1.

Zhou, X., Liu, Z., Wang, F., Xie, Y., & Zhang, X. (2020). Using deep learning to forecast maritime vessel flows. *Sensors*, *20*(6), 1761.

Zhu, Q., Li, P., Li, Z., Pu, S., Wu, X., Bi, N., & Wang, H. (2021). Spatiotemporal Changes of Coastline over the Yellow River Delta in the Previous 40 Years with Optical and SAR Remote Sensing. *Remote Sensing*, *13*(10), 1940. https://doi.org/10.3390/rs13101940

Zijlema, M., Stelling, G., & Smit, P. (2011). SWASH: An operational public domain code for simulating wave fields and rapidly varied flows in coastal waters. *Coastal Engineering*, *58*(10), 992–1012. https://doi.org/10.1016/j.coastaleng.2011.05.015

Zong, S., Hu, Y., Zhang, Y., & Wang, W. (2021). Identification of land use conflicts in China's coastal zones: From the perspective of ecological security. *Ocean & Coastal Management*, *213*, 105841. https://doi.org/10.1016/j.ocecoaman.2021.105841

Zou, X., Xiao, F., Yu, Z., Li, Y., & Lee, Y. J. (2023). Delving Deeper into Anti-Aliasing in ConvNets. *International Journal of Computer Vision*, *131*(1), 67–81. https://doi.org/10.1007/s11263-022-01672-y